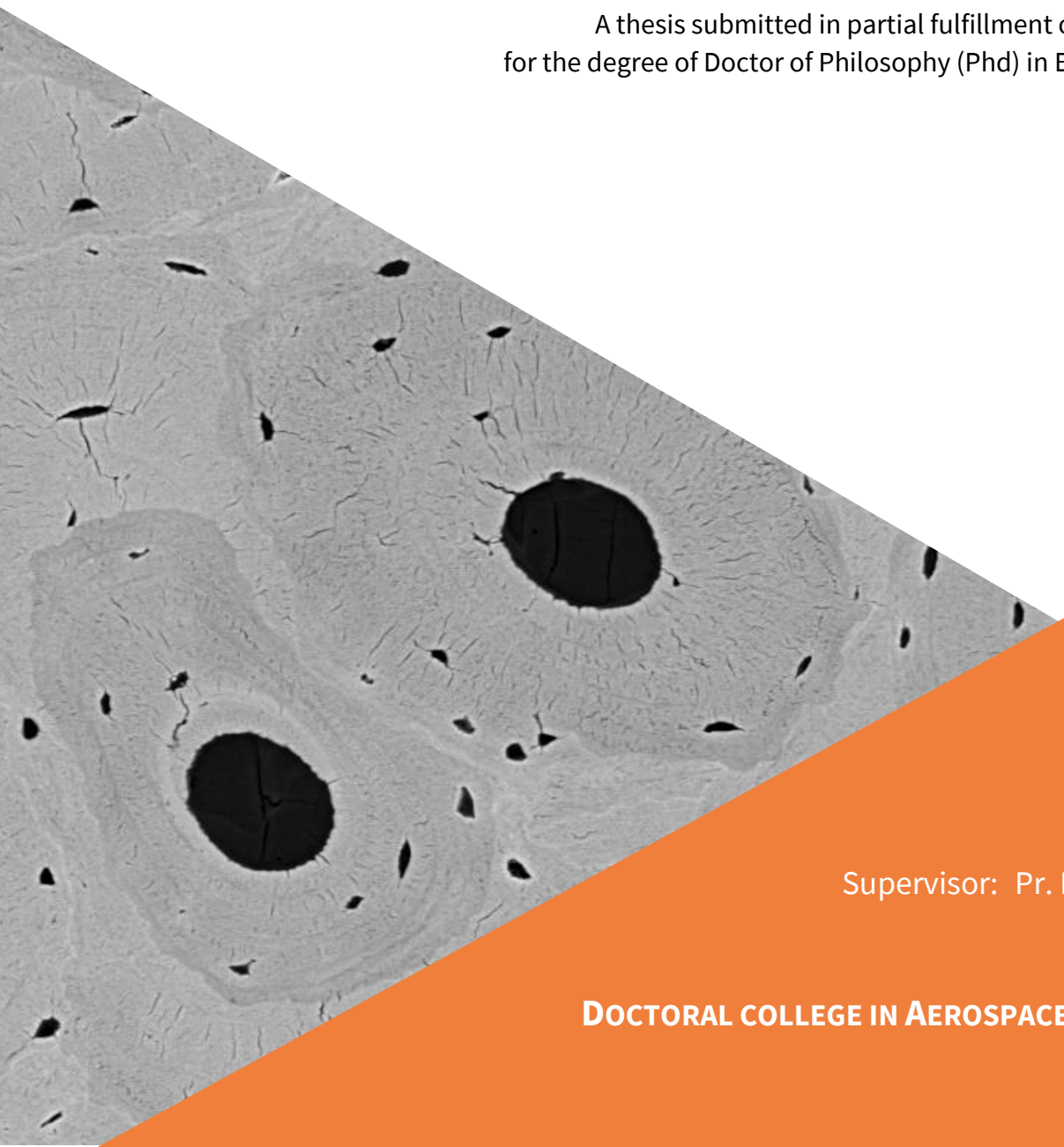
LIÈGE université
Sciences Appliquées

Looking Beyond the Boundaries

High-Resolution Multimodal Characterization of Material, Mechanical, and Biological Properties of the Cement Line in Human Osteonal Bone

A thesis submitted in partial fulfillment of the requirements
for the degree of Doctor of Philosophy (Phd) in Engineering Science



Supervisor: Pr. Davide RUFFONI

DOCTORAL COLLEGE IN AEROSPACE AND MECHANICS

APRIL 2025

University of Liège

Doctoral College in Aerospace and Mechanics

Mechanics of Biological and Bioinspired Materials Laboratory

Looking Beyond the Boundaries

High-Resolution Multimodal Characterization of Material, Mechanical, and Biological Properties of the Cement Line in Human Osteonal Bone

A thesis submitted in partial fulfillment of the requirements for the degree of Doctor of Philosophy (PhD) in Engineering Science

by

Astrid CANTAMESSA

Supervisor

Davide Ruffoni

Jury members

Cédric Schwartz
G. Harry Van Lenthe
Natalie Sims
Richard Weinkamer
Davide Ruffoni

April 2025

© Astrid Cantamessa, ULiège - Faculty of Applied Sciences - Quartier Polytech 1, Allée de la Découverte, 12 - B4000 Liège (Belgium).

All rights reserved. No part of the publication may be reproduced in any form without written permission from the author. This thesis was funded by the FRIA/FRS-FNRS (Belgian Scientific Research Fund).

Tous droits réservés. Aucun extrait de cet ouvrage ne peut être reproduit sous quelque forme que ce soit, sans le consentement écrit et préalable de l'autrice. Cette thèse a été financée par le FRIA/FRS-FNRS (Fonds de la Recherche Scientifique belge).

"Nothing in life is to be feared, it is only to be understood. Now is the time to understand more, so that we may fear less."

— Marie Curie

Abstract

Biological materials have developed remarkable structural strategies to achieve multiple mechanical functions while preserving durability. Among them, bone stands out for its unique ability to combine stiffness, strength, and toughness—properties that are typically mutually exclusive in engineering materials. This exceptional mechanical behavior arises from its complex hierarchical structure and, critically, from its internal interfaces. One such interface, the cement line (CL), is a well-known structural feature found in challenging locations such as at the soft tissue-bone junctions and bordering bone packets in trabecular bone and secondary osteons in cortical bone. Despite its ubiquity, the functional role of the CL remains poorly understood. While it is often assumed to contribute to the mechanical behavior and to alter the continuity of the osteocyte lacuno-canalicular network (OLCN), its exact material properties, structural organization, and biological significance have not been fully characterized.

In this context, the aim of this thesis is to elucidate CL mineral content and mineralization, mechanical and mineral properties and its interaction with the OLCN. We assume that the CL, despite its tiny dimension, shows specific characteristics in comparison to surrounding bone, that should be taken into consideration for a full picture on bone quality. To address these objectives, we combined different techniques at sub-micrometer resolution, following a spatial correlative approach where the same regions are interrogated with quantitative backscattered electron imaging, second harmonic generation imaging, nanoindentation, synchrotron X-ray scattering, and confocal laser scanning microscopy.

Our findings reveal that the CL in human femoral bones is consistently more mineralized than the surrounding bone tissue, with a distinct two-phase mineralization process—initially fast, then slower—differing from the corresponding osteon. Importantly, its mineralization is not universal but strongly depends on the local region where it is formed, potentially reflecting local recycling of mineral ions during remodeling. Mechanically, the CL is stiffer and harder than its corresponding osteon, yet it requires more mineral to reach the same mechanical properties as bone, thus hinting for a lower mechanical efficiency. Synchrotron data show that the nanoscale nature of the CL also differs from adjacent bone, with mineral particles at the CL being shorter but thicker. Based on a mechanical model, we interpreted the lower aspect ratio of the mineral particles as a less effective way to reinforce the collagen matrix. Damage simulations further suggest that the CL alone is unlikely to act as an efficient interface for crack deflection—challenging traditional assumptions. Finally, analysis of the OLCN reveals that the CL is not an impermeable barrier, but a semi-permeable interface allowing sparse yet efficient connectivity between lacunae. These connections may be crucial for maintaining communication and material exchange between adjacent osteons and, perhaps most critically, between osteons and interstitial bone. Indeed, at the periphery of the osteon near CL, we found a higher density of lacunae, probably reflecting a higher activity of osteoblasts and a strategic positioning of cells to enable connections with the outer bone.

Overall, this work redefines the CL as a dynamic, rapidly mineralized, structurally distinct, and functionally integrated interface. Rather than acting primarily as a barrier to damage, the CL appears to serve as a substrate that supports bone formation. These findings highlight the importance of the CL as a contributor to bone quality, and open perspectives for exploring its role in aging and disease-related fragility.

Résumé

Les matériaux biologiques ont développé des stratégies structurales remarquables pour accomplir plusieurs fonctions mécaniques tout en préservant la durabilité. Parmi eux, l'os se distingue par sa capacité unique à combiner rigidité, résistance et robustesse—des propriétés habituellement considérées comme mutuellement incompatibles dans les matériaux d'ingénierie. Ce comportement mécanique exceptionnel découle de sa structure hiérarchique complexe et, surtout, de ses interfaces internes. L'une de ces interfaces, la ligne cémentante (CL), est une structure bien connue localisée dans des zones complexes telles que les jonctions entre tissus mous et os, ainsi qu'à la périphérie des paquets osseux dans l'os trabéculaire et des ostéons secondaires dans l'os cortical. Malgré son omniprésence, le rôle fonctionnel de la CL reste mal compris. Bien qu'elle soit souvent supposée contribuer au comportement mécanique et modifier la continuité du réseau lacuno-canaliculaire des ostéocytes (OLCN), ses propriétés matérielles exactes, son organisation structurale et sa signification biologique n'ont pas été pleinement caractérisées.

Dans ce contexte, l'objectif de cette thèse est d'élucider le contenu minéral et le processus de minéralisation de la CL, ses propriétés mécaniques et minérales, ainsi que son interaction avec l'OLCN. Nous supposons que, malgré ses dimensions minuscules, la CL présente des caractéristiques spécifiques par rapport au tissu osseux environnant, caractéristiques qui devraient être prises en compte pour une compréhension complète de la qualité osseuse. Pour atteindre ces objectifs, nous avons combiné différentes techniques à résolution submicrométrique, en suivant une approche corrélative spatiale où les mêmes régions ont été analysées par imagerie électronique en rétrodiffusion quantitative, imagerie à génération de seconde harmonique, nanoindentation, diffraction des rayons X et microscopie confocale à balayage laser.

Nos résultats révèlent que la CL dans les os fémoraux humains est systématiquement plus minéralisée que le tissu osseux environnant, avec un processus de minéralisation en deux phases—rapide initialement, puis plus lent—distinct de celui de l'ostéon correspondant. De manière importante, sa minéralisation n'est pas universelle mais dépend fortement de la région locale où elle se forme, reflétant potentiellement un recyclage local des ions minéraux lors du remodelage. Mécaniquement, la CL est plus rigide et plus dure que l'ostéon adjacent, mais elle nécessite une teneur minérale plus élevée pour atteindre des propriétés mécaniques comparables, ce qui suggère une efficacité mécanique inférieure. Les données du synchrotron montrent que la structure nanoscopique de la CL diffère également de celle de l'os adjacent, avec des particules minérales plus épaisses mais plus courtes. D'après un modèle mécanique, le plus faible ratio des dimensions de ces particules minérales serait moins efficace pour renforcer la matrice de collagène. Des simulations de propagation de fissures suggèrent en outre que la CL seule n'agit probablement pas comme une interface efficace pour dévier les fissures—remettant en cause les hypothèses traditionnelles. Enfin, l'analyse de l'OLCN indique que la CL n'est pas une barrière imperméable, mais constitue une interface semi-perméable permettant des connexions rares mais efficaces entre les lacunes. Ces connexions pourraient être cruciales pour maintenir la communication et les échanges de matière entre ostéons adjacents, et plus encore entre ostéons et os interstitiel. En effet, à la périphérie des ostéons, à proximité de la CL, nous avons observé une densité plus élevée de lacunes, probablement liée à une plus forte activité des ostéoblastes à un positionnement stratégique des cellules pour permettre une connexion

avec l'os environnant.

Dans l'ensemble, ce travail redéfinit la CL comme une interface dynamique, rapidement minéralisée, distincte sur le plan structural et intégrée fonctionnellement. Plutôt que d'agir principalement comme une barrière contre les dommages mécaniques, la CL semble servir de substrat soutenant la formation osseuse. Ces résultats soulignent l'importance de la CL comme élément contribuant à la qualité osseuse et ouvrent de nouvelles perspectives pour explorer son rôle dans le vieillissement et la fragilité osseuse liée aux pathologies.

Acknowledgments

At a time when scientific exploration is often questioned, defunded, or even silenced, I find comfort in Marie Curie's words: *"Now is the time to understand more, so that we may fear less."* This thesis is my modest contribution to that belief–driven by curiosity, made possible by the trust and support of those who value knowledge, and carried through thanks to the energy, encouragement, and kindness of many.

A PhD may seem like a solitary journey, but it absolutely isn't. Behind every result, every line of code, and every moment of doubt, there are people who helped–through guidance, ideas, laughter, or simply by being there. So here's to all of you who walked part of the road with me. Thank you for being part of this, for making it better, and for reminding me that research is, above all, a very human adventure.

First and foremost, I would like to thank my PhD supervisor Davide Ruffoni. Your contagious enthusiasm, easy-going nature, and unwavering support made this whole adventure not just manageable, but genuinely enjoyable. Despite our very different ways of dealing with deadlines, we still managed to make it work (most of the time). And yes, you made me redo my figures more times than I can count (still not over it), but we ended up making the best of our results. Your questions constantly pushed me to think deeper, do better, and grow at every step. Thank you for trusting me, for being flexible with how we worked, and for believing that research and life should balance each other out. It's been a real pleasure working with you. I'll always remember our good times in Porto, Edinburgh, and Grenoble — and yes, your dance moves are forever burned into my brain.

I'm also deeply grateful to all the collaborators who helped shape this work along the way. To Markus Hartmann and Stéphane Blouin, thank you for warmly welcoming me during my research stay, for the inspiring scientific discussions, and for sharing the holy grail of resin embedding secrets. A special thank you to Phaedra Messmer, Petra Keplinger, and Sonja Lueger for your help with the sample preparation. To Richard Weinkamer, thank you for your brilliant insights and all the stimulating scientific conversations that always made me want to go one step further. I'm especially grateful we shared not one but two incredible conferences. To Victoria Schemenz and Wolfgang Wagermaier, thank you for your support during the beamtime proposal and your clear guidance at the synchrotron. Your expertise and availability made all the difference in understanding and processing these complex measurements. To Shahrouz Amini, thank you for welcoming me so kindly during my research stay, for your generosity and guidance, and for sharing the fine (and mysterious) art of nanoindentation. And finally, thank you to Maximilian Rummler for your help with SHG acquisitions and for all the great scientific exchanges along the way.

I would like to thank the members of my jury for their time, careful reading, and engagement with this work. I also gratefully acknowledge the FRIA/FRS-FNRS for their financial support throughout my PhD. I'm also thankful to the ESRF for the opportunity to carry out experiments at their facility. A special thank you to Manfred Burghammer and Jiliang Liu at the ID13 for their support—and for patiently helping solve technical issues, even while we were hiking!

To my MBBM lab colleagues, thank you for making the everyday part of research feel lighter. To Pauline, Gaëlle, Sophie, and Puhia—thank you for your energy, curiosity, and commitment during your master

theses. Supervising you was a pleasure and a very rewarding first mentoring experience. I learned a lot from working with each of you, and I'm grateful for the opportunity to have shared part of your research journey. A special thank you to Lena, for bravely diving into the world of TINA with me and making Python feel far less intimidating. Collaborating with you was not only incredibly helpful but also truly enjoyable. I know I wouldn't have achieved such solid results without you. And thank you, too, for your support during the final rush — it meant a lot. To Laura, Alex, and Valentine, thank you for being the best office mates I could have hoped for. From science and conferences to shared stress and silly chats, you were there through (almost) the entire journey. Your support, kindness, and solidarity made even the tough days easier, and I'll really miss having you just across the desk.

To keep my mind clear (and sane), I often stepped outside the lab—and along the way, met some truly wonderful people. Thank you to the PhD board, which I joined in the hope of making PhD life a little better for everyone. It was an amazing experience, and I'm especially grateful to Virginie Christophe for inviting me to get involved in the first place. To Caroline, Aline, and everyone from the PhD network "Réseau des Doctorant·es"—what a chaotic, intense, but incredibly enriching year we shared! To the MT180 gang, thank you for that unforgettable adventure and for teaching me that 3 minutes can feel both like a sprint and a lifetime. To the Pot'ingé crew, thank you for the laughs, the community spirit, and the much-needed tomato-picking breaks. I've met people there who've become true friends. And to all the wonderful people I met at conferences, advanced schools, and trainings—thank you for the inspiration, the thoughtful exchanges, and the shared love of science. I hope our paths cross again soon.

To my friends and family—thank you for being my anchor and my escape. To my PhD crew: Laura (you again!), Ana, Flo, Sven, Glaudy, Vicol, and Simon — thank you for the lunch breaks filled with laughter and mutual PhD therapy. I couldn't have asked for a better bunch to share the highs, lows, and endless deadline chaos with. To my "normal" friends (aka those outside the academic bubble)—Ani, Seba, and Arthur—thank you for keeping me grounded and reminding me that life exists beyond research papers and Matlab. To my family—thank you for your unwavering support, even if you had no idea what I was doing (I'm hoping MT180 helped a little on that front). And a very special shoutout to my best friend Ani and my sister Roxane, for both deciding to get married right at the end of my PhD. Planning two bachelorette parties and two weddings during the final sprint was pure chaos—but also gave me the best excuse to step away from my screen and focus on something joyful.

And finally, to Cyril, my partner through it all—thank you for your patience, for waiting (literally) for the trip of a lifetime, and for holding down the fort while I was buried in this thesis. Your love, support, presence—and your LaTeX skills, so badly needed during the final rush—made this possible.

P.S.: Let it be known that this PhD was completed with zero coffee. Miracles do exist.

April 2025, Liège

Astrid Cantamessa

Contents

Abstract iii

Résumé v

Acknowledgments vii

1 Introduction 1
- 1.1 Thesis motivation . . . 1
- 1.2 Outline of the thesis . . . 5

2 Scientific context and objectives 9
- 2.1 Bone . . . 9
  - 2.1.1 Introduction . . . 9
  - 2.1.2 Bone composition . . . 9
  - 2.1.3 Hierarchical organization . . . 10
  - 2.1.4 Bone modeling and remodeling . . . 12
  - 2.1.5 Bone mineralization . . . 13
  - 2.1.6 Osteon: structure, types, and material properties . . . 15
  - 2.1.7 Cement line . . . 18
- 2.2 Characterization techniques . . . 21
  - 2.2.1 Scanning electron imaging . . . 21
  - 2.2.2 Second harmonic generation . . . 25
  - 2.2.3 Confocal laser scanning microscopy . . . 26
  - 2.2.4 X-ray scattering . . . 27
  - 2.2.5 Nanoindentation . . . 31
- 2.3 Objectives of the thesis . . . 33

3 The mineralization of osteonal cement line depends on where the osteon is formed 43
- 3.1 Introduction . . . 44
- 3.2 Materials and methods . . . 45
  - 3.2.1 Sample preparation . . . 45
  - 3.2.2 Quantitative backscattered electron imaging . . . 46
  - 3.2.3 Second harmonic generation imaging . . . 46
  - 3.2.4 Mineral content of the cement line and adjacent regions: layers analysis . . . 47
  - 3.2.5 Statistical analysis . . . 47
- 3.3 Results . . . 48
- 3.4 Discussion . . . 52
- 3.5 Conclusion . . . 57

4 Cement lines are stiffer, harder but less mechanically efficient than lamellar bone 67
4.1 Introduction . . . 68
4.2 Materials and methods . . . 70
4.2.1 Sample preparation . . . 70
4.2.2 Quantitative backscattered electron imaging . . . 70
4.2.3 Second harmonic generation imaging . . . 70
4.2.4 Nanoindentation . . . 71
4.2.5 High-resolution backscattered and secondary electron imaging . . . 71
4.2.6 Correlation between mineral content and mechanical properties . . . 72
4.2.7 Small- and wide-angle X-ray scattering . . . 72
4.2.8 Statistical analysis . . . 74
4.3 Results and discussion . . . 74
4.3.1 The cement line is stiffer and harder than the corresponding osteon . . . 75
4.3.2 The cement line needs more mineral than the osteon to attain the same mechanical properties . . . 76
4.3.3 The cement line has thicker and shorter mineral particles than adjacent bone . 77
4.3.4 On the mechanical efficiency and potential protective role of the cement line . 81
4.3.5 Limitations . . . 82
4.4 Conclusion . . . 83

5 Canalicular crossings across the cement line are sparse but functional 101
5.1 Introduction . . . 102
5.2 Methods . . . 104
5.2.1 Sample preparation . . . 104
5.2.2 Quantitative backscattered electron imaging and image processing . . . 104
5.2.3 Confocal laser scanning microscopy (CLSM) . . . 105
5.2.4 Second harmonic generation imaging . . . 105
5.2.5 Image processing, network extraction, and quantitative analysis of the OLCN . 105
5.2.6 Statistical analysis . . . 108
5.3 Results . . . 108
5.3.1 Qualitative aspects . . . 109
5.3.2 Quantitative assessment of the canaliculi crossing the cement line . . . 109
5.3.3 Lacunar characteristics . . . 111
5.3.4 Canalicular orientation . . . 111
5.3.5 Network topology . . . 113
5.4 Discussion . . . 116
5.4.1 Functional connectivity across the cement line . . . 116
5.4.2 Spatial characterization of the OLCN . . . 117
5.4.3 Limitations . . . 118

5.5 Conclusion 119

6 Synthesis and perspectives **129**

6.1 Synthesis 129

6.2 Limitations and perspectives 131

6.3 Conclusion 133

7 Side projects **135**

7.1 A molecular scale understanding of misorientation toughening in corals and seashells . 135

7.2 Deep Learning Virtual Indenter Maps Nanoscale Hardness Rapidly and Non-destructively, Revealing Mechanism and Enhancing Bioinspired Design 139

7.3 Rational positioning of 3D-printed voxels to realize high-fidelity multifunctional soft-hard interfaces 142

7.4 Indentation based stress-strain analysis of fibrolamellar bone 145

7.4.1 Introduction 145

7.4.2 Methods 146

7.4.3 Results and discussion 147

Curriculum Vitae **155**

1

Introduction

1.1 Thesis motivation

Load bearing biological materials grown by Nature are masterpieces of engineering, evolved to perform multiple functions while ensuring durability and resilience. The remarkable properties and multifunctionality of biological materials are achieved through the assembly of basic building blocks into highly complex, hierarchical structures across multiple length scales [1, 2, 3, 4]. At the core of these materials lies a crucial element often overlooked in traditional engineering design: internal interfaces [5]. In contrast to man-made materials, where interfaces are typically considered disadvantages [6], nature has optimized biological interfaces to enhance properties and functionalities. A well-recognized task of internal interfaces in biological composites is to improve damage tolerance. This can be achieved by inserting weak interfaces which can hinder crack propagation by dissipating energy, contributing to the overall integrity of the material [7].

There are numerous examples in load bearing biological materials where interfaces enhance mechanical behavior. Nacre, for example, is renowned for its high fracture toughness despite being made almost entirely of brittle calcium carbonate. The secret lies in its structure: rather than having a monolithic architecture, nacre is composed of calcium carbonate (aragonite) platelets which are separated by a soft but tough organic layer, providing the material with a mechanism for absorbing and dissipating energy upon impact [8, 9] (Fig. 1.1A). In wood, the interface between cellulose microfibrils and the hemicellulos-lignin matrix is a key element for the high versatility of this material, combining both strength and flexibility [10, 11, 12] (Fig. 1.1B). These examples underline the importance of interfaces in biological materials, which are not only structural but also functional, probably evolved to be sufficiently good for performance and multifunctionality.

The more material scientists and engineers study biological materials, the more evident the importance of interfaces becomes. Although often microscopic in dimensions, interfaces play an essential role in the mechanical performance of a material. Not only strength but also the ability to absorb and dissipate energy is critically dependent on internal interfaces. Bone, a prime example of a load bearing biological material with high clinical relevance, provides a striking demonstration of how two traditionally contradictory properties—stiffness and toughness—are found into a single, highly functional material [4, 7, 13]. In-

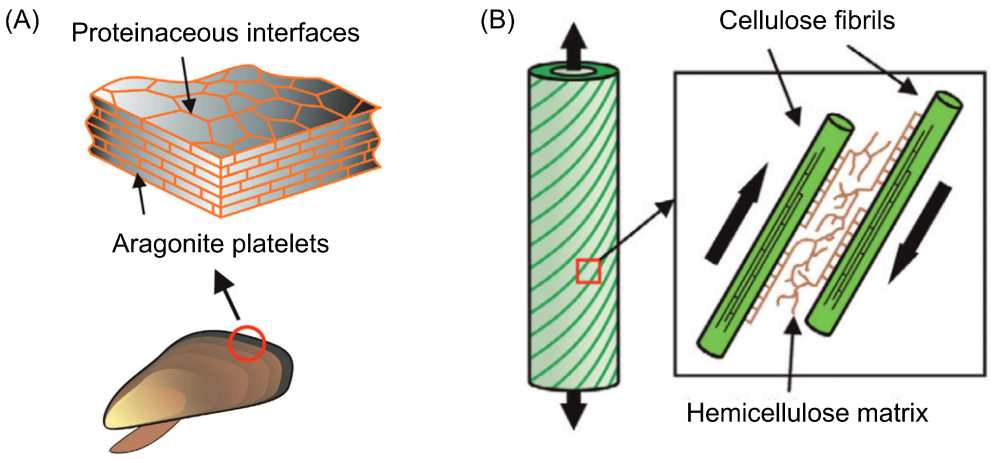


Figure 1.1: Illustrations of biological composite materials, adapted from [5]. (A) Organization of proteinaceous interfaces and aragonite platelets in nacre. (B) Arrangement of cellulose microfibrils and hemicellulose-lignin matrix in wood.

deed, bone is both stiff and tough, making it suited for the mechanical demands of daily life. Conversely, most engineering materials are typically either stiff and brittle or tough but not rigid (Fig. 1.2). How does bone manage to achieve the best of both attributes? The answer lies in the complex hierarchical structure of bone, which spans multiple length scales, and which contains numerous internal interfaces. Generally speaking, bone stiffness comes from its mineral component, primarily hydroxyapatite, which provides high resistance to deformation. On the other hand, the toughness of bone is largely attributed to its collagen matrix, which allows for energy dissipation and deformation, preventing brittle fracture. Bone can tune its mechanical properties through this intricate architecture and numerous interfaces, influencing how forces are redistributed and dissipated at the different hierarchical levels [7, 14].

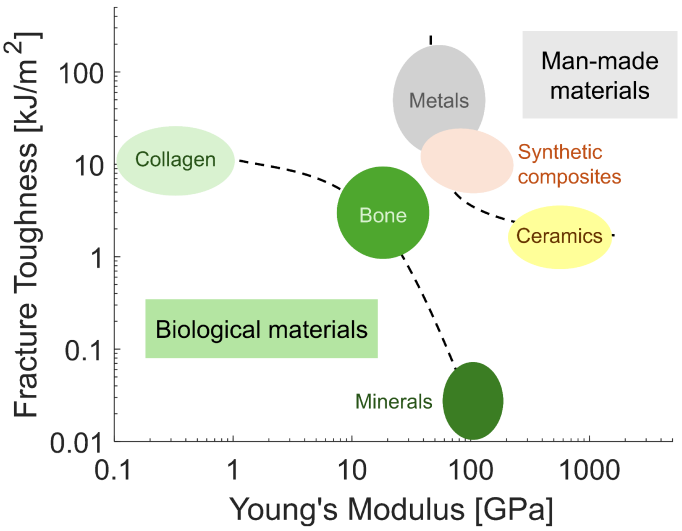


Figure 1.2: Relationship between fracture toughness and stiffness (Young's modulus), with bone combining both the high stiffness of the mineral and the high toughness of the collagen. Although engineering material may have better properties of biological material on absolute terms, relatively speaking they fail at combining efficiently the conflicting aspects of their basic constituents. Adapted from [1, 15].

While the exceptional mechanical performance of bone is rooted in its hierarchical structure, internal interfaces play a crucial role in enabling this performance. Bone toughness does not only depend on its average properties, but rather on how mineralized collagen fibrils are assembled across multiple scales, and on the quality of the interfaces between these structural units [7]. These internal interfaces occur at different levels—between collagen fibrils, between mineral and collagen, between lamellae, and between osteons. Although they represent only a small fraction of the bone volume, they are essential for energy dissipation and damage resistance. Their disruption can significantly compromise mechanical integrity. This suggests that bone fragility may arise not only from bone loss, but also from subtle changes in the structure and quality of internal interfaces, making them critical factors for understanding and preventing bone failure [7, 16].

Moreover, bone is not a static structure, but a highly dynamic material that adapts continuously to mechanical and metabolic demands through the process of bone remodeling [17, 18]. Remodeling ensures tissue renewal and repair and relies on the transport of matter and mechanical signals across the bone matrix [4, 19]. This complex exchange is made possible by a specialized, hierarchical pore system composed of vascular channels and of the osteocyte lacuno-canalicular network (OLCN) [20, 21]. The architecture of this network reflects the resolution of a central biological paradox: ensuring maximum accessibility for transport while preserving minimal disruption to the mechanical integrity of the material [4]. This balance is achieved through hierarchical design, with branching networks allowing efficient communication across scales. At the heart of the bone functional porosity, the OLCN not only facilitates the transport of nutrients and waste products but also acts as a mechanosensory interface [22, 23, 24]. Mechanical loading during daily activity induces fluid flow through the canaliculi, generating shear stresses sensed by osteocytes. These cells respond by triggering signaling cascades that modulate the activity of bone-forming and bone-resorbing cells, allowing the tissue to adapt its structure to mechanical demands [4, 24]. Additionally, the high surface area of the canalicular network enables osteocytes to locally modulate the composition of the bone matrix through osteocytic osteolysis, contributing to calcium homeostasis and tissue remodeling [4].

Among the many internal interfaces in bone, cement lines (CLs) stand out as particularly fascinating; These tiny regions are ubiquitous, delineating secondary osteons in cortical bone [25, 26], separating bone packets in trabecular bone [27], and defining boundaries at sites where bone connects with cartilage or tendon [28, 29] (Fig. 3). CLs separate newly formed bone from older bone [30], providing both a surface for bone deposition [25, 31, 32] and possibly acting as a barrier against crack propagation [33, 34, 35, 36]. Yet, their function may extend beyond contributing to fracture resistance. As interfaces between remodeled and unremodeled bone, CLs could influence the continuity of the OLCN, potentially impacting how mechanical and biochemical signals are transmitted across bone tissue. Whether canaliculi and other structural elements can cross the CL or whether it acts as a barrier to transport remains a central question with important implications for understanding both bone remodeling and mechanobiology, with long reach implications for bone quality [37, 38, 39, 40].

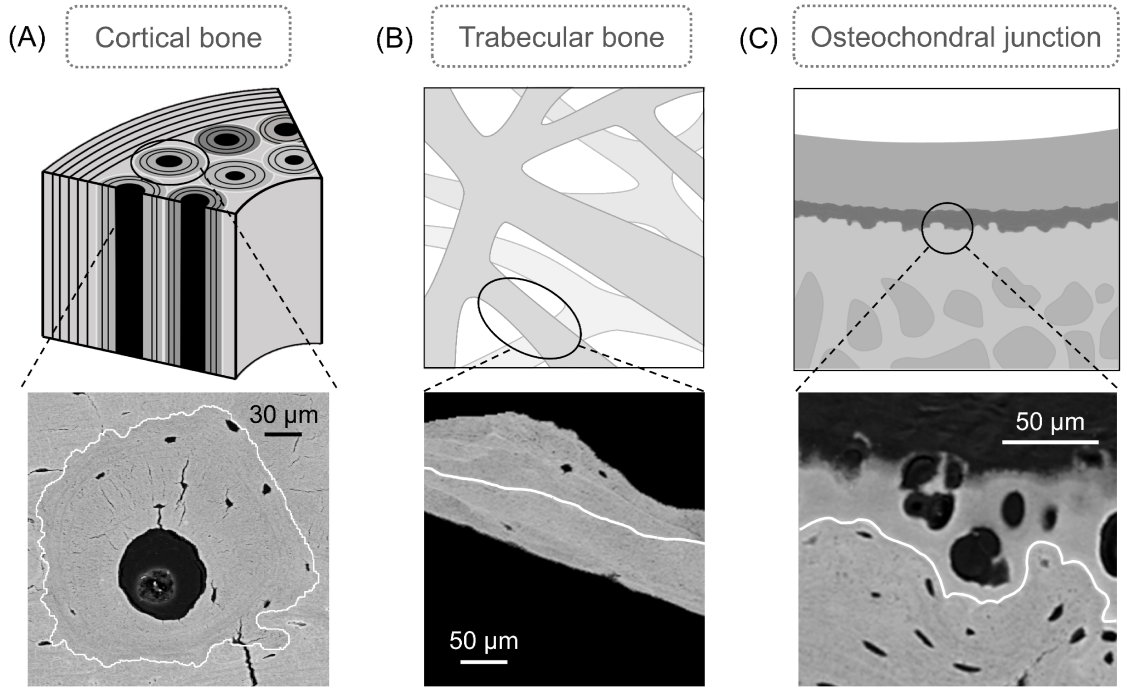


Figure 1.3: Representative images showing the CL in different bone structures. (A) Cortical bone with CL surrounding osteon. (B) Trabecular bone with CLs separating bone packets. Image curtesy of E. Pedrinazzi, MBBM Lab, ULiege. (C): Osteochondral junction, where CL separates bone from cartilage. Images curtesy of L. Müller, MBBM Lab, ULiege.

Despite their prevalence and importance, CLs remain surprisingly understudied. Even their basic mechanical nature is still debated: some studies suggest they may be softer than surrounding bone, promoting crack trapping [41, 42, 43, 44, 45], while other studies suggest they may be stiffer but more brittle, promoting crack deflection through delamination [33, 36]. Each scenario would have distinct implications for how bone resists damage, especially under complex loading conditions. Thus, elucidating the mechanical and structural properties of CLs is essential for a complete understanding of how bone integrates both strength and toughness through its internal interfaces [7].

Beyond fundamental interest for material scientists and engineers, these questions have additional clinical implications. The permeability and connectivity of the CL may influence how osteocytes communicate across different regions of bone, potentially affecting the tissue capacity to sense mechanical stimuli and initiate remodeling. Disruption of this signaling continuity could contribute to impaired remodeling dynamics, a factor linked to age-related bone loss and certain skeletal pathologies, such as osteoporosis [23, 40, 46]. Similarly, the mechanical nature of the CL and possible age-related changes may influence how cracks initiate or propagate, affecting the likelihood of fragility fractures, particularly in aged individuals [7, 47]. A deeper understanding of CL properties may thus reveal new criteria for assessing fracture risk and offer insight into the structural origins of bone fragility. Ultimately, such knowledge could inform the development of more computer simulations of bone fracture, that may even be used as diagnostic tools in future medicine.

This thesis aims to address this critical gap by focusing on the CL and its role in bone mechanics and mechanobiology. By investigating CL material and structural aspects, this work seeks to uncover their possible contribution to bone damage resistance and functional porosity. The insights gained from our research may not only deepen our understanding of bone but also provide new perspectives on how we can harness the principles of biological design to develop better materials for engineering applications.

1.2 Outline of the thesis

This thesis is organized into seven chapters.

Chapter 2 introduces the scientific background necessary to contextualize the work, including key concepts related to bone microstructure, characterization techniques, and the specific research objectives addressed throughout the thesis.

Chapter 3, 4, and 5 constitute the core of this doctoral research, each corresponding to a distinct study focused on the CL. These investigations are based on high-resolution imaging and mechanical testing techniques, combined with advanced imaged processing and quantitative analysis tools, to investigate the CL from multiple angles. Chapter 3 focuses on variations in CL mineral content and mineralization in relation to tissue age and to the local environment. Chapter 4 investigates the link between mineral content and local mechanical behavior. Chapter 5 characterizes the OLCN, with particular focus on the peripheral region near the CL and quantifies the extent of canalicular continuity across the CL.

Chapter 6 synthesizes the main findings, discusses the limitations of this work, and outlines future perspectives.

Finally, Chapter 7 presents some additional collaborative projects in which the techniques used in this Thesis were also applied to other materials, including calcium carbonate biominerals, tooth enamel, 3D-printed composites, and fibrolamellar bone.

Bibliography

[1] P Fratzl and R Weinkamer. Nature's hierarchical materials. *Progress in Materials Science*, 52(8):1263–1334, November 2007.

[2] H Gao. Application of Fracture Mechanics Concepts to Hierarchical Biomechanics of Bone and Bone-like Materials. *International Journal of Fracture*, 138(1-4):101–137, March 2006.

[3] MA Meyers, PY Chen, AYM Lin, and Y Seki. Biological materials: Structure and mechanical properties. *Progress in Materials Science*, 53(1):1–206, January 2008.

[4] R Weinkamer and P Fratzl. Solving conflicting functional requirements by hierarchical structuring—Examples from biological materials. *MRS Bulletin*, 41(09):667–671, September 2016.

[5] JWC Dunlop, R Weinkamer, and P Fratzl. Artful interfaces within biological materials. *Materials Today*, 14(3):70–78, March 2011.

[6] S Thomopoulos, V Birman, and GM Genin, editors. *Structural Interfaces and Attachments in Biology*. Springer New York, New York, NY, 2013.

[7] W Wagermaier, K Klaushofer, and P Fratzl. Fragility of bone material controlled by internal interfaces. *Calcified Tissue International*, 97(3):201–212, September 2015.

[8] B Pokroy, AN Fitch, and E Zolotoyabko. Structure of Biogenic Aragonite ($CaCO_3$). *Crystal Growth & Design*, 7(9):1580–1583, September 2007.

[9] B Pokroy, V Demensky, and E Zolotoyabko. Nacre in Mollusk Shells as a Multilayered Structure with Strain Gradient. *Advanced Functional Materials*, 19(7):1054–1059, April 2009.

[10] I Burgert, M Eder, N Gierlinger, and P Fratzl. Tensile and compressive stresses in tracheids are induced by swelling based on geometrical constraints of the wood cell. *Planta*, 226(4):981–987, August 2007.

[11] I Burgert and K Jungnikl. Adaptive Growth of Gymnosperm Branches-Ultrastructural and Micromechanical Examinations. *Journal of Plant Growth Regulation*, 23(2):76–82, June 2004.

[12] J Keckes, I Burgert, K Frühmann, M Müller, K Kölln, M Hamilton, M Burghammer, SV Roth, S Stanzl-Tschegg, and P Fratzl. Cell-wall recovery after irreversible deformation of wood. *Nature Materials*, 2(12):810–813, December 2003.

[13] RO Ritchie. The conflicts between strength and toughness. *Nature Materials*, 10(11):817–822, November 2011.

[14] DB Burr. The contribution of the organic matrix to bone's material properties. *Bone*, 31(1):8–11, July 2002.

[15] D Ruffoni. Biomechanics, 2018. Lecture slides, Biomechanics, University of Liège.

[16] Francois Barthelat, Zhen Yin, and Markus J. Buehler. Structure and mechanics of interfaces in biological materials. *Nature Reviews Materials*, 1(4):16007, March 2016.

[17] DJ Hadjidakis and II Androulakis. Bone Remodeling. *Annals of the New York Academy of Sciences*, 1092(1):385–396, December 2006.

[18] MA Hartmann, JWC Dunlop, YJM Bréchet, P Fratzl, and R Weinkamer. Trabecular bone remodelling simulated by a stochastic exchange of discrete bone packets from the surface. *Journal of the Mechanical Behavior of Biomedical Materials*, 4(6):879–887, August 2011.

[19] NA Sims and JH Gooi. Bone remodeling: Multiple cellular interactions required for coupling of bone formation and resorption. *Seminars in Cell & Developmental Biology*, 19(5):444–451, October 2008.

[20] P Schneider, M Meier, R Wepf, and R Müller. Towards quantitative 3D imaging of the osteocyte lacuno-canalicular network. *Bone*, 47(5):848–858, November 2010.

[21] R Weinkamer, P Kollmannsberger, and P Fratzl. Towards a Connectomic Description of the Osteocyte Lacunocanalicular Network in Bone. *Current Osteoporosis Reports*, 17(4):186–194, August 2019.

[22] JUA Choi, AW Kijas, J Lauko, and AE Rowan. The Mechanosensory Role of Osteocytes and Implications for Bone Health and Disease States. *Frontiers in Cell and Developmental Biology*, 9:770143, February 2022.

[23] AG Robling and LF Bonewald. The Osteocyte: New Insights. *Annual Review of Physiology*, 82(1):485–506, February 2020.

[24] AF Van Tol, V Schemenz, W Wagermaier, A Roschger, H Razi, I Vitienes, P Fratzl, BM Willie, and R Weinkamer. The mechanoresponse of bone is closely related to the osteocyte lacunocanalicular network architecture. *Proceedings of the National Academy of Sciences*, 117(51):32251–32259, December 2020.

[25] NE Lassen, TL Andersen, GG Pløen, K Søe, EM Hauge, S Harving, GET Eschen, and JM Delaisse. Coupling of bone resorption and formation in real time: new knowledge gained from human haversian BMUs. *Journal of Bone and Mineral Research*, 32(7):1395–1405, July 2017.

[26] NA Sims. Osteoclast-derived coupling factors: Origins and state-of-play Louis V Avioli lecture, ASBMR 2023. *Journal of Bone and Mineral Research*, 39(10):1377–1385, September 2024.

[27] BA Lamarche, JS Thomsen, CM Andreasen, WB Lievers, and TL Andersen. 2D size of trabecular bone structure units (BSU) correlate more strongly with 3D architectural parameters than age in human vertebrae. *Bone*, 160:116399, July 2022.

[28] HS Gupta, S Schratter, W Tesch, P Roschger, A Berzlanovich, T Schoeberl, K Klaushofer, and P Fratzl. Two different correlations between nanoindentation modulus and mineral content in the bone–cartilage interface. *Journal of Structural Biology*, 149(2):138–148, February 2005.

[29] A Tits, S Blouin, M Rummler, JF Kaux, P Drion, HG Van Lenthe, R Weinkamer, MA Hartmann, and D Ruffoni. Structural and functional heterogeneity of mineralized fibrocartilage at the Achilles tendon-bone insertion. *Acta Biomaterialia*, 166:409–418, August 2023.

[30] MD McKee and A Nanci. Osteopontin and the bone remodeling sequence: colloidal-gold immunocytochemistry of an interfacial extracellular matrix protein. *Annals of the New York Academy of Sciences*, 760(1):177–189, August 1995.

[31] V Everts, JM Delaissé, W Korper, DC Jansen, W Tigchelaar-Gutter, P Saftig, and W Beertsen. The bone lining cell: its role in cleaning Howship's lacunae and initiating bone formation. *Journal of Bone and Mineral Research*, 17(1):77–90, January 2002.

[32] MD McKee, MC Farach-Carson, WT Butler, PV Hauschka, and A Nanci. Ultrastructural immunolocalization of noncollagenous (osteopontin and osteocalcin) and plasma (albumin and α2HS-glycoprotein) proteins in rat bone. *Journal of Bone and Mineral Research*, 8(4):485–496, April 1993.

[33] KJ Koester, JW Ager, and RO Ritchie. The true toughness of human cortical bone measured with realistically short cracks. *Nature Materials*, 7(8):672–677, August 2008.

[34] S Mohsin, FJ O'Brien, and TC Lee. Osteonal crack barriers in ovine compact bone. *Journal of Anatomy*, 208(1):81–89, January 2006.

[35] RK Nalla, JJ Kruzic, JH Kinney, and RO Ritchie. Mechanistic aspects of fracture and R-curve behavior in human cortical bone. *Biomaterials*, 26(2):217–231, January 2005.

[36] EA Zimmermann, B Gludovatz, E Schaible, B Busse, and RO Ritchie. Fracture resistance of human cortical bone across multiple length-scales at physiological strain rates. *Biomaterials*, 35(21):5472–5481, July 2014.

[37] TA Curtis, SH Ashrafi, and DF Weber. Canalicular communication in the cortices of human long bones. *The Anatomical Record*, 212(4):336–344, August 1985.

[38] M Kerschnitzki, W Wagermaier, P Roschger, J Seto, R Shahar, GN Duda, S Mundlos, and P Fratzl. The organization of the osteocyte network mirrors the extracellular matrix orientation in bone. *Journal of Structural Biology*, 173(2):303–311, February 2011.

[39] M Langer, A Pacureanu, H Suhonen, Q Grimal, P Cloetens, and F Peyrin. X-ray phase nanotomography resolves the 3D human bone ultrastructure. *PLoS ONE*, 7(8):e35691, August 2012.

[40] P Milovanovic, EA Zimmermann, M Hahn, D Djonic, K Püschel, M Djuric, M Amling, and B Busse. Osteocytic canalicular networks: morphological implications for altered mechanosensitivity. *ACS Nano*, 7(9):7542–7551, September 2013.

[41] E Giner, R Belda, C Arango, A Vercher-Martínez, JE Tarancón, and FJ Fuenmayor. Calculation of the critical energy release rate G c of the cement line in cortical bone combining experimental tests and finite element models. *Engineering Fracture Mechanics*, 184:168–182, October 2017.

[42] J Jonvaux, T Hoc, and É Budyn. Analysis of micro fracture in human Haversian cortical bone under compression. *International Journal for Numerical Methods in Biomedical Engineering*, 28(9):974–998, September 2012.

[43] S Li, A Abdel-Wahab, E Demirci, and VV Silberschmidt. Fracture process in cortical bone: X-FEM analysis of microstructured models. *International Journal of Fracture*, 184(1-2):43–55, November 2013.

[44] L Vergani, C Colombo, and F Libonati. Crack propagation in cortical bone: a numerical study. *Procedia Materials Science*, 3:1524–1529, 2014.

[45] M Wang, S Li, A vom Scheidt, M Qwamizadeh, B Busse, and VV Silberschmidt. Numerical study of crack initiation and growth in human cortical bone: effect of micro-morphology. *Engineering Fracture Mechanics*, 232:107051, June 2020.

[46] SL Dallas, M Prideaux, and LF Bonewald. The Osteocyte: An Endocrine Cell ... and More. *Endocrine Reviews*, 34(5):658–690, October 2013.

[47] EA Zimmermann and RO Ritchie. Bone as a structural material. *Advanced Healthcare Materials*, 4(9):1287–1304, June 2015.

2

Scientific context and objectives

This chapter provides the scientific background necessary to understand the motivation and scope of this thesis. The first part focuses on bone as a hierarchical and dynamic tissue, progressing from general aspects to the specific structural and compositional specificities of the CL. The second part presents the main experimental techniques used to characterize CL and neighbouring bone, ranging from multiple imaging methods to nanoscale mechanical testing. Finally, the chapter ends with the main research objectives that guided the development of this thesis.

2.1 Bone

2.1.1 Introduction

Bone is a remarkable, dynamic tissue that performs both biological and mechanical functions. Structurally, it provides support to the body, protects vital organs, and allows motion. Metabolically, it serves as storage for minerals such as calcium and phosphate. Additionally, the bone marrow provides the primary site of hematopoiesis (i.e., the formation of red blood cells). These essential functions are supported by the hierarchical organization of bone, which spans multiple scales form the molecular to the macroscopic level [1, 2].

2.1.2 Bone composition

In terms of chemical composition, bone is a rather simple material made up of three primary building blocks: the organic phase, the inorganic phase and water. The organic phase, which represents approximately 30% of the total wet weight, is primarily composed of type I collagen (up to 90% of this phase), along with a smaller portion of non-collagenous proteins such as osteocalcin and osteopontin [2, 3, 4]. The latter is particularly important for this work, being an essential component of CLs. From a mechanical viewpoint, this phase provides toughness and flexibility, allowing bone to absorb energy and resist fractures.

The inorganic phase accounts for approximately 60% of the total wet weight and consists of nano-sized mineral platelets commonly reffered to as hydroxyapatite (HAP) [$Ca_5(PO_4)_3OH$] (Fig. 2.1A) [4]. How-

ever, bone mineral is more accurately described as a poorly crystalline, ion-substituted form of HAP, in which ions such as Na^+, Mg^{2+}, HPO_4^{2-}, Cl^-, F^-, and CO_3^{2-} partially replace native lattice ions. These substitutions are dynamic and evolve over times as the mineral interacts with surrounding biological fluids, influencing its composition, maturity, and potentially its mechanical properties [5]. The mineral phase reinforces the soft inorganic phase and provides stiffness and strength. Together, the organic and inorganic phases synergistically give bone its remarkable combination of rigidity and resistance to crack propagation.

Water, the third component, represents 10% of the total wet weight [4] and is the least understood. However, it is believed to play a key role in mediating interactions between the other two phases and contributing to the viscoelastic behavior of bone [6].

2.1.3 Hierarchical organization

Beyond its composition, bone exhibits a highly organized hierarchical structure that contributes to its exceptional mechanical properties.

At the nanoscale level, collagen molecules self-assemble into a triple helix structure with a diameter of approximately 1.5 nm and a length of 300 nm. These helices further organize into microfibrils with a characteristic staggered arrangement, creating periodic gap (35 nm) and overlapping zones (32 nm) (Fig. 2.1B) [2]. HAP crystals preferentially nucleate in the gap zones and grow into plate-like structures with dimensions of 2-7 nm in thickness, 15-200 nm in length, and 10-80 nm in width [5]. These mineral platelets are predominantly aligned with the long axis of the collagen fibrils and are referred to as intrafibrillar mineral. A substantial portion of mineral is also located outside the fibrils, in the spaces between them, forming the extrafibrillar mineral [7].

At the micrometer scale, mineralized collagen fibrils organize into fibril bundles that further assemble into lamellae, thin layers typically 3–7 μm thick (Fig. 2.1C-F). Lamellae are a characteristic feature of mature bone and are composed of collagen fibers aligned in a consistent direction. Their orientation gradually shifts from one lamella to the next, resulting in a rotated plywood-like structure that enhances bone resistance to fracture by deflecting cracks and distributing mechanical stresses [2, 8].

Depending on the location and remodeling history, lamellae can form various structural arrangements. They are commonly organized into concentric layers around vascular channels, forming osteons (Fig. 2.1H), which are bordered by CL approximately 1-2 μm thick [9]. Other lamellae appear as interstitial fragments between osteons, representing remnants of older bone remodeling. Additionally, broad circumferential lamellae can be found enveloping larger regions of bone tissue, aligned along internal or external surfaces. In trabecular bone, lamellae assemble into bone packets (Fig. 2.1G), also delineated by CL.

By contrast, woven bone lacks this ordered lamellar structure and is composed of randomly oriented

collagen fibrils. It is typically formed rapidly, such as during early development or fracture healing, and is mechanically less robust. Over time, woven bone is generally replaced by organized lamellar bone through remodeling processes [8].

At the macroscopic scale, bone is classified into compact cortical bone and porous trabecular bone (Fig. 2.1I). Cortical bone forms the dense outer shell of long bones, providing structural stability and resistance to bending and buckling. In large mammals (and humans), its internal architecture is primarily organized into osteons, which represent the basic structural unit of this dense bone type. In contrast, trabecular bone is found at the ends of long bones and within vertebral bodies. Its highly porous, lattice-like architecture provides high energy absorption, metabolic exchange, and adaptive remodeling. In this region, the basic structural unit consists of bone packets, assembled into interconnected trabeculae that span the porous network [2].

Finally, at the organ level, bone exhibits a wide variety of shapes, each adapted to its mechanical and physiological functions. Long bones, such as the femur, are designed to support body weight by providing stability against bending and buckling. Plate-like bones, like the skull, protect vital organs. Short bones, such as the vertebra, provide stability against compression [2]. This work focuses specifically on the CL bordering osteons in cortical bone of long bones.

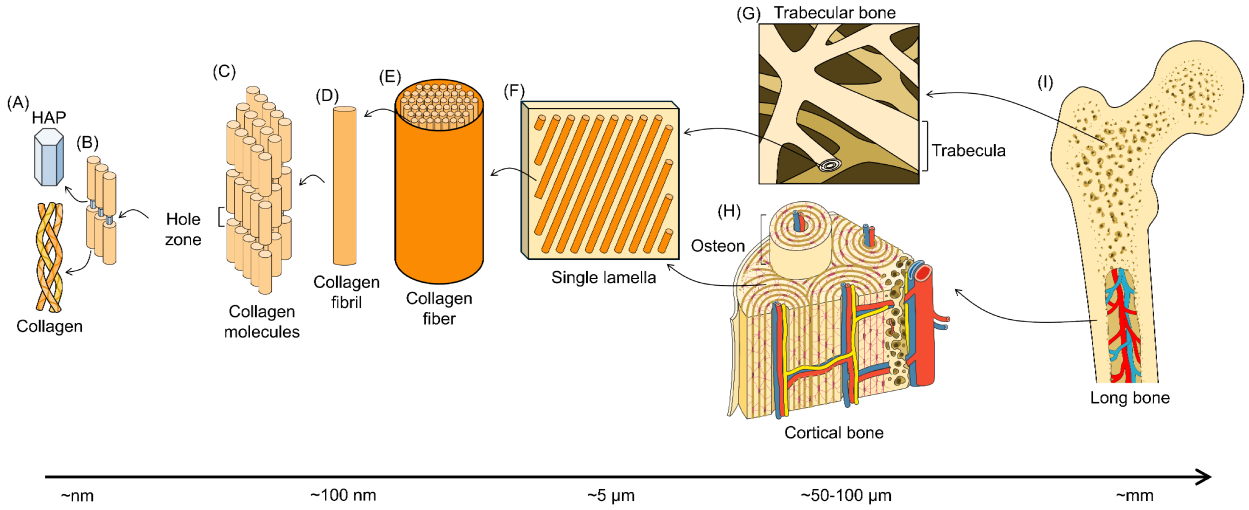


Figure 2.1: Schematic representation of the hierarchical structural organization of bone. (A) Collagen molecules and (B) HAP platelets are the two primary components of bone tissue. (C) Collagen molecules align into staggered arrays with periodic gaps, which serve as nucleation sites for mineral deposition. (D) These assemblies form collagen fibrils, which then group into (E) collagen fibers. (F) Fibers organize into single lamellae, where collagen and mineral are aligned in a given orientation. (G) In some regions, lamellae organize into bone packets that form part of the porous trabecular bone, composed of interconnected trabeculae. (H) In denser areas, lamellae form concentric arrangements around vascular canals, creating osteons, the basic structural units of compact bone. (I) These structures integrate into the whole long bone, where cortical bone forms the outer shell and trabecular bone fills the interior regions. The size scale below illustrates the approximate length scales represented in each step. This illustration includes elements adapted from Servier Medical Art, licensed under a Creative Commons Attribution 4.0 Unported License (https://creativecommons.org/licenses/by/4.0/).

2.1.4 Bone modeling and remodeling

Bone hierarchical structure not only ensures its mechanical efficiency but also facilitates its ability to adapt dynamically to mechanical and metabolic demands. This adaptability is achieved through two distinct but complementary processes: bone modeling and remodeling. Bone modeling primarily occurs during growth or in response to changes in mechanical loading. It involves the addition or removal of bone on different surfaces through the independent actions of osteoblasts and osteoclasts, leading to changes in bone shape and mass [2]. In contrast, bone remodeling is a continuous, highly regulated process that renews bone throughout life. It maintains mechanical integrity by removing old or micro-damaged bone and replacing it with newly formed bone, while preserving the overall geometry of the structure [10, 11]. Remodeling also plays a critical role in systemic mineral homeostasis, notably regulating calcium and phosphate levels [12]. In this thesis, we focus specifically on remodeling in cortical bone, where the process follows a structured sequence. It occurs within basic multicellular units (BMUs) that dig through the matrix, forming cylindrical structures known as osteons. This remodeling strategy is adapted to the dense, compact nature of cortical bone, whereas in trabecular bone, remodeling starts from trabecular surfaces.

Bone remodeling is driven by the coordinated actions of three main cell types: osteoblasts and osteoclasts, and osteocytes. Osteoblasts originate from mesenchymal stem cells and are responsible for synthesizing new bone matrix (osteoid), which later mineralizes. Osteoclasts are large, multinucleated cells derived from hematopoietic stem cells. They are specialized for bone resorption through the secretion of acid and proteolytic enzymes. Osteocytes, the most abundant and long-lived bone cells, are former osteoblasts that have become embedded within the mineralized matrix. They reside in small cavities (lacunae) and extend cytoplasmic processes through a dense 3D network of canaliculi, forming the osteocyte lacuno-canalicular network (OLCN) [13, 11]. Osteocytes act as mechanosensors and orchestrators of bone remodeling. The most widely accepted mechanism is the fluid flow hypothesis: mechanical loading induces deformation of the bone matrix, driving interstitial fluid through the canaliculi. This fluid flow generates shear stresses sensed by osteocytes, leading to the regulation of osteoblast and osteoclast activity via biochemical signals such as sclerostin, RANKL, and OPG [14, 15, 16]. Furthermore, this fluid flow helps in the diffusion of nutrients and the removal of metabolic waste within the dense mineralized matrix [13].

Within cortical bone, remodeling through BMUs follows three consecutive phases: resorption, reversal, and formation (Fig. 2.2). Remodeling is initiated by signals from osteocytes that sense damage or mechanical changes in the matrix.During the resorption phase (lasting up to 3 weeks), osteoclasts dig a cylindrical tunnel (cutting cone) at a rate of 20–40 μm/day [11]. Recent studies have shown that osteoclasts not only degrade the bone matrix but also actively prepare for subsequent bone formation by releasing specific "coupling factors". These molecules promote the recruitment, differentiation, and activation of osteoblasts [17]. This osteoclast-osteoblast coupling ensures that bone formation is tightly linked to preceding resorption, preserving the efficiency of the remodeling cycle. The reversal phase (lasting 4–5 weeks) follows resorption. During this stage, mononuclear reversal cells colonize the resorbed surface, clean debris, and deposit a thin layer of matrix to prepare the surface for osteoblast attachment [18]. A key

event during the reversal phase is the formation of the CL, a highly mineralized boundary that separates the newly forming osteon from the surrounding interstitial bone. The CL may play a biological role in coupling resorption to formation. It contains molecules such as osteopontin, which may act as a chemotactic signal attracting osteoblast progenitors to the bone surface [17]. Other components, including demineralized collagen and possibly unidentified factors, may further contribute to the recruitment and localization of osteoblast lineage cells. During the formation phase (over 3–4 months), active osteoblasts deposit osteoid onto the CL that gradually mineralizes into mature lamellar bone. Some osteoblasts become trapped and differentiate into osteocytes, while others become quiescent bone lining cells. Overall, about 5% of cortical bone is replaced annually through remodeling [2, 18], allowing bone to balance the demands of mechanical adaptation and metabolic regulation over a lifetime.

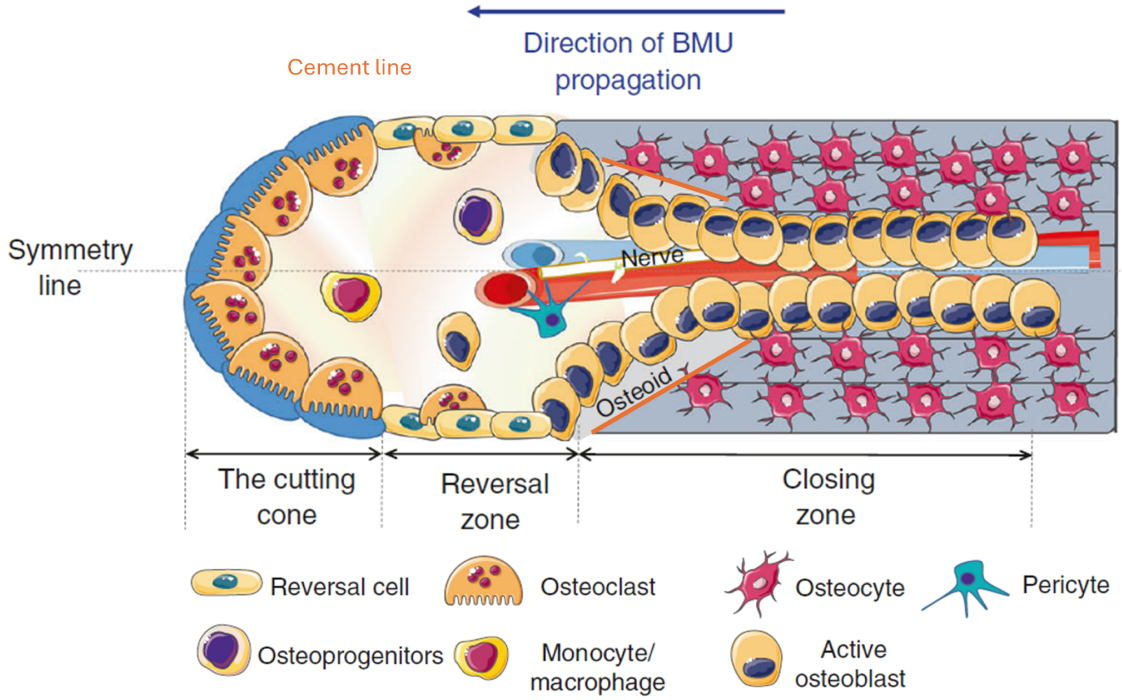


Figure 2.2: Schematic representation of bone remodeling in cortical bone. Remodeling is carried out by basic multicellular units (BMUs) that sequentially resorb and replace bone tissue. Osteoclasts at the front of the BMU form the cutting cone, excavating bone. In the reversal zone, reversal cells and osteoprogenitors prepare the resorbed surface. In the closing zone, osteoblasts deposit osteoid that later mineralizes into mature bone. Some osteoblasts become embedded as osteocytes, maintaining bone homeostasis. Adapted from [19]..

2.1.5 Bone mineralization

Following the remodeling process, the newly formed osteoid is initially unmineralized. Mineralization begins after a 13-day lag, with a fast primary phase reaching 70% of full mineralization within days [20, 21]. This is followed by a slower secondary phase that adds the remaining 30% of mineral content over several years [21, 22]. Consequently, bone tissue exhibits a heterogeneous mineral distribution, with regions at different stages of mineralization reflecting differences in tissue age. These discontinuities in mineral content significantly influence the mechanical behavior, particularly crack initiation and propagation,

and are crucial for the overall bone toughness [5].

To quantify this mineralization process, Roschger et al. [21] used tetracycline labeling combined with quantitative backscattered electron imaging (qBEI) to establish a mineralization law (Fig. 2.3). This empirical law relates the degree of mineralization to the tissue age and suggests a stereotypical progression of mineral accumulation over time, characterized by a fast initial increase followed by gradual secondary mineralization [21]. Although these mineralization kinetics were primarily characterized in trabecular bone, the same biphasic mineralization process is believed to occur in newly formed osteonal bone tissue within cortical bone. The mineral content distribution measured in healthy bone forms a specific pattern known as the Bone Mineralization Density Distribution (BMDD), which reflects the steady-state balance between remodeling dynamics and mineral accumulation.

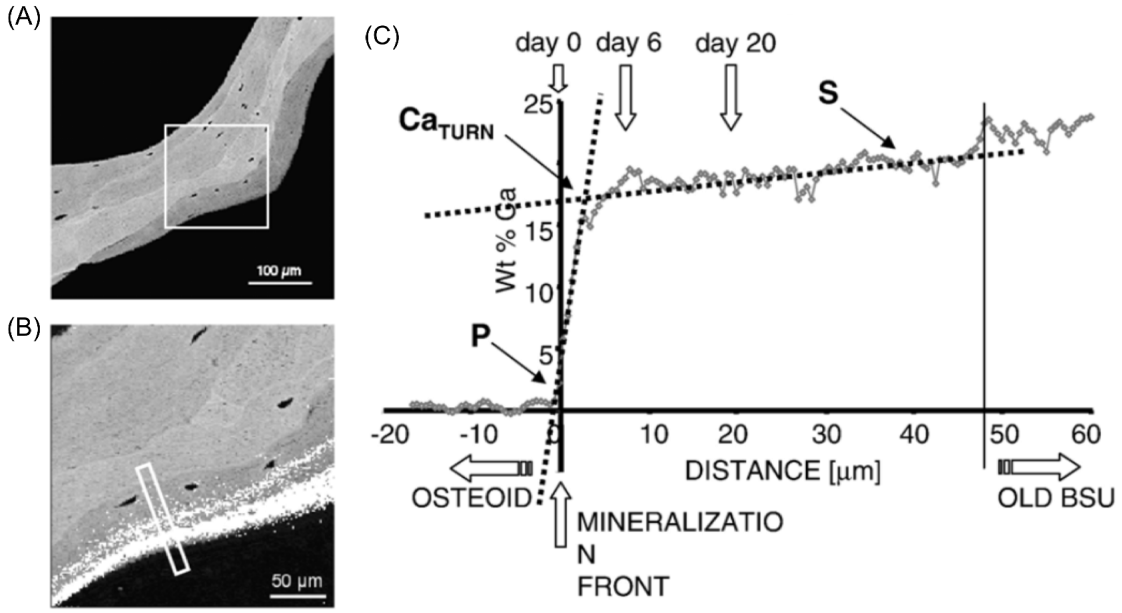


Figure 2.3: Characterization of the mineralization front in human bone tissue. (A) qBEI of a newly formed osteon adjacent to older bone tissue. (B) Magnified view of the mineralization front indicated in (A) showing newly forming bone packet (dark grey) and fluorescence double labeling by tetracycline (white dots). (C) Bone mineralization profile obtained along the white rectangle in (B), showing the progression of calcium (Ca) content (wt % Ca) with distance. The profile highlights a steep increase in calcium during the rapid primary mineralization phase (P), followed by a slower secondary mineralization phase (S). Time points (day 0, day 6, day 20) estimated from tetracycline labeling indicate the kinetics of mineral accumulation. Adapted from [21].

To better understand the origin of the BMDD, Ruffoni et al. [23] developed a computational model based on a mathematical conservation law. Their model proposed that the shape of the BMDD could be predicted by assuming a universal mineralization law combined with remodeling rates. This mathematical framework suggested that the mineralization kinetics, rather than remodeling heterogeneity, predominantly shape the BMDD fingerprint in healthy bone [23]. More information on this model can be found in Supplementary note 3.1.

However, more recent findings have questioned the universality of the mineralization law. Roschger et al. [24] compared newly formed bone during modeling with newly formed bone during remodeling

(new osteons) in human cortical bone. They found that bone formed after remodeling exhibited a lower and more heterogeneous mineral content compared to bone formed by modeling. These results suggest that mineralization kinetics are not solely determined by tissue age but are also influenced by the biological context of bone formation. Their observations further revealed that during primary mineralization, mineral crystals initially grow predominantly in thickness, and only later, during secondary mineralization, expand in length. In addition, mineral transport itself—influenced by ion accessibility and matrix permeability—may act as a limiting factor for mineral accumulation during bone formation [24]. This more complex view of mineralization dynamics indicates that while the general biphasic sequence of mineral accumulation is preserved, the kinetics and spatial patterns of mineralization can vary locally, challenging the notion of a fully universal mineralization law.

2.1.6 Osteon: structure, types, and material properties

Structure

Osteons are the primary structural units of cortical bone, organized around central vascular canals and bordered by CLs. While their general concentric lamellar structure is well described, osteons display significant variability in their organization, material properties, and cellular architecture. Understanding these internal differences is essential for appreciating their functional adaptation and for interpreting the role of CLs in bone behavior. Since the present thesis focuses specifically on the CLs that delineate osteons, it is crucial to first characterize the structure and variability of the osteons themselves, which define the biological and mechanical environment in which CLs are situated.

Types

In human cortical bone, the majority of osteons are classified as secondary osteons (Fig. 2.4A), also referred to as Type I osteons [25]. However, several variants of secondary osteons have been described. Type II osteons, also called osteon-in-osteon [26] are characterized by the presence two concentric CLs, reflecting successive remodeling events where a new osteon forms within a pre-existing one (Fig. 2.4B) [27]. Other morphological variants include drifting osteons, in which the basic multicellular unit (BMU) gradually migrates during formation [28], leading to eccentrically layered osteons (Fig. 2.4C), and double-zonal osteons, which exhibit two concentric zones with distinct lamellar organization or mineralization properties (Fig. 2.4D) [29]. These structural variants highlight the dynamic and heterogeneous nature of cortical bone remodeling.

In this thesis, we primarily focus on Type I osteons. However, Type II osteons are also considered in specific analyses related to mineralization analysis (Chapter 3) and the organization of the OLCN (Chapter 5), given their distinct remodeling history and internal architecture.

Material properties

The functional performance of osteons depends not only on their architectural organization but also on

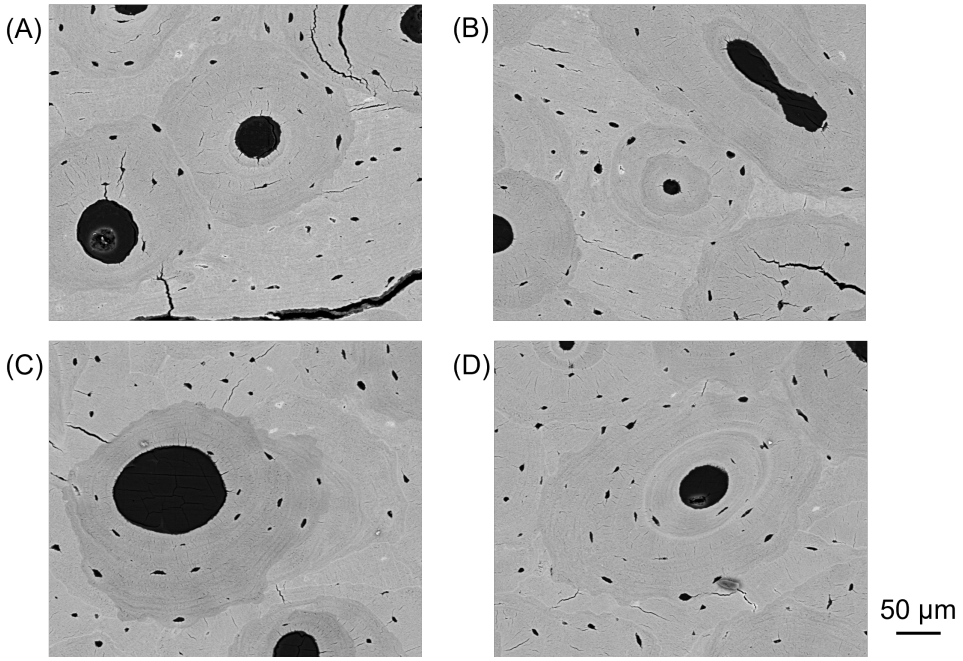


Figure 2.4: Representative qBEI images illustrating different osteon structural variants in human cortical bone. (A) Type I osteon: a typical secondary osteon exhibiting concentric lamellar organization and homogeneous mineralization. (B) Type II osteon: an osteon with an osteon-in-osteon structure, characterized by two concentric regions demarcated by a secondary CL. (C) Drifting osteon: an osteon with a non-centered vascular canal and asymmetrical lamellar deposition. (D) Double-zonal osteon : an osteon showing two distinct zones of mineralization intensity or lamellar organization.

the intrinsic material properties of their components. Specifically, the orientation of collagen fibers and the distribution of mineral content within osteons are key factors governing their mechanical behavior at the microscale [2]. These material heterogeneities contribute to the anisotropic mechanical response of bone and are critical for maintaining resistance to fatigue, damage, and fracture.

Collagen fibers within osteons are not randomly oriented but follow organized patterns that vary between lamellae. Rather than maintaining a uniform direction, collagen bundles typically exhibit a spiral or twisted arrangement across successive lamellae [2, 8, 30]. This spiral twisting has been proposed to enhance crack deflection and energy dissipation by distributing mechanical stresses along different fiber orientations [30, 31]. In addition to the structural types discussed previously, osteons can also be classified based on their collagen fiber organization and optical properties. Under polarized light microscopy, bright and dark osteons can be distinguished (Fig. 2.5), reflecting differences in collagen orientation and nano-compositional patterns [32, 33]. Dark osteons exhibit a relatively simple and homogeneous collagen organization, with fibers predominantly aligned parallel to the osteon axis. In contrast, bright osteons display a more complex, bidirectional arrangement of collagen bundles, oriented approximately at $\pm$ 45° relative to the osteon axis. These differences in collagen organization reflect adaptations to specific mechanical loading environments and influence the anisotropic mechanical behavior of osteonal bone [32].

The distribution and properties of mineral content within osteons are highly heterogeneous and evolve over time. Recent work by Wittig et al. [34] provided detailed insights into how mineral characteristics

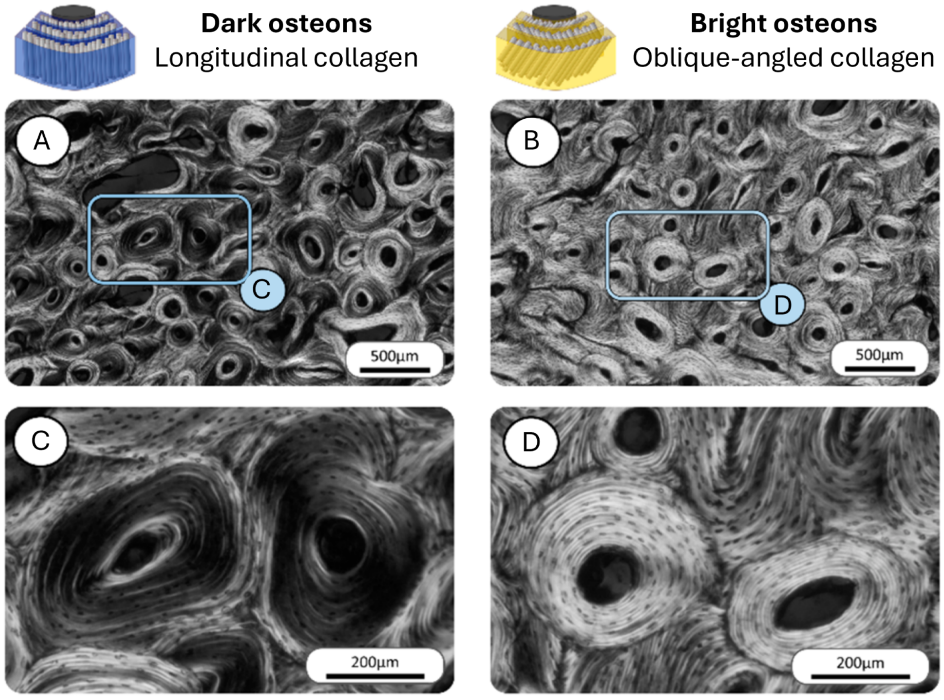


Figure 2.5: Representative polarized light microscopy images of dark and bright osteons in human cortical bone. (A) Dark osteons, characterized by a predominance of collagen fibers aligned longitudinally along the osteon axis, resulting in a dark appearance under polarized light. (B) Bright osteons, exhibiting oblique-angled collagen fiber orientations, typically around ±45° relative to the osteon axis, producing a brighter birefringence pattern. (C) Magnified view of the region indicated in (A). (D) Magnified view of the region indicated in (B). Adapted from [32].

change systematically across human osteonal bone. Their study demonstrated that the mineral content progressively increases from the central vascular canal toward the periphery as lamellae mature. This spatial gradient reflects the temporal sequence of bone formation during remodeling, with older peripheral lamellae accumulating more mineral over time compared to younger, centrally located lamellae. Complementary findings by Grünewald et al. [35] showed that not only the mineral content but also the mineral particle size and organization vary across osteons. Specifically, they observed an increase in mineral crystal thickness and a more pronounced alignment of mineral particles toward the periphery, suggesting a progressive maturation and structural ordering of bone mineral with tissue age.

Mechanical behavior

The mechanical behavior of osteonal bone at the microscale is not solely determined by the individual properties of collagen fibers and mineral crystals but also by their spatial and functional coupling [3]. Recent studies have shown that the orientation of mineral crystals closely follows that of the underlying collagen matrix, creating a tightly integrated composite structure combining load bearing and damage resistance. At the microscale, Granke et al. [36] demonstrated that microelastic properties at the lamellar scale are dominated by the orientation of collagen microfibrils. Their findings highlighted that regions with highly aligned collagen fibers exhibited greater elastic stiffness along the fiber direction, underscoring

the critical role of collagen organization in modulating local mechanical behavior. Since mineral crystals preferentially nucleate and grow along collagen fibrils, the anisotropy of mineral deposition is inherently linked to the anisotropy of the organic matrix. Complementarily, Gründewald et al. [37] used high-resolution 3D imaging techniques to to show that mineral nanocrystals exhibit complex spatial organizations, including twisted and helicoidal patterns, which mirror the underlying collagen architecture.

At a larger scale, osteons enhance cortical bone toughness through mechanisms that limit crack propagation. The concentric lamellar structure, combined with collagen fiber twisting and mineral heterogeneity, facilitates crack deflection and energy dissipation under mechanical load [38]. Cracks that form in the bone matrix are often twisted and redirected across lamellar interfaces, increasing the energy required for fracture progression [30, 31].Furthermore, osteons are bordered by CL. Although their functional implications are not discussed in detail here, they are believed to significantly influence the mechanical behavior of cortical bone. Their role will be explored more extensively in the section 2.1.7.

Organization of the OLCN

Within osteons, the OLCN displays a highly organized architecture. Repp and colleagues [15] reported a spatial heterogeneity in canalicular density, with lower densities near the central canal and increasing densities toward the periphery. Such variations may influence local mechanosensitivity and nutrient transport efficiency. Moreover, they demonstrated that canaliculi tend to co-align with the collagen fiber orientation within lamellae, suggesting a coordinated structural organization that supports efficient mechanical signaling [39]. The integration of the OLCN with the collagen and mineral matrix further reinforces the multiscale functional optimization of osteons, ensuring that cortical bone can sense mechanical stimuli and adapt to changing loading conditions.

Together, the hierarchical structure, material organization, mechanical behavior, and cellular network of osteons define a highly specialized environment within cortical bone. At the border of the osteon, there is a clear interface, which demarcates secondary osteons from the surrounding bone: the CL. In the following section, we focus specifically this interface exploring its structure, composition, formation, and functional significance in the context of cortical bone remodeling.

2.1.7 Cement line

CLs, first described by Ebner in 1887 as distinct structural boundaries within bone tissue [40], have remained a subject of scientific interest for over a century. Initially noted for their unique morphology, CLs were later recognized as key markers of bone remodeling, delineating newly formed secondary osteons from pre-existing bone [41]. Beyond osteons, CLs are also present around trabecular bone packets [42] and at the interface between bone and soft tissues such as cartilage or tendon [43, 44]. However, in the present thesis, we focus specifically on the CLs bordering secondary osteons in cortical bone. This unique feature reflects the dynamic interplay between old and new bone [45], playing critical roles that extend beyond a purely structural boundary function. Despite their importance, our understanding of

CLs remains incomplete, leaving significant gaps in knowledge regarding their contributions to bone mechanics, remodeling, and pathology.

Formation and composition of cement line

CL formation occurs probably during the reversal phase of the remodeling process on the eroded surface. Osteoclasts and/or osteoprogenitor cells would deposit this layer, rich in osteopontin–a highly charged and phosphorylated protein known for its strong calcium-binding properties [46], providing a proper surface for subsequent osteoid deposition (Fig. 2.2) [41, 47, 48, 49]. In addition, the CL may also serve a biological signaling role. It has been proposed that molecules such as osteopontin within the CL could act as chemotactic agents, attracting osteoblast progenitors to the resorbed surface and facilitating the coupling between resorption and formation phases [17]. Demineralized collagen fragments and other matrix components may further contribute to this recruitment process, although the full repertoire of coupling signals remains to be identified [17].

This initial role in bone remodeling suggests that CLs may possess distinct composition and mineral properties compared to the surrounding bone tissue. However, their precise mineralization state remains a topic of debate. Early studies reported lower mineralization levels in CLs (Fig. 2.6A) [50, 51], whereas more recent analyses suggest higher mineral content compared to both osteonal and interstitial bone (Fig. 2.6B) [9]. Advanced imaging techniques, including BEI, Raman spectroscopy, and synchrotron radiation tomography, have generally confirmed that CLs exhibit higher mineral content relative to adjacent osteons (Fig. 2.6C-D) [52, 53, 54]. Nevertheless, how CL mineralization evolves over time remains poorly characterized. Some evidence suggests that the mineral difference between the CL and osteonal bone diminishes with increasing tissue age [53], but systematic studies on the temporal evolution of CL mineralization are lacking. Further investigations into the mineralization kinetics and regional variability of CLs are presented in Chapter 3.

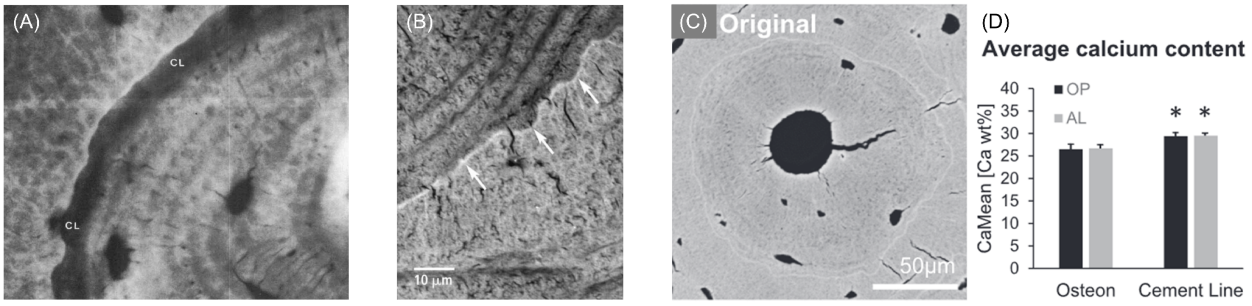


Figure 2.6: (A) BEI image (1000 ×) of a portion of an osteon with the CL as a region of low mass density (adapted from [50]). (B) BEI image (1500 ×) of a portion of an osteon with a brighter CL (arrows) compared to both osteonal and interstitial bone (adapted from [9]). (C) qBEI image of an osteon with the bone mineral density significantly higher at the CL and (D) comparison of the mean Ca content in the osteon and in the CL (adapted from [53]).

Additionally, structural differences in mineral crystal size and orientation at the CL further underscore its singularity, although these features have only been marginally studied [35]. Grünewald et al. [35] recently showed that mineral crystals at the CL are significantly thicker and less aligned compared to those in

adjacent lamellar bone, suggesting differences in the mechanisms of mineral deposition at this interface. As for the organization of the organic matrix, studies based on high-resolution imaging have reported that collagen fibrils in the CL are oriented in three or more predominant directions and with higher dispersion than lamellar bone [54]. However, further investigations are needed to confirm these observations and to understand how these nanoscale features relate to the mechanical behavior of the CL. More detailed analyses of the mineral properties at the CL are presented in Chapter 4.

Mechanical role: stiff or soft interface?

The CL is a critical mechanical interface potentially influencing load transfer and crack propagation in cortical bone. Experimental studies have shown that microcracks originating in interstitial bone often deviate at the border of the osteon (Fig. 2.7A) [55, 56, 57, 38], dissipating energy and reducing crack-driving forces [3]. This crack deflection mechanism helps preserve osteon integrity and protects the central Haversian canal and its blood vessels. Accordingly, microcracks are more frequently observed in interstitial bone than within osteons, likely reflecting differences in mineralization and material properties [58, 59].

Simulation studies further support this protective role, suggesting that the presence of the CL increases the energy required for crack propagation [60]. For instance, cohesive-based extended finite element method (X-FEM) models demonstrate that cracks initiated in interstitial bone stop at the CL (Fig. 2.7B) but continue into osteons when the CL is absent (Fig. 2.7C). Other computational models similarly confirm that the CL can either act as a barrier or facilitate crack deflection, depending on its local mechanical properties [61, 62]. Drawing an analogy with fiber-reinforced composites [63], a softer and weaker interface would favor crack arrest, while a stiffer and stronger interface would promote crack deflection. Yet, despite the mechanical relevance of the CL, its intrinsic material properties—such as stiffness, strength, and toughness—remain poorly characterized. Only a limited number of experimental studies have directly assessed CL mechanical properties, some suggesting a softer and weaker tissue compared to surrounding bone [64, 65]. However, this hypothesis appears difficult to reconcile with probable hypermineralization, given the generally positive correlation between mineral content and mechanical stiffness [43, 66]. A more detailed investigation of the mechanical properties of the CL is presented in Chapter 4.

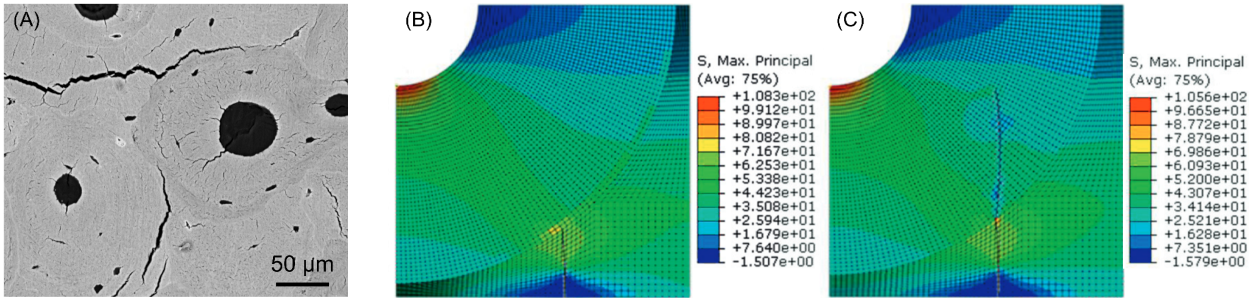


Figure 2.7: (A) qBEI image showing cracks stopped or deflected by the CL. (B) Crack paths in the three-phase model (with the CL): crack arrest. (C) Crack path in the two-phase model (without the CL): crack propagation (adapted from [60]).

Mechanobiological role: barrier or bridge?

In addition to its potential mechanical functions, the CL plays a biological role as a remnant of remodeling events and may impact the organization of the OLCN, a critical player in bone mechanobiology. The continuity of the OLCN across the CL remains a topic of debate. Confocal laser scanning microscopy (CLSM) and X-ray phase nanotomography studies suggest that canalicular connections are mainly disrupted at the CL, creating a discontinuity between neighboring osteons (Fig. 2.8A-B) [49, 52]. However, other studies using etching techniques combined with scanning electron microscopy (SEM) reported evidence of canalicular connections traversing the CL (Fig. 2.8C), suggesting that it may not form a complete barrier [67, 68]. Further supporting its biological role, variations in OLCN organization near the CL have been observed. Osteons tend to exhibit higher lacunar density close to the CL compared to the central osteonal region or interstitial bone [59]. Conversely, canalicular density appears to decrease progressively from the Haversian canal toward the CL [15]. These patterns could reflect a decline in osteoblast activity during osteon formation, with greater deposition rates and cellular embedding occurring earlier in the remodeling sequence [59]. Further investigation of these mechanisms is presented in Chapter 5.

In addition to the classic OLCN, recent discoveries using focused ion beam scanning electron microscopy (FIB-SEM) have revealed the presence of a network of nanochannels within lamellar bone (Fig. 2.8D-E) [69]. These subcanalicular channels, distinct from osteocyte canaliculi, are absent at the CL, suggesting that the CL acts as a barrier not only for cells but also for fine-scale porosity and also finding a nanoscale reason for the higher mineral content measured in the CL at the microscale. The exact role of these nanochannels remains unknown, but they may represent remnants of mineral growth domains during bone matrix maturation.

Unresolved questions

Despite their recognized importance, CLs remain one of the least understood structures in bone [70]. Their small size and complex accessibility pose significant challenges for traditional imaging and mechanical testing methods. Conventional techniques often lack the resolution needed to fully capture their compositional and structural features, as well as their interactions with adjacent bone tissue. High-resolution, multimodal imaging and mechanical testing approaches are therefore essential to advance our understanding of their role in bone mechanics, remodeling, and pathology.

2.2 Characterization techniques

2.2.1 Scanning electron imaging

Scanning electron microscopy (SEM) is a powerful technique for high-resolution material characterization. Unlike transmission electron microscopy (TEM), which captures electrons transmitted through a sample, SEM detects electrons emitted from the surface, providing information about surface topogra-

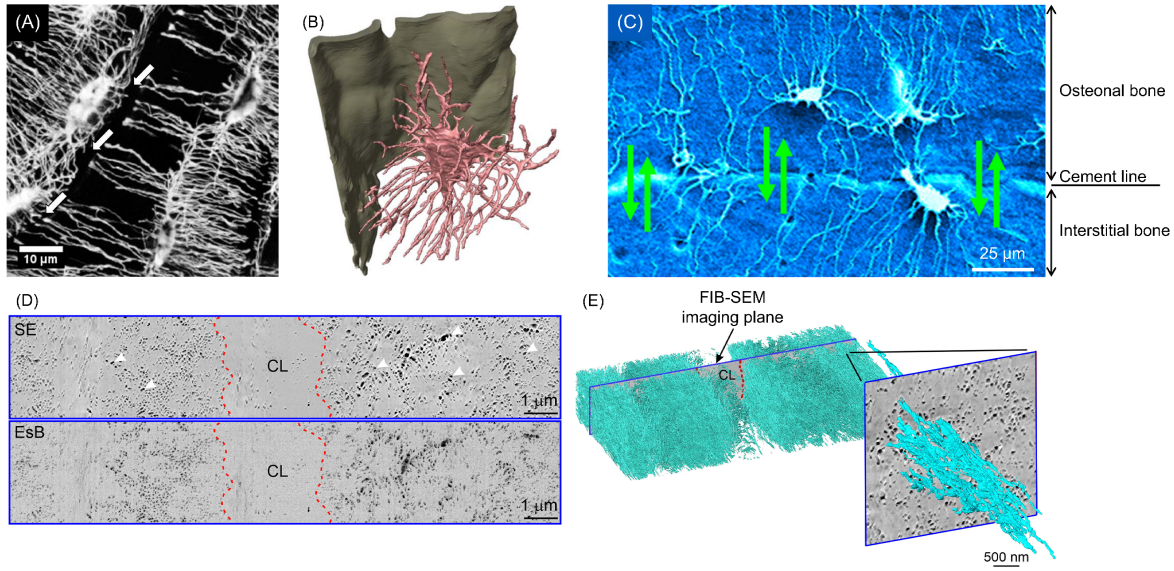


Figure 2.8: (A) CLSM image showing disruption of canalicular connections at the CL (white arrows) (adapted from [49]). (B) 3D reconstruction of the OLCN revealing canaliculi terminating at the CL interface (adapted from [52]). (C) Etching and SEM imaging revealing canalicular continuity across the CL (green arrows indicate traversing canaliculi) (adapted from [68]). (D) FIB-SEM cross-sectional images (secondary electron SE and energy selective backscattered EsB modes) showing disruption of the sub-canalicular nanochannel network at the CL (red dashed lines) and (E) 3D reconstruction showing numerous nanochannels in lamellar bone tissue and their absence at the CL region (adapted from [69]).

phy, morphology, and composition [71] [72].

SEM operates under a vacuum to avoid interactions of electrons with gas molecules in order to obtain high-resolution. When the accelerated primary electron beam hits the sample, several interactions occur (Fig. 2.9A):

- Inelastic scattering: Electrons may be ejected as secondary electrons (SE) as a result of energy transfer from the electron beam to the sample atoms (Fig. 2.9B). A distinctive X-ray can be produced by filling the vacancy left by the emission this SE with a higher-level orbital [72].
- Elastic scattering: Electrons are deflected by interaction with the atomic nucleus without suffering a significant energy loss, producing backscattered electrons (BE) (Fig. 2.9B) [72].

As a result of these elastic and inelastic interactions, the electron beam is distributed over a 3D interaction volume. This volume and the scattering of the electrons depend on several factors such as the atomic number, the atomic concentration, the angle of incidence and the accelerating voltage of the electron beam [72].

Second electron imaging

SEI captures low-energy electrons (< 50 eV) ejected from the sample during inelastic collisions. These electrons come from depths of only a few nanometers, offering high-resolution details of surface morphology and fine topographical features [72].

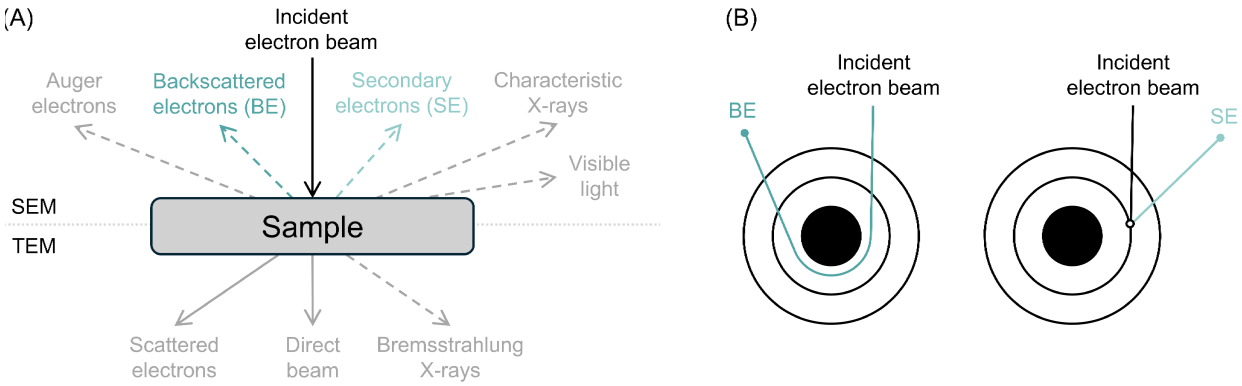


Figure 2.9: (A) Interactions between an electron beam and a sample.(B) Illustration of the interaction between BE and SE with the atom of a sample: BE are reflected back after interaction with the atom and SE are ejected after interaction with an electron from the material. Inspired from [72].

In this work, SEI was used in Chapter 4 to map the surface topography and precisely locate the indents imprints of nanoindentation experiments. This enabled correlations between local material composition and mechanical properties.

Backscattered electron imaging

BEI detects high-energy electrons (> 50 eV) that are reflected back from the sample during elastic scattering. Unlike SE, BE originate from deeper within the sample (up to 1-2 μm), providing valuable compositional contrast [73]. Indeed, the backscattered coefficient (i.e., the ratio of the number of BEs to the number of primary electrons) increases with the atomic number, making BEI particularly useful for distinguishing contrast variation in multiphase material [72].

Bone being highly heterogeneous, BEI is an effective tool for assessing mineral content distribution. In this work, BEI was used in Chapter 4 to distinguished CLs from surrounding bone based on their variaiton in composition. Combining SEI and BEI allowed for precise classification of nanoindentation locations, improving the analysis of mechanical properties and their relationship to compositional heterogeneity.

Quantitative backscattered electron imaging

Quantitative backscattered electron imaging (qBEI) builds upon BEI, allowing the precise quantification of mineral content in mineralized tissues such as bone [73]. This technique takes advantage of the linear relationship between the intensity of BE and the atomic number for materials with atomic number ($Z \leq 20$) (Fig. 2.10A) [71]. In bone tissue, calcium–being the element with the highest atomic number ($Z = 20$)–dominates the backscattered signal, making it possible to deduce the local degree of mineralization.

To achieve accurate quantification, the BE signal is calibrated using two reference materials: carbon ($Z = 6$) and aluminium ($Z = 13$). The contrast and brightness are adjusted to obtain a grey level of 25 ± 1 for carbon and 225 ± 1 for aluminium. A calibration line relating grey levels in the BE image to atomic

number is drawn between these two references and the grey level of pure hydroxyapatite of known atomic number ($Z = 14.06$) can be determined (Fig. 2.10B). Then, the grey level of osteoid, which has negligible Ca content (< 0.17 wt %), is assigned to a value of 0 wt % Ca content. Pure hydroxyapatite with a Ca content of 39.86 wt % Ca content, serves as the upper reference point. By connecting these two points, a standardization line is obtained, enabling the conversion of BE grey levels into Ca content (Fig. 2.10C) through the following equation [73, 74]:

$$\text{Ca content} = -4.332 + 0.1733 \times \text{BE grey level} \tag{2.1}$$

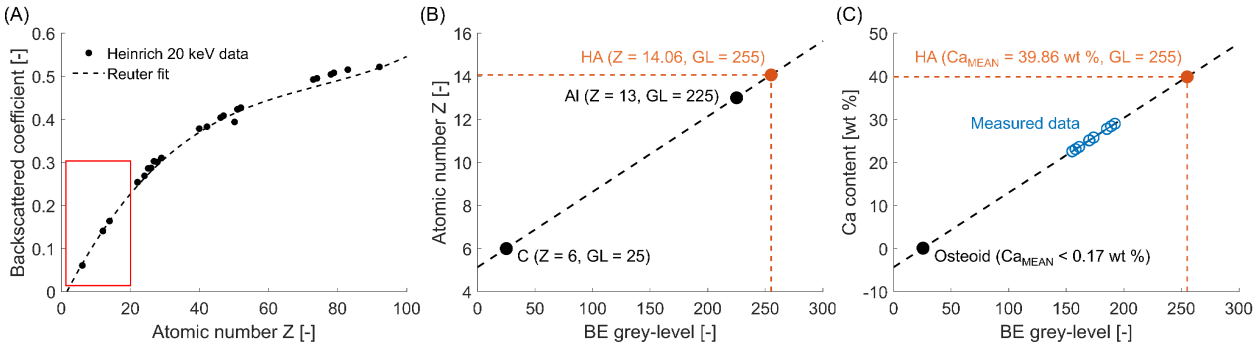


Figure 2.10: (A) Backscattered coefficient as a function of the atomic number Z for pure elements: the relationship is approximately linear for small atomic number (Z < 20). Image adapted from [71]. (B) Calibration line of BE grey level (GL) into atomic numbers (Z) for the calibration of the BE signal. Image adapted from [74]. (C) Standardization line of BE grey levels (GL) into Ca concentrations (wt %). The empty circles represents typically measured data for bone. Image adapted from [74].

The variation in mineral content within bone can then be represented as bone mineralization density distribution (BMDD) [21, 74]. BMDD is characterized by several key parameters:

- Ca_{Mean}: the average calcium content in the bone volume of interest and obtained from the integrated area under BMDD curve;
- Ca_{Peak}: the most frequent calcium content in bone area;
- Ca_{Width}: the variation in mineralization density represented by the width of the calcium content distribution;
- Ca_{Low}: the amount of lowly mineralized bone areas computed as the percentage of bone area mineralized below 5th percentile of reference range;
- Ca_{High}: the amount of highly mineralized bone areas computed as the percentage of bone area mineralized above 95th percentile of reference range in [%bone area].

In bone research and clinical diagnostic, BMDD is a valuable tool for assessing bone remodeling, mineralization kinetics, and average tissue age. For example, deviations from normal BMDD patterns can indicate pathological conditions such as osteoporosis or the effects of therapeutic interventions. To ensure reliability of qBEI results, sample preparation is critical. Proper polishing is required to minimize surface artifacts and eliminate the influence of crystal orientation. Additionally, measurements must be

conducted under standardized imaging conditions using the same device and calibration settings, as variations can significantly affect the results [73].

Despite these limitations, qBEI remains a powerful technique for ex vivo analysis of mineralized tissues. It provides not only quantitative data on the degree of mineralization but also insights into the structural and functional aspects of bone health [21]. This technique was used for this purpose in throughout this work, in Chapter 3, 4, and 5.

2.2.2 Second harmonic generation

Second harmonic generation (SHG) imaging is a powerful technique for visualizing the arrangement of collagen fibers in biological tissues. This method provides detailed information on the spatial organization, density, and alignment of collagen fibers without requiring any staining or fluorescent dyes [75].

SHG is a second-order nonlinear optical process that occurs when two photons of the same wavelength interact with a material [76]. These photons combine to produce a single photon with twice the energy and frequency (or half the wavelength) of the original photons (Fig. 2.11) [75]. This process is governed by the interaction between the material's polarization P and the electric field of light E, which is described by the material's susceptibility χ [77]:

$$P = \chi^{(1)}E^1 + \chi^{(2)}E^2 + \chi^{(3)}E^3 + ... \tag{2.2}$$

The first term accounts for linear optical effects such as absorption, scattering, and reflection, while the second-order term ($\chi^{(2)}$) represents nonlinear effects like SHG, which can only occur in non-centrosymmetric materials (i.e., those lacking a center of symmetry) [75]. Biological structures like type I and II collagen and myosin meet this condition, making them particularly suited to SHG imaging [77, 78].



Figure 2.11: Illustration of the SHG imaging process.

One condition for SHG to produce an effective signal is some alignment of the molecules in the imaging plane. The intensity of the signal depends on various factors, including collagen concentration, fibril alignment, [79] fibril diameter [80], and the amount of collagen cross-linking [81]. A strong SHG signal indicates densely packed, well-organized collagen fibrils, while a weaker signal may suggest fibrils that are randomly oriented, out-of-plane, or less densely arranged [77, 82, 83, 39].

SHG imaging has some limitations. As mentioned, the signal is highly sensitive to factors like collagen concentration, fibril alignment, and cross-linking, making quantitative analysis challenging. Moreover, the technique requires high laser intensity and is only capable of imaging a limited number of structural

proteins [75, 77, 84]. However, SHG imaging offers several advantages compared to other techniques. The signal is highly specific, and the resulting images exhibit sharp contrast. It provides endogenous contrast for visualizing collagen, eliminating the need for exogenous fluorescent dyes or labels. The process arises from induced polarization rather than from absorption, reducing substantially photobleaching and phototoxicity. Lastly, SHG typically uses near-infrared light which has lower scattering and absorption in tissues, allowing for higher resolution imaging compared to polarized light microscopy [75, 82, 84, 85].

In this work, SHG imaging was employed for the qualitative observation of collagen fiber organization in osteons in Chapter 3, 4, and 5. In Chapter 3, the technique allowed us to detect the most recently formed osteons in the analyzed regions by visualizing the continuity or interruption of lamellar arrangement. However, we did not attempt to perform quantitative analysis of the SHG signal due to the inherent complexity of the measurement.

2.2.3 Confocal laser scanning microscopy

Confocal laser scanning microscopy (CLSM) is an advanced optical imaging technique enabling high resolution 3D imaging of biological samples. This is achieved by capturing fluorescence signals from multiple focal planes and assembling them to generate comprehensive 3D reconstructions. It works by focusing the laser light source on a defined point at a specific depth within the sample and collecting the backscattered or emitted light through a pinhole. The pinhole only allows light from the focal point to reach the detector and blocks out-of-focus light. Images are acquired by scanning the region of interest point-by-point [86].

CLSM can be performed in either transmission or reflection mode and is compatible with fluorescent or non-fluorescent materials. In most biological applications, fluorescent labelling is combined with reflection mode to achieve high contrast and maximize the rejection of out-of-focus light. For this purpose, CLSM systems are equipped with multiple laser light sources, enabling the operator to select the appropriate wavelength for the detection of the different fluorochromes [87, 88].

A fluorochrome is a fluorescent molecule that can absorb a photon of light with a specific energy and wavelength, causing it to transition from the lowest energy ground state (S_0) to an excited state (S_1) (Fig. 2.12A). After a brief period, the fluorochrome's energy relaxes to the lowest vibrational level of the excited state, releasing energy as heat. It then returns to the ground state (S_0) by emitting a photon of lower energy, resulting in fluorescence at a longer wavelength than the absorbed photon (Fig. 2.12A). The difference between the absorbed and emitted wavelengths, called Stokes's shift, allows CLSM to filter out excitation light and keep only the emitted fluorescence light from the specimen providing high contrast image (Fig. 2.12B) [87, 88, 89].

Compared to traditional optical microscopy techniques, CLSM enables the collection of serial optical sections with high resolution and contrast from thick samples while keeping the sample intact. However, image acquisition is slower due to point-by-point scanning process [90].

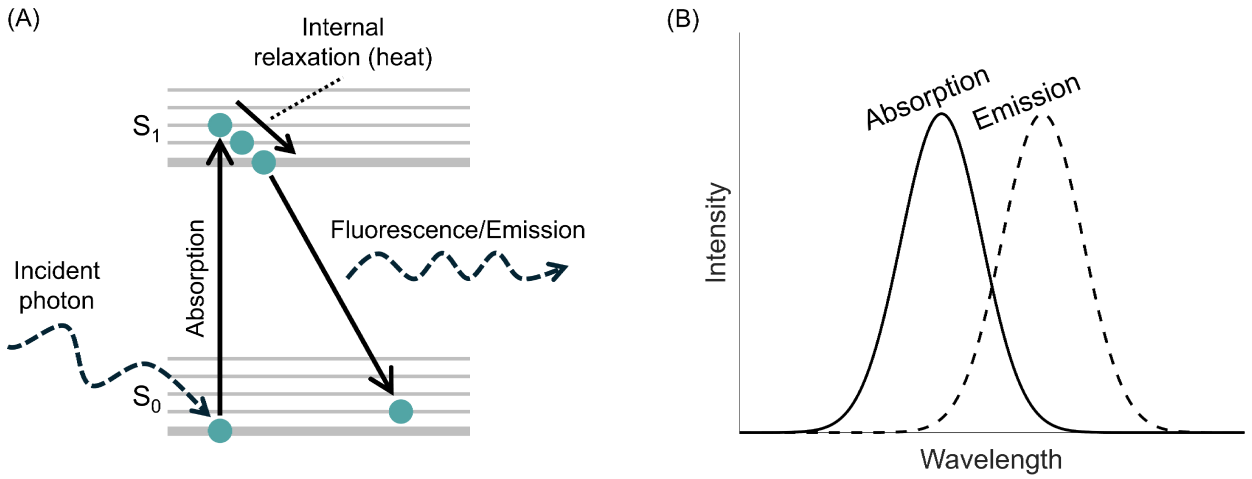


Figure 2.12: (A) Jablonski energy diagram illustrating photon absorption and emission by a fluorochrome. Image adapted from [87]. (B) Schematic plot illustrating the absorption and emission spectra. Image adapted from [87].

CLSM has become a widely used technique in biological research, allowing the imaging of various intracellular and extracellular structures or proteins. Different labelling options can be employed depending on the target structure. In this work, we used rhodamine-6G, a red fluorescent dye. Because of its small molecular dimensions (approximately 1.3 nm in length and 0.7 nm in width) [91], it can penetrate all accessible porosities in mineralized tissues, including bone vessels, lacunae, and canaliculi. This dye can be specifically detected by CLSM even after embedding in resin [89, 90]. Using this approach in Chapter 5, we imaged optical sections of the OLCN, enabling its 3D reconstruction over tens of micrometers.

2.2.4 X-ray scattering

X-ray scattering techniques are widely used to characterize hierarchical materials at submicron length scales [92]. Specifically, bone structure has been extensively analyzed using these techniques to investigate its fundamental building blocks. In Chapter 4, we used this technique to analyze the mineral particles properties of the CL and adjacent bone.

X-ray scattering involves the interaction of X-rays with the atomic and molecular structure of a material. When an incident beam of X-rays is directed at a sample, most X-rays are transmitted through without interaction. However, a small fraction interacts with the electrons in the sample, resulting in absorption, fluorescence, or scattering. The scattering process can be elastic (without energy loss) or inelastic (with energy loss). Elastic scattering, which preserves the wavelength of the incident beam, provides structural information and forms the basis of small- (SAXS) and wide-angle X-ray scattering (WAXS) techniques (Fig. 2.13A) [92, 93].

The scattering vector $\vec{q}$, defined as the difference between the wave vector of the incident ($\vec{k}$) and scattered beam ($\vec{k'}$) is given by:

$$\vec{q} = \vec{k} - \vec{k'} \tag{2.3}$$

Knowing that $|\vec{k}| = |\vec{k'}| = \frac{2\pi}{\lambda}$, the magnitude of $\vec{q}$ is expressed as:

$$|\vec{q}| = 2|\vec{k}| \sin\theta = \frac{4\pi}{\lambda} \sin\theta \tag{2.4}$$

where λ is the X-ray wavelength, and θ is the Bragg angle (half the scattering angle).

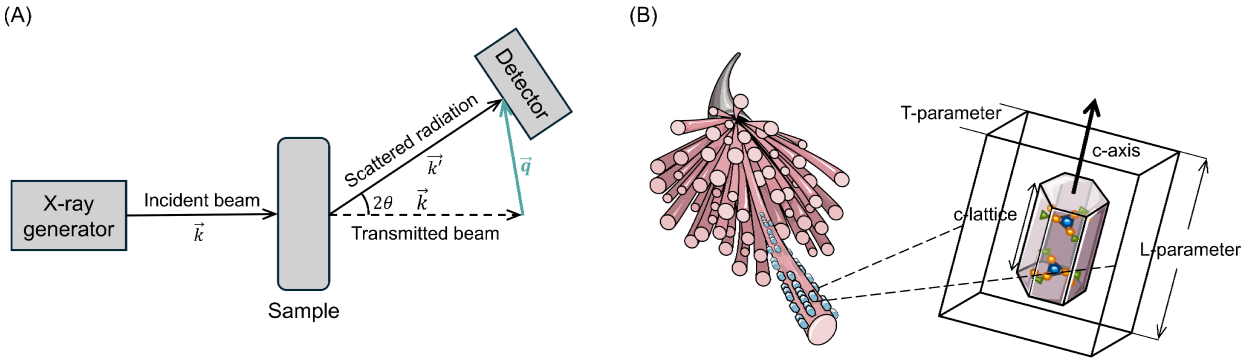


Figure 2.13: (A) Illustration of the X-ray scattering process. Image inspired from [92, 94].(B) Schematic illustration of collagen fibrils and mineral particles within, highlighting three parameters that can be derived from X-ray scattering measurements: T parameter, L parameter and *c-lattice*. This image was partly drawn using images from Servier Medical Art, licensed under a Creative Commons Attribution 4.0 Unported License (https://creativecommons.org/licenses/by/4.0/).

SAXS and WAXS probe structures at different length scales. SAXS focuses on low-q regions ($2\theta > 5°$) to study nanometer-scale structures, such as particle sizes, and their arrangement, whereas WAXS probes high-q regions ($2\theta > 5°$) to analyze atomic-scale structures, including crystal lattice parameters (Fig. 2.13B) [92].

SAXS

SAXS signal (Fig. 2.14A) arises from the contrast in electron density between two discrete phases with sharp interface [95, 96]. In the case of bone, these two phases are the organic collagen matrix with a low electron density and the mineral particles with a high electron density. SAXS analysis provides two key structural parameters: the mineral particle thickness (T parameter) (Fig. 2.13B) and degree of alignment (ρ parameter).

T parameter

According to Porod's law, in a two-phases system with different electron densities and sharp interfaces, the scattering intensity $I(q)$ (Fig. 2.14B) decreases with q^{-4} for high q [96]:

$$I(q \to \infty) \approx \frac{P}{q^4} + B \tag{2.5}$$

where P is the Porod constant, and B is a background constant resulting from incoherent inelastic scattering [97, 98]. In bone, the T parameter reflects the volume-to-surface ratio of mineral particles and can

be derived as:

$$T = \frac{4}{\pi P}\int_0^\infty q^2 I(\vec{q})dq = 4\frac{\phi(1-\phi)}{\sigma} \tag{2.6}$$

where $I*(q) = I(q)-B$, ϕ is the volume fraction of the mineral phase, and σ is the surface area of mineral particles per unit volume. Assuming mineral platelets are uniform parallelepiped of edges W, X, and Y, the equation becomes:

$$T = 2(1-\phi)\frac{WXY}{WX+XY+WY} \tag{2.7}$$

Since HAP particles are assumed to be thin mineral platelets ($W << X \leq Y$) [5], the equation simplifies as:

$$T = 2(1-\phi)W \tag{2.8}$$

Therefore, the T parameter is a good approximation for the average particle thickness ($T \approx W$) if the degree of mineralization ϕ is equal to 0.5 [99]. If the volume fraction of mineral deviates significantly from 50%, the actual volume fraction values ϕ need to be measured independently to compute the accurate T parameter ($W = \frac{T}{2(1-\phi)}$). This is often achieved thanks to qBEI. Using bone mineral density data, ϕ is computed as [100]:

$$\phi = \mathrm{HAP_{Vol}} = \frac{\mathrm{HAP_{Weight}}}{\mathrm{HAP_{Weight}} + (1-\mathrm{HAP_{Weight}}) * (\varrho_{\mathrm{HAP}}/\varrho_{\mathrm{org}})} \tag{2.9}$$

where $\mathrm{HAP_{Vol}}$ is the volume fraction of HAP in the sample, $\varrho_{\mathrm{HAP}} = 3.18\ \mathrm{g/cm^3}$ is the density of HAP, $\varrho_{\mathrm{org}} = 1.41\ \mathrm{g/cm^3}$ is the density of the organic matrix [101], and $\mathrm{HAP_{Weight}} = \mathrm{Ca_{Mean}} \times 2.51$ is the weight fraction of HAP.

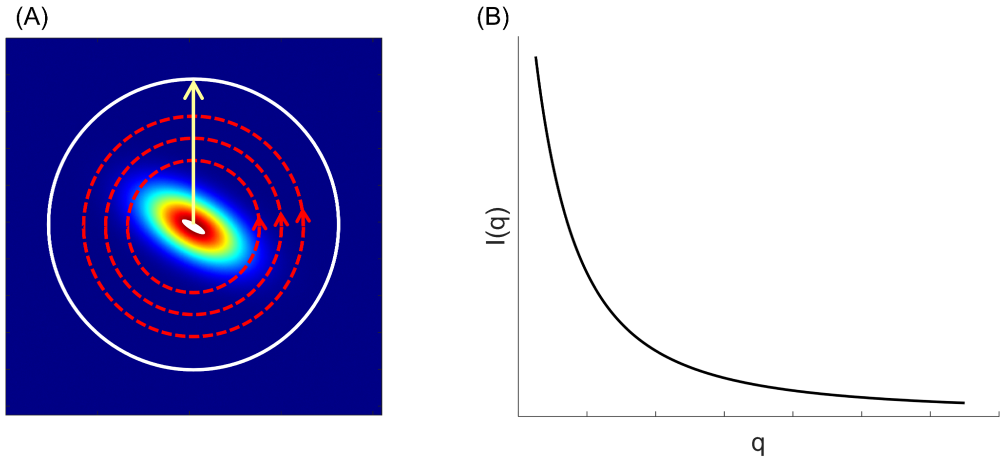


Figure 2.14: (A) SAXS pattern integrated in azimuthal direction (red dashed line), with the direction of the resulting radial plot indicated by the yellow arrow. (B) Radial intensity profile $I(q)$ obtained by binning all pixels with the same radial distance q to the beam center in the azimuthal direction. Images inspired from [94, 102].

ρ parameter

The ρ parameter quantifies the degree of alignment of the mineral particles. In SAXS patterns, an anisotropic intensity distribution (e.g., elliptical patterns) indicates that the crystals have a predominant orientation (Fig. 2.15A), whereas isotropic patterns (e.g. circular patterns) indicate randomness [92]. Therefore, ρ parameter can be estimated from the anisotropy of the elliptical SAXS pattern (Fig. 2.15A) by computing the azimuthal profile of the intensity distribution $I(\chi)$ in the radial direction (Fig. 2.15B) [98]. For oriented particles, the azimuthal plot $I(\chi)$ shows two peaks separated by 180° (Fig. 2.15B), whereas less oriented particles flatten the curve. The ρ parameter is defined as [94]:

$$\rho = \frac{\text{Mineral}_{\text{Aligned}}}{\text{Mineral}_{\text{Aligned}} + \text{Mineral}_{\text{Unaligned}}} = \frac{A_1 + A_2}{A_1 + A_2 + B} \tag{2.10}$$

where A_1 and A_2 are the peak areas, and B the background area. A value of $\rho = 1$ indicates perfect alignment of the particles, while $\rho = 0$ reflects random orientation [98].

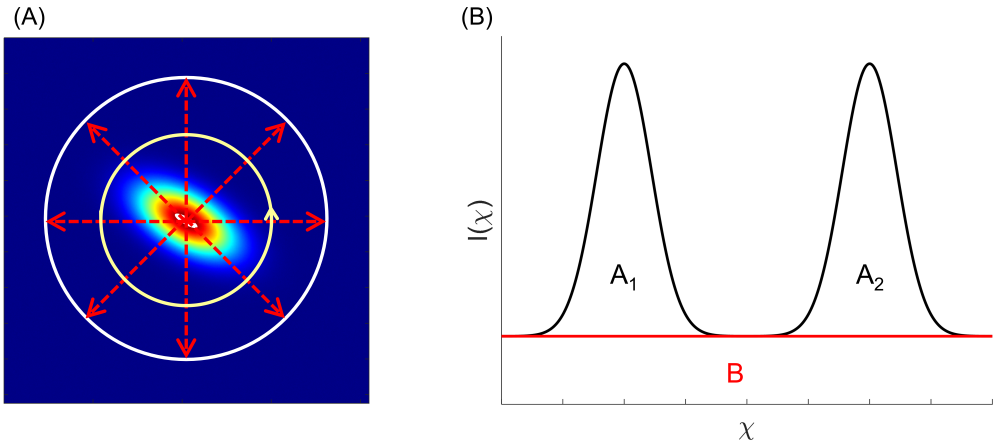


Figure 2.15: (A) SAXS pattern integrated in radial direction (red dashed line), with the direction of the resulting azimuthal plot indicated by the yellow arrow. (B) Azimuthal intensity profile $I(\chi)$ obtained by binning all pixels with the same azimuthal degree χ in the radial direction. Images inspired from [94, 102].

WAXS

WAXS signal arises from the diffraction of X-rays by crystalline materials, such as the periodic atomic arrangement in HAP [103]. In bone, WAXS patterns typically display wide-angle rings called Debye-Scherrer rings, with the (002) lattice plane reflection being the strongest (Fig. 2.16A). The position and width of this ring provide information on the lattice spacing (i.e., the distance between imaginary planes formed by the atoms of HAP along the c axis) [104] and the mean length of the mineral platelets (L parameter) along the c axis (Fig. 2.13B) [105].

L parameter

The L parameter is computed using the Scherrer equation [106, 107, 108]:

$$L = \frac{k\lambda}{B\cos\theta} \tag{2.11}$$

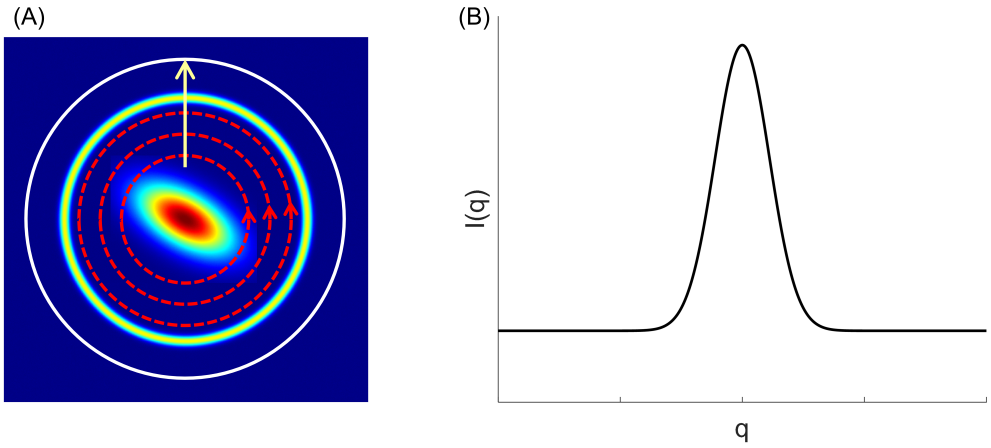


Figure 2.16: (A) WAXS pattern integrated in azimuthal direction (red dashed line), with the direction of the resulting radial plot indicated by the yellow arrow. (B) Radial intensity profile $I(q)$ obtained by binning all pixels with the same radial distance q in the azimuthal direction. Images inspired from [94, 102].

where L is the crystal length, λ is the X-ray wavelength, B is the full width at half maximum of the (002) peak, θ is the Bragg angle, and k is a constant related to the crystalline shape.

c-lattice

The lattice spacing is determined using Bragg's law [109]:

$$N\lambda = 2d \sin\theta \tag{2.12}$$

where d is the c-lattice, n is the diffraction order, λ is the X-ray wavelength, and θ is the Bragg angle.

2.2.5 Nanoindentation

Nanoindentation is a high-resolution mechanical technique used to measure the local mechanical properties of various materials, and it is particularly useful for heterogeneous biological samples such as bone [110]. During a nanoindentation test, an indenter tip–typically made of hard material (e.g., diamond) and designed with a well-defined geometry–penetrates the surface of a softer material under a controlled load or displacement. This process induces two types of deformations: elastic deformation which is reversible, and plastic deformation, which is permanent. Upon unloading, the elastic deformation is recovered, while the plastic deformation remains as a permanent imprint (Fig. 2.17) [111, 112].

Throughout the test, the load and displacement are continuously recorded. Using the method of Oliver and Pharr [111], two key mechanical properties can be derived from these measurements: the elastic modulus E and the hardness H. The elastic modulus E is determined from the contact stiffness S, which represents the initial unloading stiffness. The following equation, applicable to elastic contacts [111, 113], is used:

$$S = \frac{dP}{dh} = \frac{2}{\sqrt{\pi}} E_r \sqrt{A} \tag{2.13}$$

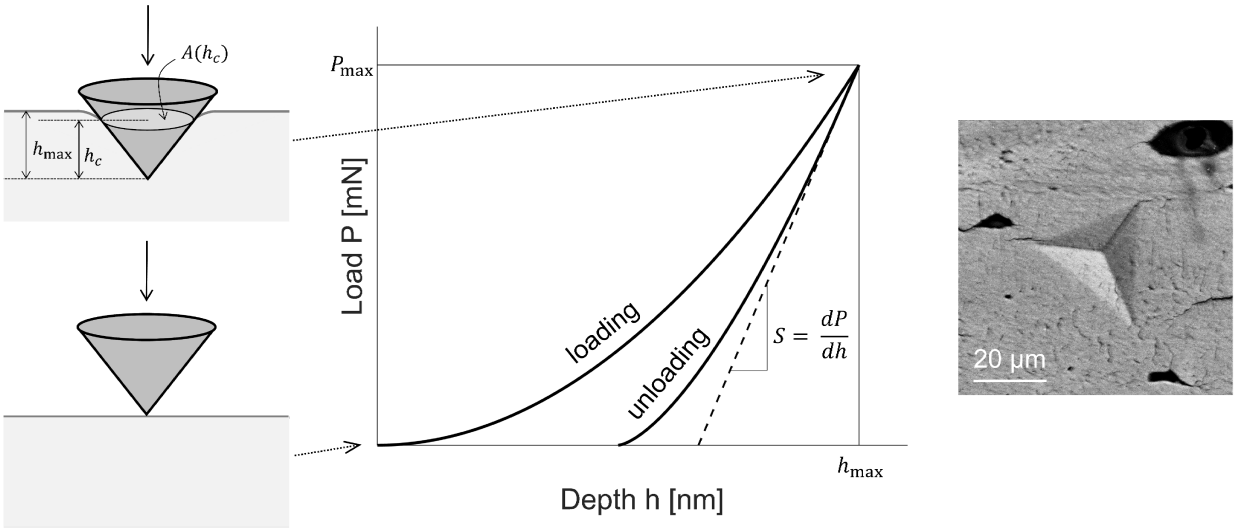


Figure 2.17: Schematic representations and load-displacement curve of nanoindentation testing, highlighting the loading and unloading behavior (inspired from [111]), as well as SEM image of the residual indentation, showing the imprint of the indenter on the surface of the material.

Here, A is the contact area, and E_r is the reduced modulus, accounting for the combined elastic response of the tip and the sample. The reduced modulus is expressed as:

$$\frac{1}{E_r} = \frac{(1-\nu_i^2)}{E_i} + \frac{(1-\nu^2)}{E} \tag{2.14}$$

where E_i and ν_i are the elastic modulus and Poisson's ratio of the indenter, while E and ν are those of the sample. For a diamond indenter, since $E_i \gg E$, the expression simplifies to:

$$\frac{1}{E_r} \approx \frac{(1-\nu^2)}{E} \tag{2.15}$$

The hardness H, defined as the resistance of a solid to local plastic deformation, is computed using the following relationship:

$$H = \frac{P_{\text{max}}}{A} \tag{2.16}$$

where P_{max} is the peak indentation load.

Both E and H require accurate knowledge of the contact area A at the peak load. This can be obtained by calibrating the tip geometry with a reference sample (e.g., fuzed quartz), which is homogeneous and has known elastic properties (E_i and ν_i). This involves performing a series of nanoindentation tests on the reference sample. From the unloading curves of these tests, the contact stiffness S is measured for each depth. Using the relationship for S (Eq. 2.2.5), the contact area A is determined for each depth, allowing the construction of the tip area function $A(h_c)$, where h_c is the contact depth (Fig. 2.17) [110, 112].

In this work, nanoindentation proved to be a highly effective tool, offering significant advantages, such as

the high resolution and the ability to measure local mechanical properties in heterogeneous materials like bone (see Chapter 4). These strengths were particularly valuable for studying the mechanical differences at the microstructural level. However, to ensure the accurate interpretation of the mechanical data, SEM was employed to verify the nanoindentation locations. This was necessary because the optical microscope used for navigation during the test did not allow precise identification of the CL position, which introduced initial uncertainty in targeting specific regions. Additionally, two challenges were addressed during this study. First, to maximize the probability of positioning indents on the CL, a minimal lateral spacing was selected. To prevent interactions between neighboring indents, however, this spacing was maintained at least three times the contact radius [114]. Secondly, a low surface roughness was essential for reliable measurements. The indentation depth was chosen to exceed the threshold of ten times the surface roughness, as recommended [115, 116]. Despite these adjustments and the inherent assumptions of the analysis models, nanoindentation proved to be a powerful tool for localized mechanical testing, enabling the investigation of spatial variations in bone properties that would be challenging with other techniques.

2.3 Objectives of the thesis

The overall aim of this thesis is to characterize material, mechanical and biological aspects of the CL, a key structural feature in bone that should play a crucial yet still debated role in tissue organization, mechanical behavior, and cells connectivity. Specifically, this work focuses on CL mineral content and mineral properties, local mechanical behavior, and interaction with the OLCN. This is done through successive and complementary research studies. High-resolution multimodal imaging techniques are employed across all three studies, allowing for detailed comparisons of the CL with its corresponding osteon and surrounding bone tissue, using a correlative approach with submicrometer spatial resolution as required by the tiny dimension of the CL.

- The first objective of this thesis is to characterize how the mineral content of CLs varies in relation to their surrounding environment and how it may evolve over time. By examining osteons with different values of mineral content, used here as a proxy for tissue age, we gain new insights into the dynamics of CL mineralization and its variability within the bone matrix.

- Building on these findings, our second objective focuses on how mineral content and mineral characteristics of CLs relate to its local mechanical behavior, looking for specificities of the CL in comparison to adjacent tissue. This study investigates the composition-mechanics relationship at the microscale, which is an essential knowledge to understand the potential role of the CL in bone quality, particularly in bone damage tolerance.

- Finally, the third objective addresses the characterization of the OLCN organization near the CLs. We investigate whether the OCLN shows a specific architecture close to the CL and how the CL influences the connectivity between osteocytes lacunae. Specifically, we quantify the extent to

which canaliculi cross the outer border of the osteons and reach osteocytes lacunae belonging to other osteons or interstitial bone. This analysis considers a biological aspect of CLs which is still poorly understood: the interplay between the CL and the bone functional porosity is relevant for possible inter-osteon communication, with implications for bone remodeling and functional adaptation.

Bibliography

[1] JY Rho, L Kuhn-Spearing, and P Zioupos. Mechanical properties and the hierarchical structure of bone. *Medical Engineering & Physics*, 20(2):92–102, March 1998.

[2] P Fratzl and R Weinkamer. Nature's hierarchical materials. *Progress in Materials Science*, 52(8):1263–1334, November 2007.

[3] W Wagermaier, K Klaushofer, and P Fratzl. Fragility of bone material controlled by internal interfaces. *Calcified Tissue International*, 97(3):201–212, September 2015.

[4] JD Currey. *Bones: Structure and Mechanics*. Princeton University Press, 2002.

[5] P Fratzl, HS Gupta, EP Paschalis, and P Roschger. Structure and mechanical quality of the collagen–mineral nanocomposite in bone. *J. Mater. Chem.*, 14(14):2115–2123, 2004.

[6] RK Surowiec, MR Allen, and JM Wallace. Bone hydration: How we can evaluate it, what can it tell us, and is it an effective therapeutic target? *Bone Reports*, 16:101161, June 2022.

[7] L Yu and M Wei. Biomineralization of Collagen-Based Materials for Hard Tissue Repair. *International Journal of Molecular Sciences*, 22(2):944, January 2021.

[8] JD Currey. The many adaptations of bone. *Journal of Biomechanics*, 36(10):1487–1495, 2003.

[9] JG Skedros, JL Holmes, EG Vajda, and RD Bloebaum. Cement lines of secondary osteons in human bone are not mineral-deficient: new data in a historical perspective. *The Anatomical Record Part A: Discoveries in Molecular, Cellular, and Evolutionary Biology*, 286A(1):781–803, September 2005.

[10] MA Hartmann, JWC Dunlop, YJM Bréchet, P Fratzl, and R Weinkamer. Trabecular bone remodelling simulated by a stochastic exchange of discrete bone packets from the surface. *Journal of the Mechanical Behavior of Biomedical Materials*, 4(6):879–887, August 2011.

[11] DJ Hadjidakis and II Androulakis. Bone Remodeling. *Annals of the New York Academy of Sciences*, 1092(1):385–396, December 2006.

[12] AG Robling, AB Castillo, and CH Turner. Biomechanical and molecular regulation of bone remodeling. *Annual Review of Biomedical Engineering*, 8(1):455–498, August 2006.

[13] B Chang and X Liu. Osteon: structure, turnover, and regeneration. *Tissue Engineering Part B: Reviews*, page ten.teb.2020.0322, March 2021.

[14] J Klein-Nulend and AD Bakker. Osteocytes: Mechanosensors of Bone and Orchestrators of Mechanical Adaptation. *Clinical Reviews in Bone and Mineral Metabolism*, 5(4):195–209, December 2007.

[15] F Repp, P Kollmannsberger, A Roschger, M Kerschnitzki, A Berzlanovich, GM Gruber, P Roschger, W Wagermaier, and R Weinkamer. Spatial heterogeneity in the canalicular density of the osteocyte network in human osteons. *Bone Reports*, 6:101–108, June 2017.

[16] R Weinkamer and P Fratzl. Solving conflicting functional requirements by hierarchical structuring—Examples from biological materials. *MRS Bulletin*, 41(09):667–671, September 2016.

[17] NA Sims. Osteoclast-derived coupling factors: Origins and state-of-play Louis V Avioli lecture, ASBMR 2023. *Journal of Bone and Mineral Research*, 39(10):1377–1385, September 2024.

[18] NA Sims and TJ Martin. Coupling the activities of bone formation and resorption: a multitude of signals within the basic multicellular unit. *BoneKEy Reports*, 3, January 2014.

[19] S Bolamperti, I Villa, and A Rubinacci. Bone remodeling: An operational process ensuring survival and bone mechanical competence. *Bone Research*, 10(1):48, July 2022.

[20] BM Misof, DW Dempster, H Zhou, P Roschger, N Fratzl-Zelman, P Fratzl, SJ Silverberg, E Shane, A Cohen, E Stein, TL Nickolas, RR Recker, J Lappe, JP Bilezikian, and K Klaushofer. Relationship of Bone Mineralization Density Distribution (BMDD) in Cortical and Cancellous Bone Within the Iliac Crest of Healthy Premenopausal Women. *Calcified Tissue International*, 95(4):332–339, October 2014.

[21] P Roschger, EP Paschalis, P Fratzl, and K Klaushofer. Bone mineralization density distribution in health and disease. *Bone*, 42(3):456–466, March 2008.

[22] O Akkus, A Polyakova-Akkus, F Adar, and MB Schaffler. Aging of Microstructural Compartments in Human Compact Bone. *Journal of Bone and Mineral Research*, 18(6):1012–1019, June 2003.

[23] D Ruffoni, P Fratzl, P Roschger, K Klaushofer, and R Weinkamer. The bone mineralization density distribution as a fingerprint of the mineralization process. *Bone*, 40(5):1308–1319, May 2007.

[24] A Roschger, W Wagermaier, S Gamsjaeger, N Hassler, I Schmidt, S Blouin, A Berzlanovich, GM Gruber, R Weinkamer, P Roschger, EP Paschalis, K Klaushofer, and P Fratzl. Newly formed and remodeled human bone exhibits differences in the mineralization process. *Acta Biomaterialia*, 104:221–230, March 2020.

[25] KM Cooke, P Mahoney, and JJ Miszkiewicz. Secondary osteon variants and remodeling in human bone. *The Anatomical Record*, 305(6):1299–1315, June 2022.

[26] AF van Tol, A Roschger, F Repp, J Chen, P Roschger, A Berzlanovich, GM Gruber, P Fratzl, and R Weinkamer. Network architecture strongly influences the fluid flow pattern through the lacunocanalicular network in human osteons. *Biomechanics and Modeling in Mechanobiology*, 19(3):823–840, June 2020.

[27] MF Eriksen. Histologic estimation of age at death using the anterior cortex of the femur. *Journal of physical anthropology*, 84(2):171–179, December 1991.

[28] A. Robling and SD Stout. Morphology of the Drifting Osteon. *Cells Tissues Organs*, 164(4):192–204, 1999.

[29] E Raguin and MA Streeter. Brief communication: Test of a method to identify double-zonal osteon in polarized light microscopy. *American Journal of Physical Anthropology*, 167(2):407–415, October 2018.

[30] W Wagermaier, HS Gupta, A Gourrier, M Burghammer, P Roschger, and P Fratzl. Spiral twisting of fiber orientation inside bone lamellae. *Biointerphases*, 1(1):1–5, March 2006.

[31] H Razi, J Predan, FD Fischer, O Kolednik, and P Fratzl. Damage tolerance of lamellar bone. *Bone*, 130:115102, January 2020.

[32] KE Stockhausen, M Qwamizadeh, EM Wölfel, H Hemmatian, IAK Fiedler, S Flenner, E Longo, M Amling, I Greving, RO Ritchie, FN Schmidt, and B Busse. Collagen fiber orientation is coupled with specific nano-compositional patterns in *dark* and *bright* osteons modulating their biomechanical properties. *ACS Nano*, 15(1):455–467, January 2021.

[33] MG Ascenzi, A Ascenzi, A Benvenuti, M Burghammer, S Panzavolta, and A Bigi. Structural differences between "dark" and "bright" isolated human osteonic lamellae. *Journal of Structural Biology*, 141(1):22–33, January 2003.

[34] NK Wittig, J Palle, M Østergaard, S Frølich, ME Birkbak, KM Spiers, J Garrevoet, and H Birkedal. Bone biomineral properties vary across human osteonal bone. *ACS Nano*, 13(11):12949–12956, November 2019.

[35] TA Grünewald, A Johannes, NK Wittig, J Palle, A Rack, M Burghammer, and H Birkedal. Bone mineral properties and 3D orientation of human lamellar bone around cement lines and the haversian system. *IUCrJ*, 10(2):189–198, March 2023.

[36] M Granke, A Gourrier, F Rupin, K Raum, F Peyrin, M Burghammer, A Saïed, and P Laugier. Microfibril orientation dominates the microelastic properties of human bone tissue at the lamellar length scale. *PLoS ONE*, 8(3):e58043, March 2013.

[37] TA Grünewald, M Liebi, NK Wittig, A Johannes, T Sikjaer, L Rejnmark, Z Gao, M Rosenthal, M Guizar-Sicairos, H Birkedal, and M Burghammer. Mapping the 3D orientation of nanocrystals and nanostructures in human bone: indications of novel structural features. *Science Advances*, 6(24):eaba4171, June 2020.

[38] EA Zimmermann, B Gludovatz, E Schaible, B Busse, and RO Ritchie. Fracture resistance of human cortical bone across multiple length-scales at physiological strain rates. *Biomaterials*, 35(21):5472–5481, July 2014.

[39] F Repp, P Kollmannsberger, A Roschger, A Berzlanovich, GM Gruber, P Roschger, W Wagermaier, and R Weinkamer. Coalignment of osteocyte canaliculi and collagen fibers in human osteonal bone. *Journal of Structural Biology*, 199(3):177–186, September 2017.

[40] VV Ebner. Über den feineren bau der skelettheile der kalkschwämme nebst bemerkungen über kalkskelete überhaupt. *Sonder Berichte der Akademie der Wissenschaften Wien Abt*, 1:55–149, 1887.

[41] NE Lassen, TL Andersen, GG Pløen, K Søe, EM Hauge, S Harving, GET Eschen, and JM Delaisse. Coupling of bone resorption and formation in real time: new knowledge gained from human haversian BMUs. *Journal of Bone and Mineral Research*, 32(7):1395–1405, July 2017.

[42] BA Lamarche, JS Thomsen, CM Andreasen, WB Lievers, and TL Andersen. 2D size of trabecular bone structure units (BSU) correlate more strongly with 3D architectural parameters than age in human vertebrae. *Bone*, 160:116399, July 2022.

[43] HS Gupta, S Schratter, W Tesch, P Roschger, A Berzlanovich, T Schoeberl, K Klaushofer, and P Fratzl. Two different correlations between nanoindentation modulus and mineral content in the bone–cartilage interface. *Journal of Structural Biology*, 149(2):138–148, February 2005.

[44] A Tits, S Blouin, M Rummler, JF Kaux, P Drion, HG Van Lenthe, R Weinkamer, MA Hartmann, and D Ruffoni. Structural and functional heterogeneity of mineralized fibrocartilage at the Achilles tendon-bone insertion. *Acta Biomaterialia*, 166:409–418, August 2023.

[45] MD McKee and A Nanci. Osteopontin and the bone remodeling sequence: colloidal-gold immunocytochemistry of an interfacial extracellular matrix protein. *Annals of the New York Academy of Sciences*, 760(1):177–189, August 1995.

[46] MD McKee and A Nanci. Osteopontin at mineralized tissue interfaces in bone, teeth, and osseointegrated implants: ultrastructural distribution and implications for mineralized tissue formation, turnover, and repair. *Microscopy Research and Technique*, 33(2):141–164, February 1996.

[47] V Everts, JM Delaissé, W Korper, DC Jansen, W Tigchelaar-Gutter, P Saftig, and W Beertsen. The bone lining cell: its role in cleaning Howship's lacunae and initiating bone formation. *Journal of Bone and Mineral Research*, 17(1):77–90, January 2002.

[48] MD McKee, MC Farach-Carson, WT Butler, PV Hauschka, and A Nanci. Ultrastructural immunolocalization of noncollagenous (osteopontin and osteocalcin) and plasma (albumin and α2HS-glycoprotein) proteins in rat bone. *Journal of Bone and Mineral Research*, 8(4):485–496, April 1993.

[49] M Kerschnitzki, W Wagermaier, P Roschger, J Seto, R Shahar, GN Duda, S Mundlos, and P Fratzl. The organization of the osteocyte network mirrors the extracellular matrix orientation in bone. *Journal of Structural Biology*, 173(2):303–311, February 2011.

[50] MB Schaffler, DB Burr, and RG Frederickson. Morphology of the osteonal cement line in human bone. *The Anatomical Record*, 217(3):223–228, March 1987.

[51] DB Burr, MB Schaffler, and RG Frederickson. Composition of the cement line and its possible mechanical role as a local interface in human compact bone. *Journal of Biomechanics*, 21(11):939–945, January 1988.

[52] M Langer, A Pacureanu, H Suhonen, Q Grimal, P Cloetens, and F Peyrin. X-ray phase nanotomography resolves the 3D human bone ultrastructure. *PLoS ONE*, 7(8):e35691, August 2012.

[53] P Milovanovic, A vom Scheidt, K Mletzko, G Sarau, K Püschel, M Djuric, M Amling, S Christiansen, and B Busse. Bone tissue aging affects mineralization of cement lines. *Bone*, 110:187–193, May 2018.

[54] E Raguin, K Rechav, R Shahar, and S Weiner. Focused ion beam-SEM 3D analysis of mineralized osteonal bone: lamellae and cement sheath structures. *Acta Biomaterialia*, 121:497–513, February 2021.

[55] RK Nalla, JJ Kruzic, JH Kinney, and RO Ritchie. Mechanistic aspects of fracture and R-curve behavior in human cortical bone. *Biomaterials*, 26(2):217–231, January 2005.

[56] KJ Koester, JW Ager, and RO Ritchie. The true toughness of human cortical bone measured with realistically short cracks. *Nature Materials*, 7(8):672–677, August 2008.

[57] S Mohsin, FJ O'Brien, and TC Lee. Osteonal crack barriers in ovine compact bone. *Journal of Anatomy*, 208(1):81–89, January 2006.

[58] S Qiu, D Sudhaker Rao, DP Fyhrie, S Palnitkar, and AM Parfitt. The morphological association between microcracks and osteocyte lacunae in human cortical bone. *Bone*, 37(1):10–15, July 2005.

[59] R Gauthier, H Follet, C Olivier, D Mitton, and F Peyrin. 3D analysis of the osteonal and interstitial tissue in human radii cortical bone. *Bone*, 127:526–536, October 2019.

[60] L Vergani, C Colombo, and F Libonati. Crack propagation in cortical bone: a numerical study. *Procedia Materials Science*, 3:1524–1529, 2014.

[61] S Nobakhti, G Limbert, and PJ Thurner. Cement lines and interlamellar areas in compact bone as strain amplifiers – Contributors to elasticity, fracture toughness and mechanotransduction. *Journal of the Mechanical Behavior of Biomedical Materials*, 29:235–251, January 2014.

[62] E Giner, R Belda, C Arango, A Vercher-Martínez, JE Tarancón, and FJ Fuenmayor. Calculation of the critical energy release rate G c of the cement line in cortical bone combining experimental tests and finite element models. *Engineering Fracture Mechanics*, 184:168–182, October 2017.

[63] D Hull and TW Clyne. *An Introduction to Composite Materials*. Cambridge Solid State Science Series. Cambridge University Press, Cambridge, 2 edition, 1996.

[64] T Montalbano and G Feng. Nanoindentation characterization of the cement lines in ovine and bovine femurs. *Journal of Materials Research*, 26(8):1036–1041, April 2011.

[65] Y Zhou, MJ Kastner, TB Tighe, and J Du. Elastic modulus mapping for bovine cortical bone from submillimeter- to submicron-scales using peakforce tapping atomic force microscopy. *Extreme Mechanics Letters*, 41:101031, November 2020.

[66] I Jäger and P Fratzl. Mineralized Collagen Fibrils: A Mechanical Model with a Staggered Arrangement of Mineral Particles. *Biophysical Journal*, 79(4):1737–1746, October 2000.

[67] TA Curtis, SH Ashrafi, and DF Weber. Canalicular communication in the cortices of human long bones. *The Anatomical Record*, 212(4):336–344, August 1985.

[68] P Milovanovic, EA Zimmermann, M Hahn, D Djonic, K Püschel, M Djuric, M Amling, and B Busse. Osteocytic canalicular networks: morphological implications for altered mechanosensitivity. *ACS Nano*, 7(9):7542–7551, September 2013.

[69] T Tang, W Landis, S Blouin, L Bertinetti, MA Hartmann, A Berzlanovich, R Weinkamer, W Wagermaier, and P Fratzl. Subcanalicular nanochannel volume is inversely correlated with calcium content in human cortical bone. *Journal of Bone and Mineral Research*, 38(2):313–325, December 2022.

[70] R Shahar and S Weiner. Open questions on the 3D structures of collagen containing vertebrate mineralized tissues: a perspective. *Journal of Structural Biology*, 201(3):187–198, March 2018.

[71] JI Goldstein, DE Newbury, P Echlin, DC Joy, CE Lyman, E Lifshin, L Sawyer, and JR Michael. *Scanning Electron Microscopy and X-Ray Microanalysis*, pages 61–98. Plenum Press, New York, 2nd ed edition, 2017.

[72] K Akhtar, SA Khan, SB Khan, and AM Asiri. *Handbook of Materials Characterization*, chapter Scanning Electron Microscopy: Principle and Applications in Nanomaterials Characterization, pages 113–124. Springer, New York, 3rd ed edition, 2018.

[73] MA Hartmann, S Blouin, BM Misof, N Fratzl-Zelman, P Roschger, A Berzlanovich, GM Gruber, PC Brugger, J Zwerina, and P Fratzl. Quantitative backscattered electron imaging of bone using a thermionic or a field emission electron source. *Calcified Tissue International*, 109(2):190–202, August 2021.

[74] P Roschger, P Fratzl, J Eschberger, and K Klaushofer. Validation of quantitative backscattered electron imaging for the measurement of mineral density distribution in human bone biopsies. *Bone*, 23(4):319–326, October 1998.

[75] R Gauderon, PB Lukins, and CJR Sheppard. Optimization of second-harmonic generation microscopy. *Micron*, 32(7):691–700, October 2001.

[76] PA Franken, AE Hill, CW Peters, and G Weinreich. Generation of Optical Harmonics. *Physical Review Letters*, 7(4):118–119, August 1961.

[77] X Chen, O Nadiarynkh, S Plotnikov, and PJ Campagnola. Second harmonic generation microscopy for quantitative analysis of collagen fibrillar structure. *Nature Protocols*, 7(4):654–669, April 2012.

[78] G Cox, E Kable, A Jones, I Fraser, F Manconi, and MD Gorrell. 3-Dimensional imaging of collagen using second harmonic generation. *Journal of Structural Biology*, 141(1):53–62, January 2003.

[79] I Freund, M Deutsch, and A Sprecher. Connective tissue polarity. optical second-harmonic microscopy, crossed-beam summation, and small-angle scattering in rat-tail tendon. *Biophysical journal*, 50(4):693–712, October 1986.

[80] R LaComb, O Nadiarnykh, SS Townsend, and PJ Campagnola. Phase matching considerations in second harmonic generation from tissues: Effects on emission directionality, conversion efficiency and observed morphology. *Optics Communications*, 281(7):1823–1832, May 2008.

[81] V Lutz, M Sattler, S Gallinat, H Wenck, R Poertner, and F Fischer. Impact of collagen crosslinking on the second harmonic generation signal and the fluorescence lifetime of collagen autofluorescence. *Skin research and technology*, 18(2):168–79, May 2012.

[82] MA Houle, CA Couture, S Bancelin, J Van Der Kolk, E Auger, C Brown, K Popov, L Ramunno, and F Légaré. Analysis of forward and backward Second Harmonic Generation images to probe the nanoscale structure of collagen within bone and cartilage. *Journal of Biophotonics*, 8(11-12):993–1001, November 2015.

[83] T Tang, V Ebacher, P Cripton, P Guy, H McKay, and R Wang. Shear deformation and fracture of human cortical bone. *Bone*, 71:25–35, February 2015.

[84] A Aghigh, S Bancelin, M Rivard, M Pinsard, H Ibrahim, and F Légaré. Second harmonic generation microscopy: A powerful tool for bio-imaging. *Biophysical Reviews*, 15(1):43–70, February 2023.

[85] R Ambekar, M Chittenden, I Jasiuk, and KC Toussaint. Quantitative second-harmonic generation microscopy for imaging porcine cortical bone: Comparison to SEM and its potential to investigate age-related changes. *Bone*, 50(3):643–650, March 2012.

[86] M Minsky. Memoir on inventing the confocal scanning microscope. *Scanning*, 10(4):128–138, January 1988.

[87] RL Price and WG Jerome, editors. *Basic Confocal Microscopy*. Springer New York, New York, NY, 2011.

[88] M Kerschnitzki. *Bone Material Characteristics Influenced by Osteocytes*. PhD thesis, Mathematisch-Naturwissenschaftlichen Fakultät I der Humboldt-Universität zu Berlin, 2012.

[89] A Roschger. *Quantitative Analysis of Local Mineral Content and Composition During Bone Growth and Remodeling*. PhD thesis, Mathematisch-Naturwissenschaftlichen Fakultät I der Humboldt-Universität zu Berlin, 2015.

[90] S Blouin, A Roschger, F Varga, B Misof, S Spitzer, P Roschger, and K Klaushofer. Confocal laser scanning microscopy—a powerful tool in bone research. *Wiener Medizinische Wochenschrift*, 168(11-12):314–321, September 2018.

[91] AJ Bain, P Chandna, G Butcher, and J Bryant. Picosecond polarized fluorescence studies of anisotropic fluid media. II. Experimental studies of molecular order and motion in jet aligned rhodamine 6G and resorufin solutions. *The Journal of Chemical Physics*, 112(23):10435–10449, June 2000.

[92] W Wagermaier, A Gourrier, and B Aichmayer. CHAPTER 3. Understanding Hierarchy and Functions of Bone Using Scanning X-ray Scattering Methods. In Peter Fratzl, John W.C. Dunlop, and Richard Weinkamer, editors, *Smart Materials Series*, pages 46–73. Royal Society of Chemistry, Cambridge, 2013.

[93] V Schemenz. *Correlations between osteocyte lacuno-canalicular network and material characteristics in bone adaptation and regeneration*. PhD thesis, Mathematisch-Naturwissenschaftlichen Fakultät der Universität Potsdam, 2022.

[94] S Pabisch, W Wagermaier, T Zander, C Li, and P Fratzl. Imaging the nanostructure of bone and dentin through small- and wide-angle X-ray scattering. In *Methods in Enzymology*, volume 532, pages 391–413. Elsevier, 2013.

[95] O Kratky, G Porod, and L Kahovec. Einige neuerungen in der technik und auswertung von röntgen-kleinwinkelmessungen. *Zeitschrift für Elektrochemie und angewandte physikalische Chemie*, 55(1):53–59, 1951.

[96] G Porod. Die röntgenkleinwinkelstreuung von dichtgepackten kolloiden systemen: I. Teil. *Kolloid-Zeitschrift*, 124(2):83–114, November 1951.

[97] P Fratzl, N Fratzl-Zelman, K Klaushofer, G Vogl, and K Koller. Nucleation and growth of mineral crystals in bone studied by small-angle X-ray scattering. *Calcified Tissue International*, 48(6):407–413, June 1991.

[98] S Rinnerthaler, P Roschger, HF Jakob, A Nader, K Klaushofer, and P Fratzl. Scanning small angle X-ray scattering analysis of human bone sections. *Calcified Tissue International*, 64(5):422–429, May 1999.

[99] I Zizak, P Roschger, O Paris, B.M Misof, A Berzlanovich, S Bernstorff, H Amenitsch, K Klaushofer, and P Fratzl. Characteristics of mineral particles in the human bone/cartilage interface. *Journal of Structural Biology*, 141(3):208–217, March 2003.

[100] P Roschger, HJr Plenk, K Klaushofer, and J Eschberger. A new scanning electron microscopy approach to the quantification of bone mineral distribution: Backscattered electron image grey-levels correlated to calcium ka-line intensities. *Scanning Microscopy Scanning Microscopy*, 9(1):75–88, 1995.

[101] JK Gong, JS Arnold, and SH Cohn. The density of organic and volatile and non-volatile inorganic components of bone. *The Anatomical Record*, 149(3):319–324, July 1964.

[102] T Zander, C Li, I Zenke, I Schmidt, D Werner, and W Wagermaier. Evaluation of X-ray scattering data sets, collected with a 2-D detector.

[103] A Engström and JB Finean. Low-angle X-Ray Diffraction of Bone. *Nature*, 171(4352):564–564, March 1953.

[104] RG Handschin and WB Stern. X-ray diffraction studies on the lattice perfection of human bone apatite (Crista Iliaca). *Bone*, 16(4), April 1995.

[105] SN Danilchenko, OG Kukharenko, C Moseke, I Yu Protsenko, LF Sukhodub, and B Sulkio-Cleff. Determination of the bone mineral crystallite size and lattice strain from diffraction line broadening. *Crystal Research and Technology*, 37(11):1234–1240, November 2002.

[106] P Scherrer. Bestimmung der inneren Struktur und der Größe von Kolloidteilchen mittels Röntgenstrahlen. In *Kolloidchemie Ein Lehrbuch*, pages 387–409. Springer Berlin Heidelberg, Berlin, Heidelberg, 1912.

[107] U Holzwarth and N Gibson. The Scherrer equation versus the 'Debye-Scherrer equation'. *Nature Nanotechnology*, 6(9):534–534, September 2011.

[108] J. I. Langford and A. J. C. Wilson. Scherrer after sixty years: A survey and some new results in the determination of crystallite size. *Journal of Applied Crystallography*, 11(2):102–113, April 1978.

[109] W Bragg. The analysis of crystals by the x-ray spectrometer. *Proceedings of The Royal Society A: Mathematical, Physical and Engineering Sciences*, 89:468–489, 1914.

[110] L.-H. He and M.V. Swain. 3.9 Microindentation. In *Comprehensive Biomaterials II*, pages 144–168. Elsevier, 2017.

[111] WC Oliver and GM Pharr. An improved technique for determining hardness and elastic modulus using load and displacement sensing indentation experiments. *Journal of Materials Research*, 7(6):1564–1583, June 1992.

[112] A B Mann. Nanoindentation. In *Surfaces and Interfaces for Biomaterials*, pages 225–247. Elsevier, 2005.

[113] K Kendall and D Tabor. An utrasonic study of the area of contact between stationary and sliding surfaces. *Proceedings of the Royal Society of London. A. Mathematical and Physical Sciences*, 323(1554):321–340, June 1971.

[114] SE Campbell, VL Ferguson, and DC Hurley. Nanomechanical mapping of the osteochondral interface with contact resonance force microscopy and nanoindentation. *Acta Biomaterialia*, 8(12):4389–4396, December 2012.

[115] E Donnelly, SP Baker, and AL Boskey. Effects of surface roughness and maximum load on the mechanical properties of cancellous bone measured by nanoindentation. *Journal of Biomedical Materials Research Part A*, 2006.

[116] MS Bobji and SK Biswas. Estimation of hardness by nanoindentation of rough surfaces. *Journal of Materials Research*, 13(11):3227–3233, November 1998.

3

The mineralization of osteonal cement line depends on where the osteon is formed

Adapted from: Astrid Cantamessa[1], Stéphane Blouin[2], Maximilian Rummler[3], Andrea Berzlanovich[4], Richard Weinkamer[3], Markus A. Hartmann[2], Davide Ruffoni[1], The mineralization of osteonal cement line depends on where the osteon is formed, under review in *JBMR Plus*.

[1] Mechanics of Biological and Bioinspired Materials Laboratory, Department of Aerospace and Mechanical Engineering, University of Liège, Liège, Belgium;

[2] Ludwig Boltzmann Institute of Osteology at Hanusch Hospital of OEGK and AUVA Trauma Centre Meidling, 1st Medical Department Hanusch Hospital, Vienna, Austria;

[3] Department of Biomaterials, Max Planck Institute of Colloids and Interfaces, Potsdam, Germany;

[4] Center of Forensics Medicine, Vienna, Austria.

Keywords

Cement line, Mineralization, Osteon, Human bone, Quantitative backscattered electron imaging, Mineralization process, Mineral content, Mineral recycling, Tissue age.

Abstract

The cement line (CL) is a thin layer, 1-2 μm in width, separating secondary osteons from interstitial bone and other osteons. Despite the possible role for bone quality, the CL is still one of the least understood microstructural features of bones. This study on CL mineralization aims to investigate how the mineral content of the CL varies with the surrounding environment. Using quantitative backscattered electron imaging to measure the mineral content at high resolution (about 0.6 μm/pixel), we analyzed 35 osteons from femoral bone of two male individuals (40 and 81 years old). The selected osteons had different mineralization, ranging from 21.37 wt % to 26.43 wt % calcium content. We implemented a spatially resolved analysis of the mineral content in layers along the CL, considering both regions inside the osteon (i.e., formed soon after CL deposition) and outside (i.e., already present at the time of CL deposition). We found that the CLs had always higher mineral content than the corresponding osteon ($p < 0.001$). As-

suming the mineral content of the osteon as a proxy of its age, we demonstrate that not only the osteon, but also the CL increases its mineral content with time. However, after a rapid primary phase where the CL incorporates more mineral than the osteon, the rate of increase is about 60% lower in the CL. Importantly, the specific value of the high initial mineral content of the CL depends on the mineral content of the local surrounding, in which the osteon was formed. This is supported by a strong correlation between the mineral content of the CL and outside the osteon ($R = 0.75$, $p < 0.001$), but not inside. The strong correlation suggests that mineral which was freed at the final stage of bone resorption gets "recycled" in the formation of the CL.

Lay summary

Bone is a dynamic tissue that self-renews through remodeling and mineralization. This leads to the formation of secondary osteons, tubular structures surrounded by a thin layer called cement line. This study explores the mineralization of the cement line. By examining osteons of different age in human femoral bone, we found that the mineral content in a newly deposited cement line is higher than in the corresponding osteon and that the mineralization of the cement line depends on the surrounding in which it is formed. This suggests that the cement line is built with mineral "recycled" during remodeling.

3.1 Introduction

Cement lines (CLs) are thin interphases, typically 1-2 μm in width, which are ubiquitous in bone. They are found at: i) the border of secondary osteons in cortical bone [1], ii) around individual bone packets in trabecular bone [2] and iii) between bone and mineralized cartilage at entheses [3, 4] and osteochondral junctions [4]. Despite their small thickness, CLs are assumed to contribute to bone fracture resistance by deflecting or arresting microcracks. In cortical bone, studies have shown that microcracks coming from the interstitial tissue, can deviate when meeting the CL [5, 6, 7, 8]. Such a mechanism allows to dissipate energy, to reduce the force driving crack propagation [9], and also to preserve the overall integrity of the osteon. Indeed, microcracks are more likely observed in interstitial bone than inside osteons [10].

The ability of the CL to interact with damage depends on its basic mechanical properties such as stiffness, strength and toughness [11]. However, these properties are still not well characterized: there are only very limited data on CL stiffness and strength [12] and, to our knowledge, no data on fracture toughness. CL mineral content is one factor of fundamental importance for the mechanical behavior. Yet, the composition of CLs remains controversial: both lower [13] and higher [14] mineral content of CLs compared to surrounding bone are reported. More recent data indicate that CLs tend to have higher mineral content than the corresponding osteons [10, 15, 16], with the difference decreasing with tissue age [16]. At the same time, the dimensions of the osteon do not seem to influence the degree of mineralization of the CL [16].

The mineral content of the osteon is not static but evolves in time according to a specific mineralization

process. Current understanding is that a fast primary mineralization, bringing the mineral content up to about 70% of the final value within a few days, is followed by a much slower secondary mineralization. The latter leads to a gradual maturation of the mineral phase, which takes up to several years [17, 18, 19, 20]. Conversely, knowledge about how much mineral is incorporated during CL formation, and to which extent the mineral content of the CL evolves with time is insufficient.

CLs are found around secondary osteons, which are a result of cortical bone remodeling [21], with CLs providing a proper "cleaned" surface for osteoid deposition [1, 22, 23]. CLs have higher content of osteopontin (a CL marker) than adjacent bone [23]. The examination of cutting cones in osteons with serial sectioning has provided clues that CLs are formed during or immediately after bone resorption by osteoclasts/osteoprogenitor cells [1].

A further element that can impact tissue mineralization is the transport of mineral ions to the mineralization site. There is evidence that locations of bone modeling and remodeling present differences in the mineralization process, resulting in specific mineral characteristics such as crystal composition and dimensions [24]. This is likely due to different avenues to transport ionic precursors. Usually bone modeling requires transport over large distances and, thus, ionic precursors should be stabilized by compositional modifications, whereas in bone remodeling this is not necessary as resorbed mineral may be locally recycled [24]. As the formation of CL and osteonal bone are somewhat dephased, both in space and time, differences in available mineral ions may be present, impacting the mineralization process.

The aim of this work is to characterize how the mineral content of CLs varies with the surrounding environment and changes over time. By examining osteons of different mineral content, potentially reflecting differences in tissue age, new insights into CL mineral content and mineralization can be obtained.

3.2 Materials and methods

3.2.1 Sample preparation

Human femurs from two male donors (40 and 81 years old) without known metabolic bone disease were obtained from the Department of Forensic Medicine of the Medical University of Vienna, in accordance with the ethical commission of the institution (EK no. 1757/2013). After extraction, the bones were kept frozen at -20°C until further preparation. Cross sections (perpendicular to the longitudinal axis of the femurs) of about 1.5 cm in thickness were cut from the femoral shaft far from the metaphysis (Figs. 3.1A and B) using a water-cooled diamond saw (Buehler Isomet 1000, Germany). The sections were then prepared following a well-established procedure [25, 26], which involved dehydration in graded ethanol series, followed by immersion in ethanol/acetone baths, and embedding in poly-methyl methacrylate (PMMA). The transverse surfaces were ground with sandpapers having decreasing grit size (P1200, P2400) and polished using a diamond suspension down to 1 μm particle size on a silk cloth under glycol irrigation (Logitech PM5, UK), to minimize the formation of microcracks [27].

3.2.2 Quantitative backscattered electron imaging

The local mineral content of cortical bone was quantified with qBEI, a well-established technique based on scanning electron microscopy (SEM), providing quantitative two-dimensional spatial maps of calcium content by measuring the intensity of the backscattered signal [26, 28]. To obtain a conducting surface, a thin carbon layer was deposited on the polished samples by vacuum evaporation (Agar SEM carbon coater, Agar, Stansted, UK). The SEM, equipped with a zirconium-coated field emission cathode (Zeiss SEM SUPRA 40, Germany), was operated at 20 kV with a working distance of 10 mm, and a probe current of 280 – 320 pA. First, overview scans (Fig. 3.1C) with a larger field of view and a lower resolution (1.76 μm/pixel) were performed to select the osteons of interest for subsequent higher resolution analysis. The selected osteons had to feature a central Haversian canal and a continuous border, i.e., they should not be interrupted by more recent osteons. In the analysis, we included osteons with different sizes and mineral contents, which is assumed as a proxy of tissue age. The chosen osteons (n = 35, 15 coming from the younger donor and 20 from the older one) and the surrounding bone were measured at higher magnification (pixel resolution 0.57 μm with a field of view of 1024 $\times$ 768 pixels). This resolution is high enough to resolve the CLs, which have a thickness in transverse sections of about 1-2 μm and low enough to allow for a quantitative measurement of the calcium content without additional contrast due to, e.g., orientation of bone lamellae. A calibration of the SEM backscattered signal with carbon and aluminum standards was performed as previously reported [26, 29], to establish a quantitative relation between the measured grey level and the local mineral content, expressed as calcium weight percent (Ca wt %).

3.2.3 Second harmonic generation imaging

Second harmonic generation (SHG) imaging was performed at the same locations analyzed with qBEI to ensure that the selected osteons are the most recently deposited in their neighborhood. This can be challenging when two osteons with similar mineral content slightly overlap (Fig. 3.1D). By inspecting the lamellar organization accessible with SHG (Figs. 3.1F, G and S1), we look for osteons with uninterrupted lamellae, which is a clear indication of being the most recent ones. Samples were imaged using confocal laser scanning microscopy (Leica TCS SP8 DLS, Germany) with a 40$\times$ oil immersion objective (HC PL APO 40$\times$/1.30 OIL). A pulsed infrared laser (Spectra-Physics, Milpitas) at a wavelength of 910 nm was used, and the backward direction signal was detected at 450–460 nm wavelength. Images were acquired with a nominal pixel size of 379 nm and a field of view of 1024 $\times$ 1024 pixels at a scan rate of 400 Hz. Several neighboring regions were measured with a slight overlapping, ensuring proper alignment when stitching them together using the software of the Leica microscope. For an appropriate detection of lamellar arrangement, the SHG resolution was chosen to be smaller than typical lamellar thickness ($\sim$4 - 6 μm).

3.2.4 Mineral content of the cement line and adjacent regions: layers analysis

Before evaluating the mineral content, a 2-pixel erosion was applied to minimize boundary effects [17] using the software CTAn (v1.19.4.0, Skyscan, US). Background pixels, including osteocytes lacunae, Haversian canals, and microcracks, were removed by discarding all pixels with a calcium content below 5.2 wt %. This ensured that only mineralized bone regions and no voids were included in the analysis. The mineral content of the CL and of neighboring bone was evaluated according to the following layer analysis, implemented in CTAn. First, a mask of each osteon (not including the CL) was generated by manually contouring the osteon border as delimited by the CL (Figs. S2A and B). This choice is motivated by the fact that the boundary between the CL and the osteon was usually easier to detect than between the CL and the interstitial bone. The manual contouring process was performed by a single operator to maintain consistency, and the results were visually inspected by a second operator. The extracted mask was dilated with a round kernel of 2 pixels to include the CL, and the original mask of the osteon was subtracted from the dilated mask to obtain a 2-pixel (or 1.14 μm) thick circular layer representing the CL. Next, the bone around the CL was subdivided into several concentric circular layers having the same nominal thickness of the CL and located both inside and outside the osteon, in regions adjacent to the CL as well as further away (Figs.3.1D and E). The layers were obtained by multiple cycles of erosion and dilation applied to the mask of the osteon (Figs. S2C and D). Specifically, we considered layers close to the CL and placed at 1 and 4 pixels (or 0.57 μm and 2.28 μm) away from the CL border: 2 layers inside the osteon (I1, I2) and 2 layers outside (O1, O2). Two additional layers were defined 20 pixels (or 11.4 μm) away from the CL (I3 and O3, respectively). Inner layers include only osteonal bone, whereas outer layers may intersect with other (older) osteons and interstitial bone. Furthermore, all concentric circular layers were radially sliced into 16 sectors (using MATLAB 2022a), which served to investigate the spatial variation of mineral content around the osteons (Fig. S2E). A custom MATLAB routine was implemented to compute the mean calcium content (Ca_{Mean}), its standard deviation, as well as the frequency distribution of the calcium content, within each layer and in the whole osteon. Considering the limited number of pixels in the layers, to improve readability of the plots, all frequency distributions were slightly smoothed with a running average filter (window size 10).

3.2.5 Statistical analysis

We compared differences in mineralization among the layers by performing a Friedman test, chosen due to the non-normal distribution of the paired data. When significant differences were detected, pairwise comparisons between layers were conducted using post-hoc tests with Bonferroni correction to control for multiple comparisons and minimize false positive. We examined the strength of the relationships between the mean calcium content of osteon, CL and different layers using Spearman's rank correlation, selected for its suitability with non-normal distribution of the data. Significance levels were set at $p < 0.05$, and all p-values were two-sided. All statistical analyses were performed in MATLAB 2022a.

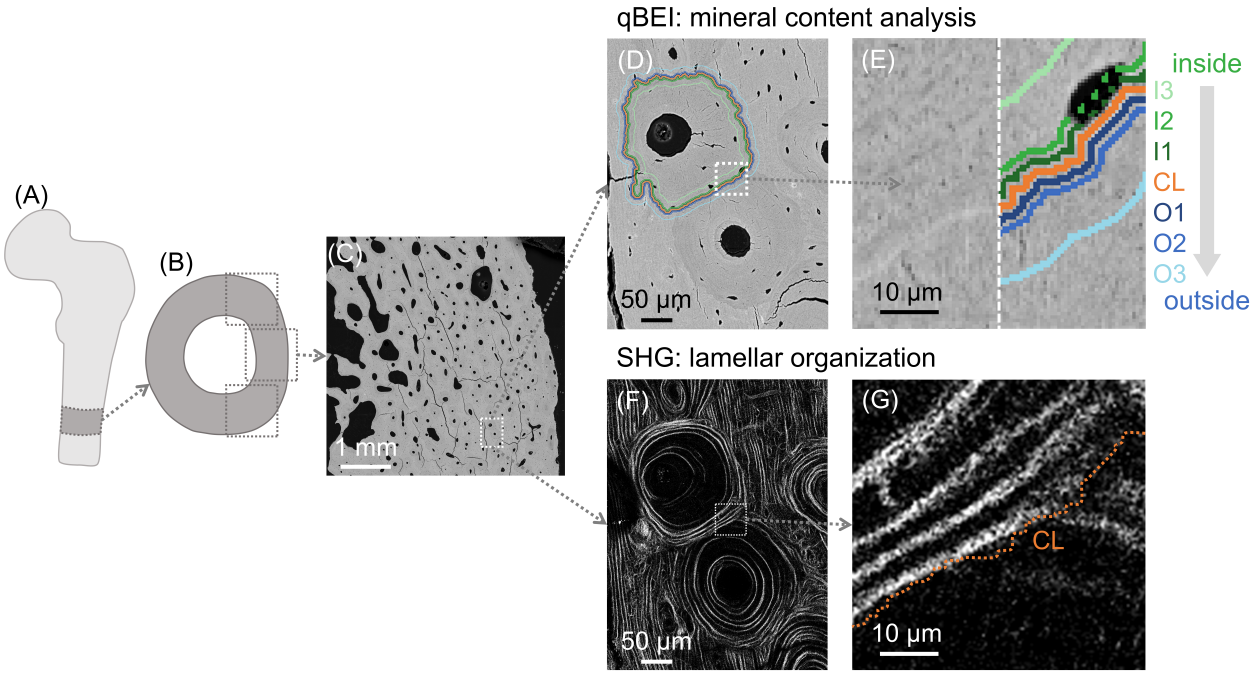


Figure 3.1: Analysis of human osteonal bone. (A) Schematic of a human femur and (B) transverse cross-section where (C) qBEI scans were performed to select the osteons to be analyzed. (D) High resolution qBEI map of an uninterrupted osteon neighboring other osteons (top and bottom) and interstitial bone (left and right). (E) Magnified view of a CL and the different layers around the CL, located both inside (I_1, I_2, I_3) and outside (O_1, O_2, O_3) the selected osteon. (F) SHG image of the same region highlighting the uninterrupted lamellar organization of the selected osteon. (G) Close-up of the SHG image with the orange dashed line representing the location of the CL, detected by superimposing SHG and qBEI maps.

3.3 Results

From a qualitative observation of the qBEI maps, the CL appears as a thin line around the osteon (Fig. 3.1E). In the SHG images there were no evident features allowing a clear discrimination between CL and adjacent lamellar bone (Fig. 3.1G). However, superimposing qBEI and SHG maps indicates that the CL tends to fall in regions with no (or very weak) SHG signal.

We explore possible links between the mineralization of the CL and immediately adjacent bone, considering regions both outside and inside the osteon, i.e. formed before and after CL deposition, respectively. We first report detailed findings on two osteons having low and high mean mineral content that are representative for younger and older tissue (assuming mineral content as an indirect measure of tissue age) and extracted from the adult (40 years old) and aged (81 years old) individual, respectively. We then present results of all 35 osteons, with mean calcium content ranging from 21.37 ± 2.26 wt % to 26.43 ± 2.2 wt %, and therefore covering a large spectrum of tissue age. Less mineralized younger osteons were more likely found in the adult individual, whereas older more mineralized osteons in the aged individual.

As a first example, we investigated an osteon with relatively low mean mineral content (Ca_{Mean} = 21.72 ± 2.09 wt %) coming from the adult individual and surrounded by older osteons and interstitial bone (Fig. 3.2A). SHG imaging reveals bone lamellae at the osteon periphery, confirming that the selected osteon is

not interrupted by other osteons (Fig. 3.2B). The local and layer-based analysis of qBEI maps indicates a clear increase in mineral content of about 15% when going from the inner layers of the osteon to the CL, which has Ca_{Mean} of 25.54 ± 1.52 wt % (Fig. 3.2C). The difference in mineral content between the CL and the outer layers is much smaller (around 2%) but still statistically significant ($p < 0.001$). The same trend is confirmed when inspecting the frequency distributions of the calcium content of the layers, which essentially split into two groups (Fig. 3.2D): inner layers have similar distributions, overlapping with the distribution of the whole osteon, whereas the distributions of the outer layers are shifted towards higher mineral content. The frequency distribution of the CL displays an additional (albeit small) right-shift, making it distinguishable from all other curves. Owing to the circular shape of the osteon, the spatial correlation among the layers is further explored with a polar plot (Fig. 3.2E), based on the subdivision into 16 sectors (see section 3.2). In the polar plot, the mean calcium content in each sector is plotted as distance from the center. If two layers have similar calcium content in the same sector, the corresponding polar plots overlap. A central observation is that in each sector around the osteon, the mean calcium content of the CL follows very closely the mineral content of immediately adjacent bone located just outside the osteon and therefore deposited potentially long before the CL. The polar plot also gives an idea of how the spatial correlation varies across the 16 sectors: for example, when the osteon is close to interstitial bone with higher mineral content (top region of the plot), the mineral content of both the CL and the outer layer O1 slightly increases. An additional quantification is obtained by computing the Spearman correlation coefficient between the calcium content of the CL and of the adjacent outer layer O1 in the 16 sectors around osteon (Fig. 3.2F): with $R = 0.9$ ($p < 0.001$), such correlation can be considered as very strong [30]. Conversely, no spatial relationship between the mean mineral content of CL and inner layers is evident: the correlation between the calcium content of the CL and of the inner layer I1 in the 16 sectors is not statistically significant (Fig S3A, $R = -0.4$, $p = 0.108$).

The second example is an osteon with higher mineral content (Ca_{Mean} = 25.95 ± 2.45 wt %) representative for older tissue and extracted from the aged individual. Again, this osteon is surrounded by a heterogeneous environment featuring older osteons as well as interstitial bone (Fig. 3.3A and B). The SHG analysis underlines a clear pattern of alternating and uninterrupted bone lamellae within the selected osteon (Fig. 3.3B). In this "aged" scenario, the CL has still higher mineral content than the osteon (about 9%) as well as than the external surrounding bone layers (about 5%, Fig. 3.3C). The frequency distributions of inner and outer layers are closer to each other's with respect to the previous case of the younger osteon, whereas the distribution of the CL still displays a noticeable shift to higher mineral content (Fig. 3.3D). The polar plot suggests a statistically significant spatial relationship between the mineral content of CL and adjacent outer layers (Fig. 3.3E), which is characterized by a moderate correlation coefficient ($R = 0.58$, $p < 0.05$). Also in this example, the correlation between the CL and the inner layer I1 is not significant (Fig S3B, $R = 0.41$, $p = 0.101$).

Extending the layer analysis to all osteons (Fig. 3.4), confirms that the CLs always exhibit the highest mean mineral content (27.35 ± 1.58 wt % Ca), not only in comparison with the layers inside the osteons

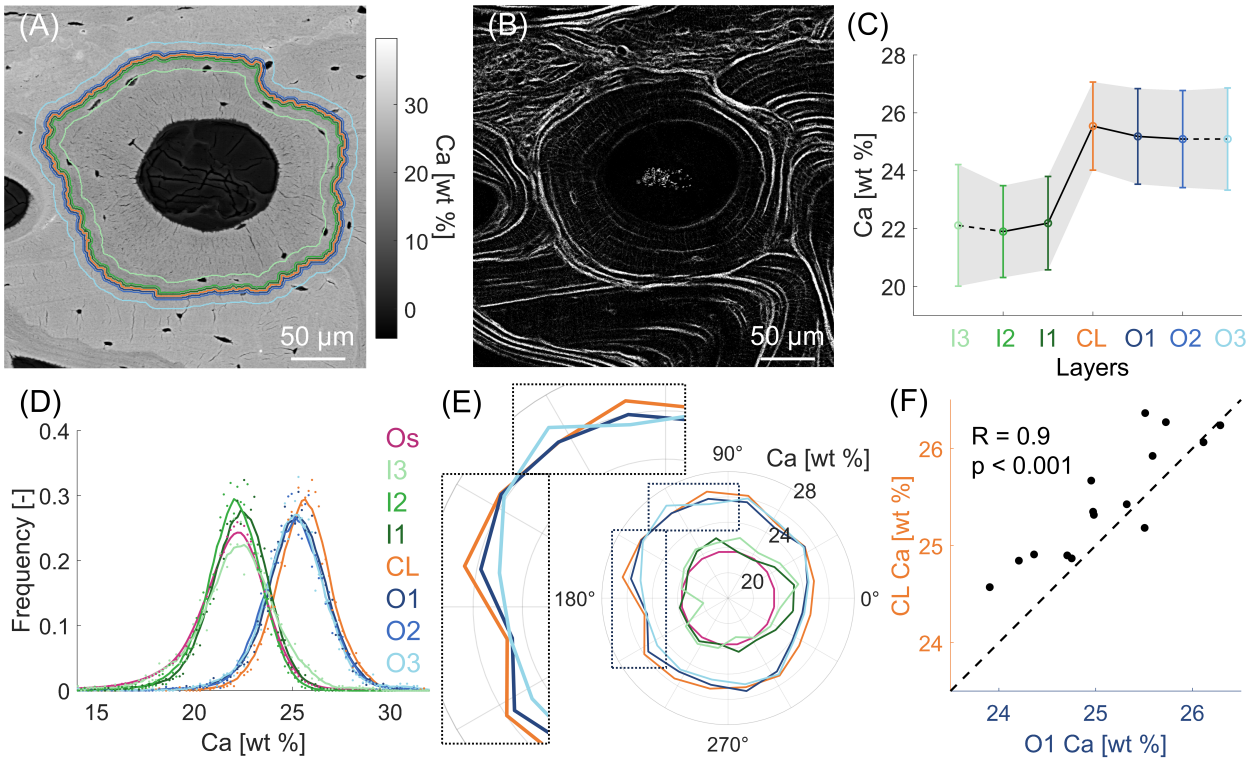


Figure 3.2: Mineral content analysis of a lowly mineralized osteon from the adult (40 years) individual. (A) qBEI map with CL and layers highlighted by the colored lines. (B) SHG image showing the lamellar organization. (C) Mean calcium content of the inner layers (I_3, I_2, I_1), CL and outer layers (O_1, O_2, O_3). Data shown as mean ± standard deviation (the shaded area delimits a one-standard deviation interval around the mean). Data points are connected by lines to visualize the trend: full lines connect points equally spaced, whereas dashed lines indicate that I_3 and O_3 are further away. (D) Frequency distributions of the calcium content of the entire osteon (Os), CL and layers. Original data represented as scattered points and smoothed data (with moving average) as full lines. (E) Polar plot of the calcium content in selected regions (CL, O_1, O_3, I_1, I_3 and Os), averaged over 16 sectors around the osteon. The mean Ca content in each sector is plotted as distance from the center. (F) Correlation between the calcium content of CL and O_1 considering all 16 sectors. The dotted line with a unit slope and passing through the origin is shown to improve the readability of the plot.

but also with the layers outside, apart from O_1. The difference in mineral content between the CL and the outer layers is less pronounced than between the CL and the inner layers. The outer layers show a smaller spreading in the mean mineral content when compared to the inner layers.

The mineralization of the CL is explored in Fig. 3.5. Firstly, we observed that the mineral content of the CL is always higher than the osteon mineral content, and that a strong correlation is present between them ($R = 0.75$, $p < 0.001$, Fig. 3.5A), suggesting that the CL mineral content progresses with tissue age. At the same time, the mineral content of the bone outside the osteon (represented by the outer layer O_1) had only a moderate correlation ($R = 0.4$, $p = 0.018$) with the mineral content of the osteon (Fig. 3.5B). In contrast, the relationship between the mineral content of CL and outer layer O_1 (Fig. 3.5C) displays a strong correlation ($R = 0.75$) with statistical significance ($p < 0.001$). As in Fig. 3.5A, all experimental points are above the line with a slope of 1 (i.e., 45°, dashed line in Figs. 3.5A-C). This confirms that the CL is the highest mineralized structure in all 35 investigated osteons compared to either the inside or the outside of the osteon. Virtually identical results are found when considering instead of the outer layer

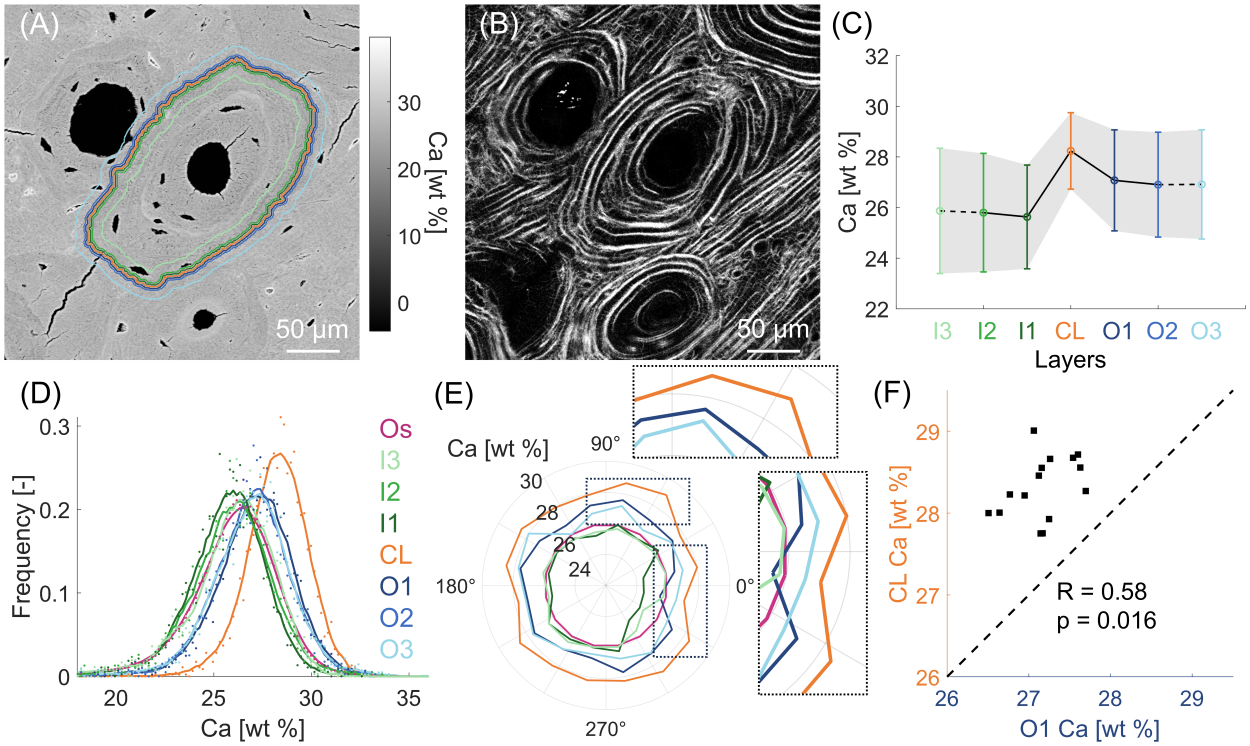


Figure 3.3: Mineral content analysis of a highly mineralized osteon from the aged (81 years) individual. (A) qBEI map with CL and layers highlighted by the colored lines. (B) SHG image showing the lamellar organization. (C) Mean calcium content of the inner layers (I_3, I_2, I_1), CL and outer layers (O_1, O_2, O_3). Data shown as mean ± standard deviation (the shaded area delimits a one-standard deviation interval around the mean). Data points are connected by lines to visualize the trend: full lines connect points equally spaced, whereas dashed lines indicate that I_3 and O_3 are further away. (D) Frequency distributions of the calcium content of the entire osteon (Os), CL and layers. Original data represented as scattered points and smoothed data (with moving average) as full lines. (E) Polar plot of the calcium content in selected regions (CL, O_1, O_3, I_1, I_3 and Os), averaged over 16 sectors around the osteon. The mean Ca content in each sector is plotted as distance from the center. (F) Correlation between the calcium content of CL and O_1 considering all 16 discrete sectors. The dotted line with a slope of one and passing through the origin is shown to improve the readability of the plot.

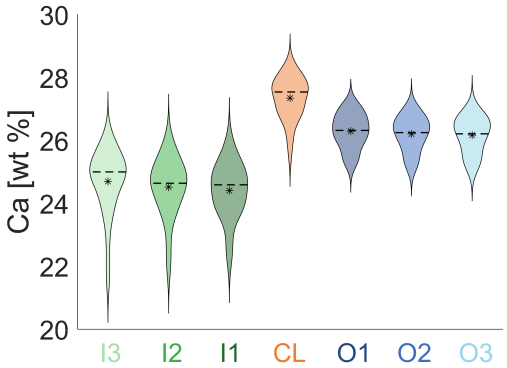


Figure 3.4: Violin plots (mirrored histograms) of the calcium content for each segmented region (CL, inner, and outer layers) considering all analyzed osteons (n=35). The mineral content of the CL is significantly higher ($p < 0.001$) than all other layers but O_1. The median and mean values are indicated by dashed lines and asterisks, respectively.

O_1, the outer layer O_2, which is further away from the CL (Figs. S4A and B). The strong correlation between the mineral content of the CL and the outer layer O_1 motivates to investigate how the difference

between these two quantities (CL – O1) behaves when plotted versus the osteon mineral content (Fig. 3.5D). The obtained correlation is strong ($R = 0.75$) and statistically significant ($p < 0.001$). The positive slope of the correlation (full line in Fig. 3.5D) shows that the mineral content of the CL deviates more from the mineral content of the surrounding, the older (i.e., the higher mineralized) the osteon is. An opposite trend is observed when plotting (CL – I1) versus the osteon mineral content (Fig. S5).

Motivated by the strong correlation between the mineral content of the CL and of the outer layer O1 (Fig. 3.5C), we performed a spatially resolved analysis of the relationships between the mineralization of the CL and the outer/inner layers, by considering the calcium content within each circular sector around the osteon, for a total of 3920 different regions inspected (Fig. 3.6). Pooling all sector-wise data together (Fig. S6) confirmed the trend observed in Fig. 3.5, with CL and O1 showing the highest correlation and data points spread close to a line of unit slope. We applied the sector analysis (presented in Fig. 3.2F and 3.3F) to all osteons (Fig. 3.6A): for 21 out of 35 osteons, we detected a statistically significant correlation ($p < 0.05$) between the mineral content of the CL and outer layer O1, ranging from moderate ($0.4 < R < 0.7$) to strong ($0.7 < R < 0.9$). The osteons which did not show a significant correlation are likely to have higher mineral content ($Ca_{Mean} > 24.6$ wt %). The differences in mineral content between the CL and the closest outer layer (CL - O1) as well as between the CL and the closest inner layer (CL - I1) were then calculated in each discrete sector and averaged for each osteon (Fig. 3.6B). The results further underline that the degree of mineralization of the CL is extremely close to the mineral content of the outer layer O1, with the difference CL - O1 being always less than 2 wt % and showing a small increase for more mineralized osteons. In comparison, the differences between CL and I1 are higher (up to 3.5 - 4 wt %) and show a slight decreasing trend with osteon mineral content. A similar behavior is observed when considering all individual sectors (Fig. 3.6C). Here, we report results as 2D maps with differences (CL - O1) and (CL - I1) calculated in each sector but not averaged in the osteons. In Fig. 3.6C, the 16 individual sectors are on the vertical axis and the 35 osteons, sorted from lower to higher mineral content, are on the horizontal axis. Results indicate that even in discrete regions around the osteon, the mineral content of the CL is very similar to the degree of mineralization of the outer layer O1; this similarity being particularly strong for osteons with lower mineral content, i.e. assumed to be younger.

3.4 Discussion

We investigated the mineral content of CL and neighboring tissue in human cortical bone of two individuals using qBEI at submicrometer resolution, combined with a spatially resolved layer analysis. The main results of our analysis are summarized in Figures 3.5 and 3.6. An important assumption for the interpretation of the plots in these figures is that the mineral content of the osteon serves as a proxy of tissue age. This allows us to deduce the following important aspects of CL mineralization.

Firstly, our results are consistent for the osteons of both individuals despite their very different ages (40 and 81 years). Consequently, we conclude that the tissue age (i.e., the mineral content of the osteon) is

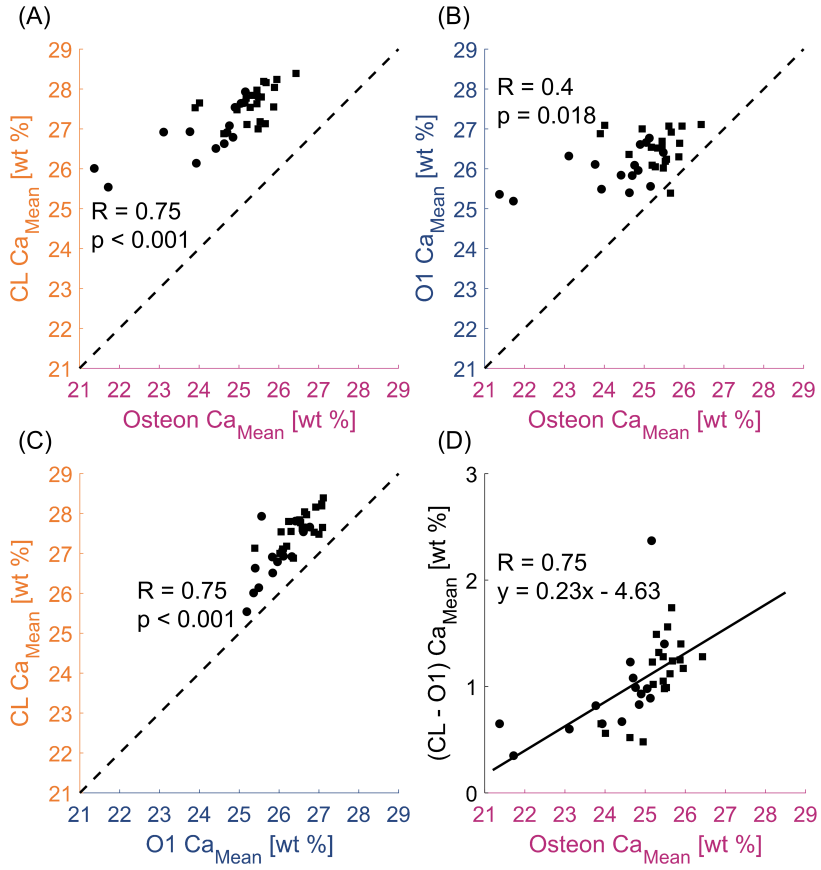


Figure 3.5: Relationship between CL, osteon and the outer bone. (A) Correlation between average calcium content (CaMean) of the CL and the corresponding osteon, (B) outer layer O1 and osteon, (C) CL and O1, and (D) difference between CL and O1 (CL-O1) and osteon. The dotted line (with a unit slope and passing through the origin) is inserted to improve the readability of the plot. The full line in (D) represents the result of a linear regression. Circles represent osteons from the adult individual (40 years) and square from the aged individual (81 years).

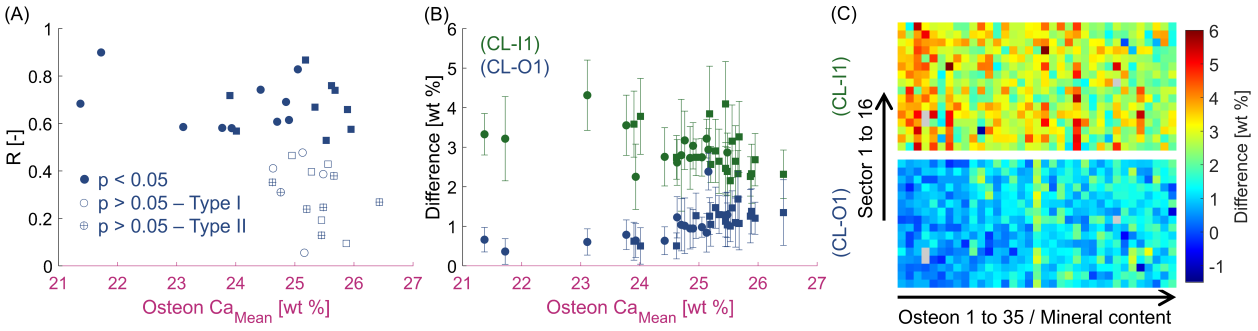


Figure 3.6: Spatial analysis of the mineral content. (A) Spearman correlation coefficients between the mineral content of the CL and the outer layer O1. All osteons that show a statistically significant correlation are of type I, whereas among the osteons where no correlation is detected, there are several osteons of type II (i.e., osteon-in-osteon). (B) Differences in mineral content between the CL and the neighboring layers computed as average difference (CL-O1) and (CL-I1) in the circular sectors and plotted versus the mean degree of mineralization of the osteon. Data points represent the mean value and error bars the standard deviation for each osteon. In (A) and (B), circles represent osteons from the adult individual (40 years) and squares from the aged individual (81 years). (C) Local differences (CL-O1) and (CL-I1) calculated in each sector (vertical axis) and reported for each osteon sorted according to increasing mineral content (horizontal axis). A few grey pixels indicate sectors where the mineral content could not be calculated, for example due to pores or cracks.

the crucial time parameter and it is not confounded by the age of the individual.

Secondly, the mineral content of the CL is always higher than the one of the corresponding osteon and there is a strong correlation between the mineral content of the CL and of the osteon (Fig. 3.5A) This demonstrates that the mineral content of the CL also evolves in time following a characteristic time course, with differences with respect to the mineralization of the osteon. To describe the mineralization process, a separation into a fast primary and a much slower secondary phase is useful. Osteon and CL have a similar tissue age. Nevertheless, the higher mineral content of the CL suggests that in primary mineralization, the CL can incorporate more mineral than the osteon. A previous study on postmenopausal women has also reported that the mineral content of the CL is higher than the corresponding osteon, that this difference decreases with osteon mineral content and that a high correlation exists between osteon and CL mineral content [16]. However, our work demonstrates that much more can be learned when the focus is not restricted to the osteon itself. Our approach to explore the outer environment around the CL allowed us to obtain several original insights into CL mineralization.

Our third main finding is that the mineral content of the CL after primary mineralization is closely related to the mineral content of the surrounding in which the CL and the new osteon are formed. This is true not only when considering the average mineralization (Fig. 3.5C) but extends to the very local environment of the CL, as shown when the CL is subdivided into 16 segments (Fig. 3.6). The local influence of the environment could be explained considering the events leading to the CL formation. The common picture is that the CL is formed on the eroded surface immediately after, or perhaps even during, bone resorption. In this process, osteoclasts generate a local acidic environment allowing to mobilize the inorganic phase of bone [31]. Mineral ions/clusters are then transported through the osteoclasts and released nearby in the extracellular space [32]. At the same time, osteoclasts (and osteoprogenitors cells) produce osteopontin, a protein that could enhance the accumulation of minerals in the newly forming CL [33, 34]. The higher the mineral content of the region undergoing resorption, the more mineral ions/clusters may be released and locally "captured" to build the CL. Such local "recycling" of minerals may affect the primary mineralization of the CL, which might be faster in the presence of more mineral ions and could explain the strong correlation between the mineral content of the CL and of layer O1 (Fig. 3.5C). This correlation is higher than the correlation between osteon and O1 (Fig. 3.5B), meaning that secondary mineralization alone cannot be the only cause for the observed trend. The formation of the bone inside the osteon is somewhat "dephased", both in space and time, with respect to the deposition of the CL. The distance separating the initial resorption and formation fronts can be even around 1 mm [1] and assuming a bone resorption rate of about 20-40 μm/day [35], this distance would correspond to 20-50 days. Thus, the concentration of mineral ions from resorbed bone available during osteonal bone deposition may be different than during the formation of the CL. This could be one reason why there is only a weak correlation (in several cases not statistically significant) between CLs and bone layers inside the osteon (Fig. S7).

Investigating the difference between the mineral content of the CL and of nearby outer bone provides

specific information on the secondary mineralization of the CL, which is our fourth main message. Figure 3.5D clearly shows that the difference between the mineral content of the CL and of its outside surrounding increases with tissue age. Since the surrounding of the selected osteons is older bone tissue, which is already in advanced secondary mineralization, it can be assumed that its mineral content hardly changes any more. Consequently, the increasing trend observed in Figure 3.5D corresponds to the rather slow secondary mineralization of the CL. We may even attempt to estimate the rate of CL secondary mineralization by looking at Figure 3.5D. Based on available data on turnover rate in osteonal bone [36, 37, 38], we estimate an age difference of about 15 years between the youngest and the oldest osteon. This means that the mineral content of the CL increases due to secondary mineralization of about 2 wt % over 15 years. In contrast, within the same time span, the increase in osteon mineral content is about 5 wt % (Fig. 3.5A). A secondary mineralization, which is slower in the CL compared to the osteon, is also consistent with the finding that the higher the mean mineral content of the osteon, the less is the difference in mineralization between the osteon and the CL (Fig. S8). It is conceivable that variations in the mineral content have a direct impact on CL stiffness. In newly formed osteons, the more mineralized CLs should also be stiffer, hence providing a mechanical contrast between osteon and CL that may hamper damage propagation. As osteons age, the mineral content of osteonal bone increases faster than that of the CL, leading to a diminished contrast between the two regions. This may weaken the mechanical functionality of the CL, potentially making older osteons more vulnerable to microcracks. At the same time, a CL which has a similar mineral content than adjacent outer bone may improve the attachment between a compliant osteon and a more rigid interstitial bone.

Fifth, we could identify a reason why in some cases the correlation between the mineral content of the CL and the outer surrounding is weak. Many of the osteons with a weak correlation are classified as type II osteons [39, 40, 41] also known as "osteon-in-osteon" [42] (Fig. 3.6A). This term refers to a specific type of relatively large osteon containing a smaller osteon in its center, both being surrounded by concentric CLs [39, 43]. In type II osteons, the degree of mineralization of the external environment around the osteon tends to be more homogenous in comparison to osteons surrounded by both interstitial bone and older osteons (Fig. S9). In our dataset "osteon-in-osteon" are more likely seen in the bone sample of the aged donor.

In summary, both the osteon and the CL undergo a mineralization process that can be described by a very fast primary mineralization followed by a much slower secondary mineralization. For bone this is well understood and can be even quantitatively described [18]. Here, we provide information on the mineralization process of the CL. After primary mineralization, the mineral content of the CL is substantially higher than the mineral content in osteonal bone. Most importantly, the mineral content of the CL after primary mineralization is clearly not universal but depends on the location where the remodeling event occurs, with the CL being more mineralized when the osteon is surrounded by bone of higher mineral content. The CL shows also a secondary mineralization which proceeds at much slower rates than in osteonal bone. One reason for the slower pace may be the high mineral content already attained at

the end of primary mineralization. The interplay between primary and secondary mineralization of the CL can be explored with the help of a previously developed mathematical model for the mineralization process of bone [18] (Supplementary note 3.1 and Fig. S10): if the CL has an augmented primary mineralization (which is also location-specific), the secondary mineralization needs to be reduced to avoid attaining unrealistically high values of the mineral content (Fig. S10). For an intuitive representation of CL mineralization, one could imagine that the "driving force" to mineralize is somehow proportional to the difference between the current mineral content and the maximum mineral content, defined as the maximum amount of calcium that can be stored in bone. As the actual mineral content increases (due to mineralization), there is a natural decrease in the "driving force", leading to an asymptotic approach of the mineral content to its maximum value.

The found higher mineral content of all CLs compared to the mineral content of the neighboring osteonal bone agrees with previous works [10, 14, 16]. One possible explanation for the observed higher mineral content of the CL has been obtained by analyzing osteonal bone with focused ion beam scanning electron microscopy (FIB-SEM). A network of nanochannel, much smaller than the canaliculi connecting osteocytes lacuna has been found in osteonal bone, with a volume fraction of about 10%. Interestingly, the CLs contain almost no nanochannels. It was shown that the mineral content measured with qBEI is dependent on the volume fraction of nanochannels, with regions having fewer nanochannels appearing more mineralized. As CL and lamellar bone had a large difference in nanochannel volume, a possible reason for the higher mineralization of the CL may be due to a reduced nanoporosity inside the probed volume, rather than to a higher degree of mineralization of the organic matrix [25]. As the CL reaches a very high mineral content already at the end of the primary mineralization, the slower secondary mineralization may be due to the closing of the nanochannels.

The following limitations of this work should be mentioned. First, we acquired qBEI maps with a resolution of 0.57 μm/pixel and the typical width of the CL in 2D sections is about 1-3 μm. Consequently, there may be a fraction of pixels only partially filled by the CL, leading to partial volume artifacts impacting the detected mineral content. We tried to minimize this issue by considering a 2-pixel layer centered on the CL. While this approach likely underestimates the true thickness of the CL around each osteon in most cases, it provides a conservative estimation of its mineral content. In our work as well as in the literature [16, 24, 44, 45], the osteon mineral content is used as an indicator of tissue age. Although we cannot exclude that mineralization progresses at different speeds in different osteons, the mineral content remains a valuable quantity for studying mineralization in the absence of direct tissue age markers [46]. Another point concerns the limited sample size of only two male individuals and 35 osteons, mainly because of the time-consuming approach of our analysis. Yet, we could identify and analyze in depth many osteons, specifically targeting different stages of mineralization. We have selected males for this first investigation to rule out the possible impact on bone mineral content following menopause in women [47]. Future studies using (semi-)automated segmentation algorithms for the CL should incorporate larger and more diverse samples, coming from individuals of different gender and age, as well as considering different

anatomical locations. Finally, although improbable, it cannot be completely ruled out that freezing and treatment of samples affects the measured mineral content. Nevertheless, all samples were prepared in the identical way, allowing for comparisons between osteons and ensuring validity of found correlations.

3.5 Conclusion

In conclusion, previous work has shown a link between osteon and CL mineral content in cortical bone from elderly postmenopausal women [16], and here we report similar findings in osteonal bone from adult and old male individuals. Most important, by taking into consideration the bone outside the osteon, we demonstrate a close spatial interplay between the mineralization of the CL and the mineral content of the surrounding older bone, suggesting that CL mineralization is different in different osteons. Bone diseases or treatments affecting bone mineralization may have a direct impact on the mineral content, and therefore on the mechanical behavior of the CLs.

Conflicts of Interest

The authors declare no competing interests.

Acknowledgements

AC is supported by the French Community of Belgium as part of a FRIA (Fund for Research Training in Industry and Agriculture) grant (n°1E03621F). We warmly thank Phaedra Messmer, Petra Keplinger, and Sonja Lueger from LBIO for the sample preparation. MH and SB gratefully acknowledge financial support from the Austrian Social Health Insurance Fund (OEGK) and the Austrian Workers' Compensation Board (AUVA). MR and RW thank the Max Planck Queensland Centre for the Materials Science of Extracellular Matrices for support.

Supplementary information

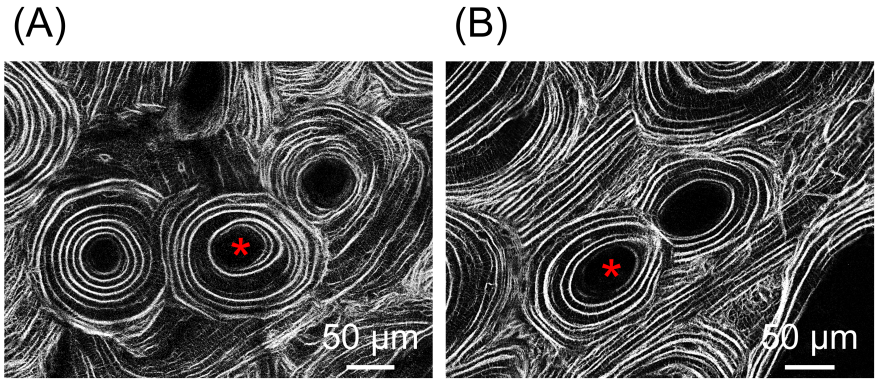


Figure S1: SHG images of uninterrupted (red asterisks) and interrupted osteons.

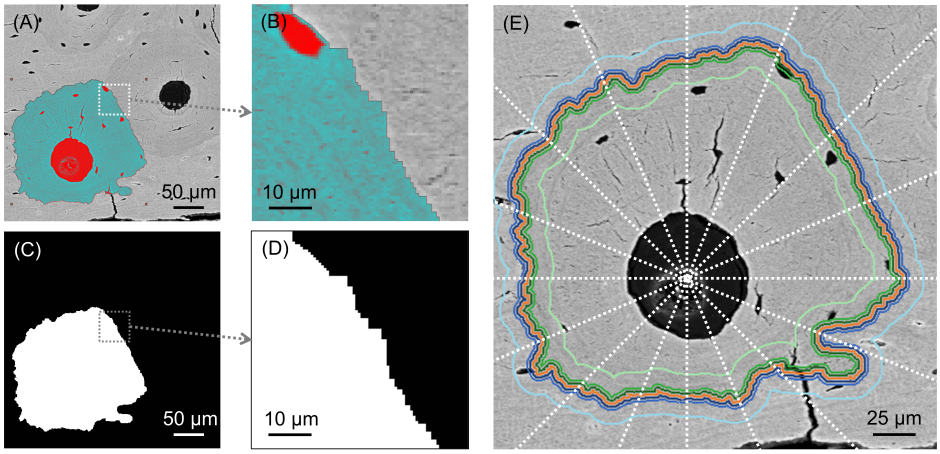


Figure S2: Layer analysis of human osteonal bone. (A) Mask of the osteon obtained by manual segmentation of the quantitative backscattered electron imaging (qBEI) maps and (B) magnified view of the osteon border delimited by the CL, appearing brighter in qBEI. (C) Binarized mask of the osteon used to obtain each layer and (D) magnified view of the osteon border. (E) Subdivision of the circular-shaped layers into 16 sectors to investigate the spatial variation of mineral content around the osteons.

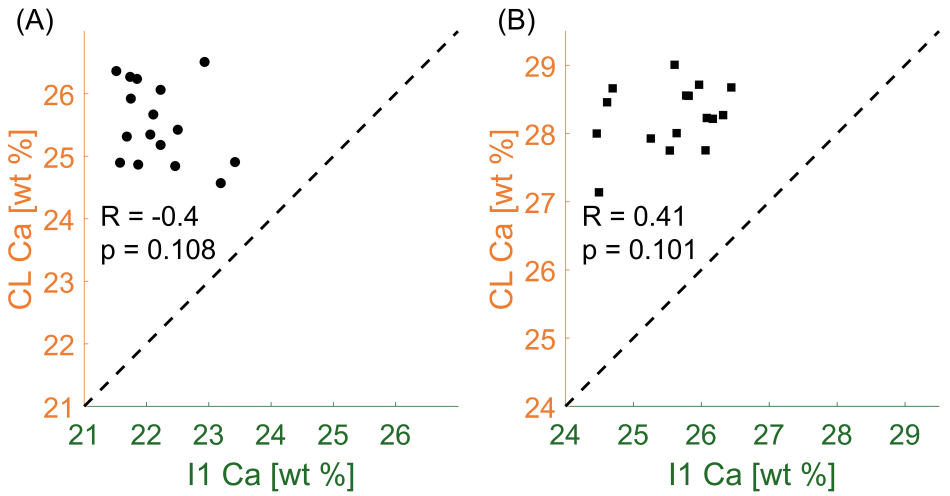


Figure S3: Correlation between the calcium content of the CL and of the adjacent inner layer (I1) measured in 16 discrete sectors around the osteon. Results are shown for (A) an osteon with a low mineral content (CaMean = 21.72 ± 2.09 wt %) and (B) an osteon with a high mineral content (CaMean = 25.95 ± 2.45 wt %). The dotted line with a unit slope and passing through the origin is shown to improve the readability of the plot. Circles represent osteons from the adult individual (40 years) and squares from the aged individual (81 years).

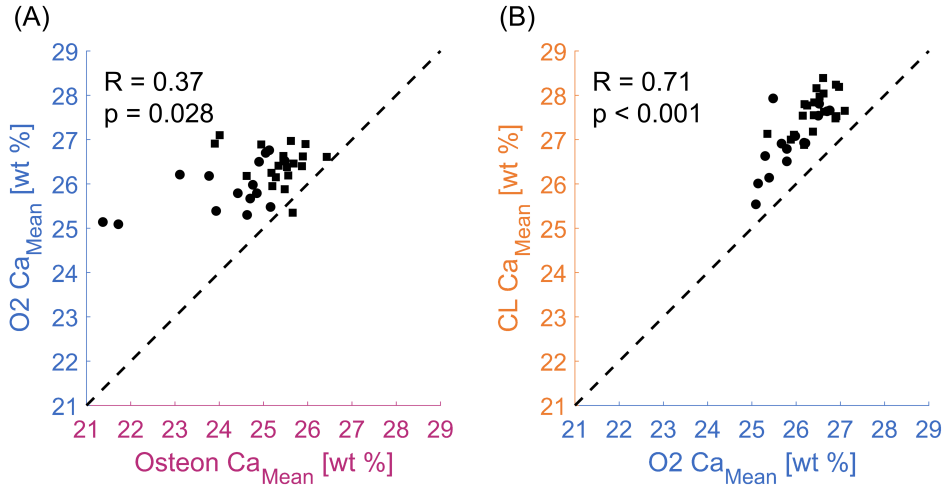


Figure S4: Mineral content of osteon, CL and outer region. Correlation between the average calcium content (Ca_{Mean}) of (A) the osteon and the outer layer O2, and (B) the CL and O2. The dotted line with a unit slope and passing through the origin is shown to improve the readability of the plot. Circles represent osteons from the adult individual (40 years) and squares from the aged individual (81 years).

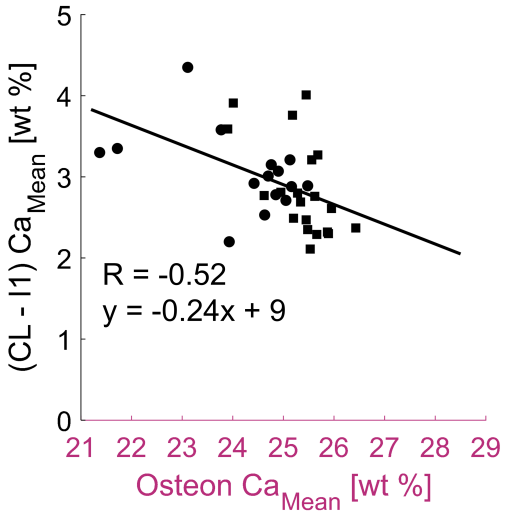


Figure S5: Difference in mineral content between CL and closest neighboring environment inside the osteon (represented by the first inner layer I1), computed as average difference (CL-I1) in each osteon and plotted versus the mean degree of mineralization of the osteon. Circles represent osteons from the adult individual (40 years) and squares from the aged individual (81 years).

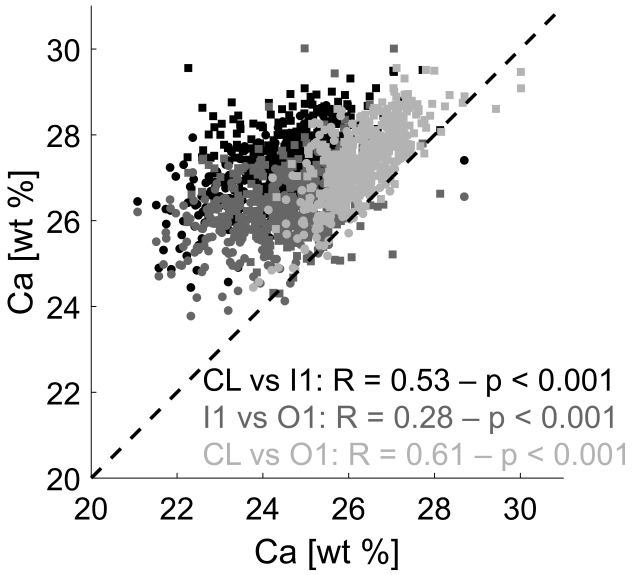


Figure S6: Correlations between the calcium content of the CL and adjacent layers with datapoints representing individual sectors. The following regions are correlated: CL versus inner layer I1, CL versus outer layer O1 and inner (I1) versus outer layer (O1). The dotted line with a unit slope and passing through the origin is shown to improve the readability of the plot. Circles represent osteons from the adult individual (40 years) and squares from the aged individual (81 years).

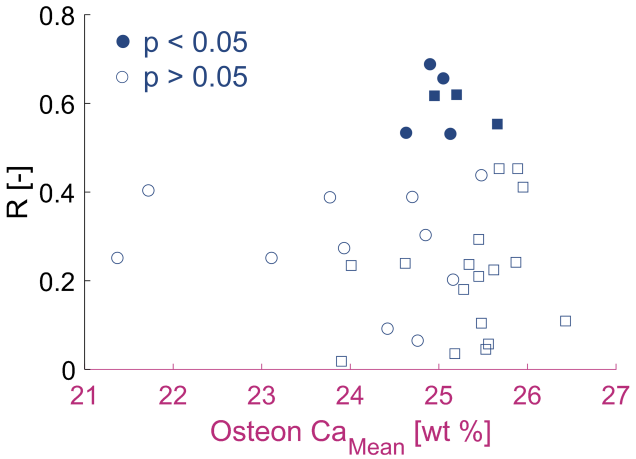


Figure S7: Spearman correlation coefficients between the mineral content of the CL and inner layer I1, computed according to a spatially resolved analysis around each osteon and represented according to the statistical significance of their correlation. Circles represent osteons from the adult individual (40 years) and squares from the aged individual (81 years).

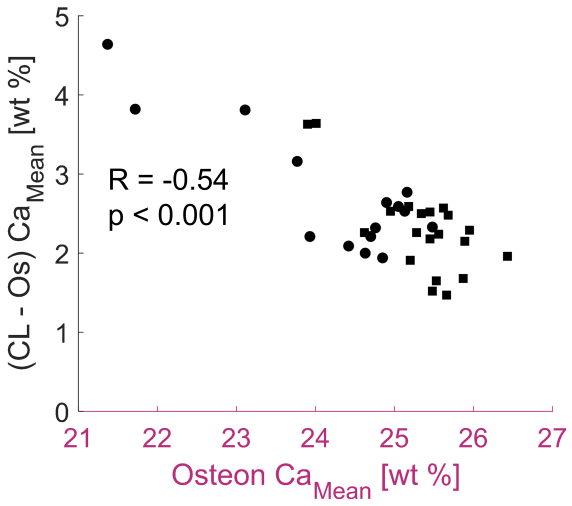


Figure S8: Differences in the mean degree of mineralization between CL and corresponding osteon plotted versus the average calcium content of the osteon as a surrogate measure of osteon age. Circles represent osteons from the adult individual (40 years) and squares from the aged individual (81 years).

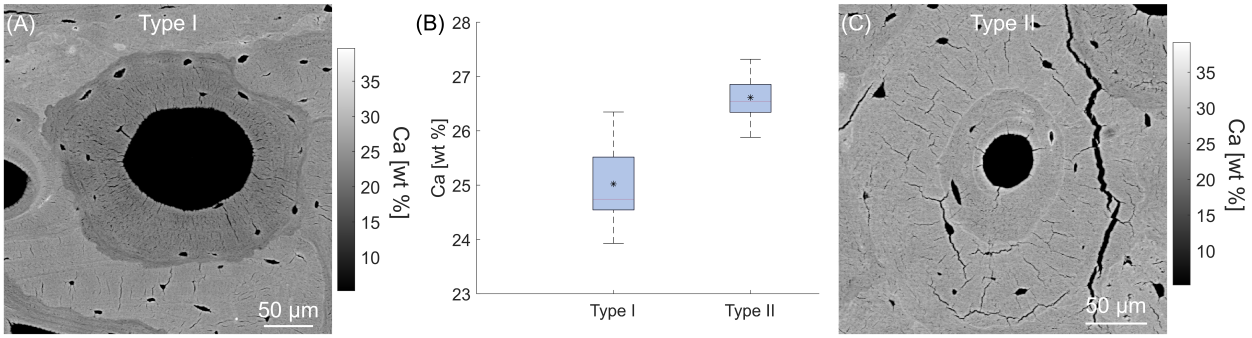


Figure S9: Examples of two osteons of different types and associated heterogeneity of the mineral content in the outer environment around the osteons. qBEI maps of the mineral content for (A) type I and (C) type II osteon (referred to as osteon-in-osteon scenario). In type II osteon, only the CL of the inner osteon was considered as the outer osteon was in some cases interrupted by other osteons. (B) Boxplot of the mean calcium content of the outer layer O2 around the two osteons. The boxes represent the interquartile range, encompassing 50% of the data, with the lower quartile at the bottom and the upper quartile at the top. The median and mean values are indicated by a line and an asterisk, respectively. The whiskers extend to show the range of data, reaching from the 5th percentile to the 95th percentile.

Supplementary note 3.1

To understand the interplay between primary and secondary mineralization, it is instructive to introduce a mathematical description of the mineralization law, quantifying the increase in calcium content Ca as a function of time t (elapsed from osteoid deposition) expressed in units of turnover time (which is defined as the time it takes to remodel an amount of bone equal to the actual bone volume). In trabecular bone, the mineralization law can be well-represented as a sum of two hyperbolic growth functions [18]:

$$Ca(t) = C_1 \frac{t/t_1}{1 + t/t_1} + C_2 \frac{t/t_2}{1 + t/t_2} \tag{3.1}$$

with C_1, t_1 and C_2, t_2 being parameters describing primary and secondary mineralization, respectively. We assume that such analytical description is also valid for osteonal bone, but most likely with different parameters [38] and with a different turnover time [39]. Starting from a reference mineralization law, we explore the impact of an increased primary mineralization, with both C_1 and t_1 varied by 5, 10, 15 and 20% (Fig. S10A). Without modifying the secondary mineralization, the final mineral content attained by CL is higher than experimentally measured. Such behavior is not seen when, following a higher primary mineralization, there is a slower secondary mineralization, as detected in this study (Fig. S10B).

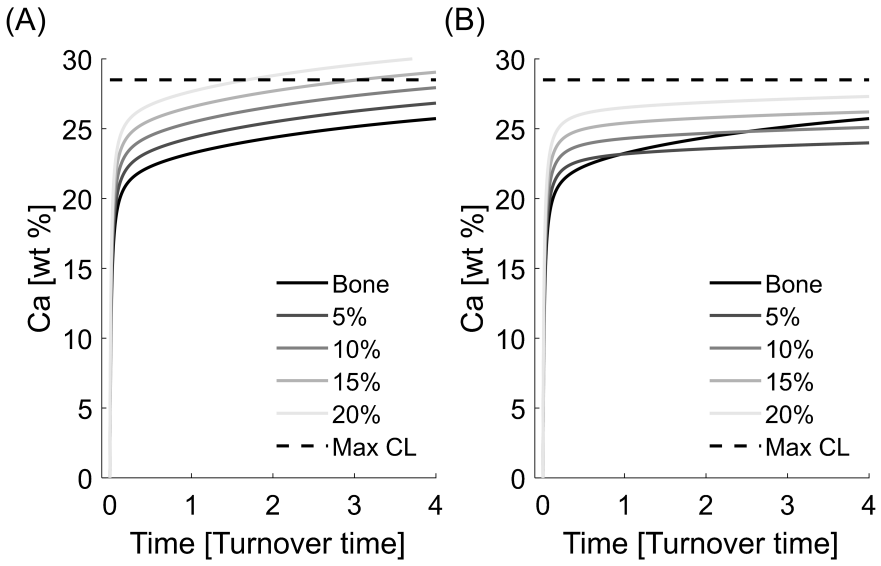


Figure S10: Mathematical description of the mineralization process. (A) Mineralization laws of CL assuming an increased primary mineralization by 5, 10, 15 and 20%. (B) Mineralization laws of CL assuming an increased primary mineralization (by 5, 10, 15 and 20%) and a decreased secondary mineralization (by a factor of 2.5) with respect to the mineralization of the bone. The dotted line is the maximum mineral content measured in the CL in this work.

Bibliography

[1] NE Lassen, TL Andersen, GG Pløen, K Søe, EM Hauge, S Harving, GET Eschen, and JM Delaisse. Coupling of bone resorption and formation in real time: new knowledge gained from human haversian BMUs. *Journal of Bone and Mineral Research*, 32(7):1395–1405, July 2017.

[2] BA Lamarche, JS Thomsen, CM Andreasen, WB Lievers, and TL Andersen. 2D size of trabecular bone structure units (BSU) correlate more strongly with 3D architectural parameters than age in human vertebrae. *Bone*, 160:116399, July 2022.

[3] A Tits, S Blouin, M Rummler, JF Kaux, P Drion, HG Van Lenthe, R Weinkamer, MA Hartmann, and D Ruffoni. Structural and functional heterogeneity of mineralized fibrocartilage at the Achilles tendon-bone insertion. *Acta Biomaterialia*, 166:409–418, August 2023.

[4] HS Gupta, S Schratter, W Tesch, P Roschger, A Berzlanovich, T Schoeberl, K Klaushofer, and P Fratzl. Two different correlations between nanoindentation modulus and mineral content in the bone–cartilage interface. *Journal of Structural Biology*, 149(2):138–148, February 2005.

[5] RK Nalla, JJ Kruzic, JH Kinney, and RO Ritchie. Mechanistic aspects of fracture and R-curve behavior in human cortical bone. *Biomaterials*, 26(2):217–231, January 2005.

[6] KJ Koester, JW Ager, and RO Ritchie. The true toughness of human cortical bone measured with realistically short cracks. *Nature Materials*, 7(8):672–677, August 2008.

[7] S Mohsin, FJ O'Brien, and TC Lee. Osteonal crack barriers in ovine compact bone. *Journal of Anatomy*, 208(1):81–89, January 2006.

[8] EA Zimmermann, B Gludovatz, E Schaible, B Busse, and RO Ritchie. Fracture resistance of human cortical bone across multiple length-scales at physiological strain rates. *Biomaterials*, 35(21):5472–5481, July 2014.

[9] W Wagermaier, K Klaushofer, and P Fratzl. Fragility of bone material controlled by internal interfaces. *Calcified Tissue International*, 97(3):201–212, September 2015.

[10] R Gauthier, H Follet, C Olivier, D Mitton, and F Peyrin. 3D analysis of the osteonal and interstitial tissue in human radii cortical bone. *Bone*, 127:526–536, October 2019.

[11] A Gustafsson, M Wallin, H Khayyeri, and H Isaksson. Crack propagation in cortical bone is affected by the characteristics of the cement line: a parameter study using an XFEM interface damage model. *Biomechanics and Modeling in Mechanobiology*, 18(4):1247–1261, August 2019.

[12] T Montalbano and G Feng. Nanoindentation characterization of the cement lines in ovine and bovine femurs. *Journal of Materials Research*, 26(8):1036–1041, April 2011.

[13] DB Burr, MB Schaffler, and RG Frederickson. Composition of the cement line and its possible mechanical role as a local interface in human compact bone. *Journal of Biomechanics*, 21(11):939–945, January 1988.

[14] JG Skedros, JL Holmes, EG Vajda, and RD Bloebaum. Cement lines of secondary osteons in human bone are not mineral-deficient: new data in a historical perspective. *The Anatomical Record Part A: Discoveries in Molecular, Cellular, and Evolutionary Biology*, 286A(1):781–803, September 2005.

[15] M Langer, A Pacureanu, H Suhonen, Q Grimal, P Cloetens, and F Peyrin. X-ray phase nanotomography resolves the 3D human bone ultrastructure. *PLoS ONE*, 7(8):e35691, August 2012.

[16] P Milovanovic, A vom Scheidt, K Mletzko, G Sarau, K Püschel, M Djuric, M Amling, S Christiansen, and B Busse. Bone tissue aging affects mineralization of cement lines. *Bone*, 110:187–193, May 2018.

[17] P Roschger, EP Paschalis, P Fratzl, and K Klaushofer. Bone mineralization density distribution in health and disease. *Bone*, 42(3):456–466, March 2008.

[18] D Ruffoni, P Fratzl, P Roschger, K Klaushofer, and R Weinkamer. The bone mineralization density distribution as a fingerprint of the mineralization process. *Bone*, 40(5):1308–1319, May 2007.

[19] Y Bala, D Farlay, PD Delmas, PJ Meunier, and G Boivin. Time sequence of secondary mineralization and microhardness in cortical and cancellous bone from ewes. *Bone*, 46(4):1204–1212, April 2010.

[20] C Lukas, D Ruffoni, FM Lambers, FA Schulte, G Kuhn, P Kollmannsberger, R Weinkamer, and R Müller. Mineralization kinetics in murine trabecular bone quantified by time-lapsed in vivo micro-computed tomography. *Bone*, 56(1):55–60, September 2013.

[21] MD McKee and A Nanci. Osteopontin and the bone remodeling sequence: colloidal-gold immunocytochemistry of an interfacial extracellular matrix protein. *Annals of the New York Academy of Sciences*, 760(1):177–189, August 1995.

[22] V Everts, JM Delaissé, W Korper, DC Jansen, W Tigchelaar-Gutter, P Saftig, and W Beertsen. The bone lining cell: its role in cleaning Howship's lacunae and initiating bone formation. *Journal of Bone and Mineral Research*, 17(1):77–90, January 2002.

[23] MD McKee, MC Farach-Carson, WT Butler, PV Hauschka, and A Nanci. Ultrastructural immunolocalization of noncollagenous (osteopontin and osteocalcin) and plasma (albumin and α2HS-glycoprotein) proteins in rat bone. *Journal of Bone and Mineral Research*, 8(4):485–496, April 1993.

[24] A Roschger, W Wagermaier, S Gamsjaeger, N Hassler, I Schmidt, S Blouin, A Berzlanovich, GM Gruber, R Weinkamer, P Roschger, EP Paschalis, K Klaushofer, and P Fratzl. Newly formed and remodeled human bone exhibits differences in the mineralization process. *Acta Biomaterialia*, 104:221–230, March 2020.

[25] T Tang, W Landis, S Blouin, L Bertinetti, MA Hartmann, A Berzlanovich, R Weinkamer, W Wagermaier, and P Fratzl. Subcanalicular nanochannel volume is inversely correlated with calcium content in human cortical bone. *Journal of Bone and Mineral Research*, 38(2):313–325, December 2022.

[26] P Roschger, P Fratzl, J Eschberger, and K Klaushofer. Validation of quantitative backscattered electron imaging for the measurement of mineral density distribution in human bone biopsies. *Bone*, 23(4):319–326, October 1998.

[27] P Roschger, J Eschberger, and HJr Plenk. Formation of ultracracks in methacrylate-embedded undecalcified bone samples by exposure to aqueous solutions. *Cells and materials*, 3:3, 1993.

[28] C Lukas, P Kollmannsberger, D Ruffoni, P Roschger, P Fratzl, and R Weinkamer. The heterogeneous mineral content of bone – Using stochastic arguments and simulations to overcome experimental limitations. *Journal of Statistical Physics*, 144(2):316–331, July 2011.

[29] MA Hartmann, S Blouin, BM Misof, N Fratzl-Zelman, P Roschger, A Berzlanovich, GM Gruber, PC Brugger, J Zwerina, and P Fratzl. Quantitative backscattered electron imaging of bone using a thermionic or a field emission electron source. *Calcified Tissue International*, 109(2):190–202, August 2021.

[30] DE Hinkle, W Wiersma, and SG Jurs. *Applied statistics for the behavioral sciences*. Houghton Mifflin ; [Hi Marketing] (distributor), Boston, Mass., [London], 5th ed edition, 2003.

[31] SL Teitelbaum. Bone resorption by osteoclasts. *Science*, 289(5484):1504–1508, September 2000.

[32] J Vääräniemi, JM Halleen, K Kaarlonen, H Ylipahkala, SL Alatalo, G Andersson, H Kaija, P Vihko, and HK Väänänen. Intracellular machinery for matrix degradation in bone-resorbing osteoclasts. *Journal of Bone and Mineral Research*, 19(9):1432–1440, September 2004.

[33] MD McKee and A Nanci. Osteopontin at mineralized tissue interfaces in bone, teeth, and osseointegrated implants: ultrastructural distribution and implications for mineralized tissue formation, turnover, and repair. *Microscopy Research and Technique*, 33(2):141–164, February 1996.

[34] T Tang, W Landis, E Raguin, P Werner, L Bertinetti, M Dean, W Wagermaier, and P Fratzl. A 3D network of nanochannels for possible ion and molecule transit in mineralizing bone and cartilage. *Advanced NanoBiomed Research*, page 2100162, April 2022.

[35] J Webster. *Integrated bone tissue physiology: anatomy and physiology*. CRC Press, January 2001.

[36] EF Eriksen, F Melsen, E Sod, I Barton, and A Chines. Effects of long-term risedronate on bone quality and bone turnover in women with postmenopausal osteoporosis. *Bone*, 31(5):620–625, November 2002.

[37] AM Parfitt. Misconceptions (2): turnover is always higher in cancellous than in cortical bone. *Bone*, 30(6):807–809, June 2002.

[38] C Lerebours, R Weinkamer, A Roschger, and PR Buenzli. Mineral density differences between femoral cortical bone and trabecular bone are not explained by turnover rate alone. *Bone Reports*, 13:100731, December 2020.

[39] MF Eriksen. Histologic estimation of age at death using the anterior cortex of the femur. *Journal of physical anthropology*, 84(2):171–179, December 1991.

[40] IS Maggiano, CM Maggiano, JG Clement, CDL Thomas, Y Carter, and DML Cooper. Three-dimensional reconstruction of haversian systems in human cortical bone using synchrotron radiation-based micro-CT: morphology and quantification of branching and transverse connections across age. *Journal of Anatomy*, 228(5):719–732, May 2016.

[41] AF van Tol, A Roschger, F Repp, J Chen, P Roschger, A Berzlanovich, GM Gruber, P Fratzl, and R Weinkamer. Network architecture strongly influences the fluid flow pattern through the lacunocanalicular network in human osteons. *Biomechanics and Modeling in Mechanobiology*, 19(3):823–840, June 2020.

[42] R Redelstorff. Unique bone histology in partial large bone shafts from Aust Cliff (England, Upper Triassic): an early independent experiment in gigantism. *Acta Palaeontologica Polonica*, 2014.

[43] M Yoshino, K Imaizumi, S Miyasaka, and S Seta. Histological estimation of age at death using microradiographs of humeral compact bone. *Forensic science international*, 64(2):191–198, 1994.

[44] S Gamsjaeger, B Hofstetter, E Zwettler, R Recker, JA Gasser, EF Eriksen, K Klaushofer, and EP Paschalis. Effects of 3 years treatment with once-yearly zoledronic acid on the kinetics of bone matrix maturation in osteoporotic patients. *Osteoporosis International*, 24(1):339–347, January 2013.

[45] S Gourion-Arsiquaud, JC Burket, LM Havill, E DiCarlo, SB Doty, R Mendelsohn, MCh Van Der Meulen, and AL Boskey. Spatial variation in osteonal bone properties relative to tissue and animal age. *Journal of Bone and Mineral Research*, 24(7):1271–1281, July 2009.

[46] E. P. Paschalis, F. Betts, E. DiCarlo, R. Mendelsohn, and A. L. Boskey. FTIR Microspectroscopic Analysis of Normal Human Cortical and Trabecular Bone. *Calcified Tissue International*, 61(6):480–486, December 1997.

[47] D Farlay, Y Bala, S Rizzo, S Bare, JM Lappe, R Recker, and G Boivin. Bone remodeling and bone matrix quality before and after menopause in healthy women. *Bone*, 128:115030, November 2019.

4

Cement lines are stiffer, harder but less mechanically efficient than lamellar bone

Adapted from: Astrid Cantamessa[1], Victoria Schemenz[2*], Stéphane Blouin[3*], Timothy Volders[1], Manfred Brughammer[4], Jiliang Liu[4], Andrea Berzlanovich[5], Richard Weinkamer[6], Wolfgang Wagermaier[6], Markus A. Hartmann[3], Davide Ruffoni[1], Stiffer, harder but but less efficient: comparing CL with lamellar bone, to be finalized and submitted to *ACS Nano*.

[1] Mechanics of Biological and Bioinspired Materials Laboratory, Department of Aerospace and Mechanical Engineering, University of Liège, Liège, Belgium;

[2] Charité – Universitätsmedizin, Berlin, Germany;

[3] Ludwig Boltzmann Institute of Osteology at Hanusch Hospital of OEGK and AUVA Trauma Centre Meidling, 1st Medical Department Hanusch Hospital, Vienna, Austria;

[4] ESRF, European Synchrotron Radiation Facility, Grenoble, France;

[5] Department of Biomaterials, Max Planck Institute of Colloids and Interfaces, Potsdam, Germany;

[6] Center of Forensics Medicine, Vienna, Austria.

Keywords

Cement line, nanoindentation, SAXS, WAXS, quantitative backscattered electron imaging, mineral properties, osteon.

Abstract

The remarkable mechanical performance of bone comes from its complex, hierarchical structure, based on three simple constituents–mineral, collagen and water–assembled in a variety of motifs at many length scales. The presence of numerous internal interfaces joining the different components is another key feature of bone. Formed during bone remodeling, the cement line (CL) is a thin interface surrounding osteons. Although often overlooked due to its small size, the CL is believed to contribute to bone frac-

*These authors contributed equally to this work.

ture resistance. However, the specific mechanical properties of this interface are debated: is it stiffer or softer than bone? In this study, we investigate the composition-mechanics relationship at the CL and surrounding bone in human osteons using multimodal imaging at sub-micrometer resolution and in a correlative manner. We found that the CL is stiffer and harder than adjacent osteonal tissue, which is in line with its higher mineral content. However, the CL requires more mineral than bone to attain the same stiffness and hardness, suggesting a lower mechanical efficiency. Analyzing the nanoscale properties of the mineral, we found thicker but shorter particles at the CL. Using a mechanical model, we interpreted the lower aspect ratio of the mineral particles as a less effective way to reinforce the collagen matrix. Casting our findings in a damage-based computational model, we questioned the possible protective role of the CL, which is not a soft interface as traditionally believed. The experimentally observed crack deflection around osteons is probably due to its concentric lamellar arrangement rather than to the CL.

4.1 Introduction

Bone is as load bearing material which needs to be stiff, strong and tough [1]. The stiffness is required to prevent excessive deformation under daily loadings, even exceeding body weight. The toughness is needed above all to avoid low-energy impacts causing bone fractures, especially considering that bone is not overdesigned with high safety factors as traditionally done in engineering [2, 3]. While healthy bone nicely combines those conflicting requirements, aged and diseased bone becomes weaker and more susceptible to fractures [2, 4, 5].

It is fascinating that the remarkable mechanical behavior of healthy bone is obtained using limited and relatively simple chemical elements: bone is essentially composed of a mineral phase (stiff but brittle), a collagen-based matrix (tough but compliant) and water [2]. The ability of bone to make the best out of its elementary constituents comes from the complex three-dimensional hierarchical organization, which offers the opportunity to adapt each level of the hierarchical structure to different requirements [6]. A hierarchical structure also implies that building blocks of different dimensions have to be assembled, generating numerous internal interfaces at many length scales [7]. Therefore, bone mechanical behavior, especially fracture resistance, depends not only on the building blocks but also on the properties of the interfaces joining them [4]. At the nanoscale, bone features collagen molecules reinforced by tiny mineral particles: at the interface between these two elements, there are ionic bonds to link amino acids (from the protein) to calcium ions (from the mineral) [8]. Several collagen molecules assemble into mineralized collagen fibrils and the space between fibrils is occupied by a thin interface containing non collagenous proteins and proteoglycans. These interfaces are critical for the deformation of bone at the nanoscale where load shearing between mineral and collagen occurs though interface shear [9], which causes the breaking of sacrificial bonds to dissipate energy and increase bone toughness [10]. At the next hierarchical level, mineralized collagen fibrils are arranged into fiber bundles, which appear in different structural motifs, including the more disorganized woven bone and the ordered lamellar bone [11]. A distinct feature of

lamellar bone is the organization in sheet of parallel collagen fibers, which are stacked under different orientations to form the so-called rotated plywood structure [12]. Between these sheets and between lamellae there should be weaker interfaces characterized by more disordered bone [13, 14]. Numerous works have shown that lamellar bone can enhance fracture toughness by several mechanisms, including a periodic modulation of elastic properties [15] and the deviation of cracks at the interface between lamellae [16]. Lamellar bone is further organized in osteons, which are characteristic structures of cortical bone, where a central Haversian canal (hosting blood vessels) is surrounded by a concentric arrangement of lamellae [17]. Secondary osteons, formed during bone remodeling, are bordered by a thin interface known as the cement line (CL). Although discovered more than 150 years ago, the CL is still poorly understood [18], with open questions on CL composition, mechanical behavior and function. Owning to their tiny dimensions (only 1-2 μm in width), CLs are difficult to be characterized quantitatively and to clearly distinguish their properties from those of surrounding bone.

The present work focuses on the CL. We know that the CL is the first part of the new osteon which is deposited during a remodeling event. [19, 20, 21] There is quite some evidence that the CL is enriched with osteopontin (a non-collagenous protein) [22] and that it is often more mineralized than the surrounding bone [23, 24, 25], as a result of a different mineralization process [23]. Structurally, there is preliminary data that the CL has lower collagen content [24] and different mineral characteristics [26] than osteonal bone. Considering function, the CL may act as a rigid substrate that facilitates the initial assembly and alignment of many osteoblasts, which is required for the subsequent formation of organized lamellar bone [27]. Mechanically, the CL has been suggested to influence crack propagation, contributing to bone toughness. This comes from the experimental evidence that (micro)cracks are more frequently detected in the outer interstitial bone than within the osteons [28, 29], as well as from the observation of crack deflection at the other boundary of osteons. [30, 31, 32] Yet, the understanding of the possible role of CL in bone fracture resistance requires knowledge of CL material properties. In analogy with fiber reinforced composite [33], a soft and weak CL may protect the osteon by arresting cracks, whereas a stiff and strong CL may deflect the crack around the osteon [4]. In this context, several computational works have investigated those mechanisms in great details [34, 35, 36, 37], yet making assumptions on CL properties giving the lack of experimental data. Indeed, our current knowledge of CL material behavior is clearly insufficient: only a very limited number of studies have focused on CL mechanical characteristics, suggesting a softer (weaker) response compared to surrounding bone [38, 39]. However, this appears hard to reconcile with the hypermineralization of the CL, given the close relationship between mechanical properties and mineral content [40, 41].

In this work we aim to: i) quantify the local mechanical properties and the relationship mineral content-mechanical properties of the CL and surrounding bone, and ii) to measure the mineral characteristics of the CL for elucidating its mechanical performance. By employing several techniques with submicrometer resolution in a spatially resolved and correlative manner we advance our knowledge of this enigmatic

interface.

4.2 Materials and methods

4.2.1 Sample preparation

Femurs from two male donors, aged 40 and 81, with no known bone conditions, were acquired from the Department of Forensic Medicine of the Medical University of Vienna. This study complied with institutional ethical guidelines (EK no. 1757/2013). Immediately after extraction, the femurs were frozen at -20°C for preservation. The femoral shafts far from the metaphysis were cut transversally and sectioned into 6 cubic samples (3 per femur), each approximately 1.5 cm in size, using a water-cooled wire diamond saw (WireTec, Germany). Following this, the samples underwent dehydration and embedding in polymethyl methacrylate (PMMA) [42, 43]. The upper transverse surfaces were then ground with sandpapers of progressively finer grit sizes (P1200, P2400) and polished using a diamond suspension down to 1 μm particle size on a silk cloth under glycol irrigation (Logitech PM5, UK), to minimize microcrack formation during preparation [44].

4.2.2 Quantitative backscattered electron imaging

We used quantitative backscattered electron imaging (qBEI) to measure the local mineral content of the CL and surrounding bone. This technique enables a quantitative two-dimensional assessment of the calcium content with a spatial resolution of less than 1 μm, as required by the tiny dimensions of the CL. Briefly, qBEI counts the electrons which are backscattered from the sample surface during scanning electron microscopy (SEM). The backscattered-electron signal is calibrated with carbon and aluminum standards to convert grey level images into spatial maps of the calcium content (in Ca wt %), according to a well-established procedure [43, 45, 46, 47]. Prior to qBEI experiments, the samples were coated with a thin carbon layer using vacuum evaporation (Agar SEM carbon coater, Agar, Stansted, UK) to achieve a conductive surface. qBEI measurements were performed with a SEM equipped with a zirconium-coated field emission cathode (Zeiss SEM SUPRA 40, Germany). The SEM operated at 20 kV, with a working distance of 10 mm and a probe current ranging between 280 and 320 pA. Initial overview scans were done at a lower resolution (1.76 μm/pixel) with a wider field of view to identify osteons with a visible CL in different locations. A total of 76 osteons of various dimensions and mineral content, were preselected and analyzed at higher magnification (isotropic pixel size of 0.57 μm and field of view of 1024 × 768 pixels).

4.2.3 Second harmonic generation imaging

To qualitatively assess the lamellar organization of the selected osteons and surrounding bone, second harmonic generation (SHG) imaging was conducted on the same regions previously measured by qBEI. Imaging was performed using a confocal laser scanning microscope (Leica TCS SP8 DLS, Germany)

equipped with a 40× oil immersion objective (HC PL APO 40×/1.30 OIL). A pulsed infrared laser (Spectra-Physics, Milpitas, US) operating at 910 nm was utilized, with backward signal collected at wavelengths between 450 and 460 nm. Images were captured with a nominal pixel size of 379 nm across a 1024 × 1024 pixels field of view, scanned at a rate of 400 Hz. Multiple regions were imaged and subsequently stitched together with a slight overlapping using the software of the Leica microscope.

4.2.4 Nanoindentation

To measure the local mechanical properties, we used nanoindentation (nIND) on regions identified and characterized with qBEI (Fig. 4.1A-B). To map the mechanical properties with a similar resolution as used for measuring the mineral content, we imposed a maximum load of 500 μN, corresponding to a penetration depth of about 150 nm. This depth allows a spacing between adjacent indents of 1 μm, which should be roughly 7 times the contact depth to avoid overlapping the inelastic deformation fields [48]. Nanoindentation was performed with a Triboindenter TI 950 (Bruker, US) equipped with a Berkovich diamond tip (100 nm tip radius). A force-controlled trapezoidal load function was employed, involving loading for 8 seconds, holding for 20 seconds and unloading for 8 seconds. Prior to indentation, sample surfaces were scanned with the tip at 2 μN contact force over regions of 50 × 50 μm to measure the average surface roughness, which was 7.97 ± 10.47 nm. As the indentation depth was about ten times the surface roughness, the impact of roughness can be neglected [49, 50]. Several indentation grids with a constant spacing of 1 μm were performed on a subset of the osteons previously analyzed with qBEI. We selected 9 regions belonging to 8 different osteons, where the CLs were most visible and had the largest width , resulting in 4966 indents. Before indentation, the probe contact area was calibrated on fused quartz. Force-depth curves were analyzed with the well-established Oliver-Pharr method [51], to obtain indentation hardness (H) and reduced modulus (E_r).

4.2.5 High-resolution backscattered and secondary electron imaging

To locate the position of the indents with respect to the CLs, the indented regions were rescanned using the same SEM at higher magnification, yielding an isotropic pixel size of approximately 76 nm. The high-resolution images were captured in two modalities simultaneously: secondary electron imaging (SEI) was used to map the surface topography allowing to detect the tiny traces of the indents caused by permanent deformation (Fig. 4.1C); backscattered electron imaging (BEI) facilitated the distinction between CLs (appearing brighter) and the surrounding bone based on different grey values (atomic number contrast), and allowed to distinguish layers with different textures, reflecting the lamellar structure of osteonal bone (Fig. 4.1D). Here, we used the terminology of thin and thick lamellae referring to the thin and thick layers visible in BEI. The distinction between lamellae was further verified by comparing SHG and BEI images (Fig. S1). In SHG, thick lamellae appear dark and thin lamellae bright, one reason being differences in collagen orientation: while in plane collagen fibers generate SHG signal, out-of-plane do not [52]. By overlaying the indent traces (visible in SEI) on the high resolution BE images of the bone surface, we

could classify the indents as belonging to the CLs, the thick or thin lamellae (of the same osteon of the CL) or the surrounding older bone outside the osteon (Fig. 1E). Indents located within cracks or pores (e.g. osteocytes lacunae) were excluded from the analysis. We also neglected indents only partially falling into the CLs (red symbols in Fig. 4.1E).

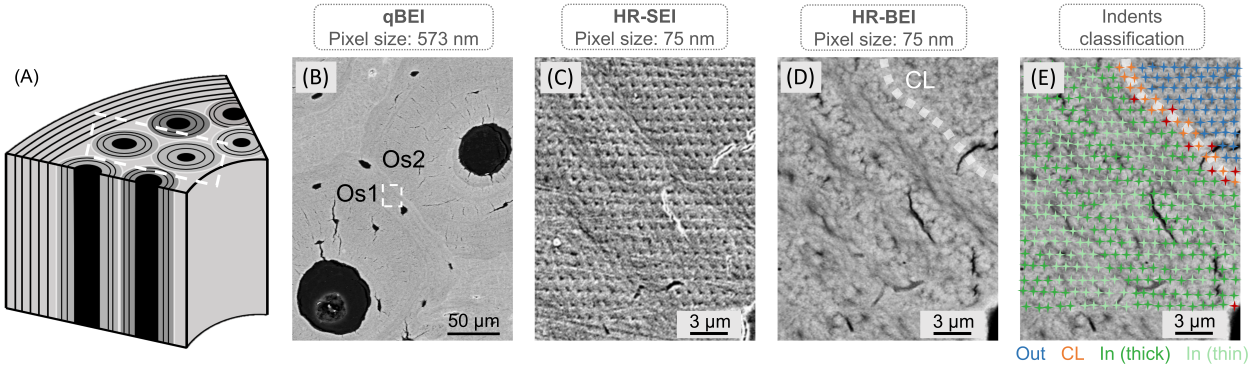


Figure 4.1: Analysis of human osteons. (A) Schematic representation of cortical bone. (B) qBEI scans of osteons and their surroundings. (C) Magnified view with SEI of the regions where nanoindentation was performed, highlighting indent imprints. (D) BEI image of the same region highlighting the CL and the different texture reflecting lamellar organization. (E) Indents classified as part of the CL (orange), the corresponding osteons (In, dark green or bright green depending on the lamella type), or the surrounding older bone (Out, blue). Indents located within cracks or cells were excluded from the analysis, as well as those near but not directly on a CL (red).

4.2.6 Correlation between mineral content and mechanical properties

To extract the mineral content at the very same positions probed with nanoindentation, quantitative maps of the mineral content obtained with qBEI were overlaid and matched with high resolution qualitative BEI/SEI images, enriched with indent traces (Fig. 4.1E). Using a custom image registration technique implemented in MATLAB, five to six landmarks were manually selected in both qBEI and BEI/SEI images. These landmarks included for example the porosities, and were used to compute a similarity transformation, which preserves angles and aspect ratios while allowing for translation, rotation, and uniform scaling, using the *fitgeotrans* function from MATLAB Image Processing Toolbox (R2022a, The MathWorks, Natick, MA, USA). Indent coordinates could be mapped to the qBEI reference frame using the obtained transformation matrix . For the correlation with the mechanical properties, the mineral content was averaged over a 3 × 3 pixels region centered around each indent.

4.2.7 Small- and wide-angle X-ray scattering

After assessing the mineral content (qBEI), the fiber organization (SHG) and the local mechanical properties (nIND), the same samples were examined with scanning small- and wide-angle X-ray scattering (SAXS and WAXS) to measure mineral particles properties, with sub-micrometer resolution. The samples were sectioned into ultra-thin slices, approximately 2-3 μm thick, using a microtome (Leica SM2500E, Leica Microsystems, Bensheim, Germany). The thin sections were mounted on a silicon nitride X-ray transparent window (Norcada Inc., Canada) and fixed to custom made aluminum frames

for SAXS/WAXS experiments (Fig. S2). All regions to be analyzed were preselected with qBEI and, prior to X-ray scattering experiments, the slices were imaged with an optical microscope (Keyence VHX Microscope, Belgium) to locate the positions of the pre-selected regions. Scanning X-ray scattering was performed at the nanofocus beamline (ID13) of the European Synchrotron Radiation Facility (ESRF, Grenoble, France). A monochromatic beam with an energy of 15.2 keV and focal spot size of 0.5 μm was used. SAXS and WAXS patterns were recorded simultaneously using a 16-bit CCD detector (MAR-CCD, Mar Inc., USA) configured in binning mode of 2070 × 2167 pixels. The sample-to-detector distance was 237.25 mm, calibrated with an alumina standard. Each measurement point was illuminated for 20 ms. Parallel to the scattering measurements, quantitative X-ray fluorescence (XRF) maps (Fig. S3) were recorded using an XRF detector placed approximately 20 mm away from the sample. A total of 22 regions having typical dimensions of 200 × 200 μm^2, belonging to 20 different osteons were mapped with an isotropic pixel size of 0.5 μm. The SAXS and WAXS data were processed with the software named DPDAK (Directly Programmable Data Analysis Kit) [53]. After background correction, the SAXS and WAXS profiles have been integrated over the azimuthal angle to obtain radial intensity profiles $I(q)$, with q being the length of the scattering vector $\mathbf{q}$ [54, 55]. The radial intensity profile has been used to obtain information on mineral [56]. The average mineral particle thickness is commonly estimated using the so-called T parameter, defined as $T = 4\frac{\phi(1-\phi)}{\sigma}$, with ϕ representing the mineral volume fraction and σ denoting the platelet surface per unit volume, assuming that mineral crystals exhibit a thin platelet morphology [57]. The T parameters is a good approximation for the average particle thickness if the mineral volume fraction in the interaction volume is close to 0.5 [58]. As in our study we compared regions with large differences in mineral content, including lowly mineralized osteons and highly mineralized CLs [23], we also calculated the W parameter, which is a modified version of the T parameters based on local measures of the mineral content [58]. The W parameter is defined as $W = \frac{T}{2(1-\phi)}$, with ϕ being now the spatially varying volume fraction, which is measured with qBEI on approximately the same locations characterized by X-ray scattering. To assess the platelet length L along the c axis, the full width at half maximum (FWHM) of the (002) peak intensity in the WAXS signal is used. Specifically, we applied Scherrer's equation: $L = \frac{k\lambda}{B\cos\theta}$, where λ is the wavelength, θ is the Bragg angle, k is the Scherrer constant (related to crystallite shape), and B is the FWHM of the peak [59]. The position of the (002) peak indicates the lattice spacing (i.e. the space between atoms) in the crystallographic (002) direction. This is used to compute the *c-lattice* constant, which informs on possible distortions of the HAP crystal, for example due to trace elements [60]. Finally, we derived the degree of orientation, denoted as ρ parameter, by integrating the azimuthal SAXS intensity profile [54]. The degree of orientation describes how well the mineral platelets are aligned along a common direction within the plane perpendicular to the incident X-ray beam: ρ value of 1 indicates a uniform orientation, while $\rho = 0$ represents a completely random orientation [61].

Pixels with insufficient scattering signal to derive mineral crystal parameters were excluded from the analysis by setting thresholds for the total scatter intensity [62]. To locate the CL in the position resolved maps of the crystal parameters, we used XRF images acquired alongside the X-ray scattering. As calcium maps

were heavily influenced by surface waviness (Fig. S3), we relied on zinc maps, which provided a good contrast between the CL and the surrounding bone (Fig. S3). Indeed, it is known that zinc and other heavy metals accumulate in the CL [63]. The identification of the CL was further verified by overlaying zinc and qBEI maps, in the latter the CL appears brighter [23] (Fig. S4).

Mineral parameters were analyzed in the proximity of the CL and plotted as a function of the distance to the CL (Fig. 4.4). In the distance plots, three regions were identified: the CL, the corresponding inner osteon (In), and the surrounding outer bone (Out). The CL was defined as a 2-μm-thick layer centered around the peak in the Zn signal. Due to the heterogeneity of mineral properties, we analyzed only zones in the vicinity of the CL: inner and outer regions extended up to 8 μm away from the CL. To compare mineral properties, we calculated frequency distributions of mineral parameters in the CL and in two additional regions having the same width of the CL and located ± 2 μm from the CL, thus falling inside and outside the osteon, respectively (Fig. 4.5). To enhance readability, all frequency distributions were smoothed using a local regression with weighted linear least squares and a first-degree polynomial model (loess fit). Overall, we measured 22 locations belonging to 20 different osteons. Six locations were discarded due to technical issues and ten locations due to sample artifacts (waviness and cracks), which cannot be avoided when preparing large and thin sections as required for synchrotron experiments at sub-micrometer resolution. In the remaining dataset, we analyzed a total of 6 osteons (Fig. S4) with 18 distance plots (3 for each osteon), corresponding to a bone surface of 3600 μm^2.

4.2.8 Statistical analysis

We compared differences in mechanical properties and mineral properties among the three regions (CL, In, and Out) by performing a Kruskal-Wallis test, chosen due to the non-normal distribution of the unpaired data. When significant differences were detected, pairwise comparisons between locations were conducted using post-hoc tests with Bonferroni correction to control for multiple comparisons and minimize false positive. We examined the strength of the relationships between the mean calcium content of osteon, CL and different regions using Spearman's rank correlation, selected for its suitability with non-normal distribution of the data. Significance levels were set at $p < 0.05$, and all p-values were two-sided. All statistical analyses were performed in MATLAB 2022a.

4.3 Results and discussion

Using a multimodal approach, we obtained quantitative 2D maps of mechanical properties, composition and mineral characteristics of the CL and surrounding bone in human osteons with sub-micrometer spatial resolution. Thanks to a correlative approach we gained knowledge on CL properties. We first present findings on mechanical and compositional aspects, measured with nIND and qBEI at the same locations. We complement this analysis by characterizing mineral particles using synchrotron nano-focus scanning x-ray scattering. Micromechanical modeling is subsequently employed to link the mineral features to

the mechanical behavior of the CL. Finally, a proof-of-concept damage-based finite element analysis is proposed to challenge the mechanical role of the CL.

4.3.1 The cement line is stiffer and harder than the corresponding osteon

Figure 4.2 illustrates typical high-resolution maps of local mechanical properties and mineral content obtained across the border between two osteons. Qualitative observations reveal a spatial modulation of indentation modulus (Fig. 4.2B) and hardness (Fig. 4.2C) in the most recently deposited osteon (Os1). Variations in mechanical properties mirror the lamellar organization inferred by SHG imaging (Fig. 4.2E): bright lamellae in SHG, indicative of (predominantly) in-plane collagen fibers, correspond to a more compliant and softer mechanical behavior; dark regions in SHG, representing out-of-plane fibers, correspond to stiffer and harder lamellae. The region-matched map of the mineral content (Fig. 4.2D) also shows variations at the lamellar level, albeit less evident. A clear feature of Figure 4.2D is the increase in mineral content in the CL. Consistent with the greater amount of mineral, the CL shows higher indentation modulus and hardness compared to its corresponding osteon. Elevated mechanical properties are maintained in the outer region belonging to the neighboring osteon (Os2), although the mean mineral content there is lower than in the CL and similar to Os1 (Fig. 4.2D). A possible explanation of this trend is the absence of SHG signal coming from Os2 (Fig. S5), which may indicate out-of-plane fibers, consistent with a stiffer behavior.

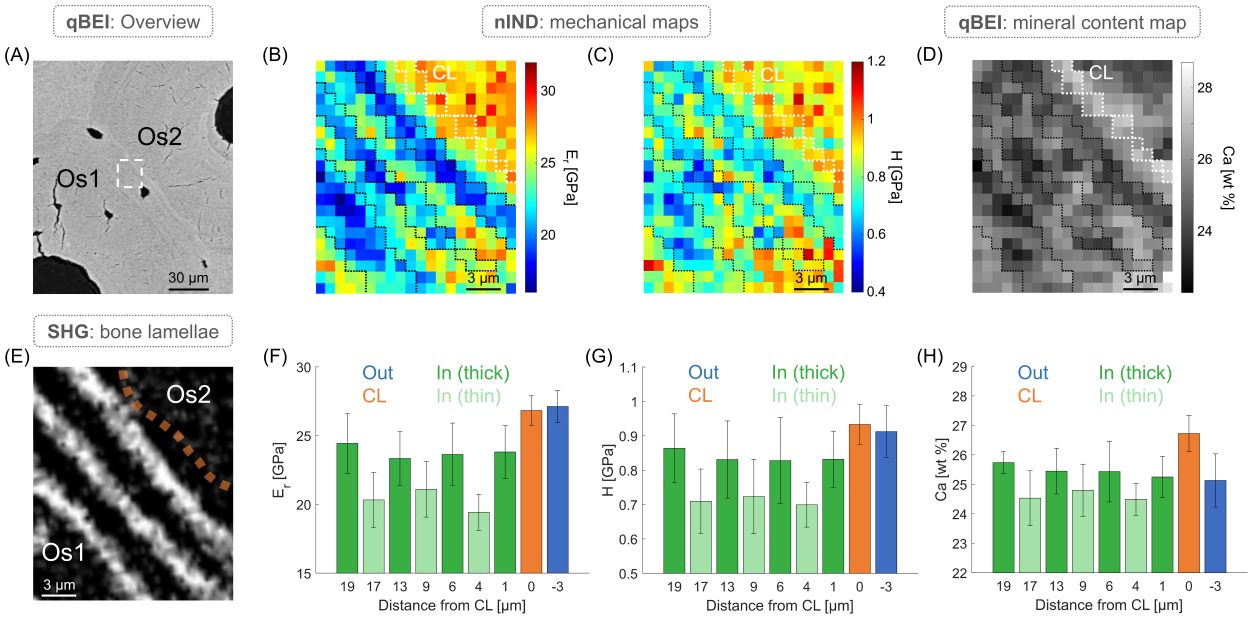


Figure 4.2: Fig. 2: Correlative analysis of mineral content and mechanical properties in a region containing a CL separating two osteons of similar mineral content. (A) qBEI overview image showing two osteons (Os1 and Os2) and the location where nanoindentation was performed. 2D maps show (B) indentation modulus (E_r), (C) hardness (H), and (D) mineral content (Ca wt %) across the osteons and CL. (E) SHG image highlighting the lamellar structure in the same region and the position of the CL (orange dashed line). (F-H) Bar plots show mean and standard deviation of E_r, H, and mineral content in different classified regions: outer osteon (Out, blue), CL (orange), and inner osteon lamellae (thick and thin, green shades).

The precise localization of the indents in the mineral content maps (see section 4.2) allowed us to calculate

mean stiffness (Fig. 4.2F), hardness (Fig. 4.2G) and mineral content (Fig. 4.2H) in the different regions. The CL is the stiffest (E_r = 26.82 ± 1.08 GPa) and the hardest (H = 0.93 ± 0.06 GPa) feature of Os1, being about 20% stiffer ($p < 0.01$) and 18% harder ($p < 0.01$) than the corresponding osteon. A pronounced mechanical contrast is observed between thick (E_r = 23.66 ± 2.12 GPa, H = 0.83 ± 0.11 GPa) and thin (E_r = 20.27 ± 1.92 GPa, H = 0.71 ± 0.09 GPa) lamellae within Os1, corresponding to a 15.4% difference in stiffness ($p < 0.01$) and 15.6% in hardness. The mineral content also shows variations between thick (Ca_{Mean} = 25.44 ± 0.86 wt %) and thin (Ca_{Mean} = 24.6 ± 0.82 wt %) lamellae, with the difference being around 3% ($p < 0.01$). In line with greater mechanical properties, a pronounced peak in mineral content is observed at the CL (Ca_{Mean} = 26.72 ± 0.62 wt %), exceeding the mean mineral content of the corresponding osteon and of the outer bone by more than 6% ($p < 0.01$). However, no significant differences were found between the mechanical properties of the CL and the outer bone ($p = 0.99$ and $p = 87$ for E_r and H, respectively). These trends are consistently observed in all samples (Fig. S6), with the CL exhibiting always higher mineral content (+8.93%) and mechanical properties (+21.92% for E_r and +25.87% for H) compared to its osteon ($p < 0.01$). Although the CL remains more mineralized than the surrounding outer bone (+3.44%, $p < 0.01$), its stiffness and hardness are comparable to those of the outer regions (0.53% in E_r, $p = 0.9$; 3.25% in H, $p < 0.01$).

The periodic variations in mechanical properties at the lamellar level seen in Os1 align with previous studies [64, 65, 66, 67] and, most likely, reflect different arrangements of the mineralized collagen fibers in thick and thin lamellae. Although being deposited within the same remodeling cycle, and therefore having a similar tissue age, the CL appears more mineralized than lamellar bone inside the osteon, suggesting potential differences in the mineralization process [23]. One additional reason for the higher mineral content measured at CL is a reduced nanoscale porosity [42]. The mechanical behavior of the CL uncovered here challenges current knowledge: we found that the CL is stiffer and harder than the corresponding osteon. At the same time, we also found that the CL is mechanically comparable to (older) surrounding bone. In contrast, previous works assessing CL mechanical properties with nanoscale methods reported that the CL is more compliant and softer than neighboring tissue [38, 39, 68]. This discrepancy could be due to different samples (human femurs analyzed here versus bovine and ovine bones considered in the literature), testing protocols and conditions. A distinctive feature of our approach is that the mechanical characterization of the CL is supported by correlative local measurements of the mineral content as well as by a careful identification of the indent positions with SEM.

4.3.2 The cement line needs more mineral than the osteon to attain the same mechanical properties

We explore the relationship between mechanical properties and mineral content of the CL and neighboring bone by collecting and plotting values of indentation modulus and hardness versus calcium content at the same locations. A dependence is observed between mineral content and mechanical properties (Fig. 4.3A and S7A), but data appears quite scattered and the corresponding Spearman correlation coef-

ficients are moderate/weak. This is not surprising considering the underlying heterogenous arrangement of mineralized collagen fibrils (e.g. thin and thick lamellae highlighted by SHG) [69, 70]. Qualitative similarly scattered data were obtained at the bone-tendon [71] and bone-cartilage [40] interface. We can learn much more by binning indentation modulus (and hardness) and by calculating the corresponding value of calcium content which is needed to attain specific values of mechanical properties in each bin.

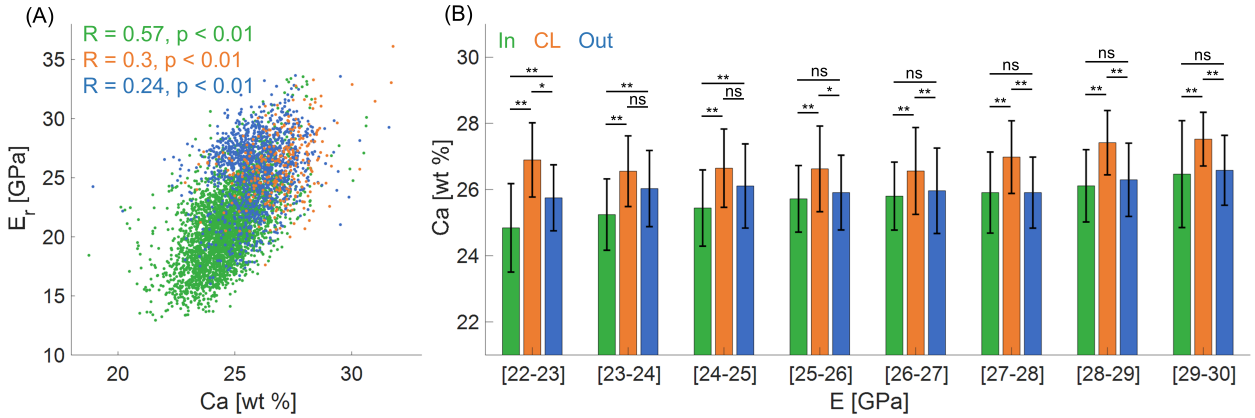


Figure 4.3: Quantitative relationship between indentation modulus (E_r) and mineral content at the CL, corresponding inner osteon (In), and outer bone (Out). (A) E_r plotted against mineral content for the 3 regions (total of 4966 indents). The Spearman correlation coefficients are reported. (B) Mean mineral content required to achieve specific stiffness values, ranging from 22 to 30 GPa (bin width 1 GPa). Error bars represent standard deviations. Statistical significance between the data sets is indicated as follows: *p < 0.05, **p < 0.01, and ns (not significant).

Figure 4.3B reveals a key trend: for a given tissue stiffness, the mean mineral content is consistently higher in the CL compared to lamellar bone, both inside the osteon as well as in the outer neighborhood. A similar pattern is observed for hardness (Fig. S7B). This is a central finding on the composition-mechanical property relationship of the CL, which requires a higher mineral content to attain the same stiffness and hardness of the surrounding bone. This could be due to differences in the collagen-based matrix, mineral crystals or mineral-collagen packing. Considering the mineral phase, there are some indications, albeit limited to a small portion of a single osteon, that the CL may have different mineral characteristics than adjacent bone [26]. Therefore, we further investigate the property of the mineral crystals on the same samples and when possible same osteons, to clarify mineral content-mechanical properties relationship.

4.3.3 The cement line has thicker and shorter mineral particles than adjacent bone

High resolution SAXS and WAXS are used to analyze the nanostructural properties of the mineral particles, including thickness (T and W), length (L), degree of orientation (ρ) and lattice expansion (*c-lattice*), in a position-resolved manner.

Figure 4.4 presents 2D maps and line profiles of mineral particle properties across the CL separating two osteons. Based on a distinct peak in Zinc at the border between the two osteons (Fig. 4.4B), we can locate the position of the CL. Considering the thickness of the mineral particles, the so-called T

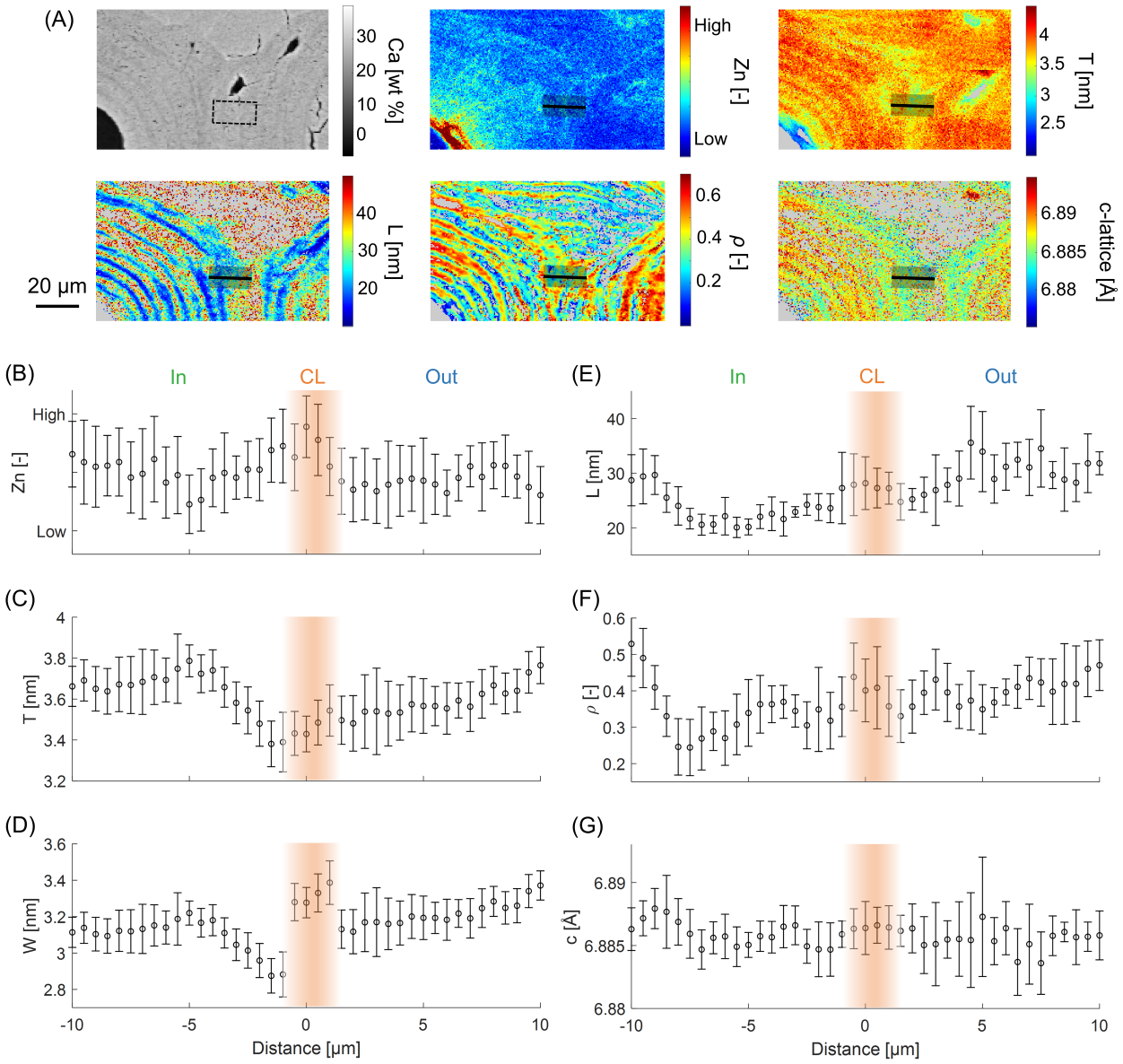


Figure 4.4: (A) 2D high resolution maps of mineral particle characteristics in Os3. Highlighted in the maps is the location across the CL where data is extracted and analyzed. Profile plots of (B) Zinc content and (C-G) particle properties plotted as a function of the distance from the CL (highlighted by the shaded area). Negative values correspond to regions inside the osteon and positive values outside. To reduce noise, at each position data are averaged over 20 pixels and displayed as mean values ± standard deviations.

parameter shows a decrease that colocalizes with the CL (Fig. 4.4C). As the mineral content of the CL is significantly different from the surrounding bone (Fig. S8A), we also computed the W parameter, which takes into consideration differences in mineral volume fraction [58], and which reveals that the CL has thicker mineral particles. The profile plot of W shows sharp variations at the CL due to the correction of the T parameter with 3 averaged values of mineral volume fraction representative for the CL and the neighboring regions (inside and outside the corresponding osteons). A spatially resolved profile of mineral volume fraction should yield more gradual variations of the W parameter. As mineral content was measured with qBEI on a different section (about 15 μm away) than analyzed with X-ray scattering,

we prefer to correct with average values. Nevertheless, even when using a profile plot of mineral volume fraction coming from a roughly corresponding region, data appears noisier, but the main message does not change: the W parameter is higher at the CL (Fig. S8). The profile plots of the other parameters (Figs. 4.4E-G) do not highlight specificities at the CL, one reason being a high heterogeneity also evident from the 2D maps. Qualitative similar results are obtained when inspecting other three regions (Fig. S9-S11).

To overcome the challenges of such high tissue heterogeneity combined with a limited thickness of the CL, we further compare CL against adjacent bone using frequency distributions based on all collected data (14400 pixels). This comparison reinforces the message that mineral particles at the CL (Fig. 4.5C) are significantly thicker (W = 3.35 ± 0.28 nm) compared to the surrounding bone tissue, both inside the corresponding osteon (W = 3.22 ± 0.22 nm, $p < 0.01$) as well as outside (W = 3.33 ± 0.18 nm, $p = 0.048$). Considering the length of the mineral particles (Fig. 4.5D), all three distributions are asymmetric, with tails extending towards larger values. The distribution of the CL is bimodal, with a higher peak at 30 nm and a lower peak at 19 nm. The CL exhibits significantly shorter crystals (L = 23.73 ± 8.14 nm) than the osteon (L = 25.88 ± 7.57 nm, $p < 0.01$) and the outer bone (L = 26.43 ± 8.22 nm, $p < 0.01$). In terms of degree of orientation (Fig. 4.5E), mineral particles in the CL seem to be slightly more oriented (ρ = 0.34 ± 0.1) than those inside the osteon (ρ = 0.32 ± 0.11, $p < 0.01$) and outside (ρ = 0.33 ± 0.1, $p < 0.01$), where the frequency distribution is also more heterogenous. Finally, the lattice expansion (Fig. 4.5F) is marginally lower at the CL (*c-lattice* = 6.8836 ± 0.0029 Å) compared to the other two regions (osteon: *c-lattice* = 6.8842 ± 0.0025 Å, $p < 0.01$; outer: *c-lattice* = 6.8849 ± 0.0026 Å, $p < 0.01$), indicating a minor contraction of the c axis at the CL.

Despite the strong heterogeneity of the analyzed regions, we could show that the CL features shorter but thicker mineral particles and has a slight contracted c axis in comparison to the surrounding bone. Our finding on particle length is consistent with a previous work analyzing a portion of a single osteon with X-ray scattering tensor tomography [26]. Considering the T parameter, similarly to Grünewald et al. [26], we found smaller values at the CL. However, when accounting for variations in the mineral volume fraction and computing the so-called W parameter, it turns out that the CL has thicker mineral particles than adjacent tissue. The geometrical dimensions of the mineral particles are known to change during the mineralization process: growth in length happens earlier and at a faster rate than growth in thickness [62]. These two timescales should correspond to a rapid primary mineralization (growth in length), followed by a slower secondary mineralization (growth in thickness) [56, 72]. We have previously demonstrated that both primary and secondary mineralization are different in the CL relative to the osteon, and that the mineralization of the CL is not universal but depends strongly on the region where the CL is formed [23]. The CL has a faster primary mineralization than the osteon: assuming a similar growth kinetics of the mineral particles, a shorter particle length may reflect a reduced duration of primary mineralization. The same reasoning does not apply to particle thickness: the secondary mineralization of the CL is slower than the one of the osteon, yet the CL has thicker particles - even in comparison to older bone outside the osteon, which had much more time to mineralized. There are several factors that can

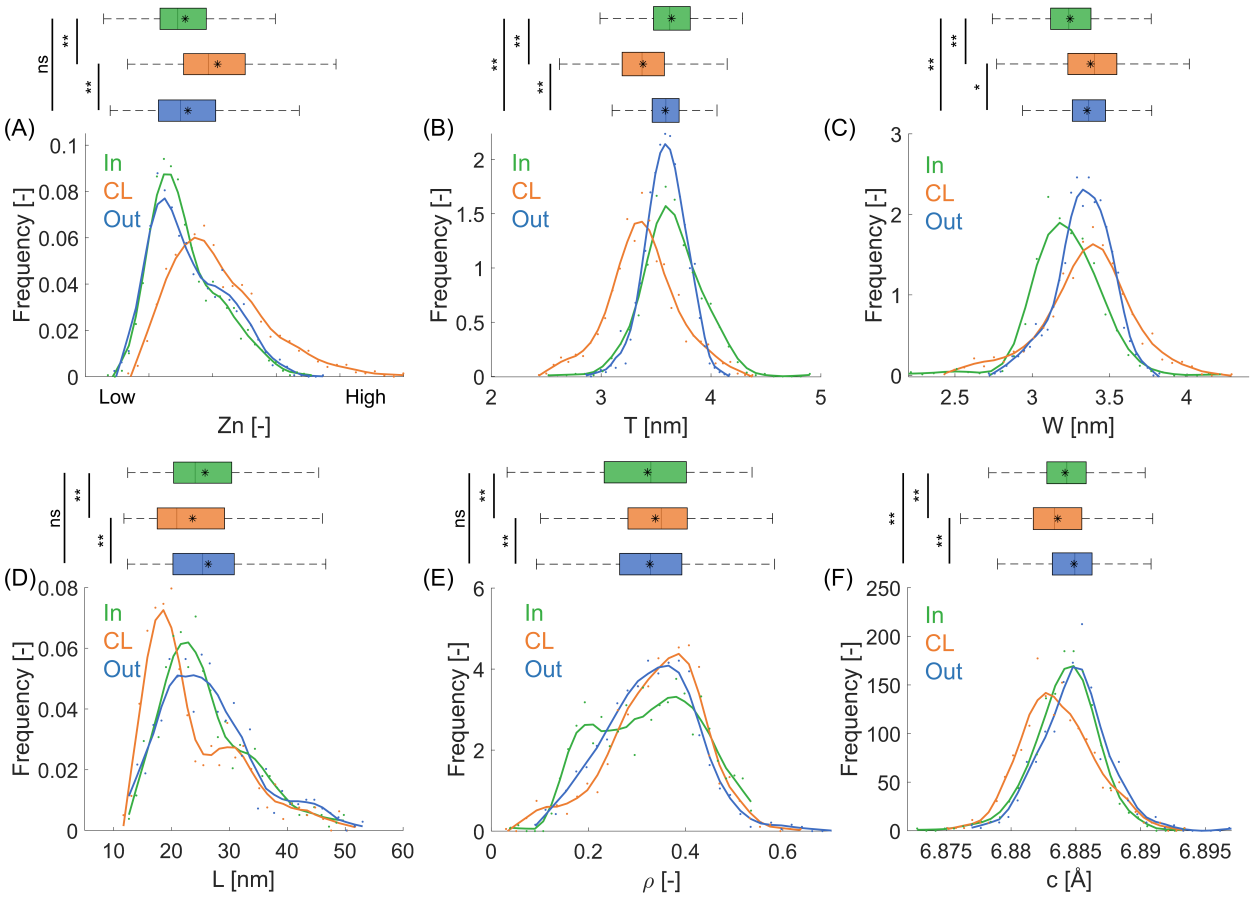


Figure 4.5: Frequency distributions and boxplot representations of (A) zinc intensity Zn, (B) uncorrected particle thickness T, (C) corrected particle thickness W, (D) particle length L, (E) degree of alignment ρ, (F) lattice expansion *c-lattice*. All parameters calculated in 3 regions having the same number of pixels: inner osteon (In), cement line (CL) and outer bone (Out). Original data represented as scattered points and smoothed data (loess) as full lines. Boxes range from the 25th to the 75th percentiles, the median and mean values are indicated by a vertical line and an asterisk, respectively. Whiskers show the range of data, reaching from the 5th to the 95th percentile. Statistical significance between the data sets is indicated as follows: *p < 0.05, **p < 0.01, and ns (not significant).

influence particle dimensions, ranging from matrix composition to water content [73]. The CL is rich in non-collagenous proteins such as osteocalcin and osteopontin [20, 22, 25, 74], which have the ability to regulate crystal growth, size and shape [75]. The CL also contains lower amount of collagen compared to the surrounding bone matrix [24], which may be one additional factor influencing collagen packing and particle dimension. A slightly shorter c axis at the CL agrees a with previous work [26], and it may be due to the presence of trace elements, it may indicates a lower degree carbonate substitution typically occurring during bone maturation [60] or it could even be a fingerprint of compressive strains in the mineral [76]. The organization of mineralized collagen fibrils at the CL is quite complex, with fibrils oriented in three or more predominant directions and with higher directional dispersion than lamellar bone, as revealed through FIB-SEM analysis [70]. The degree of alignment quantified here with the ρ parameter shows great spatial variability across the different regions (Fig. 4.4F and S12). This is also reflected in the frequency distributions of ρ: the CL tends to have a marginally higher (3-6%) degree of alignment than

immediately adjacent bone (Fig. 4.5E) but no differences are detected when including a larger region (Fig. S12). In conclusion, our analysis based on several osteons could not confirm that the organization of collagen fibrils at the CL is less regular and more disordered than in lamellar bone.

4.3.4 On the mechanical efficiency and potential protective role of the cement line

Experimentally, we found that the CL requires a higher mineral content to achieve the same stiffness and hardness as the surrounding bone. We searched for a possible explanation by focusing on the mineral characteristics, and we observed that mineral particles at the CL appear thicker and shorter compared to nearby tissue. These findings can be interpreted with a mechanical shear-lag model (Supplementary note 4.1) [41]. Assuming a staggered arrangement of the mineral particles into the organic matrix (Fig. 4.6A), the model allows to compute the elastic modulus and the tensile strength of the resulting composite as a function of mineral volume fraction and mineral particle dimensions [2, 71]. Introduction of the aspect ratio of the mineral particles as length over thickness, we obtain an average value of about 8 for the lamellar bone and 7 for the CL. Mechanically, a low aspect ratio is clearly reflected in lower stiffness and tensile strength for the same volume fraction of mineral (Fig. 4.6B and C). This suggests that mineral particles in the CL are less effective at reinforcing the organic matrix. Previous works based on more sophisticated models and computer simulations have highlighted that a higher aspect ratio is beneficial for nanoscale stiffness thanks to an increased stress transfer along the crystal length [77, 78]. Longer mineral particles should also provide a higher surface area for mineral-collagen interactions [79] and restrict collagen mobility [80]. In contrast, shorter crystals may leave a greater number of unreinforced regions in the collagen network, leading to higher post-yield deformability [81]. Finally, we use a damage-based computational model [82] to challenge the assumed ability of the CL to protect the osteon (Supplementary note 4.2, Fig. S13). We choose a simplified scenario featuring a central Haversian canal, a homogeneous osteon bordered by a CL and surrounded by interstitial bone (Fig. 4.6D). We define the mechanical contrast as the ratio between stiffness and strength of the CL and osteon compared to a reference value. Our simulations show that a CL can deflect damage only if it has much higher mechanical properties than surrounding bone: a mechanical contrast of more than 2.75 is required (Fig. 4.6E), which is significantly greater than the 20% difference measured experimentally. A soft and weak CL may also protect the osteon by trapping damage, but the required decrease in properties for full trapping is again substantial, i.e. a factor of 3 (Fig. 4.6F). Several previous computational works have explored the role of the CL in the damaging behavior of osteonal bone, and considering the uncertainties on CL properties, both weaker or stiffer CL have been assumed [34, 35, 36, 37, 83, 84, 85]. Our results support the view of a stiffer (stronger) CL but also highlight that the required increase in mechanical properties may be substantial and unlikely to be achieved. If the CL alone can only be of limited help for the mechanical protection of the osteon, why are cracks observed experimentally to propagate along CL [31, 36, 86] and are most often detected into interstitial bone rather than in the osteon [86]? Clearly, protecting the osteon and the blood vessels hosted in the Haversian canal is a critical task that cannot be solved only by the CL. The plywood lamellar architec-

ture around the osteon has been demonstrated to be a very effective way to improve strength, toughness and damage tolerance [12, 82]. Lamellar bone also occupies a considerable portion of the osteon, much greater than the space reserved to the thin CL. Lamellar architectures are not limited to bone but this is a universal strategy of nature to build damage tolerant mineral-reinforced materials [2, 87, 88, 89].

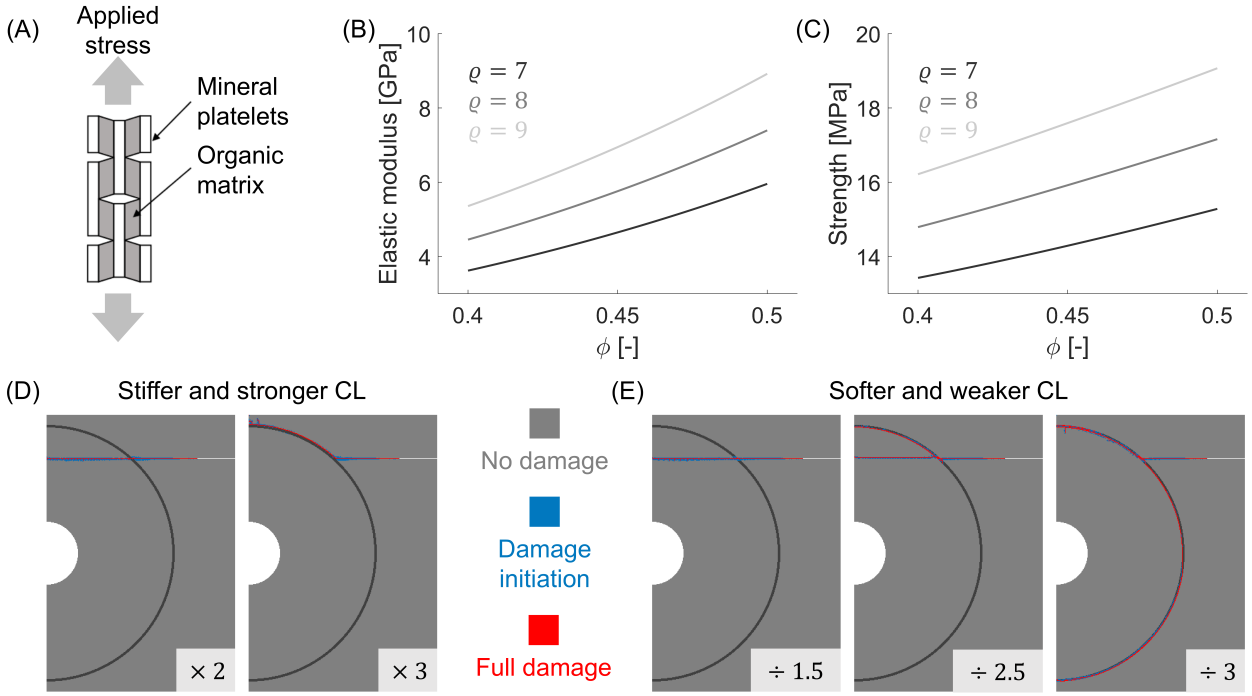


Figure 4.6: (A) Schematic representation of the staggered model assuming mineral platelets embedded in a ductile organic matrix under tensile loading. (B-C) Theoretical predictions of composite elastic modulus (B) and strength (C) as a function of mineral volume fraction ϕ, for different aspect ratios ϱ of the mineral particles. (D-E) Damage simulations in an osteon model with a surrounding CL and interstitial matrix. (D) Simulations with a stiffer and stronger CL compared to the adjacent bone. (E) Simulations with a softer and weaker CL compared to adjacent bone. Damage patterns are color-coded: blue indicates damage initiation and red indicates full damage.

4.3.5 Limitations

Some limitations of this study should be acknowledged. First, we considered a limited number of samples and osteons due to technical and time constraints of our multimodal analysis, also limited by available synchrotron beamtime. Like many studies focusing on micro- and nanoscopic material properties [40, 42, 64, 90, 91], we prioritized the detailed characterization of a limited number of samples rather than broader, less in-depth testing of many samples. Despite this limitation, all measured compositional, structural, and mechanical properties were consistent across all analyzed regions. To further increase the robustness our findings, future research should include larger and more diverse sample groups, incorporating variations in sex, age, and anatomical location. Second, bone samples were tested in a dehydrated state to enable measurements of the mineral content and a correlative analysis with the mechanical properties. It is known that ethanol removes water while maintaining hydrogen bonding with collagen [92]. As a consequence, indentation modulus and hardness in dehydrated samples tend to be higher compared

to hydrated conditions [66, 93]. Being interested in relative differences between CL and neighboring bone, rather than in absolute values, we did not see this as a major shortcoming. Third, a pixel-by-pixel superimposition of measurements of mechanical (nIND) and mineral (SAXS/WAXS) properties was not possible due to slight differences in the analyzed sections (about 15 μm apart). As a result, only qualitative correlations could be established. However, the analyzed regions still display comparable structural features, such as Haversian canals and CL. These features were identifiable in both zinc fluorescence and qBEI maps, allowing for manual image registration and approximate alignment. Finally, qBEI was performed at a high resolution to have enough pixels inside the CL minimizing partial volume effects [45]. Although at such resolution the qBEI signal should not be influenced by additional contrast coming from the lamellar arrangement, we did see small mineral differences at the level of bone lamellae having different orientations. We cannot say how much of this variation in mineral content is due to orientation effects. This is much less problematic at the CL considering the higher values of mineral content measured there.

4.4 Conclusion

We demonstrated that the CL is stiffer and harder than the adjacent osteonal tissue challenging the widespread assumption that it acts as a soft, compliant interface. The central finding of our investigation is that the CL requires more minerals to attain the same stiffness and hardness than surrounding bone, hinting for a lower mechanical efficiency of this region. We look for a possible explanation of this reduced efficiency by investigating the nanoscale structure of the mineral particles, which are thicker but shorter in the CL. With the help of a micromechanical model we showed that indeed mineral particles with a lower aspect ratio are much less effective at reinforcing the collagen matrix. Using a finite element damage-based model with a limited number of assumptions and parameters, we challenged the assumed role of the CL to deviate cracks as the mechanical properties required for such task would be much different than those measured here.

Conflicts of Interest

The authors declare no competing interests.

Acknowledgments

The authors thank Alexandra Tits and Sarvesh Bhogaokar for their help during the beamtime and acknowledge the European Synchrotron Radiation Facility (ESRF) in Grenoble, France for granting us beamtime. They also thank Phaedra Messmer, Petra Keplinger, and Sonja Lueger from LBIO for the sample preparation. AC is supported by the French Community of Belgium as part of a FRIA (Fund for Research Training in Industry and Agriculture) grant (n°1E03621F). MH and SB gratefully acknowledge

financial support from the Austrian Social Health Insurance Fund (OEGK) and the Austrian Workers' Compensation Board (AUVA). MR and RW thank the Max Planck Queensland Centre for the Materials Science of Extracellular Matrices for support. VS acknowledges support by the German Research Foundation within SFB1444.

Supplementary information

Materials and methods

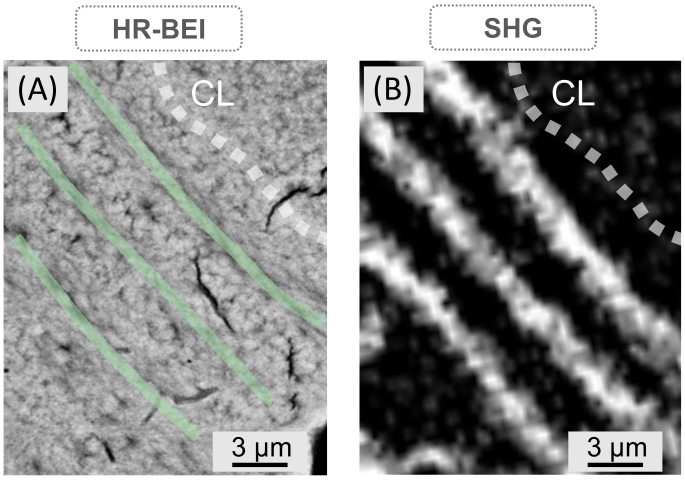


Figure S1: Comparison of lamellar structure in (A) HR-BEI and (B) SHG imaging. The CL is highlighted by a dashed line. Thin and thick lamellae are visible in both modalities, with thick lamellae appearing dark and thin lamellae (highlighted in green in BEI) bright in SHG.

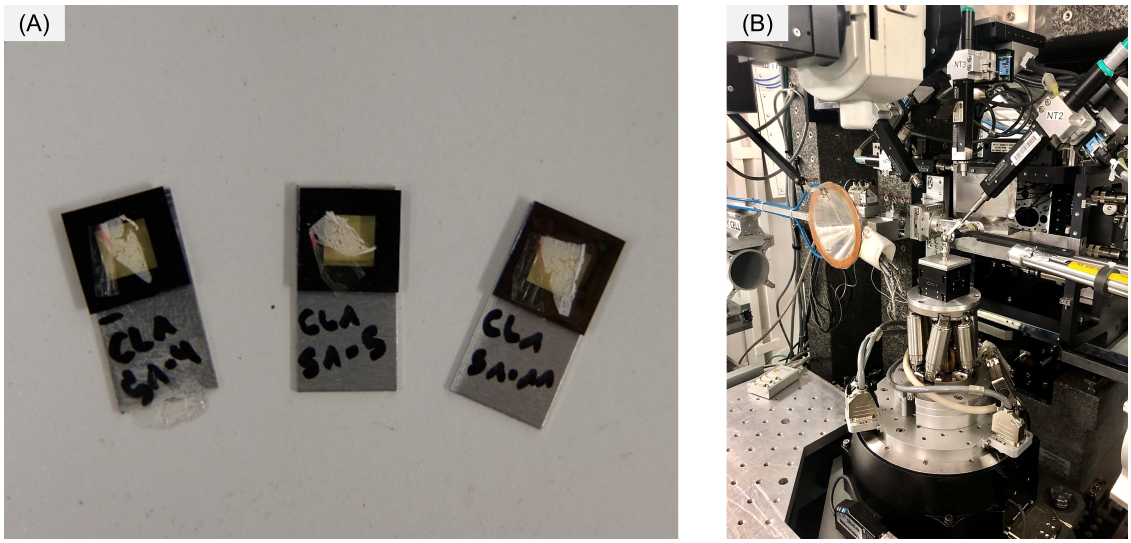


Figure S2: (A) Thin bone slices mounted on X-ray transparent silicon nitride membranes and fixed to custom-made aluminum frames for SAXS/WAXS measurements. (B) Sample mounted on the experimental stage at European Synchrotron Radiation Facility (ESRF) ID13 beamline.

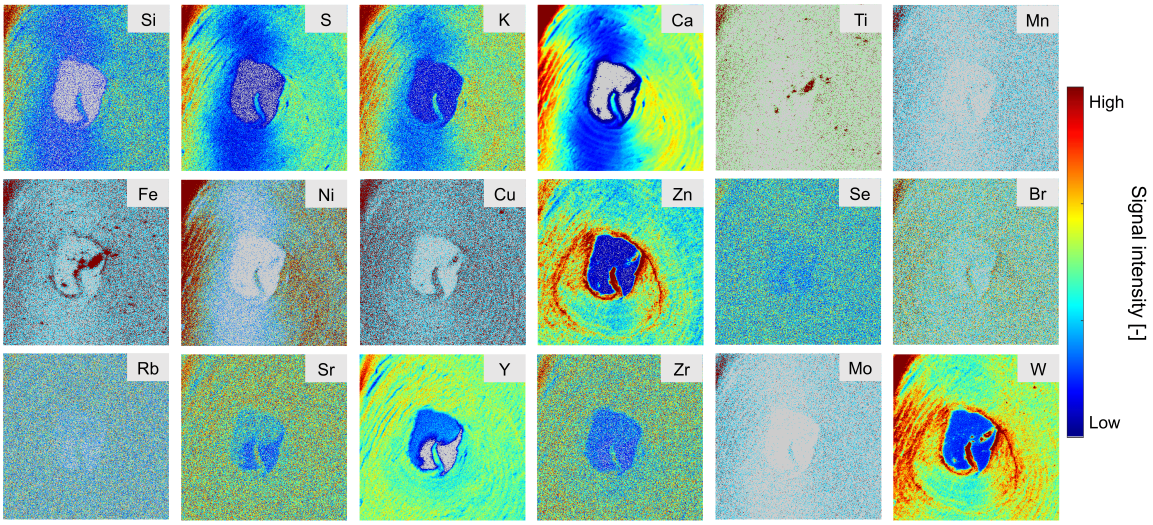


Figure S3: Elemental maps of Si, S, K, Ca, Ti, Mn, Fe, Ni, Cu, Zn, Se, Br, Rb, Sr, Y, Zr, Mo, and W measured by XRF.

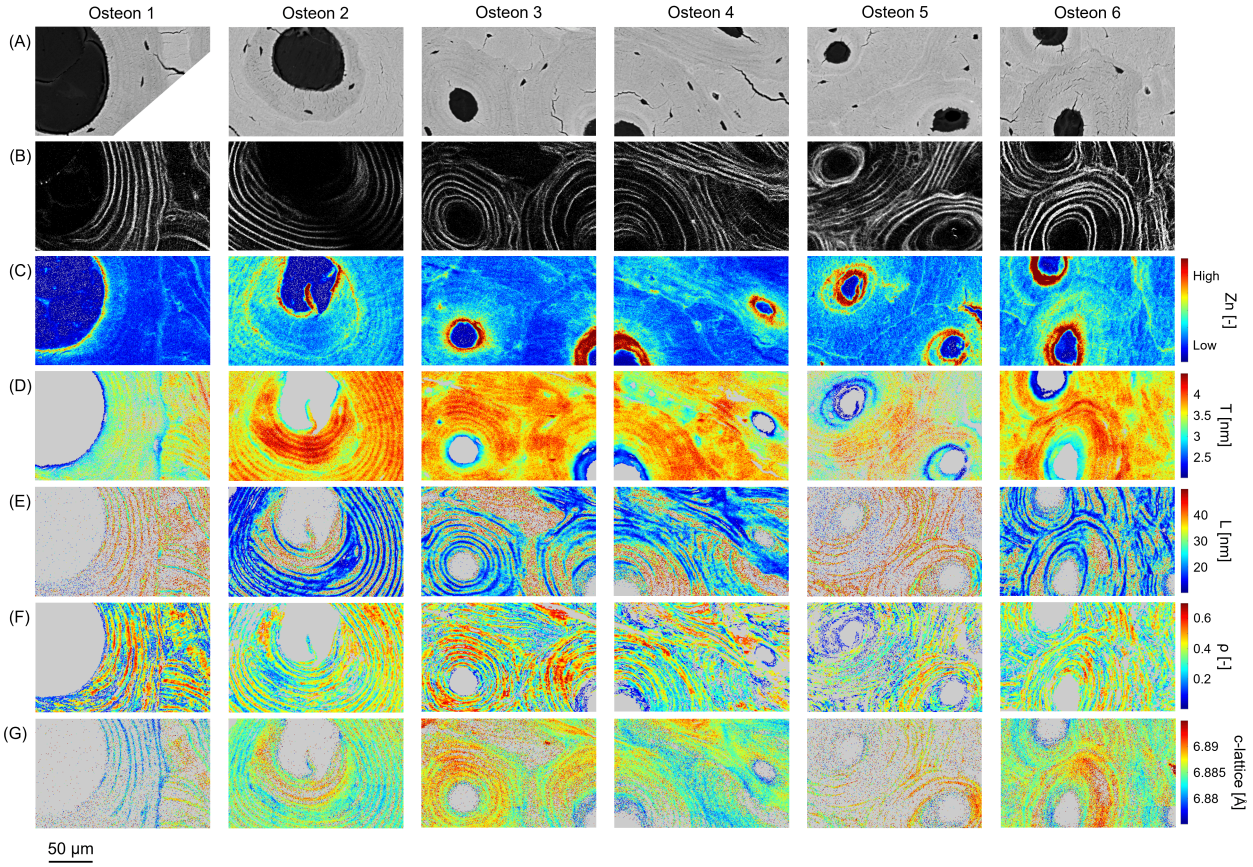


Figure S4: 2D colored maps of (A) mineral content, (B) collagen fibers organization, (C) zinc signal intensity, (D) mineral particle thickness T, (E) crystal length L, (F) degree of orientation ρ, and (F) lattice spacing (*c-lattice*) for the analyzed 6 osteons and surrounding bone tissue. Gray colored regions represent the discarded pixels, which did not give a sufficient X-ray scattering signal. Qualitative observations: a pronounced lamellar modulation of L and ρ is observed and, to a lesser extent also of T and *c-lattice*. These periodic variations in mineral properties seems to follow a similar lamellar pattern as highlighted by SHG, although differences in imaging planes prevent a pixel-to-pixel correlation. Despite a strong heterogeneity we can observe that near the Haversian canals, mineral thickness and lattice expansion are lower, while zinc intensity is higher compared to more peripheral regions.

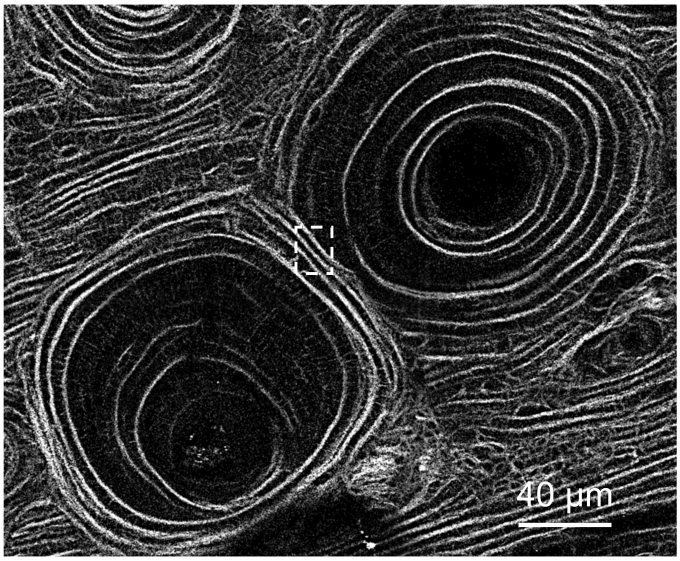


Figure S5: Enlarged SHG overview of Os1 and Os2 presented in Figure 4.2A.

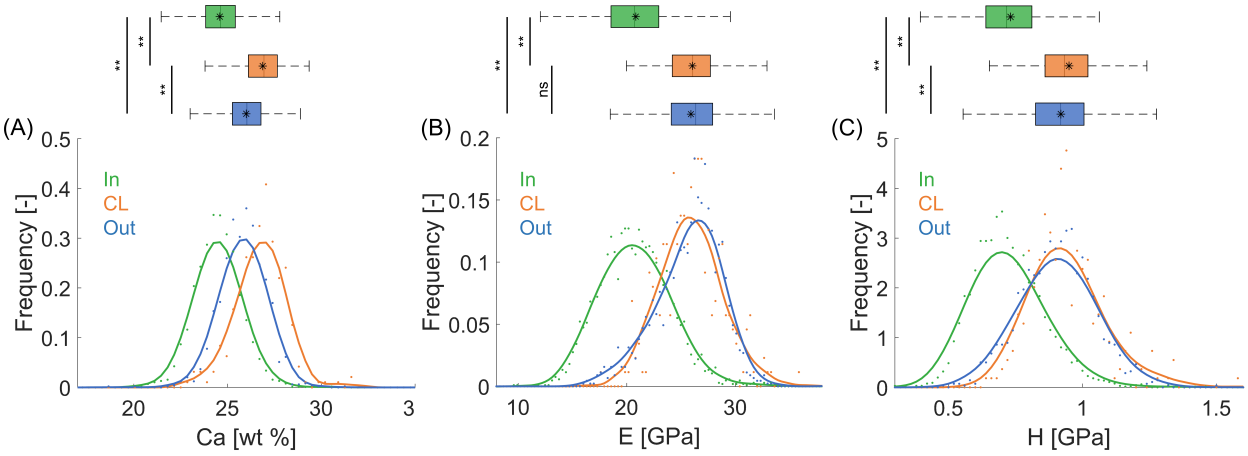


Figure S6: Frequency distributions and boxplot representations of (A) mineral content, (B) E_r and (C) H according to the different regions (In: inner osteon, CL: cement line, Out: external bone outside the osteon). Original data represented as scattered points and smoothed data (with loess filter) as full lines. Boxes range from the 25th to the 75th percentiles, the median and mean values are indicated by a vertical line and an asterisk, respectively. Whiskers show the range of data, reaching from the 5th to the 95th percentile. Statistical significance between the data sets is indicated as follows: *$p < 0.05$, **$p < 0.01$, and ns (not significant).

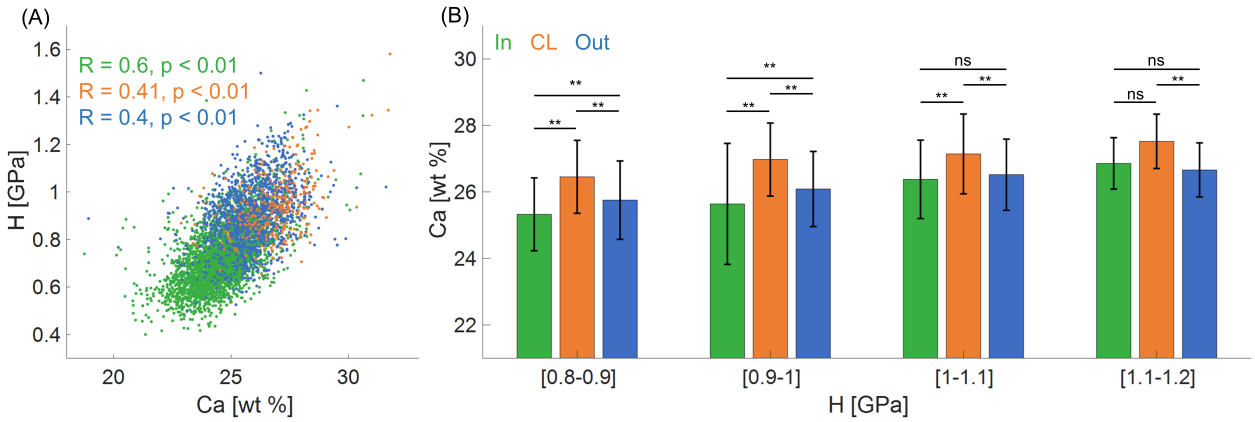


Figure S7: Quantitative relationship between indentation hardness (H) and mineral content in the cement line (CL), inner osteon (In), and outer osteon (Out). (A) H plotted against mineral content for each region. (B) Mean mineral content required to achieve specific H values ranging from 0.8 to 1.2 GPa (bin width 0.1 GPa) for each region. Error bars represent standard deviations. Statistical significance between the data sets is indicated as follows: *p < 0.05, **p < 0.01, and ns (not significant).

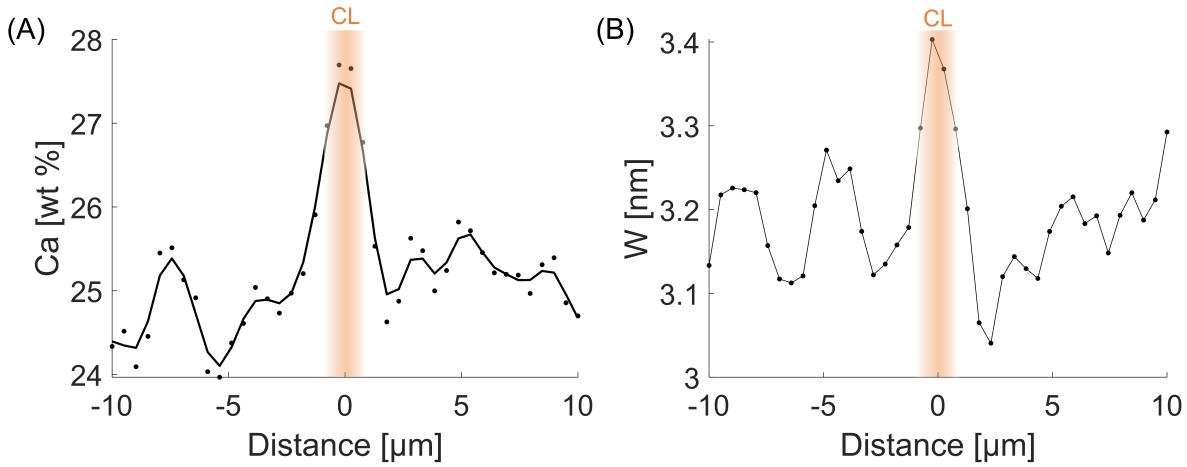


Figure S8: (A) Line profile of Ca content across the CL fitted with a loess fit used to compute the (B) W parameter.

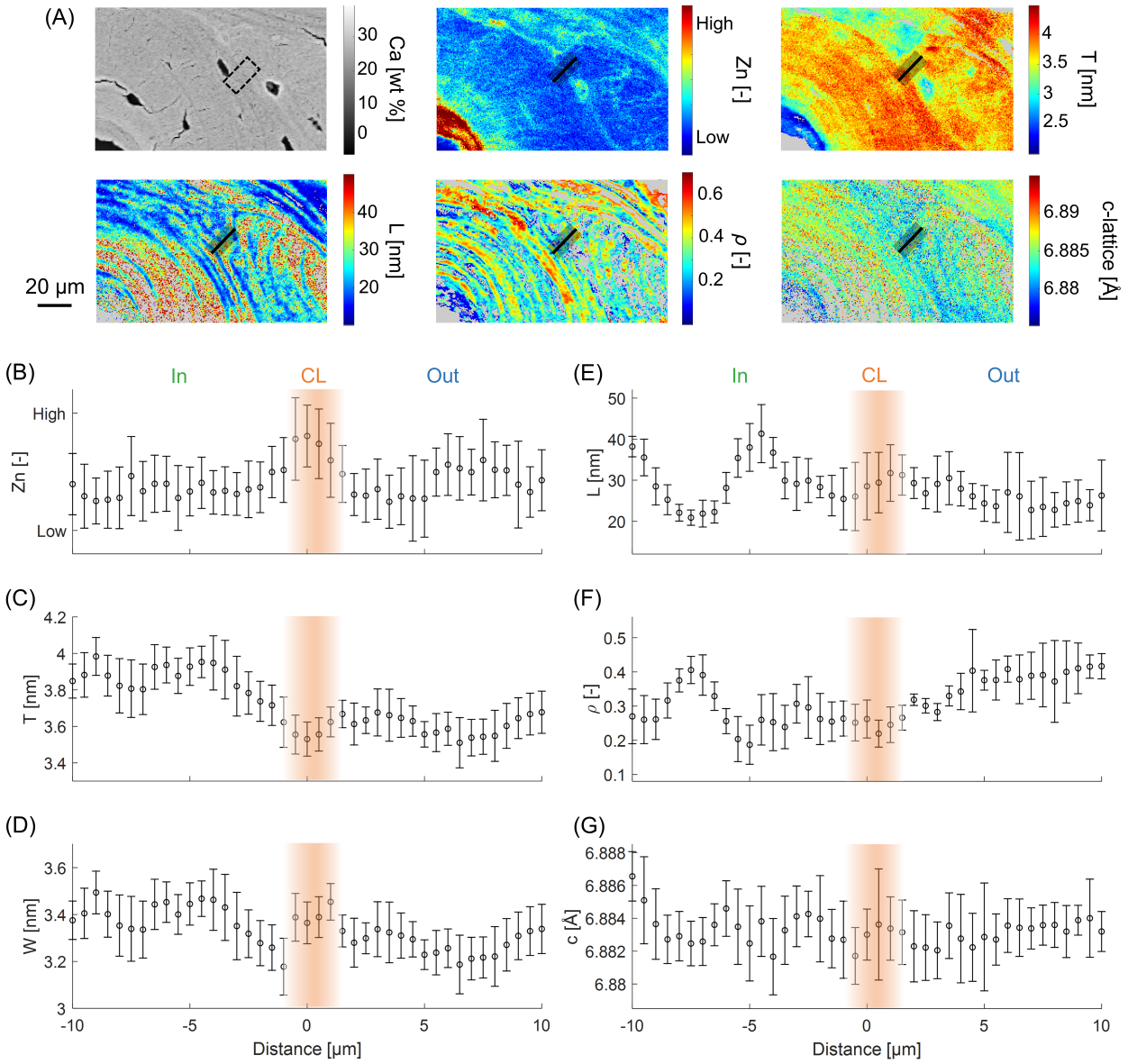


Figure S9: (A) 2D high resolution maps of mineral particle characteristics in Os4. Highlighted in the maps is the location across the CL where data is extracted and analyzed. Profile plots of (B) Zinc content and (C-G) particle properties plotted as a function of the distance from the CL (highlighted by the shaded area). Negative values correspond to regions inside the osteon and positive values outside. To reduce noise, at each position data are averaged over 20 pixels and displayed as mean values ± standard deviations.

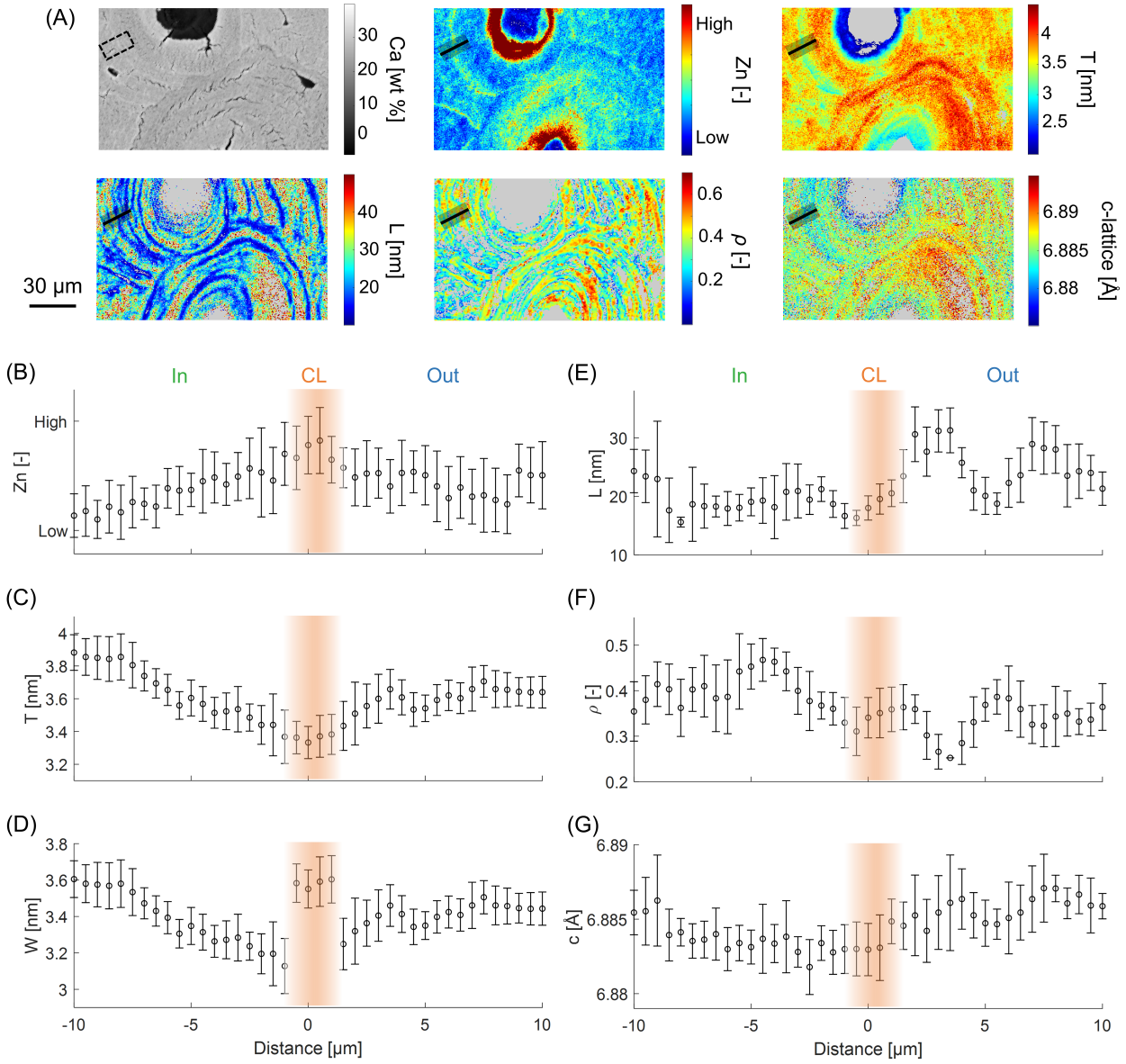


Figure S10: (A) 2D high resolution maps of mineral particle characteristics in Os6. Highlighted in the maps is the location across the CL where data is extracted and analyzed. Profile plots of (B) Zinc content and (C-G) particle properties plotted as a function of the distance from the CL (highlighted by the shaded area). Negative values correspond to regions inside the osteon and positive values outside. To reduce noise, at each position data are averaged over 20 pixels and displayed as mean values ± standard deviations.

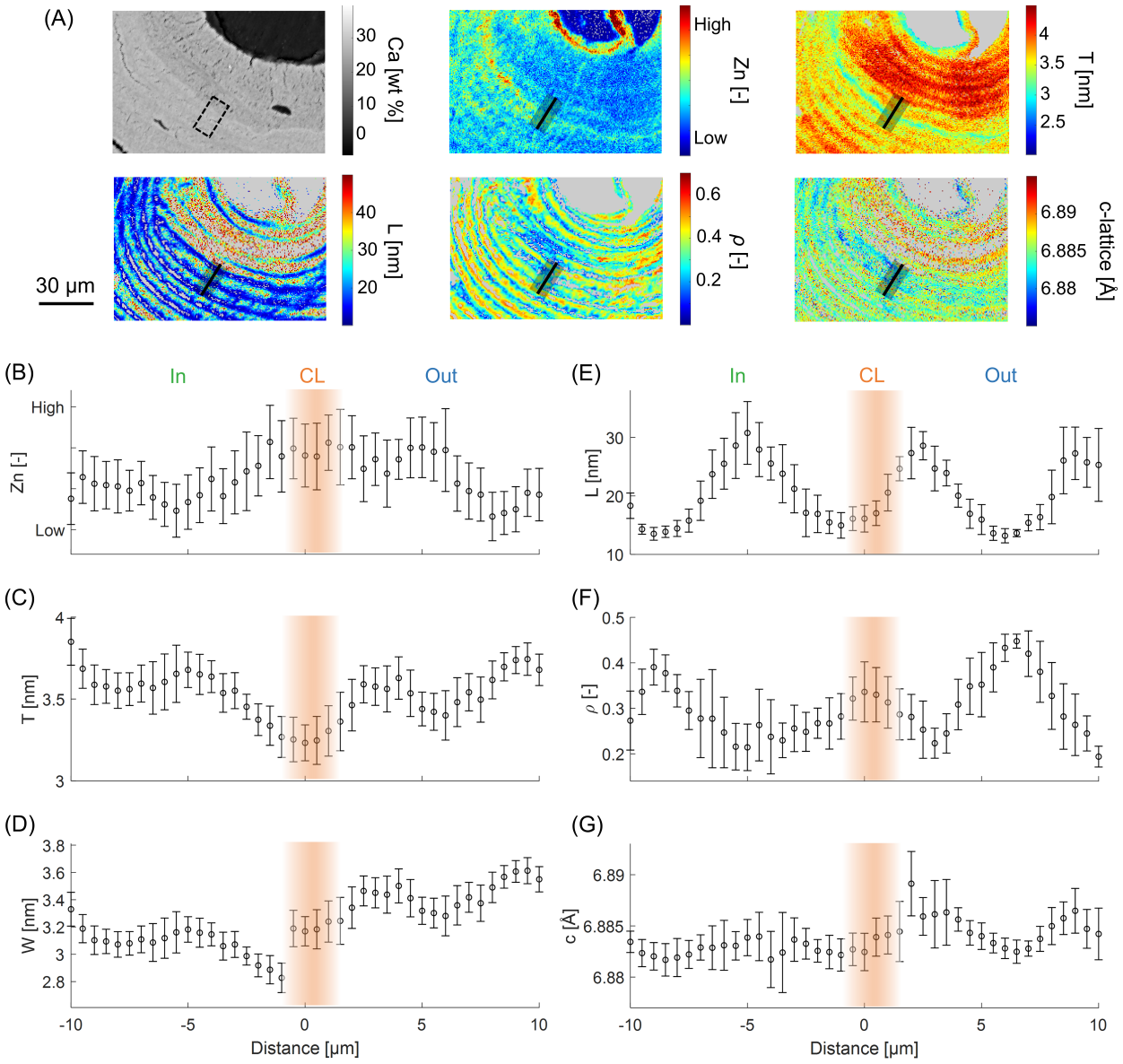


Figure S11: (A) 2D high resolution maps of mineral particle characteristics in Os2. Highlighted in the maps is the location across the CL where data is extracted and analyzed. Profile plots of (B) Zinc content and (C-G) particle properties plotted as a function of the distance from the CL (highlighted by the shaded area). Negative values correspond to regions inside the osteon and positive values outside. To reduce noise, at each position data are averaged over 20 pixels and displayed as mean values ± standard deviations.

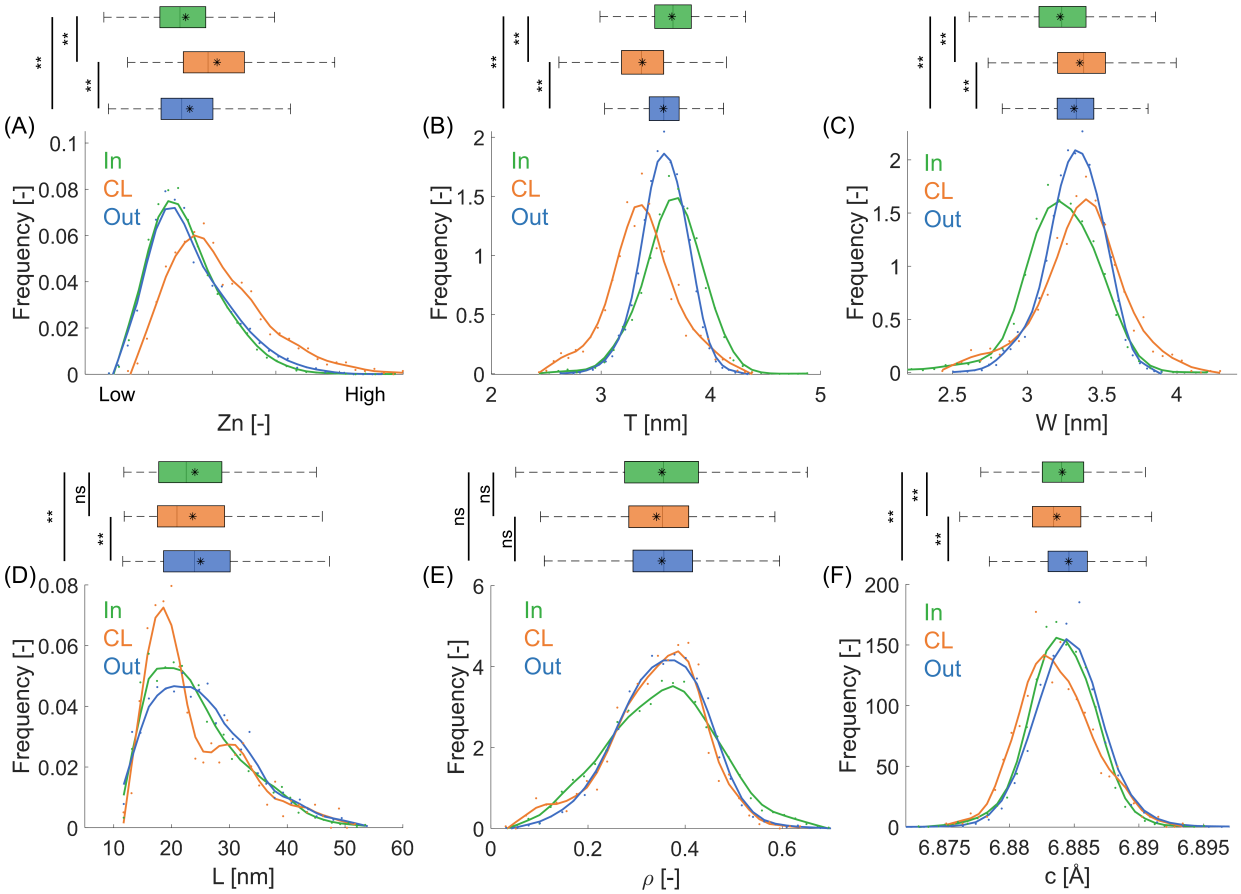


Figure S12: Frequency distributions and boxplot representations of (A) zinc intensity Zn, (B) uncorrected particle thickness T, (C) mineral content corrected particle thickness W, (D) particle length L, (E) degree of alignment ρ, (F) lattice expansion *c-lattice*. All parameters were calculated in the three entire regions from the profile lines: inner osteon (In), cement line (CL) and outer bone (Out). Original data represented as scattered points and smoothed data (loess) as full lines. Boxes range from the 25th to the 75th percentiles, the median and mean values are indicated by a vertical line and an asterisk, respectively. Whiskers show the range of data, reaching from the 5th to the 95th percentile. Statistical significance between the data sets is indicated as follows: *p < 0.05, **p < 0.01, and ns (not significant).

Supplementary note 4.1: Staggered-model

Assuming a staggered mineral composite model as proposed by Jäger and Fratzl [41], in which elastic-brittle mineral crystals are glued together by a ductile elasto-plastic protein matrix [2], the elastic modulus of the composite E_C can be expressed as:

$$E_C = \phi \frac{E_m}{K} + (1-\phi) E_p \tag{4.1}$$

$$\text{with} \quad K = 1 + \frac{1-\phi}{\phi} \frac{4}{\varrho^2} \frac{E_m}{G_p} \tag{4.2}$$

where $E_m = 100$ GPa is the tensile modulus of HAP, $\varrho = \frac{L}{W}$ is the aspect ratio of the mineral particles, ϕ is the mineral volume fraction, and $G_p = 1$ GPa and $E_p = 1$ GPa are the shear and tensile moduli of the organic matrix. The mineral platelet aspect ratio ϱ considered here are 7, 8, and 9, and the mineral

volume fraction ϕ is taken between 0.4 and 0.5 to reflect our experimental data.

The model further assumes that beyond a critical shear stress τ_p^*, the protein matrix flows plastically. In the staggered arrangement, the stress on the mineral particles σ_m and the shear stress inside the protein matrix τ_p are related by:

$$\tau_p = \frac{2}{\varrho}\sigma_m \tag{4.3}$$

Therefore, if τ_p^* is smaller than the fracture stress of the brittle mineral σ_m^f, the matrix will yield before the mineral crystals fail. Here, we assumed $\sigma_m^f = 100$ MPa and $\tau_p^* = G_p\eta_p^y$ with $\eta_p^y = 0.8\%$ being the critical yield shear strain at which plastic flow initiates in the matrix, likely corresponding to the breaking of ionic bonds [2].

The composite strength is defined as the maximum stress σ_C^{max} reached at the end of the elastic regime, just before matrix yielding. This can be computed as [71]:

$$\sigma_C^{max} = E_c\varepsilon_C = E_m\varepsilon_m = E_C\frac{K\varrho}{2E_m}\tau_p^* \tag{4.4}$$

Supplementary note 4.2: Damage simulations

We used a damage-based computational model [82] to investigate the assumed ability of the CL to protect the osteon. We chose a simplified 2D rectangular geometry (150 × 220 μm) featuring a central Haversian canal, a homogeneous osteon bordered by a CL and surrounded by interstitial bone. The radii for the Haversian canal and osteon are set to 25 μm and 100 μm respectively, with a CL having a thickness of 2 μm. A ductile damage plasticity approach is used, including two main steps: damage initiation and damage evolution [82]. Damage begins once the material has undergone enough plastic deformation defined by an incremental fracture strain parameter. From that point on, the damage increases linearly as the material keeps deforming. The evolution of damage is controlled by another key parameter, the fracture energy (0.01 J/m^2 corresponding to a brittle behavior), which represents the energy absorbed as the material breaks down. Reference average material properties for the osteon and interstitial bone are taken from Razi et al. [82], with the two tissues are considered homogenous. The properties of the CL are varied by proportionally adjusting (increasing or decreasing) Young's modulus and yield stress (by the same factor) [94]. Firstly, we considered osteon and interstitial bone having the same material behavior. Then, the properties of the osteon are varied using the same rescaling approach adopted for the CL. The simulations are carried out using an explicit solver. The mesh includes around 129000 four-node plane stress elements, having a size of 0.5 μm. A lateral notch corresponding to 20% of the sample width is introduced by disconnecting two adjacent rows of elements, positioned at 75% of the osteon radius along the vertical axis. A vertical displacement of 2 mm/s is applied on the top side nodes, while the bottom nodes are fixed. Additionally, both top and bottom nodes are restrained from moving horizontally.

Our results show that the required contrast in CL properties relative to the osteon and interstitial bone must be to very large to enable protective mechanisms. Specifically, an increase of 2.75 or a decrease of 3 is needed to trigger crack deflection or trapping, respectively. Allowing also the properties of the osteon to vary, some additional trends are highlighted. In case of a stiffer CL, crack deflection is more easily achieved if the osteon is either softer or stiffer relative to the interstitial tissue. Considering a softer CL, a distinct pattern is observed: lowering the stiffness of the osteon weakens the CL effectiveness in trapping the crack. On the other hand, increasing osteon stiffness enhances the CL ability to capture the crack, even when the CL had low mechanical contrast.

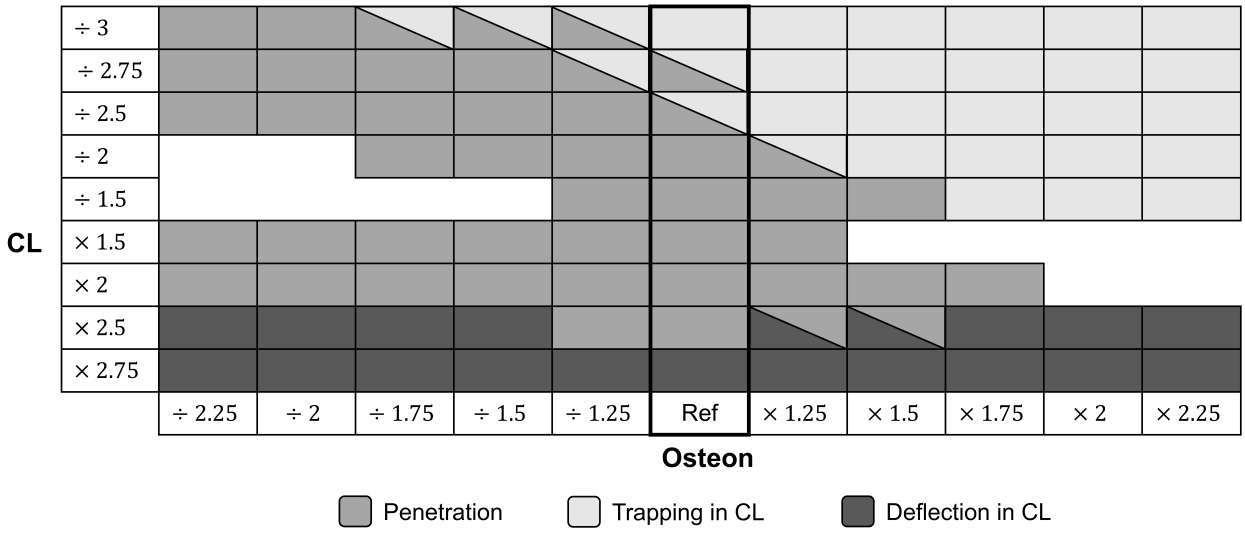


Figure S13: Summary table of damage outcomes as a function of mechanical contrast between the CL, the osteon, and the interstitial bone. Each cell in the table represents a simulation result, with varying mechanical properties for the CL (vertical axis) and the osteon (horizontal axis) based on a reference value (interstitial bone). Color code indicates the observed damage pattern: Gray for full penetration into the osteon, light grey for damage trapping in the CL, and dark grey for deflection along the CL border.

Bibliography

[1] JD Currey. *Bones: Structure and Mechanics*. Princeton University Press, 2002.

[2] P Fratzl and R Weinkamer. Nature's hierarchical materials. *Progress in Materials Science*, 52(8):1263–1334, November 2007.

[3] AR Studart. Biological and Bioinspired Composites with Spatially Tunable Heterogeneous Architectures. *Advanced Functional Materials*, 23(36):4423–4436, September 2013.

[4] W Wagermaier, K Klaushofer, and P Fratzl. Fragility of bone material controlled by internal interfaces. *Calcified Tissue International*, 97(3):201–212, September 2015.

[5] EA Zimmermann and RO Ritchie. Bone as a structural material. *Advanced Healthcare Materials*, 4(9):1287–1304, June 2015.

[6] R Weinkamer and P Fratzl. Solving conflicting functional requirements by hierarchical structuring—Examples from biological materials. *MRS Bulletin*, 41(09):667–671, September 2016.

[7] JWC Dunlop, R Weinkamer, and P Fratzl. Artful interfaces within biological materials. *Materials Today*, 14(3):70–78, March 2011.

[8] E Beniash, CA Stifler, CY Sun, GS Jung, Z Qin, MJ Buehler, and PUPA Gilbert. The hidden structure of human enamel. *Nature Communications*, 10(1):4383, September 2019.

[9] HS Gupta, J Seto, W Wagermaier, P Zaslansky, P Boesecke, and P Fratzl. Cooperative deformation of mineral and collagen in bone at the nanoscale. *Proceedings of the National Academy of Sciences*, 103(47):17741–17746, November 2006.

[10] GE Fantner, T Hassenkam, JH Kindt, JC Weaver, H Birkedal, L Pechenik, JA Cutroni, GAG Cidade, GD Stucky, DE Morse, and PK Hansma. Sacrificial bonds and hidden length dissipate energy as mineralized fibrils separate during bone fracture. *Nature Materials*, 4(8):612–616, August 2005.

[11] S Weiner and HD Wagner. The Material Bone: Structure-Mechanical Function Relations. *Annual Review of Materials Science*, 28(1):271–298, August 1998.

[12] W Wagermaier, HS Gupta, A Gourrier, M Burghammer, P Roschger, and P Fratzl. Spiral twisting of fiber orientation inside bone lamellae. *Biointerphases*, 1(1):1–5, March 2006.

[13] N Reznikov, R Shahar, and S Weiner. Bone hierarchical structure in three dimensions. *Acta Biomaterialia*, 10(9):3815–3826, September 2014.

[14] N Reznikov, R Shahar, and S Weiner. Three-dimensional structure of human lamellar bone: The presence of two different materials and new insights into the hierarchical organization. *Bone*, 59:93–104, February 2014.

[15] P Fratzl, HS Gupta, FD Fischer, and O Kolednik. Hindered Crack Propagation in Materials with Periodically Varying Young's Modulus—Lessons from Biological Materials. *Advanced Materials*, 19(18):2657–2661, September 2007.

[16] H Peterlik, P Roschger, K Klaushofer, and P Fratzl. From brittle to ductile fracture of bone. *Nature Materials*, 5(1):52–55, January 2006.

[17] S Weiner, W Traub, and HD Wagner. Lamellar Bone: Structure–Function Relations. *Journal of Structural Biology*, 126(3):241–255, June 1999.

[18] R Shahar and S Weiner. Open questions on the 3D structures of collagen containing vertebrate mineralized tissues: a perspective. *Journal of Structural Biology*, 201(3):187–198, March 2018.

[19] MD McKee and A Nanci. Osteopontin and the bone remodeling sequence: colloidal-gold immunocytochemistry of an interfacial extracellular matrix protein. *Annals of the New York Academy of Sciences*, 760(1):177–189, August 1995.

[20] NE Lassen, TL Andersen, GG Pløen, K Søe, EM Hauge, S Harving, GET Eschen, and JM Delaisse. Coupling of bone resorption and formation in real time: new knowledge gained from human haversian BMUs. *Journal of Bone and Mineral Research*, 32(7):1395–1405, July 2017.

[21] NA Sims. Osteoclast-derived coupling factors: Origins and state-of-play Louis V Avioli lecture, ASBMR 2023. *Journal of Bone and Mineral Research*, 39(10):1377–1385, September 2024.

[22] MD McKee and A Nanci. Osteopontin at mineralized tissue interfaces in bone, teeth, and osseointegrated implants: ultrastructural distribution and implications for mineralized tissue formation, turnover, and repair. *Microscopy Research and Technique*, 33(2):141–164, February 1996.

[23] A Cantamessa, S Blouin, M Rummler, A Berzlanovich, R Weinkamer, MA Hartmann, and D Ruffoni. The mineralization of osteonal cement line depends on where the osteon is formed, October 2024. Manuscript under review in JBMR Plus.

[24] P Milovanovic, A vom Scheidt, K Mletzko, G Sarau, K Püschel, M Djuric, M Amling, S Christiansen, and B Busse. Bone tissue aging affects mineralization of cement lines. *Bone*, 110:187–193, May 2018.

[25] JG Skedros, JL Holmes, EG Vajda, and RD Bloebaum. Cement lines of secondary osteons in human bone are not mineral-deficient: new data in a historical perspective. *The Anatomical Record Part A: Discoveries in Molecular, Cellular, and Evolutionary Biology*, 286A(1):781–803, September 2005.

[26] TA Grünewald, A Johannes, NK Wittig, J Palle, A Rack, M Burghammer, and H Birkedal. Bone mineral properties and 3D orientation of human lamellar bone around cement lines and the haversian system. *IUCrJ*, 10(2):189–198, March 2023.

[27] M Kerschnitzki, W Wagermaier, P Roschger, J Seto, R Shahar, GN Duda, S Mundlos, and P Fratzl. The organization of the osteocyte network mirrors the extracellular matrix orientation in bone. *Journal of Structural Biology*, 173(2):303–311, February 2011.

[28] S Qiu, D Sudhaker Rao, DP Fyhrie, S Palnitkar, and AM Parfitt. The morphological association between microcracks and osteocyte lacunae in human cortical bone. *Bone*, 37(1):10–15, July 2005.

[29] R Gauthier, H Follet, C Olivier, D Mitton, and F Peyrin. 3D analysis of the osteonal and interstitial tissue in human radii cortical bone. *Bone*, 127:526–536, October 2019.

[30] RK Nalla, JJ Kruzic, JH Kinney, and RO Ritchie. Mechanistic aspects of fracture and R-curve behavior in human cortical bone. *Biomaterials*, 26(2):217–231, January 2005.

[31] S Mohsin, FJ O'Brien, and TC Lee. Osteonal crack barriers in ovine compact bone. *Journal of Anatomy*, 208(1):81–89, January 2006.

[32] KJ Koester, JW Ager, and RO Ritchie. The true toughness of human cortical bone measured with realistically short cracks. *Nature Materials*, 7(8):672–677, August 2008.

[33] D Hull and TW Clyne. *An Introduction to Composite Materials*. Cambridge Solid State Science Series. Cambridge University Press, Cambridge, 2 edition, 1996.

[34] L Vergani, C Colombo, and F Libonati. Crack propagation in cortical bone: a numerical study. *Procedia Materials Science*, 3:1524–1529, 2014.

[35] A Gustafsson, M Wallin, H Khayyeri, and H Isaksson. Crack propagation in cortical bone is affected by the characteristics of the cement line: a parameter study using an XFEM interface damage model. *Biomechanics and Modeling in Mechanobiology*, 18(4):1247–1261, August 2019.

[36] E Giner, R Belda, C Arango, A Vercher-Martínez, JE Tarancón, and FJ Fuenmayor. Calculation of the critical energy release rate G c of the cement line in cortical bone combining experimental tests and finite element models. *Engineering Fracture Mechanics*, 184:168–182, October 2017.

[37] S Nobakhti, G Limbert, and PJ Thurner. Cement lines and interlamellar areas in compact bone as strain amplifiers – Contributors to elasticity, fracture toughness and mechanotransduction. *Journal of the Mechanical Behavior of Biomedical Materials*, 29:235–251, January 2014.

[38] T Montalbano and G Feng. Nanoindentation characterization of the cement lines in ovine and bovine femurs. *Journal of Materials Research*, 26(8):1036–1041, April 2011.

[39] Y Zhou, MJ Kastner, TB Tighe, and J Du. Elastic modulus mapping for bovine cortical bone from submillimeter- to submicron-scales using peakforce tapping atomic force microscopy. *Extreme Mechanics Letters*, 41:101031, November 2020.

[40] HS Gupta, S Schratter, W Tesch, P Roschger, A Berzlanovich, T Schoeberl, K Klaushofer, and P Fratzl. Two different correlations between nanoindentation modulus and mineral content in the bone–cartilage interface. *Journal of Structural Biology*, 149(2):138–148, February 2005.

[41] I Jäger and P Fratzl. Mineralized Collagen Fibrils: A Mechanical Model with a Staggered Arrangement of Mineral Particles. *Biophysical Journal*, 79(4):1737–1746, October 2000.

[42] T Tang, W Landis, S Blouin, L Bertinetti, MA Hartmann, A Berzlanovich, R Weinkamer, W Wagermaier, and P Fratzl. Subcanalicular nanochannel volume is inversely correlated with calcium content in human cortical bone. *Journal of Bone and Mineral Research*, 38(2):313–325, December 2022.

[43] P Roschger, P Fratzl, J Eschberger, and K Klaushofer. Validation of quantitative backscattered electron imaging for the measurement of mineral density distribution in human bone biopsies. *Bone*, 23(4):319–326, October 1998.

[44] P Roschger, J Eschberger, and HJr Plenk. Formation of ultracracks in methacrylate-embedded undecalcified bone samples by exposure to aqueous solutions. *Cells and materials*, 3:3, 1993.

[45] P Roschger, EP Paschalis, P Fratzl, and K Klaushofer. Bone mineralization density distribution in health and disease. *Bone*, 42(3):456–466, March 2008.

[46] C Lukas, P Kollmannsberger, D Ruffoni, P Roschger, P Fratzl, and R Weinkamer. The heterogeneous mineral content of bone – Using stochastic arguments and simulations to overcome experimental limitations. *Journal of Statistical Physics*, 144(2):316–331, July 2011.

[47] MA Hartmann, S Blouin, BM Misof, N Fratzl-Zelman, P Roschger, A Berzlanovich, GM Gruber, PC Brugger, J Zwerina, and P Fratzl. Quantitative backscattered electron imaging of bone using a thermionic or a field emission electron source. *Calcified Tissue International*, 109(2):190–202, August 2021.

[48] SE Campbell, VL Ferguson, and DC Hurley. Nanomechanical mapping of the osteochondral interface with contact resonance force microscopy and nanoindentation. *Acta Biomaterialia*, 8(12):4389–4396, December 2012.

[49] E Donnelly, SP Baker, and AL Boskey. Effects of surface roughness and maximum load on the mechanical properties of cancellous bone measured by nanoindentation. *Journal of Biomedical Materials Research Part A*, 2006.

[50] MS Bobji and SK Biswas. Estimation of hardness by nanoindentation of rough surfaces. *Journal of Materials Research*, 13(11):3227–3233, November 1998.

[51] WC Oliver and GM Pharr. An improved technique for determining hardness and elastic modulus using load and displacement sensing indentation experiments. *Journal of Materials Research*, 7(6):1564–1583, June 1992.

[52] X Chen, O Nadiarynkh, S Plotnikov, and PJ Campagnola. Second harmonic generation microscopy for quantitative analysis of collagen fibrillar structure. *Nature Protocols*, 7(4):654–669, April 2012.

[53] G Benecke, W Wagermaier, C Li, M Schwartzkopf, G Flucke, R Hoerth, I Zizak, M Burghammer, E Metwalli, P Müller-Buschbaum, M Trebbin, S Förster, O Paris, SV Roth, and P Fratzl. A customizable software for fast reduction and analysis of large X-ray scattering data sets: applications of the new *DPDAK* package to small-angle X-ray scattering and grazing-incidence small-angle X-ray scattering. *Journal of Applied Crystallography*, 47(5):1797–1803, October 2014.

[54] S Pabisch, W Wagermaier, T Zander, C Li, and P Fratzl. Imaging the nanostructure of bone and dentin through small- and wide-angle X-ray scattering. In *Methods in Enzymology*, volume 532, pages 391–413. Elsevier, 2013.

[55] P Fratzl, S Schreiber, and K Klaushofer. Bone Mineralization as Studied by Small-Angle X-Ray Scattering. *Connective Tissue Research*, 34(4):247–254, January 1996.

[56] P Fratzl, HS Gupta, EP Paschalis, and P Roschger. Structure and mechanical quality of the collagen–mineral nano-composite in bone. *J. Mater. Chem.*, 14(14):2115–2123, 2004.

[57] P Fratzl. Statistical model of the habit and arrangement of mineral crystals in the collagen of bone. *Journal of Statistical Physics*, 77(1-2):125–143, October 1994.

[58] I Zizak, P Roschger, O Paris, B.M Misof, A Berzlanovich, S Bernstorff, H Amenitsch, K Klaushofer, and P Fratzl. Characteristics of mineral particles in the human bone/cartilage interface. *Journal of Structural Biology*, 141(3):208–217, March 2003.

[59] SN Danilchenko, OG Kukharenko, C Moseke, I Yu Protsenko, LF Sukhodub, and B Sulkio-Cleff. Determination of the bone mineral crystallite size and lattice strain from diffraction line broadening. *Crystal Research and Technology*, 37(11):1234–1240, November 2002.

[60] RG Handschin and WB Stern. X-ray diffraction studies on the lattice perfection of human bone apatite (Crista Iliaca). *Bone*, 16(4), April 1995.

[61] S Rinnerthaler, P Roschger, HF Jakob, A Nader, K Klaushofer, and P Fratzl. Scanning small angle X-ray scattering analysis of human bone sections. *Calcified Tissue International*, 64(5):422–429, May 1999.

[62] A Roschger, W Wagermaier, S Gamsjaeger, N Hassler, I Schmidt, S Blouin, A Berzlanovich, GM Gruber, R Weinkamer, P Roschger, EP Paschalis, K Klaushofer, and P Fratzl. Newly formed and remodeled human bone exhibits differences in the mineralization process. *Acta Biomaterialia*, 104:221–230, March 2020.

[63] B Pemmer, A Roschger, A Wastl, JG Hofstaetter, P Wobrauschek, R Simon, HW Thaler, P Roschger, K Klaushofer, and C Streli. Spatial distribution of the trace elements zinc, strontium and lead in human bone tissue. *Bone*, 57(1):184–193, November 2013.

[64] M Granke, A Gourrier, F Rupin, K Raum, F Peyrin, M Burghammer, A Saïed, and P Laugier. Microfibril orientation dominates the microelastic properties of human bone tissue at the lamellar length scale. *PLoS ONE*, 8(3):e58043, March 2013.

[65] J Xu, JY Rho, SR Mishra, and Z Fan. Atomic force microscopy and nanoindentation characterization of human lamellar bone prepared by microtome sectioning and mechanical polishing technique. *Journal of Biomedical Materials Research Part A*, 67A(3):719–726, December 2003.

[66] S Hengsberger, A Kulik, and P Zysset. Nanoindentation discriminates the elastic properties of individual human bone lamellae under dry and physiological conditions. *Bone*, 30(1):178–184, January 2002.

[67] D Carnelli, P Vena, M Dao, C Ortiz, and R Contro. Orientation and size-dependent mechanical modulation within individual secondary osteons in cortical bone tissue. *Journal of The Royal Society Interface*, 10(81):20120953, April 2013.

[68] M Conward and J Samuel. Machining characteristics of the haversian and plexiform components of bovine cortical bone. *Journal of the Mechanical Behavior of Biomedical Materials*, 60:525–534, July 2016.

[69] P Varga, A Pacureanu, M Langer, H Suhonen, B Hesse, Q Grimal, P Cloetens, K Raum, and F Peyrin. Investigation of the three-dimensional orientation of mineralized collagen fibrils in human lamellar bone using synchrotron X-ray phase nano-tomography. *Acta Biomaterialia*, 9(9):8118–8127, September 2013.

[70] E Raguin, K Rechav, R Shahar, and S Weiner. Focused ion beam-SEM 3D analysis of mineralized osteonal bone: lamellae and cement sheath structures. *Acta Biomaterialia*, 121:497–513, February 2021.

[71] A Tits, S Blouin, M Rummler, JF Kaux, P Drion, HG Van Lenthe, R Weinkamer, MA Hartmann, and D Ruffoni. Structural and functional heterogeneity of mineralized fibrocartilage at the Achilles tendon-bone insertion. *Acta Biomaterialia*, 166:409–418, August 2023.

[72] Y Bala, D Farlay, PD Delmas, PJ Meunier, and G Boivin. Time sequence of secondary mineralization and microhardness in cortical and cancellous bone from ewes. *Bone*, 46(4):1204–1212, April 2010.

[73] N Reznikov, JAM Steele, P Fratzl, and MM Stevens. A materials science vision of extracellular matrix mineralization. *Nature Reviews Materials*, 1(8):16041, June 2016.

[74] NA Sims and TJ Martin. Coupling the activities of bone formation and resorption: a multitude of signals within the basic multicellular unit. *BoneKEy Reports*, 3, January 2014.

[75] AA Poundarik, A Boskey, C Gundberg, and D Vashishth. Biomolecular regulation, composition and nanoarchitecture of bone mineral. *Scientific Reports*, 8(1):1191, January 2018.

[76] V Schemenz, E Scoppola, P Zaslansky, and P Fratzl. Bone strength and residual compressive stress in apatite crystals. *Journal of Structural Biology*, 216(4):108141, December 2024.

[77] B Bar-On and HD Wagner. New insights into the Young's modulus of staggered biological composites. *Materials Science and Engineering: C*, 33(2):603–607, March 2013.

[78] TJ Vaughan, CT McCarthy, and LM McNamara. A three-scale finite element investigation into the effects of tissue mineralisation and lamellar organisation in human cortical and trabecular bone. *Journal of the Mechanical Behavior of Biomedical Materials*, 12:50–62, August 2012.

[79] S Zhang, FL Bach-Gansmo, D Xia, F Besenbacher, H Birkedal, and M Dong. Nanostructure and mechanical properties of the osteocyte lacunar-canalicular network-associated bone matrix revealed by quantitative nanomechanical mapping. *Nano Research*, 8(10):3250–3260, October 2015.

[80] CW McCutchen. Do mineral crystals stiffen bone by straitjacketing its collagen? *Journal of Theoretical Biology*, 51(1):51–58, May 1975.

[81] JS Yerramshetty and O Akkus. The associations between mineral crystallinity and the mechanical properties of human cortical bone. *Bone*, 42(3):476–482, March 2008.

[82] H Razi, J Predan, FD Fischer, O Kolednik, and P Fratzl. Damage tolerance of lamellar bone. *Bone*, 130:115102, January 2020.

[83] M Wang, S Li, A vom Scheidt, M Qwamizadeh, B Busse, and VV Silberschmidt. Numerical study of crack initiation and growth in human cortical bone: effect of micro-morphology. *Engineering Fracture Mechanics*, 232:107051, June 2020.

[84] S Li, A Abdel-Wahab, E Demirci, and VV Silberschmidt. Fracture process in cortical bone: X-FEM analysis of microstructured models. *International Journal of Fracture*, 184(1-2):43–55, November 2013.

[85] J Jonvaux, T Hoc, and É Budyn. Analysis of micro fracture in human Haversian cortical bone under compression. *International Journal for Numerical Methods in Biomedical Engineering*, 28(9):974–998, September 2012.

[86] FJ O'Brien, D Taylor, and TC Lee. The effect of bone microstructure on the initiation and growth of microcracks. *Journal of Orthopaedic Research*, 23(2):475–480, March 2005.

[87] NA Yaraghi, N Guarín-Zapata, LK Grunenfelder, E Hintsala, S Bhowmick, JM Hiller, M Betts, EL Principe, JY Jung, L Sheppard, R Wuhrer, J McKittrick, PD Zavattieri, and D Kisailus. A Sinusoidally Architected Helicoidal Biocomposite. *Advanced Materials*, 28(32):6835–6844, August 2016.

[88] JC Weaver, GW Milliron, A Miserez, K Evans-Lutterodt, S Herrera, I Gallana, WJ Mershon, B Swanson, P Zavattieri, E DiMasi, and D Kisailus. The Stomatopod Dactyl Club: A Formidable Damage-Tolerant Biological Hammer. *Science*, 336(6086):1275–1280, June 2012.

[89] Y Delaunois, A Tits, Q Grossman, S Smeets, C Malherbe, G Eppe, GH Van Lenthe, D Ruffoni, and P Compère. Design strategies of the mantis shrimp spike: How the crustacean cuticle became a remarkable biological harpoon. *Natural Sciences*, 3(3):e20220060, July 2023.

[90] HS Gupta, U Stachewicz, W Wagermaier, P Roschger, HD Wagner, and P Fratzl. Mechanical modulation at the lamellar level in osteonal bone. *Journal of Materials Research*, 21(8):1913–1921, August 2006.

[91] KE Stockhausen, M Qwamizadeh, EM Wölfel, H Hemmatian, IAK Fiedler, S Flenner, E Longo, M Amling, I Greving, RO Ritchie, FN Schmidt, and B Busse. Collagen fiber orientation is coupled with specific nano-compositional patterns in *dark* and *bright* osteons modulating their biomechanical properties. *ACS Nano*, 15(1):455–467, January 2021.

[92] M Granke, MD Does, and JS Nyman. The Role of Water Compartments in the Material Properties of Cortical Bone. *Calcified Tissue International*, 97(3):292–307, September 2015.

[93] AJ Bushby, VL Ferguson, and A Boyde. Nanoindentation of bone: Comparison of specimens tested in liquid and embedded in polymethylmethacrylate. *J. Mater. Res.*, 19(1), 2004.

[94] T Volders, L Zorzetto, H Razi, R Weinkamer, and D Ruffoni. Designing architectured materials with tunable damaging inspired by osteonal bone. Manuscript in preparation, 2025.

5

Canalicular crossings across the cement line are sparse but functional

Adapted from: Astrid Cantamessa[1], Lena Demeuldre[1], Stéphane Blouin[2], Alexandra Tits[3], Andrea Berzlanovich[4], Richard Weinkamer[3], Markus A. Hartmann[2], Davide Ruffoni[1], Canalicular crossings across the cement line are sparse but functional, to be finalized and submitted to *Journal of Structural Biology*.

[1] Mechanics of Biological and Bioinspired Materials Laboratory, Department of Aerospace and Mechanical Engineering, University of Liège, Liège, Belgium;

[2] Ludwig Boltzmann Institute of Osteology at Hanusch Hospital of OEGK and AUVA Trauma Centre Meidling, 1st Medical Department Hanusch Hospital, Vienna, Austria;

[3] Department of Biomaterials, Max Planck Institute of Colloids and Interfaces, Potsdam, Germany;

[4] Center of Forensics Medicine, Vienna, Austria.

Keywords

Cement line, osteocyte lacuna-canalicular network, lacuna, canalicular density, canalicular orientation, network analysis, confocal microscopy, mechanobiology, osteon.

Abstract

The osteocyte lacuno-canalicular network (OLCN) plays a central role in the transport of matter and information and it is therefore essential for bone remodeling, mechanosensation, communication and mineralization. While the OCLN inside osteons has been attracted considerable attention, the structural integrity of the OLCN near tissue interfaces such as the cement line (CL), which separates newly formed osteons from older bone, remains under investigated and debated. In this study, we used confocal laser scanning microscopy to characterize the 3D architecture of the OLCN in human osteonal bone, with a focus on the osteon periphery and the possible ability of canaliculi to cross the CL. Our results show that although canaliculi crossings at the CL are relatively sparse (around 3.6% of the total number of canaliculi found in the periphery of the osteon), they are sufficient to establish functional connections between lacunae, with roughly 36% of peripheral lacunae inside the osteon connected to lacunae sitting in the external bone. These connections may be essential for maintaining communication and material

exchange between adjacent osteons and, perhaps even most important, between osteons and interstitial bone. We also observe that the OCLN at the periphery of the osteon has some specific features: lacunar density is higher, particularly near the CL, probably reflecting a higher activity of the osteoblasts and perhaps a strategic positioning of cells to enable some degree of communication with the outer bone. Canaliculi near the CL exhibit a lateral orientation while in the osteons they are oriented radially. At the same time, canalicular density decreases from the Haversian canal toward the CL, with the network becoming sparser and less interconnected, possibly due to partial disruption at the boundary. Finally, we identified network-free zones, especially in interstitial bone, often associated with hypermineralized lacunae, which may impact bone quality. This work highlights the spatial heterogeneity and functionality of the OLCN, showing that even limited canalicular crossings can sustain osteocyte network function across the CL. These insights may be critical for understanding age-related changes in bone quality and the possible role of structural interfaces in skeletal health.

5.1 Introduction

Bone is a dynamic tissue that continuously adapts to mechanical and metabolic demands thanks to bone remodeling. During this biological process, old or damaged bone is replaced with new tissue [1, 2]. Remodeling maintains the mechanical integrity of our bones and regulates calcium homeostasis [3]. This process is orchestrated by osteoclasts, which mediate bone resorption; osteoblasts, which form new bone; and osteocytes, which regulate remodeling by sensing mechanical stimuli and coordinating cellular responses [4]. Osteocytes are buried into the mineralized bone matrix, where they occupy holes called lacunae and extend their dendritic processes through small channels called canaliculi, forming the so-called osteocyte lacuno-canalicular network (OLCN) [5, 6]. This 3D network is essential for cell communication and metabolic functions [2, 7], mechanosensation [8, 9, 10], and even mineralization [11].

In osteons, bone remodeling occurs within basic multicellular units (BMUs), where bone resorption, reversal, and formation take place following a well-organized sequence [4, 12]. Osteoclasts first excavate a tunnel ($\approx$20-40 μm/day) [2], followed by a reversal phase where the surface is probably cleaned-up and prepared for osteoblast activity [2]. Osteoblasts then deposit osteoid (unmineralized bone matrix) at a much slower pace, about 0.5-1 μm/day [13]. During the formation phase, some osteoblasts remain trapped into the collagen matrix and then differentiate into osteocytes. Remodeling allows a continuous renewal of bone: in a typical healthy scenario a new osteon is generated in several months, whereas about 5-10% of cortical bone and up to 20% of trabecular bone are replaced annually [14].

During osteonal remodeling, a specialized interface known as the cement line (CL) is formed on the eroded surface, probably immediately after or even in the course of bone resorption. This interface, rich in osteopontin [15], provides a substrate for subsequent lamellar bone deposition [16], and establishes a defined boundary between the older bone and the newly formed secondary osteon [12, 17, 18]. More than 150 years after its discovery [19], the CL continues to puzzle bone researchers, as highlighted in the

perspective article of Shahar and Weiner [20]. One reason being the tiny dimension of the CL, about 1-2 μm in thickness in transverse sections. Such thickness is only two or three times larger than the spatial resolution of most of the experimental techniques used to characterize the CL, introducing artifacts (partial volume effects) which precludes a clear and unambiguous analysis of this region [21].

Previously, we have investigated the mineral content and the mineralization of the CL. After confirming that the CL is more mineralized than nearby bone, even when considering older interstitial tissue [22], we have highlighted how CL mineralization differs from osteon mineralization. We have also pointed out that CL mineralization is not universal but depends on the region where the CL is formed, suggesting some form of mineral recycling locally [23]. Considering the mechanical properties of the CL, previous works have reported a softer behavior in comparison to bone [24, 25]. Yet, this is in contradiction with the higher mineral content. Following a correlative approach with submicrometer spatial resolution, we have measured mineral content and mechanical properties of the CL at the same locations and we have shown that the CL is stiffer and harder than nearby bone. However, when comparing the two tissues at the same mineral content, we found that the CL needs more mineral than bone to attain a similar stiffness and hardness. A possible reason for such reduced mechanical efficiency lies in the mineral particles, which are thicker but shorter at the CL [26]. While these studies have provided valuable insights into composition and mechanical behavior of the CL, other biological aspects remain unresolved. One topic of high importance for bone (mechano)biology is the interplay between the CL and the OLCN.

The 3D architecture of the OCLN is experimentally accessible with various techniques including confocal laser scanning microscopy (CLSM) on stained samples [16], synchrotron radiation nano-computed tomography (SRnCT) [27] and FIB-SEM [28]. The OCLN in osteons is highly heterogenous, and the presence of large bone regions without any network has been reported [27, 29]. Moreover, there is evidence that the canalicular density, defined as length of the canaliculi in a unit volume, decreases when moving from the Haversian canal towards the CL [29], whereas lacunar density appears higher close to the CL [30]. Considering the specificity of the network at CL, some studies have suggested that the CL disrupts canalicular continuity, acting as a barrier to osteocyte communication across the osteonal border [16, 31]. Others have indicated the presence of canaliculi crossing the CL, suggesting potential paths for inter-osteon communication [32, 33].

To address these uncertainties, using CLSM on human osteonal bone, our study aims to characterize the architecture of the OLCN near the CL, and to evaluate to which extent canaliculi are able to cross the CL and to connect osteocyte lacunae inside the osteon with lacunae sitting outside. We would also like to elucidate the possible impact of tissue age on these aspects.

5.2 Methods

5.2.1 Sample preparation

Two necropsy samples of femoral midshaft were obtained from a 40-year-old and an 81-year-old male donor with no known bone-related disease. The samples were provided by the Department of Forensic Medicine of the Medical University of Vienna, in accordance with the ethical guidelines of the institution (EK no. 1757/2013). Immediately after extraction, the bone specimens were frozen and stored at -20° C until further processing. After thawing, a 1.5-cm-thick transverse section was cut from each femoral shaft, perpendicular to the longitudinal axis and away from the metaphyseal region, using a water-cooled diamond saw (Buehler Isomet 1000, Germany). The samples were then dehydrated, stained with Rhodamine 6G, which is a fluorescent molecule capable of diffusing throughout the entire interconnected OLCN thanks to its small molecular size, and embedded in polymethyl methacrylate (PMMA). This entire procedure followed a previously established protocol [34, 35]. The embedded bones were cut into sections with parallel surfaces, then ground using silicon carbide papers of decreasing grit size (P1200 and P2400). Final polishing was performed using a 1 μm diamond suspension on a silk cloth under glycol irrigation (Logitech PM5, UK), to minimize the formation of microcracks [36].

5.2.2 Quantitative backscattered electron imaging and image processing

Quantitative backscattered electron imaging (qBEI) was used to assess the local mineral content of cortical bone using a well-established technique based on scanning electron microscopy (SEM). By measuring the intensity of the backscattered electron signal, qBEI provides two-dimensional spatial maps of calcium content over large field of views with a micrometer level resolution [34, 37]. To make the sample surface conductive, a thin carbon coating was applied by vacuum evaporation (Agar SEM carbon coater, Agar, Stansted, UK). Imaging was performed using a SEM equipped with a zirconium-coated field emission cathode (Zeiss SEM SUPRA 40, Germany), operated at 20 kV with a working distance of 10 mm and a probe current between 280 – 320 pA. Initial overview scans were acquired at low resolution (1.76 μm/pixel) to identify osteons of interest for further analysis. Fourteen osteons (n = 8 from the adult donor, n = 6 from the older donor), exhibiting varying degrees of mineralization and containing a central round Haversian canal, were selected. High-resolution scans were then acquired with an isotropic pixel size of 0.57 μm and a field of view of 1024 × 768 pixels. The SEM signal was calibrated using carbon and aluminum standards, following a previously described procedure [34, 38] allowing to convert grey values into calcium weight percent (Ca wt %). To quantify the local mineral content from qBEI images, we followed a previously established protocol [23]. Briefly, a two-pixel erosion was applied to reduce boundary artifacts. Non-mineralized background regions including osteocytes lacunae, Haversian canals, and microcracks were excluded from analysis by removing all pixels with calcium content below 5.2 wt % [39]. For the extraction of the CL, a manual contouring strategy was followed: firstly, the inner border between the osteon and the CL was identified based on different grey levels between osteon and CL pixels.

This border was "handpicked" along the entire osteon border. The CL was then extracted by dilating this contour line to reach a thickness of two pixels (or 1.14 μm), resulting in a ring-shaped layer. All image processing steps were performed with the software CTAn (v1.19.4.0, Skyscan, US).

5.2.3 Confocal laser scanning microscopy (CLSM)

The same osteons were also imaged using confocal laser scanning microscopy (CLSM, TCS SP5, Leica , Germany) to visualize the OLCN. Imaging was performed with a 40× oil immersion objective having an aperture of 1.25 (HCX PL APO 40×/1.25), using a 543 nm HeNe laser for Rhodamine 6G excitation. The fluorescence emission was recorded in the 553–706 nm spectral range [8, 35]. The field of view of each scan was 388 x 388 μm^2 (1024 × 1024 pixels) at a lateral resolution of 0.379 μm/pixel. This field of view was usually sufficient to measure the entire osteon. In case the osteon did not fit entirely in the field of view, we gave priority to measure regions including a large portion of the CL. 3D images were obtained by acquiring z-stacks with 0.247 μm axial intervals, covering a depth of approximately 60 μm, limited by the inherent opacity of the mineralized tissue Additionally, image cropping was performed when necessary to exclude regions affected by microcracks with a corresponding high fluorescence signal, which could interfere with the quantification of the OLCN.

5.2.4 Second harmonic generation imaging

Second harmonic generation (SHG) imaging was performed at the same locations previously analyzed with CLSM and qBEI, to visualize the lamellar arrangement of osteonal bone. Imaging was conducted using a confocal laser scanning microscopy (Leica TCS SP8 DLS, Germany) equipped with a 40x oil immersion objective and 1.3 aperture (HC PL APO 40×/1.30 OIL). A pulsed infrared laser (910 nm, Spectra-Physics, Milpitas, US) was used for excitation, and the SHG signal was collected in the backward direction within the 450–460 nm range. Images were acquired with a field of view of 1024 × 1024 pixels and a nominal pixel size of 0.379 μm at a scan rate of 400 Hz. The spatial resolution was selected to be finer than the typical lamellae thickness ($\approx$4-6 μm) to ensure proper characterization of the lamellar organization.

5.2.5 Image processing, network extraction, and quantitative analysis of the OLCN

Osteon mask: To enable all subsequent spatial analyses, a mask of each osteon was manually generated. The binary mask has a value of 1 inside the osteon and 0 at the central canal and outside the osteon. Osteon and Haversian canal boundaries were manually delineated by a single operator based on qBEI and CLSM (both reflection and fluorescence images). All masks were reviewed and validated by two additional operators. The masks were used to restrict the OCLN analyses to the osteonal compartment, to compute normalized distances to the Haversian canal, and to characterize the interplay between the OLCN features and the outer border of the osteon.

Network extraction: 3D image stacks obtained from CLSM (Fig. 5.1A) were processed using a custom Python-based software package, *Tool for Image and Network Analysis (TINA)* [8, 29, 40], specifically developed for OLCN analysis. The processing pipeline included binarization of the dataset using a local adaptive thresholding algorithm based on the difference of Gaussians (Fig. 5.1B), followed by segmentation of lacunae and canaliculi based on their size and morphology (Fig. 5.1C). The resulting binary images were skeletonized and smoothed using third-order smoothing splines (Fig. 5.1D). From this smoothed skeleton, a spatial network was extracted based on two essential features: nodes and edges. Nodes represent branching points (connecting two or more canaliculi or canaliculi to lacunae) and edges describe canaliculi (connecting two nodes). Quantification of this network was then performed using computational tools integrated in TINA [8, 29, 35, 40].

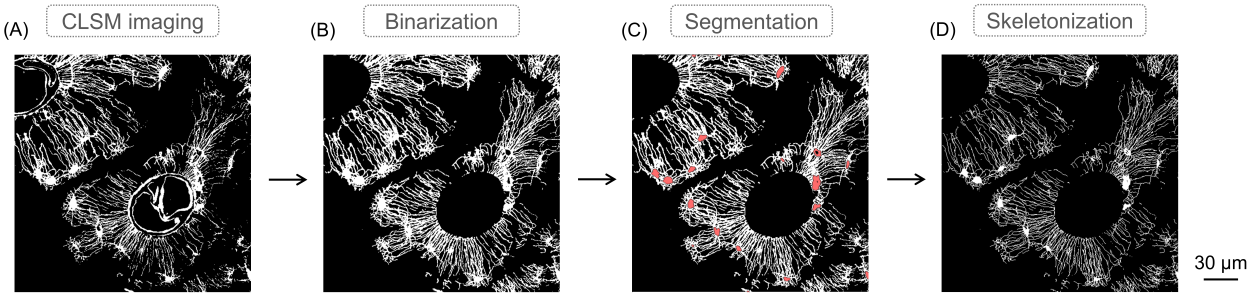


Figure 5.1: TINA image processing pipeline for OLCN extraction starting from CLSM image stacks. (A) Z-projection of 50 raw stacks (≈12 μm) showing the OLCN of an osteon and its surroundings. (B) Binarized image obtained using a local adaptive thresholding method. (C) Segmentation of the binarized image into lacunae (red) and canaliculi (white) based on morphology and size. (D) Final skeletonized network used for quantitative analyses. The skeleton preserves the topology of canaliculi and nodes, enabling subsequent network extraction and analysis.

Multimodal image correlation: To superimpose images acquired using qBEI, CLSM, and SHG, the following procedure was applied. First, SHG and qBEI were manually aligned using large pores (i.e., Haversian canals) as reference points. To visualize the OLCN, a 2D image based on projections of the CLSM z-stack was generated with ImageJ by applying a standard deviation projection over 50 slices. The resulting image was then binarized using a fixed global threshold. Because osteocyte lacunae and Haversian canals were clearly visible in both CLSM and qBEI datasets, their contours were used to accurately superimpose the corresponding images.

Analysis of canaliculi crossing the CL: To quantify canaliculi crossing the CL, we defined a peripheral region extending 10 μm inward into to osteon from the CL, corresponding approximately to the typical largest dimension of a lacunae [27, 41] and allowing to capture the majority of lacunae neighboring the outermost border of the osteons. This region was extracted on each image plane by applying a 10 μm inward erosion to the osteon mask, and its volume was computed (*V.Periph*) (Tab. S1). Figure 5.3A provides a graphical summary of the following procedure used for classifying crossing canaliculi. Firstly, we identified as peripheral canaliculi (*Can.Periph*) all edges (canaliculi) with at least one node (branching point) inside the peripheral zone, and as peripheral lacunae (*Lc.Periph*) all lacunae having at least one node (meeting point between the lacuna and an edge) within the peripheral region. To determine whether a

peripheral edge crosses the CL, we compared the radial positions of its two terminal nodes relative to the osteon boundary: edges with one node inside the osteon and the other outside are classified as crossing edges (*Can.Cross*). Among all the crossing canaliculi, we identified edges that directly connected one lacuna inside the osteon to another located outside. We verified that the shortest path between the two lacunae crossed the CL only once via the crossing edge in question. Edges fulfilling this criterion were marked as connecting canaliculi (*Can.Conn*), and all edges along the connecting path were classified as *directpath* edges. With the proposed classification, a canaliculus connecting two lacunae across the CL is composed of one *crossing* edge and several *directpath* edges.

The canalicular connectivity across the CL is then quantified with the following metrics. We computed the number of peripheral canaliculi that crossed the CL without connecting two lacunae (*Can.NoConn*), and those that crossed the CL and successfully connected a lacuna inside the osteon to one outside (*Can.Conn*). We calculated also the number of peripheral lacunae connected to at least one lacuna outside the osteon (*Lc.Conn.In*) that we normalized by the volume of the peripheral region to account for variability in the size of the osteon. Finally, we computed the average number of crossings edges per connected lacuna. We also computed the equivalent for externally connected lacunae (Supplementary note 5.1).

Canalicular orientation: The orientation of canaliculi was analyzed based on a previously established method [40]. For each edge, three angles were computed: θ, ϕ, and α (Fig. 5.7A). The angle θ represents the 3D angle between the canaliculus and the radial direction toward the center of the Haversian canal, with values ranging from 0° (perfectly radial) to 90° (perfectly lateral). Based on this angle, canaliculi were classified as radial ($\theta < 30°$) or lateral ($\theta > 60°$) [40]. The angle ϕ corresponds to the 2D projection of θ in the radial plane (x-y plane): it describes the polar angle between the projected canaliculus and the radial direction. The angle α describes the orientation of the canaliculus in the plane perpendicular to the radial vector, ranging from 0° to 360°, where $\alpha = 0°$ (or 180°) indicates alignment along the canal axis (i.e., perpendicular to the image plane), and $\alpha = 90°$ (or 270°) corresponds to alignment within the plane. To investigate whether the OLCN structure varied near the osteon boundary, we compared the frequency distributions of θ, ϕ, and α in the peripheral region with distributions computed in the entire osteon. The frequency distributions are based on 30 bins and data was weighted by the canalicular length, such that longer canaliculi contributed proportionally more to the distribution. This approach emphasizes the structural contribution of each segment rather than treating all segments equally.

Lacunar analysis: The following morphological parameters were computed: lacunar volume (*Lc.V*); lacunar degree (*Lc.Dg*), defined as the number of canaliculi emerging from a lacuna; lacunar stretch (*Lc.St*), calculated as the ratio of the longest to the shortest axis of the ellipsoid fitting the lacuna; and lacunar oblateness (*Lc.Ob*), indicating whether the intermediate axis of the ellipsoid is more similar to the shortest (i.e., rod-like lacuna) or the longest axis (i.e., plate-like lacuna) [42]. To exclude segmentation artifacts and extreme outliers, only lacunae with a volume between 50 μm^3 and 1000 μm^3 were retained for analysis [27, 41]. Morphological parameters were compared between lacunae located in the peripheral

region and in the entire osteon. Lacunar density was assessed as a function of the normalized distance to the Haversian canal by subdividing the osteons into discrete concentric rings and by dividing the volume occupied by lacunae by the total volume of these rings.

Network topology analysis: Network properties were evaluated within cubic subvolumes of 400 μm^3 (side length of 7.37 μm), chosen to be large enough to encompass several canaliculi while remaining comparable in size to a typical lacuna [29]. The extracted parameters in each subvolume includes: canalicular density (*Can.Dn*), defined as the total length of canaliculi per unit volume [$\mu m/\mu m^3$]; node number (*Nd.Nr*), corresponding to the number of nodes per unit volume [$1/\mu m^3$]; and average node degree (*Nd.Dg*), which reflects the number of branches per node excluding lacunae. We also computed the proportion of nodes with degree 1 (*pr.Nd.Dg.1*), representing the dead-ends of the network. For visual interpretation, Z-projections of these parameters were generated, excluding subvolumes without network. All parameters were analyzed as a function of the normalized distance of each subvolume to the Haversian canal, calculated using a Euclidean distance transform approach (*bwdist* function from MATLAB Image Processing Toolbox (R2022a, The MathWorks, Natick, MA, USA)). Subvolumes only partially filled by the osteon mask (i.e. having less than 1/3 of the voxels occupied by the mask) were discarded as considered not representative. To highlight spatial trends, we applied loess smoothing (span = 0.8) to all parameters and included a linear regression fit for canalicular density. Finally, we compared parameters calculated on the peripheral subvolumes close to the CL to those computed considering all subvolumes in the osteon using boxplots.

5.2.6 Statistical analysis

Statistical comparisons between the peripheral region and the entire osteon were performed using the following approach. For each comparison, data distributions were first tested for normality using the Kolmogorov-Smirnov test. If both groups followed a normal distribution, equality of variance was assessed using a two-sample F-test. When normality and equal variances were confirmed, group means were compared using a two-sided Student's t-test. If either normality or equal variance assumptions were violated, a non-parametric Wilcoxon rank-sum test was applied instead. A p-value < 0.01 was considered statistically significant.

5.3 Results

To characterize the connectivity of the OLCN across the CL, we first present qualitative results on representative osteons, followed by a quantitative characterization. We then examine the morphology and spatial distribution of lacunae, the orientation of the canaliculi, and the key topological network parameters, by systematically comparing the peripheral region to the entire osteon searching for specificities near the CL.

5.3.1 Qualitative aspects

Figure 5.2A shows a mineral content map where we can clearly osteons and surrounding bone, superimposed with the segmented OLCN (one additional region is shown in Fig. S1). The following features are highlighted: within the osteon and especially in interstitial bone there are regions lacking visible network; lacunae exhibit an elongated 2D morphology, with their short axis typically oriented along the radial direction toward the canal center; numerous lacunae are found near the CL, often aligned with the lamellar structures visible in SHG imaging (Fig. 5.2B); some canaliculi appear to cross the CL, even reaching lacunae outside the osteon.

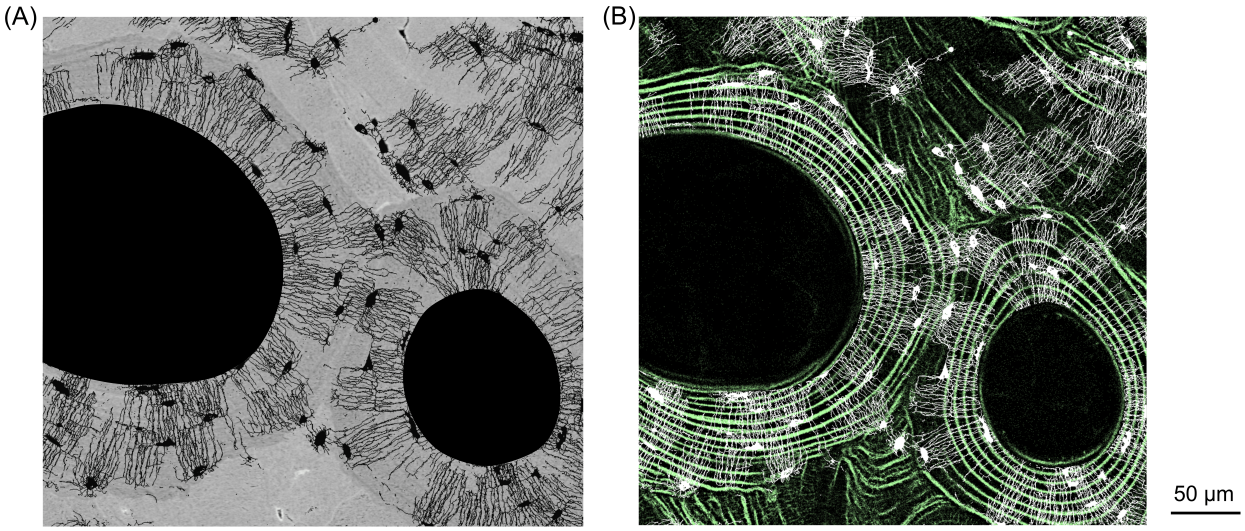


Figure 5.2: Multimodal image correlation in two representative adjacent osteons (Os7 on the left and Os3 on the right). (A) qBEI image, showing the Ca content in grey scale, overlaid with the Z-projection of CLSM data of the OCLN (black). (B) SHG image revealing bone lamellae (green), overlaid with the same CLSM (white).

5.3.2 Quantitative assessment of the canaliculi crossing the cement line

To quantify canalicular connectivity across the CL, we applied the classification approach detailed in Figure 5.3A. Segmented canaliculi in two representative osteons (Os2 and Os7) are color-coded based as follows: non-peripheral (grey), peripheral but non-crossing (cyan), crossing but non-connecting (orange), and crossing and connecting (light green). In the last scenario, we choose to represent the remaining portion of the canaliculi (i.e. the canaliculi not directly crossing the CL but in the connecting path between the two lacunae) in dark green (Figs. 5.3B–F). In some cases, there was only a single canaliculus connecting two lacunae across the CL (Fig. 5.3C), in other cases multiple connections were observed (Figs. 5.3D, F). Nevertheless, crossing events seem sparse and heterogeneously distributed along the osteon boundary.

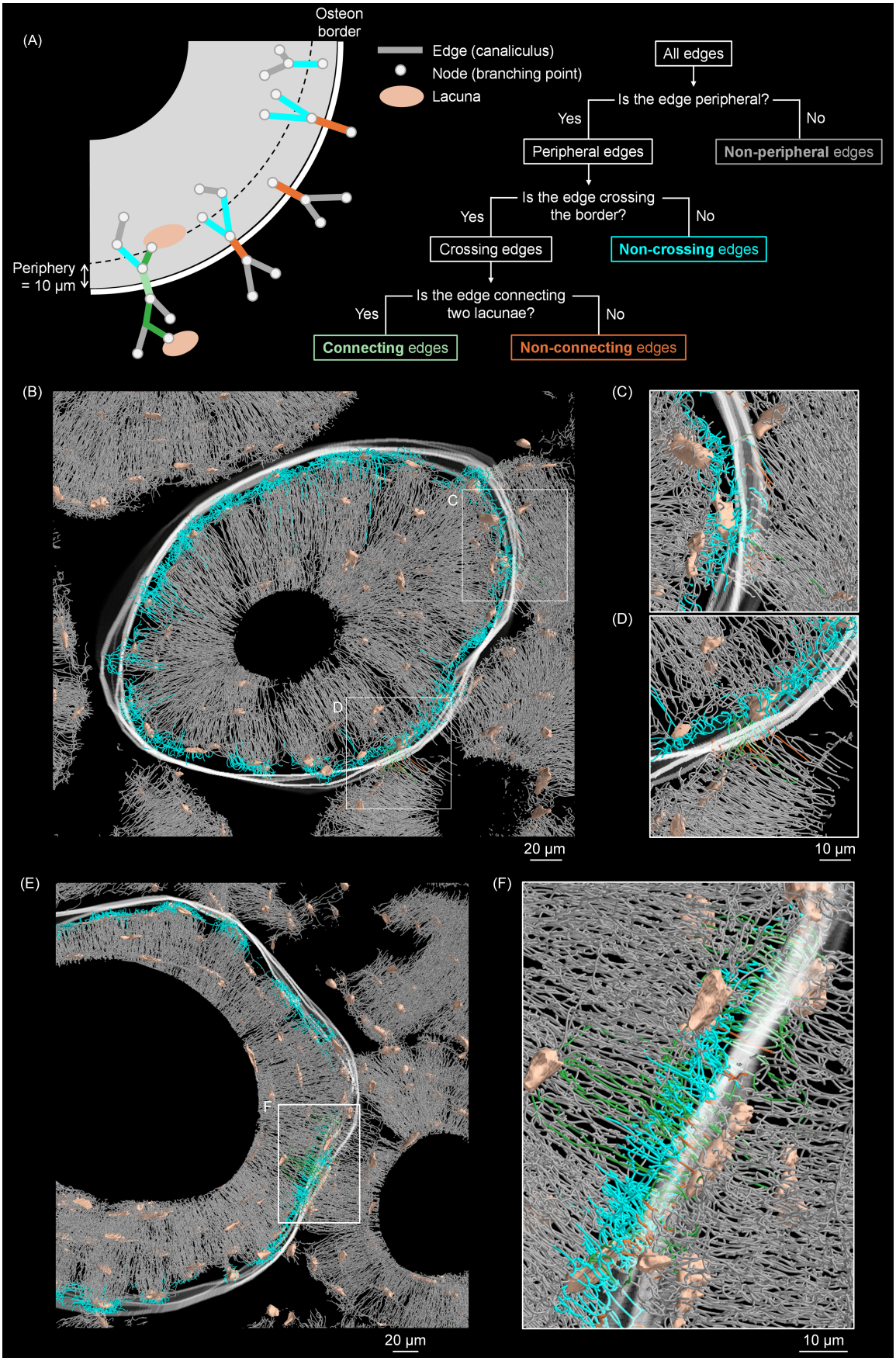


Figure 5.3: Identification of canaliculi crossing the CL and their classification based on connectivity.

Figure 5.3 (details). (A) Schematic workflow used to classify edges (canaliculi) in the peripheral region. All peripheral edges were identified and subdivided into crossing, if they reached the osteon border, or non-crossing (cyan) otherwise. Crossing edges were further classified as connecting edges (green), linking two lacunae across the border, or non-connecting edges (orange). (B–F) Representative examples (Os2 in B–D and Os7 in E–F) showing the OLCN and peripheral connections. The osteon border (CL) is shown in white, lacunae in beige, non-peripheral edges in grey, non-crossing edges in cyan, non-connecting edges in orange, and connecting edges in light green. Additionally, all edges in the path between two lacunae through the connecting edges are shown in dark green. (C, D), and (F) show magnified views of the regions outlined in white in (B) and (E), respectively.

On average, 3.61 ± 3.32% of peripheral canaliculi crossed the border of the osteon, and among these only 0.97 ± 0.98% formed connections between two lacunae (Fig. 5.4A). Three osteons (Os9, Os11, Os13) had no connections at all. The proportion of peripheral lacunae connected to at least one external lacuna across the osteon border (*Lc.Conn.In / Lc.Periph*) was 36.35 ± 28%, with a large inter-osteon variability (Fig. 5.4B). To account for volume differences, data was normalized by the volume of the peripheral regions (Fig. S2C): on average, each osteon had 7 ± 5.76 lacunae connecting to the outside tissue. Each connected lacuna had 7.17 ± 8.5 crossing canaliculi (Fig. 5.4C) but again a large variability is detected. Among all the lacunae identified as connected in the periphery of the osteon, we distinguished between connection with lacunae belonging to other osteons or to interstitial bone (Fig. S2A and D).

A graphical summary of our analysis is obtained by mapping the number of connecting canaliculi per lacuna in two representative osteons (Fig. 5). Connected lacunae are generally located close to the CL and faced each other. Os2 shows relatively few connections (up to 9 per lacuna), while Os7 exhibits significantly more (up to 52 per lacuna). In Os2, connections involved both interstitial and osteonal lacunae, whereas Os7 is predominantly connected to a neighboring osteon.

5.3.3 Lacunar characteristics

A total of 628 lacunae were analyzed across all osteons, including 264 located in the periphery region. These numbers already suggest that over 40% of osteonal lacunae are situated near the CL. When comparing lacunar properties between the peripheral region and the entire osteon, no statistical differences were observed for lacunar volume ($p = 0.22$, Fig. 5.6A), degree ($p = 0.17$, Fig. 5.6B), and oblateness ($p = 0.015$, Fig. 5.6D). However, lacunar stretch was significantly lower in the periphery ($p < 0.01$, Fig. 5.6C), indicating less elongated lacunae. Regarding the spatial distribution of the lacunae, we found higher lacunar density near the Haversian canal and close to the CL rather than in the central portion of the osteon (Fig. 5.6E).

5.3.4 Canalicular orientation

Canalicular orientation was assessed in 3D using the angles θ, α, and ϕ (Fig. 5.7A). In a representative osteon (Os2), a predominant radial orientation toward the Haversian canal was observed, as shown in

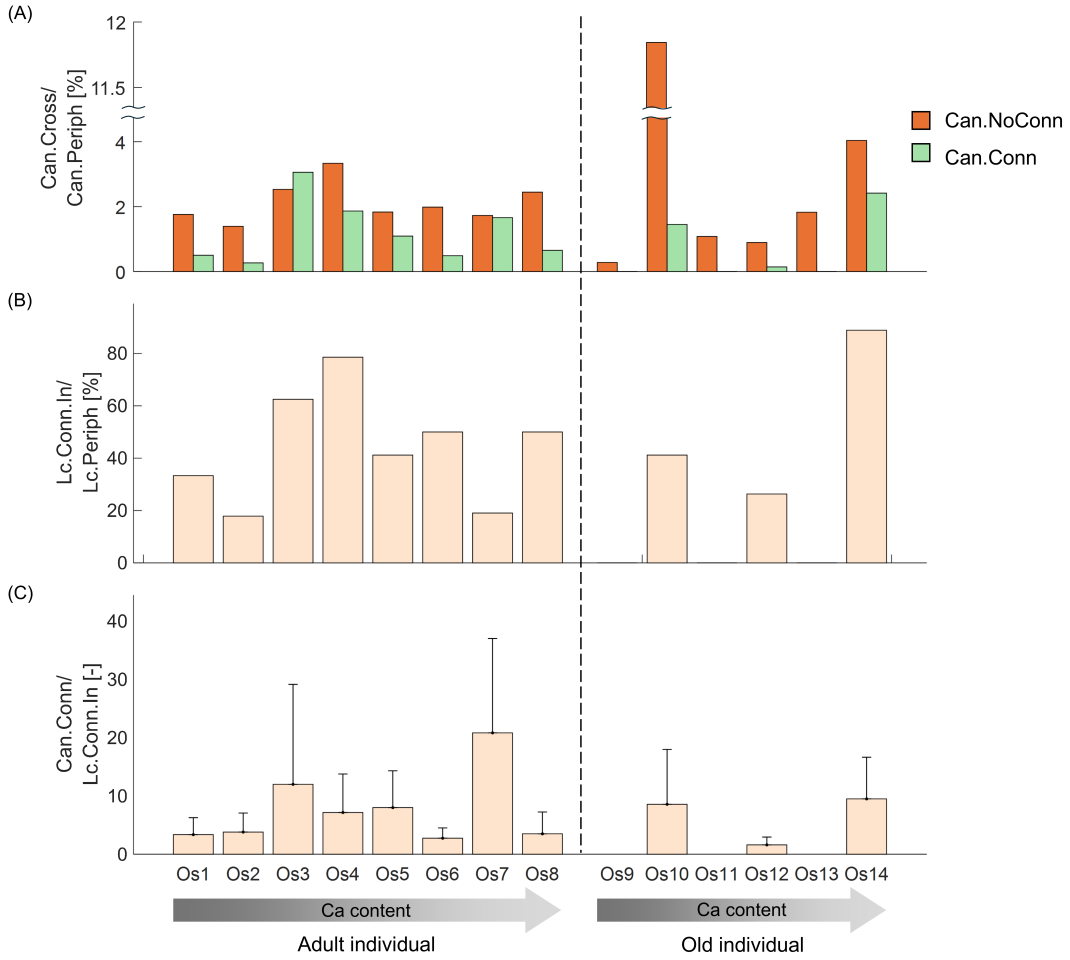


Figure 5.4: Quantification of canalicular connectivity across the CL in 14 osteons with varying mineral content (and tissue age). (A) Percentage of peripheral canaliculi crossing the CL: canaliculi connecting lacunae are shown in green and non-connecting canaliculi in orange. (B) Percentage of peripheral lacunae connected to at least one external lacuna (*Lc.Conn.In / Lc.Periph*). (C) Average number of connecting canaliculi (*Can.Conn*) per connected lacunae inside the osteon (*Lc.Conn.In*). When applicable, data presented as mean + standard deviation. Os9, Os10, and Os14 are osteon-in-osteons scenario.

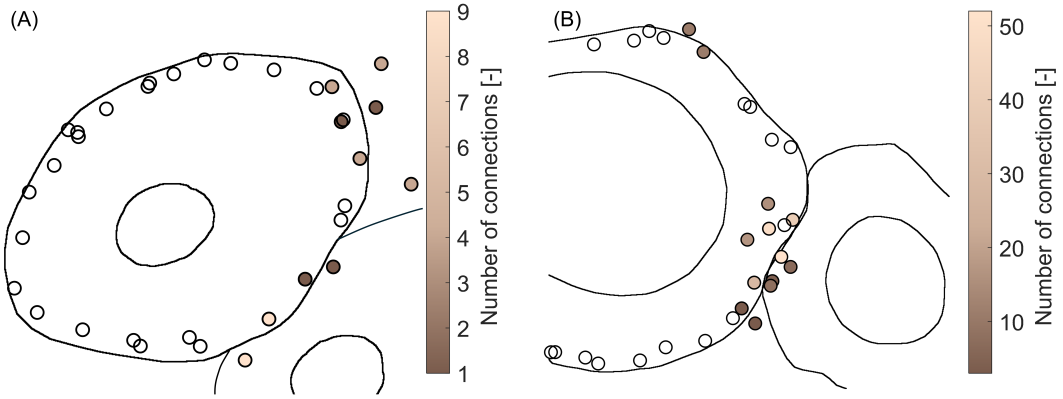


Figure 5.5: Lacunar connectivity maps. Colored circles represent connected lacunae (both inside and outside the osteon). The number of connections (*Can.Conn*) is color-coded. Unfilled circles indicate peripheral lacunae with no connections outside the osteon. (A) Osteon with relatively low lacunar connectivity (Os2). (B) Osteon exhibiting higher lacunar connectivity (Os7).

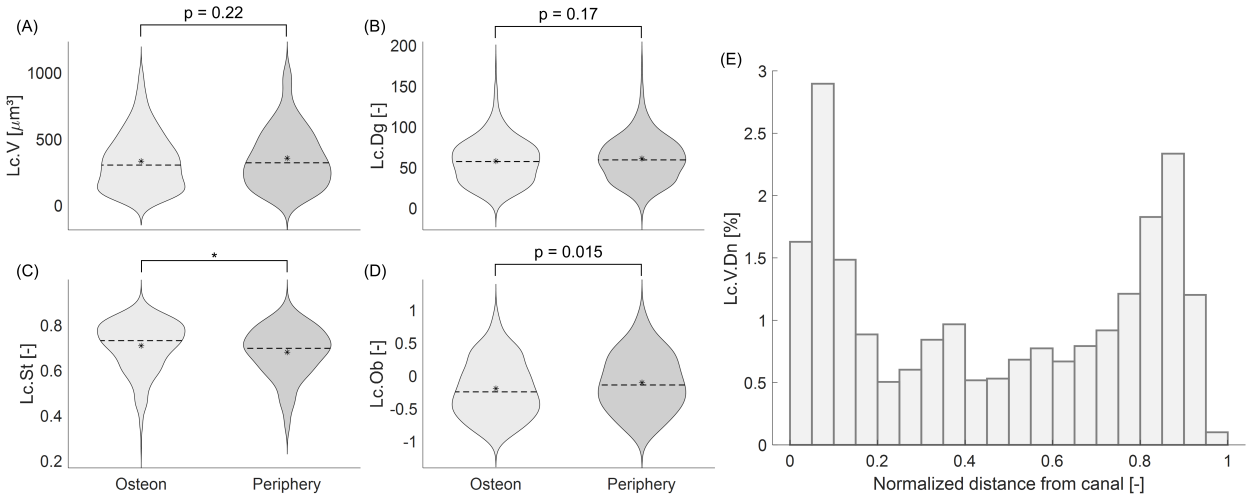


Figure 5.6: Lacunar characteristics. (A-D) Violin plots showing the distributions of (A) lacunar volume (*Lc.V*), lacunar degree (*Lc.Dg*), lacunar stretch (*Lc.St*), and (D) lacunar oblateness (*Lc.Ob*) in the osteon compared to the periphery. Dashed lines indicate medians, and asterisks mark the mean value. Statistical significance between the data sets is indicated by *p < 0.01. (E) Histogram showing the spatial distribution of the lacunar density across all osteons as a function of the normalized distance from the Haversian canal (0 = canal center, 1 = CL).

the spatial map color-coded by θ in Figure 5.7B. A few ring-shaped regions, located inside the osteon and particularly evident close to the CL, exhibited more laterally oriented canaliculi. This pattern is confirmed by plotting the frequency distribution of θ for all osteons (Fig. 5.7C): a peak around 25° is present when considering the entire osteons, indicating a predominance of radial canaliculi. Conversely, canaliculi in the peripheral region were predominantly laterally oriented, as shown by a peak at 90°. Based on the distinction between radial ($\theta < 30°$) and lateral ($\theta > 60°$) canaliculi, we found that 27.07 ± 6.15% of canalicular length is radial inside the osteon compared to only 14.8 ± 2.27 in the periphery ($p < 0.01$) (Fig. 5.7D). Conversely, lateral canaliculi accounted for 33.19 ± 4.74% of canalicular length in the periphery and 27.02 ± 2.3% in the entire osteon ($p < 0.01$) (Fig. 5.7E). The α angle showed no evident differences between the peripheral and osteonal regions (Fig. S3A), although the distribution appeared slightly more homogeneous in the periphery. Finally, the polar angle ϕ had a pronounced peak at 0° in the osteon, consistent with the high fraction of radial canaliculi. The peripheral region exhibited a more uniform distribution of ϕ, suggesting a wider range of orientations at the border of the osteons (Fig. S3B).

5.3.5 Network topology

Canalicular network parameters were spatially mapped for a representative osteon (Os2) based on subvolume analysis (Figs. 5.8A-D). As previously mentioned, large regions in the interstitial bone lack a visible network. Within the osteon, unevenly distributed areas of low density are present, particularly evident along the osteon border, with the exception of regions where canalicular crossing occurred (Fig. 5.5A). The map of node number shows localized areas with high values, in general corresponding to regions of high canalicular density. The average node degree is rather homogeneous across the osteon, with values slightly above 2, but decreases at the CL and around the Haversian canal, where values approach 1. The

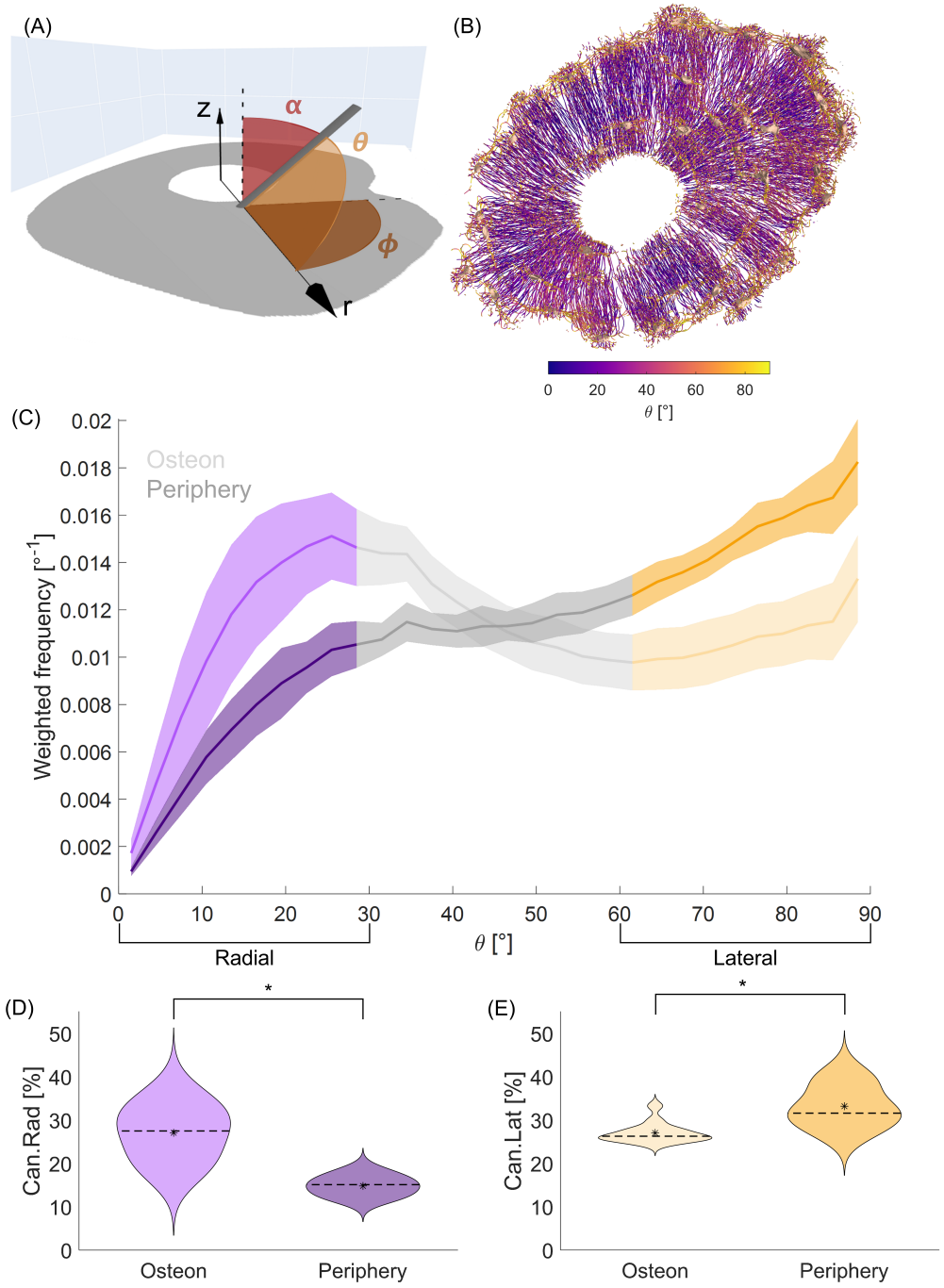


Figure 5.7: Analysis of canalicular orientation in osteonal and peripheral regions. (A) Schematic representation of the orientation angles used in this study: θ the 3D angle between a canaliculus and the radial direction (r), α the angle within the plane orthogonal to r, and ϕ the polar angle projected in the radial plane. (B) Spatial map of a representative osteon (Os2), with each canalicular segment color-coded according to its 3D orientation angle θ. (C) Frequency distribution of θ angles weighted by canalicular length for all osteons. The curve is split into three angular ranges to distinguish radial (θ < 30°), intermediate (30° ≤ θ ≤ 60°), and lateral (θ > 60°) canaliculi. Shaded areas represent the standard deviation across samples. Osteonal and peripheral regions are shown in light and dark tones, respectively. Violin plots showing the proportion of (D) radial canaliculi and (E) lateral canaliculi in both regions. Dashed lines indicate medians and asterisks show mean values. Statistical significance between the data sets is indicated by *p < 0.01.

peripheral region also exhibited a high proportion of nodes with degree 1: from 0.3-0.4 in the entire osteon to 0.6-0.7 in the periphery. These trends were confirmed by plotting the spatial variation of these parameters as a function of the normalized distance from the central canal (Fig. 5.8E–H). Canalicular density showed a decreasing behavior from the canal toward the CL. Node number decreased rapidly near the canal and then remained rather constant when moving toward the CL. Node degree followed a parabolic trend, peaking somewhere in the mid-region and decreasing toward both inner and outer borders. An inverse pattern is observed for the proportion of nodes with degree 1, with higher values near the canal and CL, and a plateau in the central osteonal region. When combining data from all osteons and comparing the peripheral region to the entire osteon (Fig.5.8I–L), statistically significant differences ($p < 0.01$) were observed for all parameters. Specifically, the periphery showed lower canalicular density (osteon: 0.0802 ± 0.0436 $\mu m/\mu m^3$; periphery: 0.0492 ± 0.0483 $\mu m/\mu m^3$), lower node number (osteon: 0.026 ± 0.0169 μm^{-3}; periphery: 0.0198 ± 0.0191 μm^{-3}), lower node degree (osteon: 2.16 ± 0.55; periphery: 1.73 ± 0.67), and higher proportion of nodes with degree 1 (osteon: 0.4021 ± 0.1888; periphery: 0.5538 ± 0.2544).

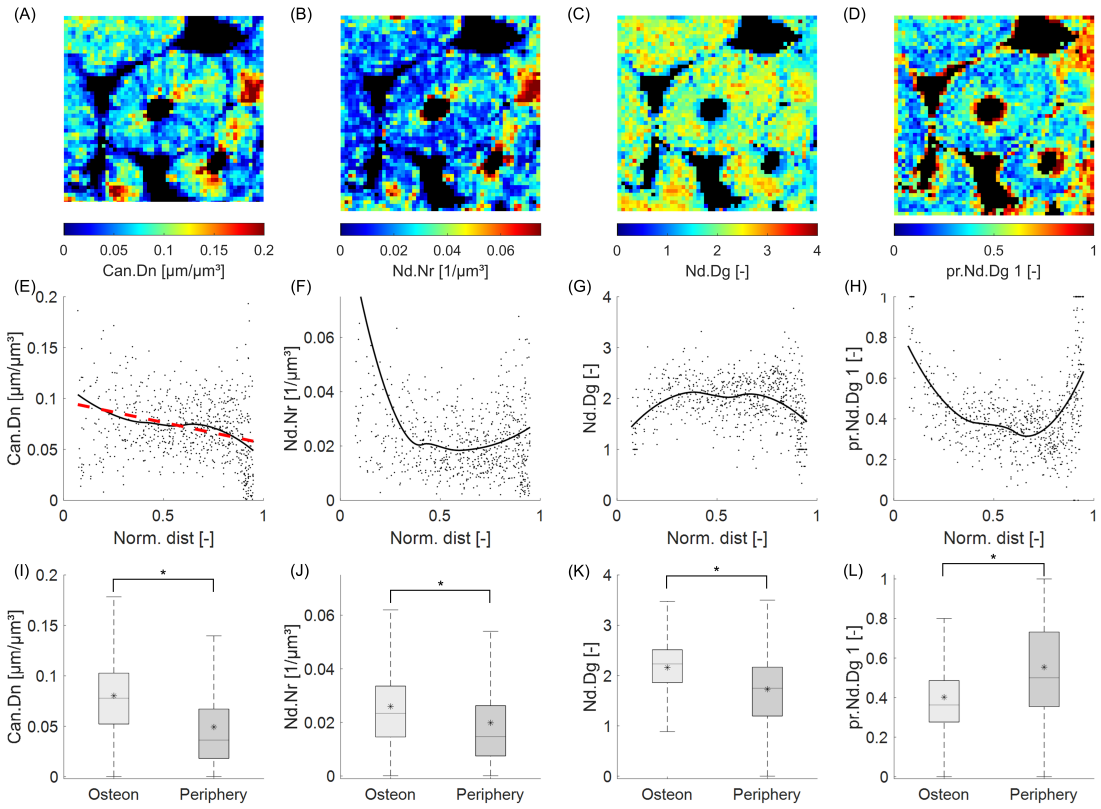


Figure 5.8: Spatial and quantitative analysis of canalicular network parameters. (A-D) Spatial maps of (A) canalicular density (*Can.Dn*), (B) node number (*Nd.Nb*), (C) node degree (*Nd.Dg*), and (D) proportion of node with degree 1 (*pr.Nd.Dg.1*) for a representative osteon and its surroundings (Os2). (E-H) Scatter plots showing the variation of (E) *Can.Dn*, (F) *Nd.Nb*, (G) *Nd.Dg*, and (H) *pr.Nd.Dg.1* as a function of normalized distance from the Haversian canal (canal = 0, CL = 1) for the same representative osteon (Os2). Solid black lines indicate smoothed trends with a loess fit (span = 0.8) and in (E), the red dashed line represents a linear regression. (I-L) Boxplots summarizing values for all osteons combined comparing osteonal and peripheral regions for (I) *Can.Dn*, (J) *Nd.Nb*, (K) *Nd.Dg*, and (L) *pr.Nd.Dg.1*. Median are indicated by solid lines and asterisks shows mean values. Statistical significance between the data sets is indicated by *p < 0.01.

5.4 Discussion

This study provides a detailed spatial characterization of the OLCN in human osteonal bone, with a particular focus on the peripheral region near the CL. By combining multimodal imaging with 3D network quantification, we investigated the possible connections between the osteon and its external environment through canaliculi crossing the CL. The following main findings are obtained.

5.4.1 Functional connectivity across the cement line

Although the CL is traditionally viewed as a structural boundary delimiting osteons, its influence on osteocyte connectivity remains debated. Some studies have described the CL as a dense interface that interrupts canalicular continuity and may act as a physical barrier to osteocyte communication [16, 31], while others have reported canaliculi crossing this boundary, suggesting some degree of inter-osteonal signaling [32, 33]. Our results contribute to this debate by showing that canaliculi crossing the CL do exists but are relatively rare, being about 3.6% of the totality of peripheral canaliculi. Importantly, we showed that canaliculi not only can cross the CL but they can also link lacunae inside the osteon to lacunae in the external bone. The proportion of peripheral lacunae connected to at least one external lacuna is fairly high (i.e. about 36%) when compared to the number of crossings, indicating that even a limited number of canalicular bridges across the CL may provide functional connections between the osteon and its surroundings. Indeed, when connections exist, they often involve several canaliculi linking the same lacuna pair. This redundancy might enhance the robustness of signaling across the CL, potentially compensating for the low number of crossing events.

How are these canalicular connections formed? During bone remodeling, osteoclasts resorb bone thereby cutting off the canaliculi within the adjacent older bone, likely resulting in canaliculi directly exposed at the eroded surface. Upon the formation of the CL, which anticipates the deposition of new lamellar bone, many of these exposed canaliculi may already be re-mineralizing, as inferred by the reduced canalicular density in the external bone close to the CL (Fig. 8A and reference [16]). However, a minor number of the exposed canaliculi may still be accessible and perhaps even contain dendrites of the osteocytes. Osteoblasts depositing new bone on the CL may recognize and connect with those canaliculi. This structural continuity may enable transport of matter and of mechanical information among different osteons as well as between osteons and interstitial bone. The latter may be important for osteocytes survival within interstitial bone, as well as for knowing when this tissue needs to be remodeled (i.e. following osteocytes death). This reasoning remains hypothetical, and further studies are needed to elucidate the precise mechanisms and reasons behind canalicular connections across the CL. We should also point out that a high variability is observed. Some osteons, like Os7, display numerous crossing connections, while others (e.g., Os9, Os11, Os13) have none. Perhaps one reason for this variability is the inclusion in our analysis of 3 "osteon-in-osteon" cases (Os9, Os10, and Os14), which showed very different behaviors. In this scenario, the investigated osteon was always the inner one.

On average, osteons from the older donor sample show fewer peripheral lacunae connected across the CL (26.06 ± 35.25%) compared to the adult sample (44.06 ± 20.83%), although this difference is not significant ($p = 0.25$) probably due to our limited sample size and high variability. This is in line with Milovanovic at al. [33], also observing comparable age-related decline in canalicular connectivity across the CL in human femoral bone. Although our sample size is limited, our results support the notion of inter-osteonal communication as a new element contributing to the quality of the OLCN, which shows age related modifications. Conversely, we did not find a consistent relationship between mineral content (as a proxy for tissue age) and the presence of connections between the osteon and the external bone.

5.4.2 Spatial characterization of the OLCN

Over 40% of osteonal lacunae were located within the peripheral region (up to 10 μm away from the CL), highlighting the relevance of the outer border of the osteons for the organization of the OCLN. Similar trends have been reported by Gauthier et al. [30] and Hannah et al. [43], both studies observing peaks in lacunar density near the CL. Considering the time course of osteon remodeling, the bone situated close to the CL is formed at earlier stages than the bone further away. There is evidence that the activity of osteoblasts decreases during bone deposition [44], resulting in slower deposition rates towards the haversian canal. It has been assumed that osteocytes density is linked to bone deposition rate [45, 46]: a higher density of lacunae close to the CL may be compatible with osteoblasts working harder there. Given that canaliculi crossing the CL mainly originate from the osteon periphery, the high density of lacunae near the CL may increase the likelihood of inter-osteonal connectivity. In terms of morphology, only minor differences were observed between the periphery and the entire osteon. Considering canalicular orientation, the frequency distribution of θ shows a clear peak around 25°, indicating a preferential 3D alignment of canaliculi toward the Haversian canal. This organization supports the view of the OLCN as a supply and signaling network, where radial canaliculi provide the shortest path for transport and communication between the osteocytes and central vascular channels, as suggested by Repp et al. [40]. In contrast to the radial canalicular orientation within the osteon, at the periphery the canaliculi shift clearly toward a predominantly lateral orientation: θ values peaked near 90°, with about 33% of canaliculi being lateral and only 15% radial. This likely reflects the need to connect neighboring lacunae arranged along the CL. Indeed, lateral canaliculi are believed to support tangential communication between adjacent lacunae, especially in regions where radial continuity is reduced, such as at the CL [16], in aged and diseased (micropetrosis) scenarios [40, 47]. In conclusion, a dual organization of the OLCN is detected: a radially oriented network inside the osteon favoring central-peripheral exchange, and a peripheral region characterized by more lateral canaliculi promoting local communication.

Among the different network parameters analyzed, canalicular density is the only one to exhibit a radial gradient, decreasing progressively from the Haversian canal toward the CL. Such decrease can be quantified by a linear regression, yielding a mean slope: $-0.043 \pm 0.05\ \mu m/\mu m^3$. The fact that canicular density is higher near the central canal and decreases radially may be partially explained by osteon geometry. Given

the roughly cylindrical shape of the osteon, the outer regions encompass larger volumes, which could reduce the apparent canalicular density even if the absolute number of canaliculi remains similar. However, geometry alone is insufficient to account for the magnitude of the density decrease. This is even more true close to the CL. Other topological parameters do not follow a monotonic trend. Of interest here is the spatial distribution of nodes with degree 1, corresponding to dead-ends of the network, which showed the largest values close to the inner and outer border of the osteon. Such values should be interpreted with caution near the Haversian canal as, due to the analysis strategy that we followed, all canaliculi ending up into the central canal are recognized as dead-ends even if they are not. This problem is not present at the CL, where the higher number of canaliculi with node degree 1 is not an artifact. When approaching the CL from the regions outside the osteon, nodes of degree 1 would reflect the distribution of the network caused by the formation of the osteon. The presence of dead-end canaliculi close to the CL but inside the osteons may reflect that osteocytes explore the environment sending their processes even towards the CL, which are then either stopping, changing direction or crossing (seldom). Comparable behavior was observed in the osteon-in-osteon structures (Os9, Os10, Os14), where most topological parameters, such as canalicular density and node degree, dropped sharply between the inner and outer osteons, while the proportion of degree 1 nodes increased (Fig. S4).

As a conclusive remark, we frequently observed regions that were entirely free of canalicular network. Since the network was visualized via rhodamine staining, we cannot confirm the complete absence of canaliculi, but only the lack of accessible porosities. The network-devoted locations were consistently associated with lacunae exhibiting signs of advanced mineralization, including fully hypermineralized lacunae (micropetrosis) (Fig. S1). These features are characteristic of osteocyte death and mineral infill, often associated with aging or mechanical overload [48, 49]. Functionally, such regions are likely disconnected from the surrounding network and may act as ”dead zones” for mechanosensation and nutrient transport. A similar phenomenon was previously reported by Yu et al. [27], who observed network-free zones in human femoral bone using synchrotron nano-CT. Although not being the primary focus of our study, the frequent appearance of large portions of interstitial bone without network across the different samples is an interesting observation with perhaps important implications for age-related degradation of bone quality. This finding also emphasizes the importance of looking “outside” the osteon and including interstitial bone in the analyses of the OLCN. Further work is needed to systematically characterize these zones and determine their broader implications for bone quality.

5.4.3 Limitations

There are some limitations that should be mentioned. Our results on canicular crossing are based on the manual segmentation of the osteon boundaries. This procedure is done by combining qBEI images (where the CL is visible) and CLSM images (where the OLCN is visible). While care was taken to manually delineate the CL, the fact that the CL was only visible in a single 2D surface section may introduce uncertainties on the precise location of the CL in the confocal images when going deeper into the bone.

Those uncertainties can clearly influence the classification of canaliculi, especially those that cross the CL but terminate shortly after, leading to a possible overestimation of crossing but non-connecting events. Additionally, when masking the central Haversian canal, we had to exclude a thin layer of the osteon due to the high fluorescence signal coming from the canal (where a lot of rhodamine is present). Doing this may have excluded canaliculi adjacent to the canal, artificially increasing the number of dead-ends and lowering node degree values near the center. We should also mention that we have analyzed osteons only coming from two male individuals, therefore limiting the generalizability of our findings. Furthermore, our results show great inter-osteon variability. One possible strategy to reduce this variability may be a more accurate pre-selection of the osteons to be analyzed. In this work we gave priority to osteons with a visible CL and varying mineral content. One refined strategy could be to select osteons always with similar dimensions, comparable average mineral content (reflecting tissue age) and always coming from the same anatomical location in the femoral cross section (e.g. anterior or posterior). Our limited sample size prevents robust statistical analysis of age-related differences. To make a clear statement on the impact of aging on the OLCN across the CL, more samples from different individuals should be analyzed. As for the image processing, we always used the same segmentation parameters across all samples. This approach, however, does not account for variability in staining or image quality, and may lead to under- or over-segmentation. Adaptive segmentation methods, for example based on machine learning algorithms, could be used in future works. Finally, although confocal imaging and staining protocol enabled high-resolution 3D visualization of the OLCN, it relies on dye penetration. This means that canaliculi in hypermineralized or poorly permeable regions, such as micropetrotic zones, may not be fully captured. Techniques like FIB-SEM or nano-CT (typically using synchrotron light) could complement CLSM measurements.

5.5 Conclusion

In this study we demonstrated not only that the CL can be crossed by the canaliculi but also that such crossings can be functional, allowing the connection between osteocytes lacunae inside the osteon with lacunae outside. We also show that the peripheral region near the CL is a "special" location with lower connectivity, more lateral canaliculi, and a higher density of lacunae in comparison to the whole osteon. Our work draws the attention not only to the osteon but also to the interplay between the osteon and the external bone, as a new aspect to be considered for improving our knowledge on the transport of matter and information through the OCLN in cortical bone.

Conflicts of Interest

The authors declare no competing interests.

Acknowledgements

The authors thank Phaedra Messmer, Petra Keplinger, and Sonja Lueger from LBIO for the sample preparation. AC is supported by the French Community of Belgium as part of a FRIA (Fund for Research Training in Industry and Agriculture) grant (n°1E03621F) and by the FWO and F.R.S.-FNRS under the Excellence of Science (EOS) programme (EOS No. 40007553). MH and SB gratefully acknowledge financial support from the Austrian Social Health Insurance Fund (OEGK) and the Austrian Workers' Compensation Board (AUVA). RW and AT thanks the Max Planck Queensland Centre for the Materials Science of Extracellular Matrices for support.

Supplementary information

	Os Ca_{Mean} [wt %]	V.Periph [μm^3]	Can.Periph	Can.Cross	Can.Conn	Lc.Periph	Lc.Conn.In	Can.Conn / Lc.Conn.In
Os1	21.72 ± 2.09	499704.64	7162	162	36	33	11	3.36 ± 2.91
Os2	23.93 ± 1.90	484142.97	7105	118	19	28	5	3.80 ± 3.27
Os3	24.44 ± 2.14	279000.88	5887	329	180	16	10	12.00 ± 17.15
Os4	24.63 ± 1.84	494412.33	9597	499	179	28	22	7.16 ± 6.61
Os5	24.70 ± 2.17	236147.10	5126	150	56	17	7	8.00 ± 6.32
Os6	24.71 ± 2.13	339753.94	6752	167	33	22	11	2.75 ± 1.76
Os7	24.85 ± 2.06	428961.67	7523	255	125	21	4	20.83 ± 16.20
Os8	25.16 ± 1.88	464284.92	6419	199	42	16	8	3.50 ± 3.75
Os9	24.62 ± 2.57	266661.56	4630	13	0	17	0	0
Os10	24.84 ± 2.67	229735.42	4137	550	60	17	7	8.57 ± 9.41
Os11	25.18 ± 2.70	213239.34	3609	39	0	8	0	0
Os12	25.56 ± 2.30	232509.72	5586	58	8	19	5	1.60 ± 1.34
Os13	25.84 ± 2.56	210156.22	3666	67	0	13	0	0
Os14	26.43 ± 2.20	167115.72	3145	203	76	9	8	9.50 ± 7.15

Table S1: Structural and canalicular connectivity parameters for individual osteons (Os1-Os14). Data are presented as raw counts or average ± standard deviation where applicable.

Supplementary note 5.1

In addition to the metrics concerning internally connected lacunae, we also computed the equivalent for externally connected lacunae: the number of lacunae outside the osteon connected with at least one lacuna inside (*Lc.Conn.out*) normalized by the volume of the peripheral region and the average number of crossing edges per externally connected lacuna (*Can.Conn/Lc.Conn.Out*). Note that *Lc.Conn.In* can be different from *Lc.Conn.out*. Moreover, we distinguished externally connected lacunae belonging to other osteons or to interstitial bone.

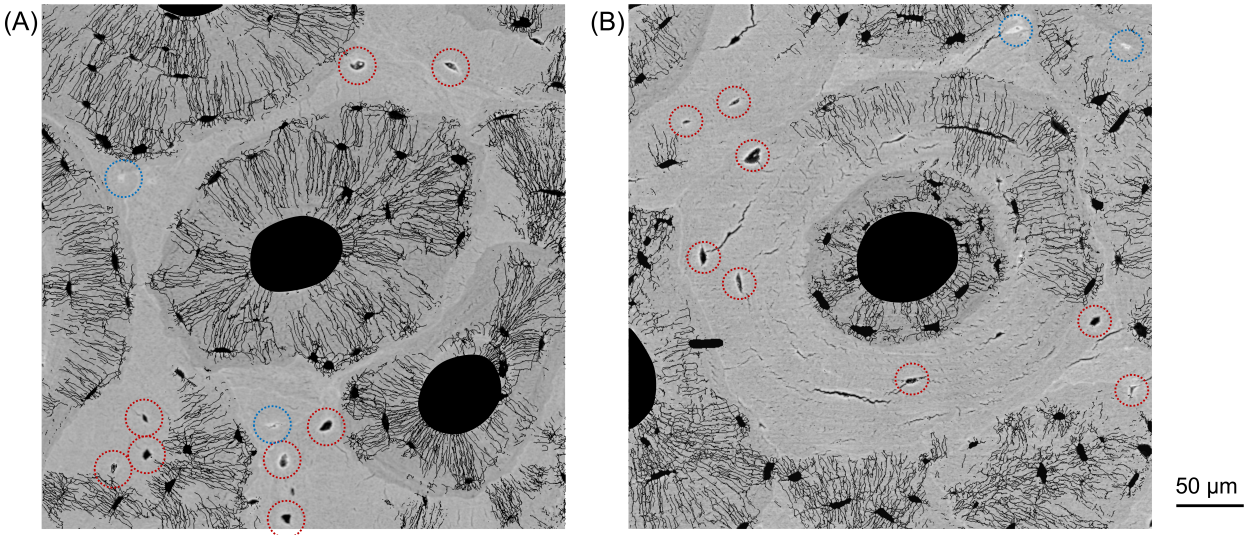


Figure S1: Visualization of lacunar mineralization stages in osteonal and interstitial bone regions based on qBEI. Two representative regions (Os2 on the left, Os9 on the right) illustrate osteons and surrounding bone. Red circles highlight lacunae exhibiting signs of initial hypermineralization, while blue circles indicate fully hypermineralized lacunae (micropetrosis).

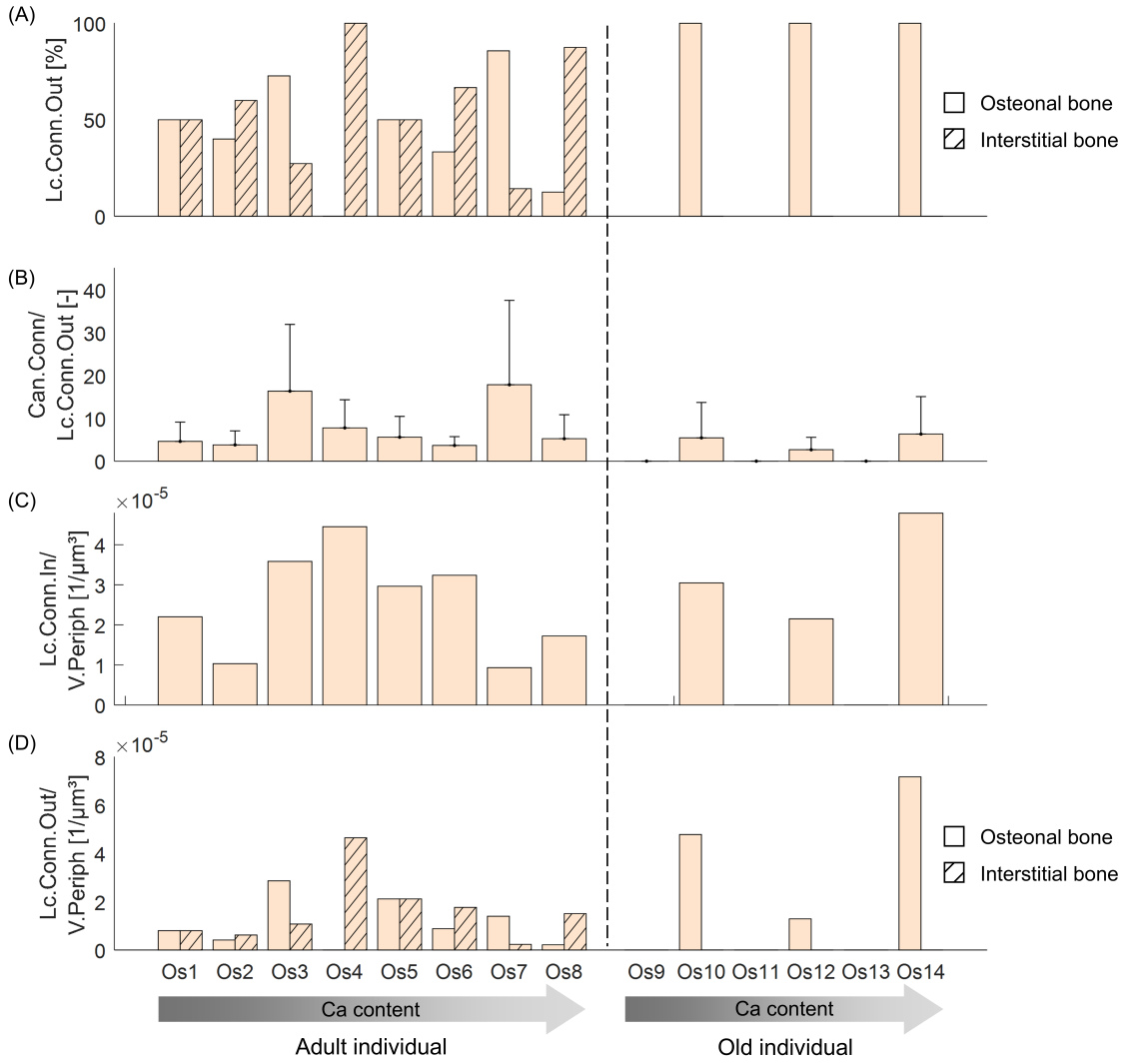


Figure S2: Quantification of canalicular connectivity across the CL in 14 osteons with varying mineral content (and tissue age). (A) Percentage number of external lacunae (i.e., outside the osteon) connecting to at least one lacuna inside the osteon (*Lc.Conn.Out*). The percentage is calculated based on number of external lacunae belonging to other osteons (plain bar) or to interstitial bone (hatched bar); for each osteon, the sum of the two bars gives 100%. One should note that, while in the adult sample we could not find a clear trend, in the old sample we only saw connections with lacunae into interstitial bone. (B) Average number of connecting canaliculi (*Can.Conn*) per connected lacuna outside the osteon (*Can.Conn / Lc.Conn.Out*). (C) Number of peripheral lacunae connected to at least one external lacuna normalized by the volume of the peripheral region (*Lc.Conn.In / V.Periph*). The average number of externally connected lacunae is similar to that of internal ones (7.64 ± 6.13). (D) Number of external lacunae (i.e., outside the osteon) connecting to at least one lacuna inside the osteon normalized by the volume of the peripheral region (*Lc.Conn.Out / V.Periph*), distinguishing external lacunae belonging to other osteons (plain bar) or to interstitial bone (hatched bar). The average number of connecting canaliculi per external lacuna is 5.66 ± 5.42. In all plots, each column represents a single osteon and data is ordered by increasing Ca content.

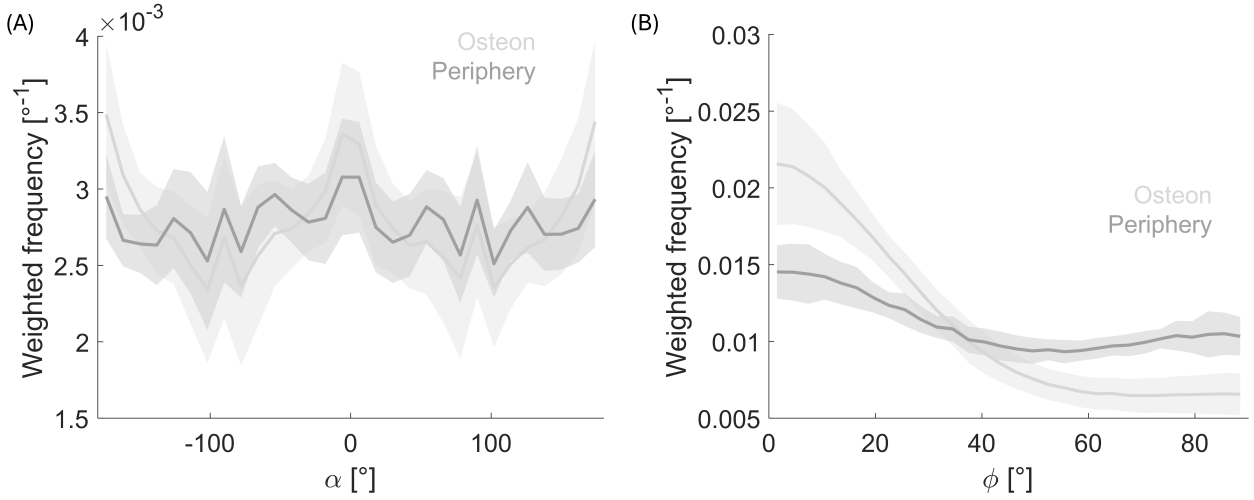


Figure S3: Frequency distributions of (A) α and (B) ϕ angles weighted by canalicular length for all osteons, comparing osteonal (light grey) and peripheral (dark grey) regions.

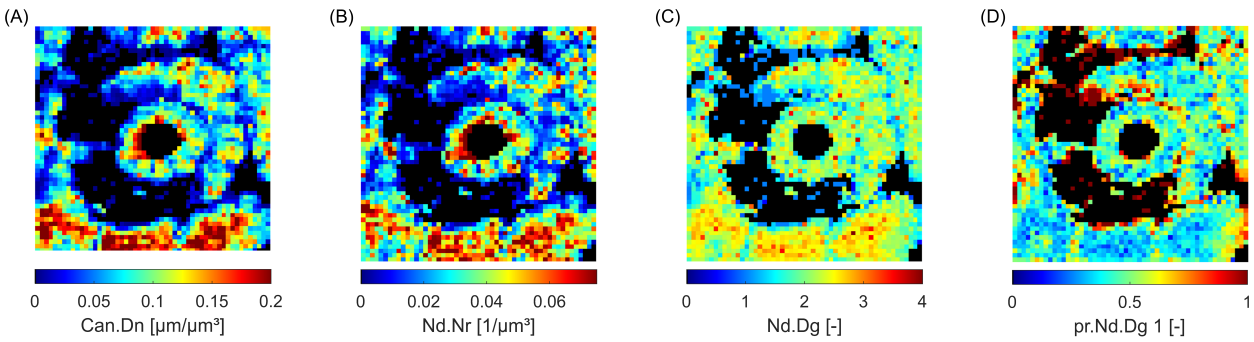


Figure S4: (A-D) Representative spatial maps of (A) canalicular density (*Can.Dn*), (B) node number (*Nd.Nb*), (C) node degree (*Nd.Dg*), and (D) proportion of node with degree 1 (*pr.Nd.Dg 1*) for an osteon-in-osteon (Os9).

Bibliography

[1] MA Hartmann, JWC Dunlop, YJM Bréchet, P Fratzl, and R Weinkamer. Trabecular bone remodelling simulated by a stochastic exchange of discrete bone packets from the surface. *Journal of the Mechanical Behavior of Biomedical Materials*, 4(6):879–887, August 2011.

[2] DJ Hadjidakis and II Androulakis. Bone Remodeling. *Annals of the New York Academy of Sciences*, 1092(1):385–396, December 2006.

[3] AG Robling, AB Castillo, and CH Turner. Biomechanical and molecular regulation of bone remodeling. *Annual Review of Biomedical Engineering*, 8(1):455–498, August 2006.

[4] NA Sims and JH Gooi. Bone remodeling: Multiple cellular interactions required for coupling of bone formation and resorption. *Seminars in Cell & Developmental Biology*, 19(5):444–451, October 2008.

[5] R Weinkamer, P Kollmannsberger, and P Fratzl. Towards a Connectomic Description of the Osteocyte Lacunocanalicular Network in Bone. *Current Osteoporosis Reports*, 17(4):186–194, August 2019.

[6] P Schneider, M Meier, R Wepf, and R Müller. Towards quantitative 3D imaging of the osteocyte lacuno-canalicular network. *Bone*, 47(5):848–858, November 2010.

[7] B Chang and X Liu. Osteon: structure, turnover, and regeneration. *Tissue Engineering Part B: Reviews*, page ten.teb.2020.0322, March 2021.

[8] AF Van Tol, V Schemenz, W Wagermaier, A Roschger, H Razi, I Vitienes, P Fratzl, BM Willie, and R Weinkamer. The mechanoresponse of bone is closely related to the osteocyte lacunocanalicular network architecture. *Proceedings of the National Academy of Sciences*, 117(51):32251–32259, December 2020.

[9] AG Robling and LF Bonewald. The Osteocyte: New Insights. *Annual Review of Physiology*, 82(1):485–506, February 2020.

[10] JUA Choi, AW Kijas, J Lauko, and AE Rowan. The Mechanosensory Role of Osteocytes and Implications for Bone Health and Disease States. *Frontiers in Cell and Developmental Biology*, 9:770143, February 2022.

[11] M Ayoubi, AF Van Tol, R Weinkamer, P Roschger, PC Brugger, A Berzlanovich, L Bertinetti, A Roschger, and P Fratzl. 3D Interrelationship between Osteocyte Network and Forming Mineral during Human Bone Remodeling. *Advanced Healthcare Materials*, 10(12):2100113, June 2021.

[12] NE Lassen, TL Andersen, GG Pløen, K Søe, EM Hauge, S Harving, GET Eschen, and JM Delaisse. Coupling of bone resorption and formation in real time: new knowledge gained from human haversian BMUs. *Journal of Bone and Mineral Research*, 32(7):1395–1405, July 2017.

[13] EF Eriksen, F Melsen, E Sod, I Barton, and A Chines. Effects of long-term risedronate on bone quality and bone turnover in women with postmenopausal osteoporosis. *Bone*, 31(5):620–625, November 2002.

[14] NA Sims and TJ Martin. Coupling the activities of bone formation and resorption: a multitude of signals within the basic multicellular unit. *BoneKEy Reports*, 3, January 2014.

[15] MD McKee and A Nanci. Osteopontin at mineralized tissue interfaces in bone, teeth, and osseointegrated implants: ultrastructural distribution and implications for mineralized tissue formation, turnover, and repair. *Microscopy Research and Technique*, 33(2):141–164, February 1996.

[16] M Kerschnitzki, W Wagermaier, P Roschger, J Seto, R Shahar, GN Duda, S Mundlos, and P Fratzl. The organization of the osteocyte network mirrors the extracellular matrix orientation in bone. *Journal of Structural Biology*, 173(2):303–311, February 2011.

[17] V Everts, JM Delaissé, W Korper, DC Jansen, W Tigchelaar-Gutter, P Saftig, and W Beertsen. The bone lining cell: its role in cleaning Howship's lacunae and initiating bone formation. *Journal of Bone and Mineral Research*, 17(1):77–90, January 2002.

[18] MD McKee, MC Farach-Carson, WT Butler, PV Hauschka, and A Nanci. Ultrastructural immunolocalization of noncollagenous (osteopontin and osteocalcin) and plasma (albumin and α2HS-glycoprotein) proteins in rat bone. *Journal of Bone and Mineral Research*, 8(4):485–496, April 1993.

[19] VV Ebner. Über den feineren bau der skelettheile der kalkschwämme nebst bemerkungen über kalkskelete überhaupt. *Sonder Berichte der Akademie der Wissenschaften Wien Abt*, 1:55–149, 1887.

[20] R Shahar and S Weiner. Open questions on the 3D structures of collagen containing vertebrate mineralized tissues: a perspective. *Journal of Structural Biology*, 201(3):187–198, March 2018.

[21] TA Grünewald, A Johannes, NK Wittig, J Palle, A Rack, M Burghammer, and H Birkedal. Bone mineral properties and 3D orientation of human lamellar bone around cement lines and the haversian system. *IUCrJ*, 10(2):189–198, March 2023.

[22] P Milovanovic, A vom Scheidt, K Mletzko, G Sarau, K Püschel, M Djuric, M Amling, S Christiansen, and B Busse. Bone tissue aging affects mineralization of cement lines. *Bone*, 110:187–193, May 2018.

[23] A Cantamessa, S Blouin, M Rummler, A Berzlanovich, R Weinkamer, MA Hartmann, and D Ruffoni. The mineralization of osteonal cement line depends on where the osteon is formed, October 2024. Manuscript under review in JBMR Plus.

[24] T Montalbano and G Feng. Nanoindentation characterization of the cement lines in ovine and bovine femurs. *Journal of Materials Research*, 26(8):1036–1041, April 2011.

[25] Y Zhou, MJ Kastner, TB Tighe, and J Du. Elastic modulus mapping for bovine cortical bone from submillimeter- to submicron-scales using peakforce tapping atomic force microscopy. *Extreme Mechanics Letters*, 41:101031, November 2020.

[26] A Cantamessa, S Blouin, V Schemenz, T Volders, M Burghammer, J Liu, A Berzlanovich, R Weinkamer, W Wagermaier, MA Hartmann, and D Ruffoni. Cement lines are stiffer, harder but less mechanically efficient than lamellar bone. Manuscript in preparation, 2025.

[27] B Yu, R Gauthier, C Olivier, J Villanova, H Follet, D Mitton, and F Peyrin. 3D quantification of the lacunocanalicular network on human femoral diaphysis through synchrotron radiation-based nanoCT. *Journal of Structural Biology*, 216(3):108111, September 2024.

[28] E Raguin, K Rechav, R Shahar, and S Weiner. Focused ion beam-SEM 3D analysis of mineralized osteonal bone: lamellae and cement sheath structures. *Acta Biomaterialia*, 121:497–513, February 2021.

[29] F Repp, P Kollmannsberger, A Roschger, M Kerschnitzki, A Berzlanovich, GM Gruber, P Roschger, W Wagermaier, and R Weinkamer. Spatial heterogeneity in the canalicular density of the osteocyte network in human osteons. *Bone Reports*, 6:101–108, June 2017.

[30] R Gauthier, H Follet, C Olivier, D Mitton, and F Peyrin. 3D analysis of the osteonal and interstitial tissue in human radii cortical bone. *Bone*, 127:526–536, October 2019.

[31] M Langer, A Pacureanu, H Suhonen, Q Grimal, P Cloetens, and F Peyrin. X-ray phase nanotomography resolves the 3D human bone ultrastructure. *PLoS ONE*, 7(8):e35691, August 2012.

[32] TA Curtis, SH Ashrafi, and DF Weber. Canalicular communication in the cortices of human long bones. *The Anatomical Record*, 212(4):336–344, August 1985.

[33] P Milovanovic, EA Zimmermann, M Hahn, D Djonic, K Püschel, M Djuric, M Amling, and B Busse. Osteocytic canalicular networks: morphological implications for altered mechanosensitivity. *ACS Nano*, 7(9):7542–7551, September 2013.

[34] P Roschger, P Fratzl, J Eschberger, and K Klaushofer. Validation of quantitative backscattered electron imaging for the measurement of mineral density distribution in human bone biopsies. *Bone*, 23(4):319–326, October 1998.

[35] A Roschger, P Roschger, W Wagermaier, J Chen, AF Van Tol, F Repp, S Blouin, A Berzlanovich, GM Gruber, K Klaushofer, P Fratzl, and R Weinkamer. The contribution of the pericanalicular matrix to mineral content in human osteonal bone. *Bone*, 123:76–85, June 2019.

[36] P Roschger, J Eschberger, and HJr Plenk. Formation of ultracracks in methacrylate-embedded undecalcified bone samples by exposure to aqueous solutions. *Cells and materials*, 3:3, 1993.

[37] C Lukas, P Kollmannsberger, D Ruffoni, P Roschger, P Fratzl, and R Weinkamer. The heterogeneous mineral content of bone – Using stochastic arguments and simulations to overcome experimental limitations. *Journal of Statistical Physics*, 144(2):316–331, July 2011.

[38] MA Hartmann, S Blouin, BM Misof, N Fratzl-Zelman, P Roschger, A Berzlanovich, GM Gruber, PC Brugger, J Zwerina, and P Fratzl. Quantitative backscattered electron imaging of bone using a thermionic or a field emission electron source. *Calcified Tissue International*, 109(2):190–202, August 2021.

[39] P Roschger, EP Paschalis, P Fratzl, and K Klaushofer. Bone mineralization density distribution in health and disease. *Bone*, 42(3):456–466, March 2008.

[40] F Repp, P Kollmannsberger, A Roschger, A Berzlanovich, GM Gruber, P Roschger, W Wagermaier, and R Weinkamer. Coalignment of osteocyte canaliculi and collagen fibers in human osteonal bone. *Journal of Structural Biology*, 199(3):177–186, September 2017.

[41] P Dong, S Haupert, B Hesse, M Langer, PJ Gouttenoire, V Bousson, and F Peyrin. 3D osteocyte lacunar morphometric properties and distributions in human femoral cortical bone using synchrotron radiation micro-CT images. *Bone*, 60:172–185, March 2014.

[42] M Rummler, A Van Tol, V Schemenz, MA Hartmann, S Blouin, BM Willie, and R Weinkamer. The Lacunocanalicular Network is Denser in C57BL/6 Compared to BALB/c Mice. *Calcified Tissue International*, October 2024.

[43] KM Hannah, CDL Thomas, JG Clement, F De Carlo, and AG Peele. Bimodal distribution of osteocyte lacunar size in the human femoral cortex as revealed by micro-CT. *Bone*, 47(5):866–871, November 2010.

[44] G Marotti, A Zambonin Zallone, and M Ledda. Number, size and arrangement of osteoblasts in osteons at different stages of formation. *Calcified tissue research*, 21:96–101, 1976.

[45] PR Buenzli, P Pivonka, and DW Smith. Bone refilling in cortical basic multicellular units: Insights into tetracycline double labelling from a computational model. *Biomechanics and Modeling in Mechanobiology*, 13(1):185–203, January 2014.

[46] PR Buenzli. Osteocytes as a record of bone formation dynamics: A mathematical model of osteocyte generation in bone matrix. *Journal of Theoretical Biology*, 364:418–427, January 2015.

[47] P Kollmannsberger, M Kerschnitzki, F Repp, W Wagermaier, R Weinkamer, and P Fratzl. The small world of osteocytes: Connectomics of the lacuno-canalicular network in bone. *New Journal of Physics*, 19(7):073019, July 2017.

[48] P Milovanovic, EA Zimmermann, A Vom Scheidt, B Hoffmann, G Sarau, T Yorgan, M Schweizer, M Amling, S Christiansen, and B Busse. The Formation of Calcified Nanospherites during Micropetrosis Represents a Unique Mineralization Mechanism in Aged Human Bone. *Small*, 13(3):1602215, January 2017.

[49] T Rolvien, FN Schmidt, P Milovanovic, K Jähn, C Riedel, S Butscheidt, K Püschel, A Jeschke, M Amling, and B Busse. Early bone tissue aging in human auditory ossicles is accompanied by excessive hypermineralization, osteocyte death and micropetrosis. *Scientific Reports*, 8(1):1920, January 2018.

6

Synthesis and perspectives

6.1 Synthesis

Bone is a remarkable biological material that achieves a remarkable balance between stiffness, strength, and toughness through its hierarchical structure, numerous internal interface and the interplay between its constituents [1]. Among the internal interfaces that contribute to this balance, the CL has long been acknowledged but remains poorly understood. In this thesis we explored CL mineral content and mineralization, mechanical and mineral properties as well as functional porosity in relationship with the corresponding osteon and external bone matrix. We combined different techniques having sub-micrometer resolution in a correlative manner to provide new insights into CL properties and possible mechanical and biological significance.

In the first study, we investigated the mineral content and mineralization process of the CL in comparison to the osteonal tissue. We showed that the CL is consistently more mineralized than the adjacent bone, and that–like bone–it follows a two phases of mineralization process but with distinct kinetics. The CL reaches higher mineral content and more rapidly than bone during the primary phase. In contrast, the secondary mineralization of the CL is much slower in comparison to the osteon. Most relevant, we showed that the mineralization of the CL is not universal but strongly depends on the region where the CL is formed. One possible reason being the local recycling of mineral ions during the bone remodeling process which leads to CL formation. As tissue ages, there is a progressive reduction in the mineral contrast between the CL and the corresponding osteon. Changes in CL mineral content may have a direct impact on its mechanical behavior: in a newly formed osteon, the CL mineral content attains quickly fairly similar values than the surrounding external bone, which may help "anchoring" the new osteon to older bone. At the same time, assuming that a higher mineral content is reflected into higher stiffness and strength, the CL may also have a role in damage tolerance acting as a protective "ring" around the osteon.

Motivated by the findings of the first study, in a second work we focused on the mechanical and mineral properties of the CL. We demonstrated that the CL is stiffer and harder than the adjacent osteonal tissue but not compared to older external bone, challenging the widespread assumption that it acts as a soft, compliant interface facilitating crack deflection. The central finding of our investigation is that the CL requires more mineral to attain the same stiffness and hardness than surrounding bone, hinting for a

lower mechanical efficiency of this region. We look for a possible explanation of this reduced efficiency by investigating the nanoscale structure of the mineral particles using synchrotron X-ray scattering. We found that mineral particles are thicker but shorter in the CL, having a lower aspect ratio. With the help of a micromechanical model we showed that indeed mineral particles with a lower aspect ratio are much less effective at reinforcing the collagen matrix. Using a finite element damage-based model with a limited number of assumptions and parameters, we challenged the assumed role of the CL to deviate cracks as the mechanical properties required for such task would be much different than those measured here.

In the third study, we explored the spatial organization of the OLCN, paying particular attention to network specificities close to and across the CL. We observed that in some cases the OCLN allows connections between the osteon and the external bone. The CL appears semi-permeable: a very limited number of canaliculi at the periphery of the osteon is able to go through the CL and link a larger fraction of peripheral lacunae inside the osteon with external lacunae. Such crossings, although sparse, seem to be quite efficient in ensuring transport across the CL. We also found that the periphery of the osteon is densely populated with lacunae, particularly near the CL, where bridging connections are likely to occur. Despite a strong spatial heterogeneity, the OCLN seems to be organized with radially orientated canaliculi within the osteon likely to facilitate nutrient transport, and with laterally oriented canaliculi in the periphery enhancing cell-cell interactions. Network connectivity decreases with distance from the canal, with more endpoints and fewer connections near the osteonal border, likely due to network disruption at the CL. Additionally, we identified network-free zones associated with hypermineralized lacunae, particularly evident in interstitial bone, which may compromise bone quality. These results emphasize the structural and functional complexity of the OLCN and suggest that the peripheral connectivity plays a key role in the transport of matter and information between the osteon and its external environment.

These three studies refine the CL as a dynamic interface that may contribute to the quality and functionality of cortical bone. The CL emerges as a specialized region, with high mineral content and high stiffness, attained very rapidly thanks to a fast primary mineralization process. Yet mechanically the CL is not as efficient as lamellar bone, one reason being differences in the nanoscale mineral particles. Taken together, these results suggest that the principal role of the CL may be to serve as a rigid substrate layer formed very rapidly to allow the coordinated deposition of lamellar bone in the building of a new osteon [2], rather than being an interface evolved to protect the osteon from mechanical damage, as traditionally believed. Biologically, the CL is functionally embedded in the surrounding tissue as it is not an impermeable barrier, but it allows some degree of inter-osteon communication and transport. These insights raise new questions about the role of the CL and its contribution to bone quality in aging and disease-related scenarios.

6.2 Limitations and perspectives

While this work provides new insights into compositional, mechanical and functional aspects of the CL in cortical bone, it also comes with certain limitations and opens up several interesting avenues for future research. First, the present findings are based on a limited sample size, two male donors and a single anatomical site (cortical bone from the femoral midshaft). To generalize our observations, future studies should incorporate a larger and more diverse sample set, encompassing female subjects, various age groups, and different skeletal sites. It would also be particularly relevant to explore the 3D organization and the properties of the CL in trabecular bone (e.g. between bone packets, Fig. 6.1), at entheses, or at osteochondral junctions, where distinct mechanical and biological environments may be reflected in CL specificities.

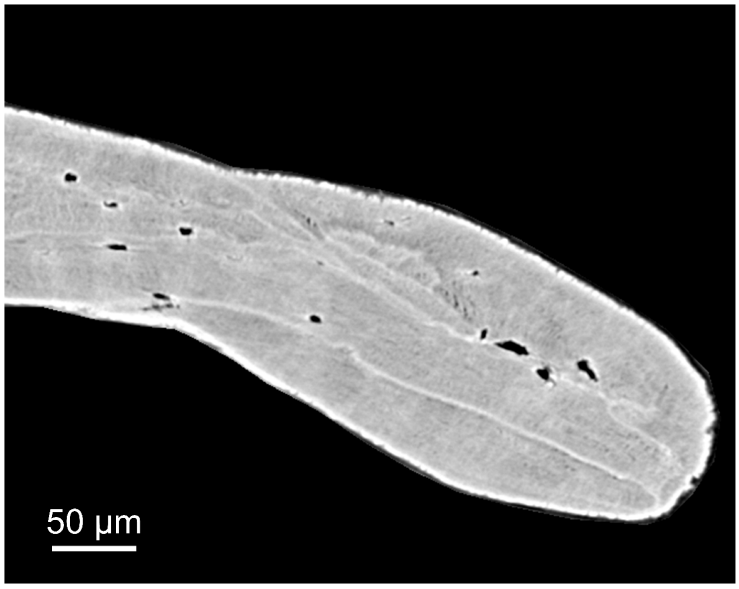


Figure 6.1: Synchrotron radiation nano-CT image of a human trabecula where we can see the CL appearing brighter. Image curtesy of E. Pedrinazzi, MBBM Lab, ULiege.

From a mechanical perspective, while our nanoindentation data revealed key information about CL stiffness and hardness, the tests were performed only in transverse sections. Performing similar experiments on longitudinal cuts could help determine whether the CL exhibits anisotropic mechanical behavior, which remains unknown. Additionally, standard nanoindentation could be extended to assess the full stress-strain behavior of the CL at the nanoscale, allowing to investigate the inelastic deformation mechanisms of the CL compared to surrounding tissues, potentially uncovering differences in strength and damage resistance (Fig. 6.2). This technique has been applied to fibrolamellar bone in Chapter 7.4.

Our results also suggest that current finite element models of bone microstructure may need to be revised. The CL is often modeled as a soft layer to facilitate crack deflection [3, 4, 5], yet our findings indicate that it is, in fact, stiffer and harder than the adjacent osteon. Incorporating more accurate, experimentally

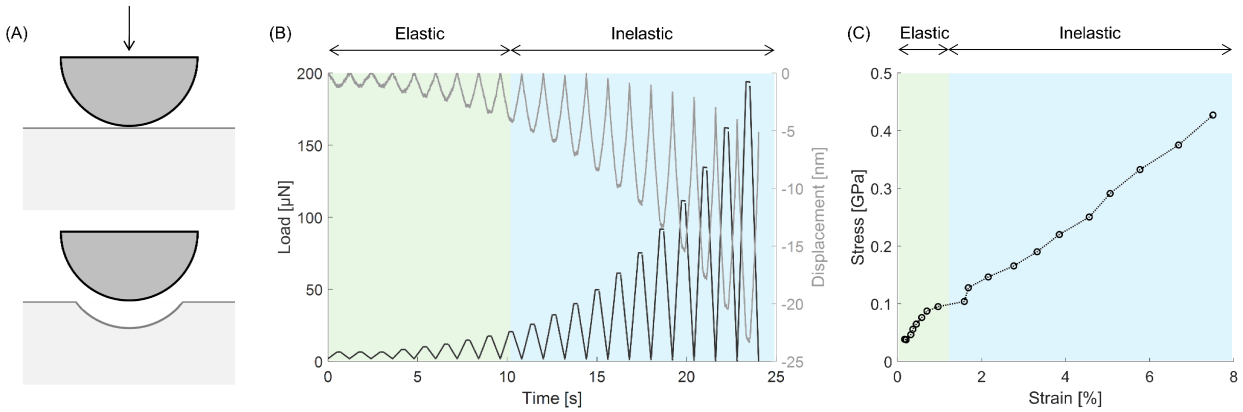


Figure 6.2: Method to extract stress-strain behavior and to characterize CL properties beyond stiffness and hardness. (A) Cyclic nanoindentation at a single location with progressively increasing loads. The experimental load-depth data (B) can be converted into nanoindentation stress-strain curve (C), informing on the full elastic and inelastic behavior of the sample.

derived material properties into multiscale mechanical models could improve predictions of crack propagation and local stress redistribution within osteons, especially under pathological conditions.

Another area that remains largely unexplored is the organic composition of the CL. While we examined mineral properties, we did not directly investigate matrix composition and organization that may influence mechanical behavior. Techniques such as Raman spectroscopy, FIB-SEM, or even mass spectrometry could provide detailed insights into the biochemical composition and architecture of the CL and can provide additional data to explain its relatively low mechanical efficiency despite high mineral content. Understanding how specific organic components, such as osteopontin, contribute to mineral organization could offer a more complete picture.

Moreover, studying the CL in the context of aging and disease remains an essential step to be completed. For example, age-related changes in bone quality and turnover, such as those observed in osteoporosis, may affect CL formation or functionality. Comparing newly formed osteons with older ones in both healthy and osteoporotic bone could help identify whether alterations in CL structure or composition contribute to bone fragility. Investigations using pre-clinical animal models could also be informative. For instance, osteopontin-deficient mice provide a unique opportunity to explore the role of specific non-collagenous proteins in CL formation and function. Interestingly, studies have shown that proteinaceous structures normally rich in osteopontin, like the CL, are still present in bones from osteopontin-deficient mice [6], suggesting that the formation of CLs can occur independently from osteopontin. This raises obvious questions on CL mineral content, mineralization and mechanical properties in this specific scenario.

Finally, given the semi-permeable nature of the CL observed in our network analysis, future work could include computational fluid flow simulations to better understand how inter-osteonal communication occurs. Existing simulations [7] have focused on intra-osteonal fluid dynamics (Fig. 3), and expanding these models to include multiple osteons separated by CLs would be a fascinating next step to shed light

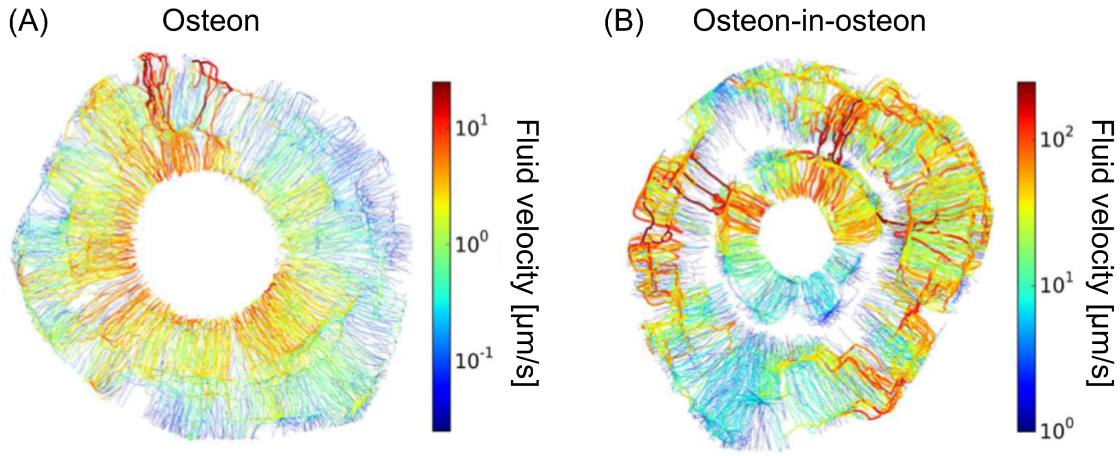


Figure 6.3: Simulated fluid flow in the OLCN of two osteon types: (A) a typical Type I osteon and (B) a Type II osteon (osteon-in-osteon). Very large differences in fluid velocity between the two scenarios are observed, reflecting differences in the underlying architecture of the OLCN. Adapted from [7].

on the characteristics of long-range interactions in bone tissue. As the network architecture and the corresponding load-induced fluid flow are closely linked to bone remodeling and mechanical adaptation [8], knowing fluid flow patterns in the interstitial bone around the osteon, which often shows occluded lacunae, may help to better understand the initiation of the remodeling process in this region.

6.3 Conclusion

Looking beyond its role as a simple boundary, the CL emerges as a rapidly formed, structurally distinct interface contributing to the structural and functional integrity of bone. Through its unique composition, mechanical properties, and biological integration, it reveals a more complex role than previously assumed. This work closes a chapter of discovery, but also opens new questions about how microstructural features like the CL contribute to bone quality in aging and disease-related degradation in bone. In exploring one of the finest interfaces of bone, it reminds us that fundamental science is a journey made of small steps — each essential for unveiling the complexity of living materials.

Bibliography

[1] W Wagermaier, K Klaushofer, and P Fratzl. Fragility of bone material controlled by internal interfaces. *Calcified Tissue International*, 97(3):201–212, September 2015.

[2] M Kerschnitzki, W Wagermaier, P Roschger, J Seto, R Shahar, GN Duda, S Mundlos, and P Fratzl. The organization of the osteocyte network mirrors the extracellular matrix orientation in bone. *Journal of Structural Biology*, 173(2):303–311, February 2011.

[3] E Giner, R Belda, C Arango, A Vercher-Martínez, JE Tarancón, and FJ Fuenmayor. Calculation of the critical energy release rate G c of the cement line in cortical bone combining experimental tests and finite element models. *Engineering Fracture Mechanics*, 184:168–182, October 2017.

[4] S Nobakhti, G Limbert, and PJ Thurner. Cement lines and interlamellar areas in compact bone as strain amplifiers – Contributors to elasticity, fracture toughness and mechanotransduction. *Journal of the Mechanical Behavior of Biomedical Materials*, 29:235–251, January 2014.

[5] L Vergani, C Colombo, and F Libonati. Crack propagation in cortical bone: a numerical study. *Procedia Materials Science*, 3:1524–1529, 2014.

[6] SR Rittling, HN Matsumoto, MD Mckee, A Nanci, XR An, KE Novick, AJ Kowalski, M Noda, and DT Denhardt. Mice Lacking Osteopontin Show Normal Development and Bone Structure but Display Altered Osteoclast Formation In Vitro. *Journal of Bone and Mineral Research*, 13(7):1101–1111, July 1998.

[7] AF van Tol, A Roschger, F Repp, J Chen, P Roschger, A Berzlanovich, GM Gruber, P Fratzl, and R Weinkamer. Network architecture strongly influences the fluid flow pattern through the lacunocanalicular network in human osteons. *Biomechanics and Modeling in Mechanobiology*, 19(3):823–840, June 2020.

[8] AF Van Tol, V Schemenz, W Wagermaier, A Roschger, H Razi, I Vitienes, P Fratzl, BM Willie, and R Weinkamer. The mechanoresponse of bone is closely related to the osteocyte lacunocanalicular network architecture. *Proceedings of the National Academy of Sciences*, 117(51):32251–32259, December 2020.

7

Side projects

This chapter presents three collaborative side projects that were undertaken during the course of the thesis. These studies have resulted in three publications in peer-reviewed international journals.

7.1 A molecular scale understanding of misorientation toughening in corals and seashells

The first project concerned the characterisation of the mechanical behavior of biominerals, in collaboration with Prof. PUPA Gilbert (University of Wisconsin, US) and Prof. MJ Buehler (MIT, Boston, US).

Full paper: AJ Lew[1], CA Stifler [2], A Tits[3], CA Schmidt[2], A Scholl[4], A Cantamessa[3], L Müller[3], Y Delaunois[3], P Compère[3], D Ruffoni[3], MJ Buehler[1], PUPA Gilbert[2], A molecular scale understanding of misorientation toughening in corals and seashells, *Advanced Materials*, 35(28):2300373, March 2023. https://doi.org/10.1002/adma.202300373.

[1] Massachusetts Institute of Technology;

[2] University of Wisconsin-Madison;

[3] University of Liège;

[4] Berkeley National Laboratory.

Abstract

Biominerals are organic–mineral composites formed by living organisms. They are the hardest and toughest tissues in those organisms, are often polycrystalline, and their mesostructure (which includes nano- and microscale crystallite size, shape, arrangement, and orientation) can vary dramatically. Marine biominerals may be aragonite, vaterite, or calcite, all calcium carbonate ($CaCO_3$) polymorphs, differing in crystal structure. Unexpectedly, diverse $CaCO_3$ biominerals such as coral skeletons and nacre share a similar characteristic: Adjacent crystals are slightly misoriented. This observation is documented quantitatively at the micro- and nanoscales, using polarization-dependent imaging contrast mapping (PIC mapping), and the slight misorientations are consistently between 1° and 40°. Nanoindentation

shows that both polycrystalline biominerals and abiotic synthetic spherulites are tougher than single-crystalline geologic aragonite. Molecular dynamics (MD) simulations of bicrystals at the molecular scale reveal that aragonite, vaterite, and calcite exhibit toughness maxima when the bicrystals are misoriented by 10°, 20°, and 30°, respectively, demonstrating that slight misorientation alone can increase fracture toughness. Slight-misorientation-toughening can be harnessed for synthesis of bioinspired materials that only require one material, are not limited to specific top-down architecture, and are easily achieved by self-assembly of organic molecules (e.g., aspirin, chocolate), polymers, metals, and ceramics well beyond biominerals.

Toughness of Slightly Misoriented versus Single-Crystalline Aragonite Crystals, Measured by Nanoindentation

To investigate the relationship between slight misorientation and fracture resistance, we measured the local fracture toughness in biogenic, geologic, and synthetic minerals using a combination of nanoindentation and scanning electron microscopy (SEM). Two sets of nanoindentation experiments were performed on polished samples using a Triboindenter TI-950 (Bruker, US). First, indentation with a low-load transducer was done using a standard Berkovich diamond probe (calibrated on fused quartz), a trapezoidal load function (10 s loading, 5 s holding, and 10 s unloading) and a reference peak load of 1500 μN (corresponding to a penetration depth of 80-180 nm). Low-load indentation was performed on at least three different locations per sample considering square grids from 9 to 25 indents each (depending on the sample), with indentation spacing of 5 μm. The main outputs of the low-load nanoindentation are the indentation elastic modulus (also called reduced modulus) E and the hardness H, quantified based on the load-depth curves using the standard Oliver-Pharr approach [1]. The local mechanical properties (E and H, presented) are used as input for the fracture study (see Eq. 7.1). In the second set of indentation experiments, the same samples were tested using a high load transducer (3D OmniProbe, Bruker) equipped with a cube corner diamond probe. Again, a trapezoidal load-controlled function was used (5 s-5 s-5 s) and peak indentation load varied from 1 mN to 1500 mN. For each load, 5 indents were done with indent spacing adapted to the higher loads and ranging from 50 to 250 μm. Considering the small dimensions and the variability of the available surface area for indentation (due to sample embedding and polishing), synthetic spherulites were indented at a fixed peak load of 100 mN, which is high enough to induce detectable cracking but small enough to avoid splitting the spherulites into two or more pieces.

Following high load indentation, the samples were gold coated (about 20 nm coating thickness) in a Balzers SCD004 sputtering unit (BAL-TEC, Switzerland) and imaged in secondary electrons (SE) in a FEG-SEM Tescan Clara (Tescan, Czech Republic) at 15 kV (high vacuum, ET-detector). SE-SEM imaging was used to measure the radius of the residual indent R_I and the radius of the cracked/damaged region R_D from the center of the indent (a measure of crack length, thus, $c = R_D$), as shown in Fig. 7.1A-D and F. For each indentation load, 2 to 5 indents were imaged. To compare diverse samples, the indentation fracture toughness K_c (Fig. 7.1G), was calculated using the following formula [2, 3]:

$$K_c = \chi \left(\frac{E}{H}\right)^{1/2} \left(\frac{P}{c^{3/2}}\right) \tag{7.1}$$

where χ is a numeric parameter characteristic of the indenter tip geometry ($\chi = 0.04$ for a cube corner), E is the elastic modulus, H is the hardness (measured with nanoindentation at low load/penetration depth, P is the indentation load, and c is the crack length, measured from the center of the indent.

Comparison of toughness values for all aragonite samples demonstrates that biominerals, including nacre and coral skeletons, are considerably tougher than single crystalline aragonite (Fig. 7.1). This is consistent with previous studies on geologic and biogenic crystals [4, 5, 6, 7, 8], identifying the role of organic inclusions and other mechanisms (e.g., friction between rough interfaces and sacrificial mineral bridges) as possible amplifiers for fracture toughness. It is worth mentioning that azimuthal orientation could also influence nanoindentation results. Specifically, changes in the azimuthal angles of the indenter were shown to impact the measured hardness, but not the indentation modulus in both geologic minerals and biominerals [9, 10]. The impact of azimuthal rotations on indentation fracture toughness is not considered here, and it could be explored in future studies. A novel aspect reported here is the fracture behavior of synthetic spherulites: Those structures were grown in the absence of anything organic, and they are on average 50% tougher than geo aragonite. Importantly, the same result is obtained also when indenting aragonite in a different direction with respect to the c-axis. This observation suggests that, besides structural characteristics such as organic interfaces [11, 12], misorientation of the minerals also contributes to the toughness of $CaCO_3$ biominerals.

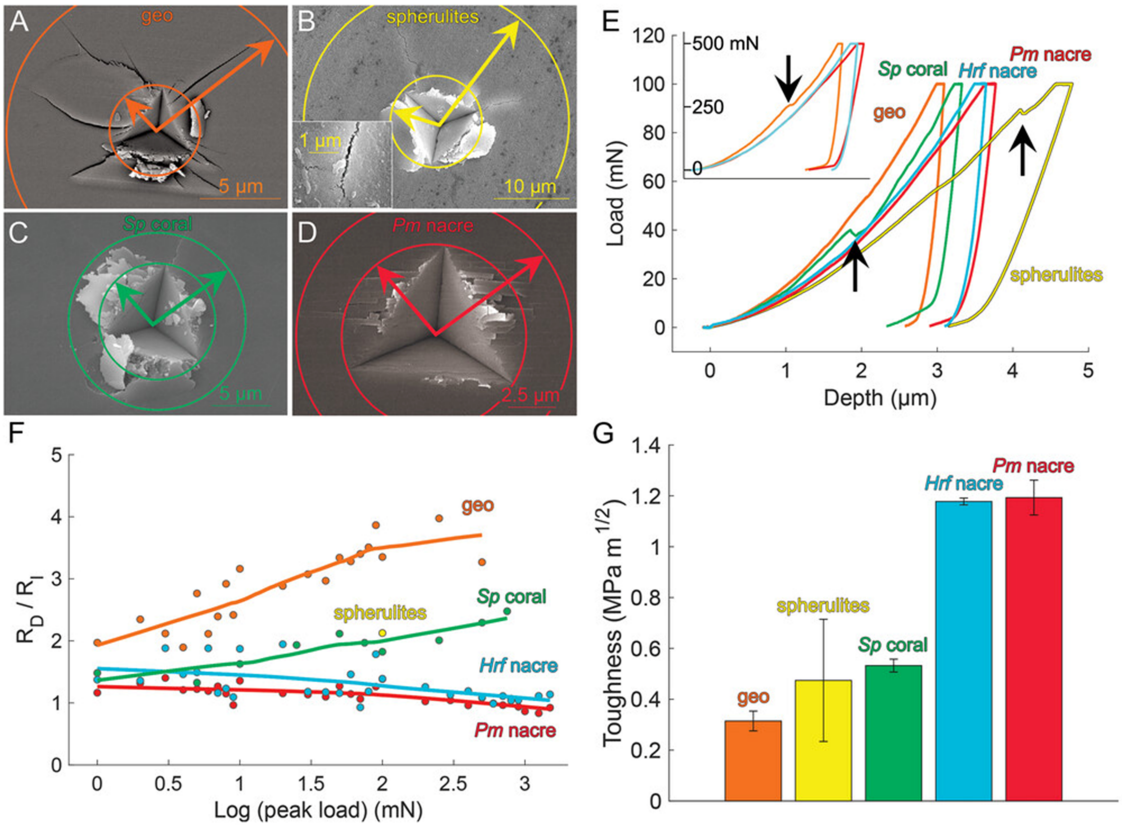


Figure 7.1: Indentation fracture toughness is greater in aragonite biominerals and synthetic spherulites, compared to single-crystalline geologic aragonite. A–D) SEM images post-indentation with a peak load of 100 mN. In (A), (B), and (D) the indentation direction was perpendicular to the aragonite c-axis, in (C) multiple crystals in coral skeleton have unknown orientations. A) Geologic aragonite crystals indented perpendicular to c-axis, B) synthetic spherulites (inset shows additional toughening mechanisms: crack deflection, microcracking, and crack branching), C) coral skeleton, and D) Pm nacre(indented perpendicular to c-axis, that is, with nacre tablet layers horizontal in the image). Hrf nacre has a behavior qualitatively similar to Pm nacre. SEM images are used to extract the radius of the residual indent R_I and of the entire damaged area R_D by fitting the smallest possible circle centered on the indent. E) Typical indentation curves at a peak load of 100 mN: synthetic and coral aragonites show characteristics pop-in events (highlighted by arrows), associated with sudden damage beneath the contact surface. Geologic aragonite also shows such dis-continuities but at higher loads, Pm and Hrf nacre do not (see inset), at either lower or higher loads, indicating a progressive damage accumulation but no abrupt pop-in events. F) Ratio of mean damage radius (R_D) and indentation radius (R_I) plotted versus indentation peak load (trend lines are locally weighted scatterplot smoothing, LOWESS, regression fits with a smoothing factor of 0.8). This metric quantifies whether damage tends to localize around the indent (as in Pm and Hrf nacre) or to propagate (as in geo aragonite). Both coral and synthetic spherulites have intermediate behavior. G) Experimentally measured indentation fracture toughness (abbreviated as "Toughness"), obtained by fitting the correlation between damage radius(R_D, a measure of crack length) and indentation load. [13, 14] Data are presented as mean ± SD over multiple locations within the same sample, except for the spherulites, where 4 different spherulites were measured. Comparison of all the samples demonstrates that slight misorientation, present in synthetic spherulites, coral skeleton, and nacre but absent from geologic aragonite, correspond to greater toughness.

7.2 Deep Learning Virtual Indenter Maps Nanoscale Hardness Rapidly and Non-destructively, Revealing Mechanism and Enhancing Bioinspired Design

A second project, in collaboration with the same teams, involved artificial intelligence (AI) models to predict and design bio-inspired materials with controlled hardness by analysing the structure-property relationship of human tooth enamel.

Full paper: AJ Lew[1], CA Stifler [2], A Cantamessa[3], A Tits[3], D Ruffoni[3], PUPA Gilbert[1], MJ Buehler[2], Deep Learning Virtual Indenter Maps Nanoscale Hardness Rapidly and Non-destructively, Revealing Mechanism and Enhancing Bioinspired Design, *Matter*, 6(6):1975-1991, June 2023. https://doi.org/10.1016/j.matt.2023.03.031.

[1] Massachusetts Institute of Technology;

[2] University of Wisconsin-Madison;

[3] University of Liège.

Abstract

Summary:
Over evolution, organisms develop complex material structures fit to their environments. Based on these time-tested designs, human-engineered bioinspired structures offer exciting possible materials configurations. However, navigating diverse structure spaces for attaining desired properties remains non-trivial. We focus on the hardest biological tissue in humans, tooth enamel, to examine the structure-property relationship. While typical hardness measurements are time consuming and destructive, we propose that AI models can predict properties directly and enable high-throughput, non-destructive characterization. We train a deep image regression neural network as a surrogate model and visualize with gradient ascent and saliency maps to identify structural features contributing most to hardness. This model demonstrates improved spatial resolution and sensitivity compared with experimental hardness maps. Using this rapid hardness testing model, a generative adversarial model, and a genetic algorithm that operates in latent space, allows for guided materials design, yielding proposed designs for bioinspired structures with precisely controlled hardness.

Highlights:

- Traditional ways of measuring hardness can be augmented with machine learning models;
- Expanded insight can be derived from known data, without experimental advancement;
- Adding generative models and genetic algorithms enables targeted bioinspired design.

Nanoindentation of human enamel

Nanoindentation tests were performed with a Triboindenter TI-950 (Bruker, Billerica, MA, US) on the polished sample using a Berkovich diamond probe calibrated on standard fused quartz. Indentation was done on the same locations characterized by PIC mapping by exploiting specific anatomical features visible in the optical microscope of the nanoindenter. A displacement-controlled trapezoidal load function (10 s loading, 4 s holding, and 10 s unloading) with a maximum depth of 100 nm (corresponding to a peak load of approximately 1200 μN) was used. Areas of the same dimensions as those studied with PIC mapping were probed, with a later spacing between indents of 2 μm. Indentation force-displacement curves were analyzed with the Oliver-Pharr method [1] to extract hardness H.

Pre- and post-indentation indexing of PIC maps and hardness data

Nanoindentation data were arranged in table form, including indent number, spatial coordinates, and measured H. PIC maps acquired before and after indentation, and the visible light microscopy (VLM) images were imported into a single file using Adobe Photoshop 2023, with one image per layer. First, the post-indentation PIC and VLM images were aligned so the indents coincided in position. Then, the pre-indentation PIC map was aligned to the post-indentation one until all enamel rods in the image coincided with the post-indentation ones. Each indent was evaluated carefully such that it could be unambiguously located on the PIC map and therefore assigned the proper measured H value. Due to image distortions present in PIC maps, as in all microscopy methods, out of many hundreds of total indents in the area utilized, here it was only possible to identify 94 measurements with certainty.

Obtaining a hardness model

A primary challenge of utilizing machine learning models is the acquisition of suitable training data, ideally of both large volume and high accuracy. However, there is often a practical trade-off between large volume and high accuracy experimentation. Thus, here we employ a strategy of combining datasets with different levels of volume and accuracy to obtain a more complete view of enamel hardness.

We first utilize the hardness dataset with accurate labeling from nanoindentation shown in Fig. 7.2A. The second dataset we use is generated via estimated labeling from cross referencing literature, shown in Fig. 7.2B. Specifically, we use enamel images from the literature of different regions of a human molar [15], subdivide each image into square 200 $\times$ 200 pixel segments, and estimate hardness labels for each square by comparing the square location with human enamel hardness maps in the literature [16, 17], for a total of 333 image-label pairs. It should be noted that this estimation runs a risk of including error between hardness values and microstructures, due to natural variation of biological samples from tooth age, oral environment, tooth position, etc. The third dataset is comprised of 17 large enamel maps from the literature [18] with noisy labeling, shown in Fig. 7.2C. Despite the large volume of image area in this third dataset, only the average hardness values and standard deviations for each image are known.

There is low granularity in the hardness labels of any exact location. To summarize, the first dataset has small volume but accurate and precise labels; the second dataset is larger but has approximate labels with fewer significant digits and the possibility for error; and the third dataset is the largest, but any local image section is likely to have some unknown deviation from the average, resulting in label errors.

We then combine these three datasets into one single dataset of 22730 image-label pairs, with a distribution of hardness values between 2 and 7 GPa as shown in Fig. 7.2D. By uniting these three streams of data, we obtain a large volume dataset that also incorporates a representation of high accuracy measurement. This united dataset is used to train an image regression model that maps enamel structure images to hardness values.

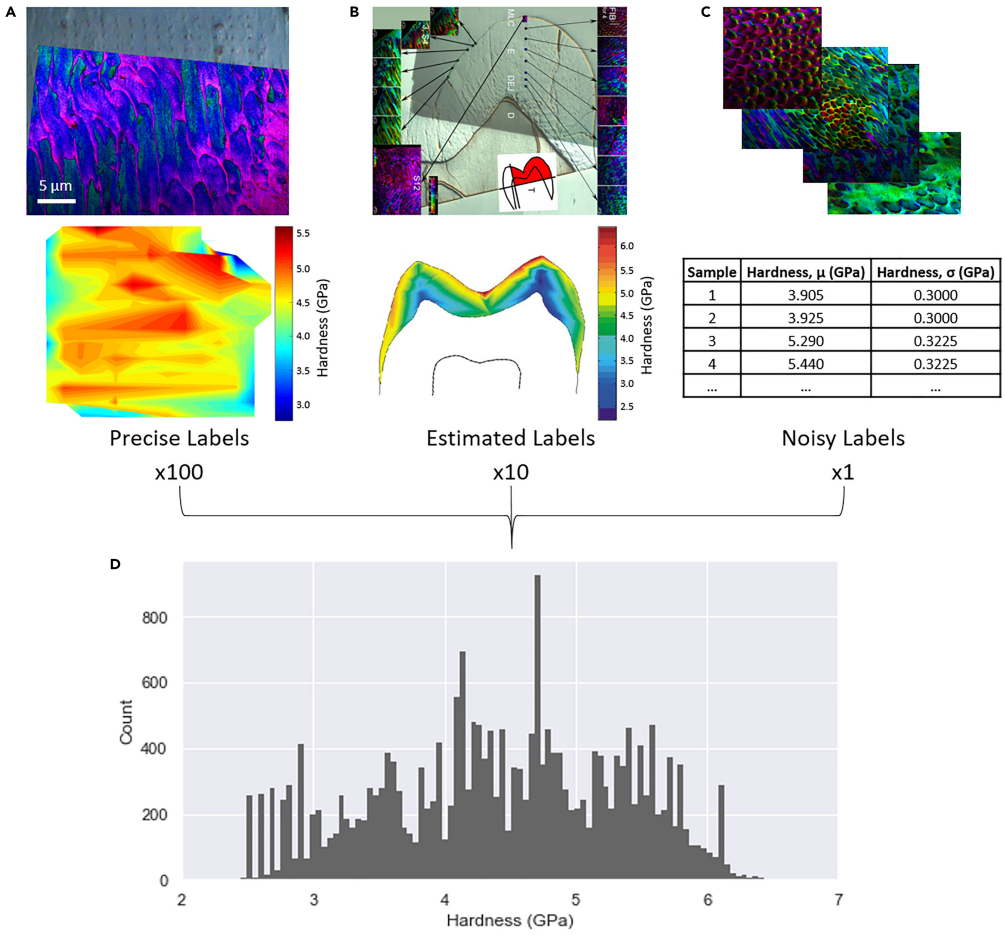


Figure 7.2: Dataset curation. Performant machine learning models require training data of both high accuracy and large volume. (A–C) To achieve this comprehensive representation of hardness, we combine three imperfect datasets together: (A) a small dataset of accurate locally measured labels, (B) a mid-size dataset with estimated labels from known literature trends [15, 16], and (C) a large dataset of structures where only the average and standard deviation of each image is known (adapted from [18]), resulting in some noise associated with any local label. (D) We obtain the united dataset by weighting the representation of the more reliable image-label pairs accordingly, for a total of 22730 image-label pairs spanning hardness values from 2 to 7 GPa.

7.3 Rational positioning of 3D-printed voxels to realize high-fidelity multifunctional soft-hard interfaces

The third project concerned the characterisation of the mechanical behavior of biominerals, in collaboration with Prof. A. A. Zadpoor (Delft University, The Netherlands).

Full paper: MC Saldívar[1], S Salehi[2,3], RPE Veeger[1], E Tay[1], M Fenu[4], A Cantamessa[5], M Klimopoulou[1], G Talò[2], M Moretti[2,6,7,8], S Lopa[2], D Ruffoni[5], GJVM Van Osch[1,4,9], LE Fratila-Apachitei[1], EL Doubrovski[10], MJ Mirzaali[1], AA Zadpoor[1], Rational positioning of 3D printed micro-bricks to realize high-fidelity, multi-functional soft-hard interfaces, *Cell Report Physical Science*, 4(9):101552, September 2023. https://doi.org/10.1016/j.xcrp.2023.101552.

[1] Department of Biomechanical Engineering, Faculty of Mechanical, Maritime, and Materials Engineering, Delft University of Technology;

[2] IRCCS Istituto Ortopedico Galeazzi, Cell and Tissue Engineering Laboratory;

[3] Department of Chemistry, Materials, and Chemical Engineering "Giulio Natta", Politecnico di Milano;

[4] Department of Otorhinolaryngology, Erasmus MC, University Medical Center Rotterdam;

[5] Mechanics of Biological and Bioinspired Materials Laboratory, Department of Aerospace and Mechanical Engineering, University of Liège;

[6] Regenerative Medicine Technologies Laboratory, Laboratories for Translational Research, Ente Ospedaliero Cantonale;

[7] Service of Orthopedics and Traumatology, Department of Surgery;

[8] Euler Institute, Faculty of Biomedical Sciences;

[9] Department of Orthopedics & Sports Medicine, Erasmus MC, University Medical Center Rotterdam;

[10] Faculty of Industrial Design Engineering, Delft University of Technology.

Abstract

Highlights:

- Co-continuous model of voxel microarrangement to macroscale properties;
- Functionally graded soft-hard interfaces boost biomimetic interface performance;
- Effects of soft-hard constructs on cell morphology and proteins are explored.

Summary:

Living organisms use functional gradients (FGs) to interface hard and soft materials (e.g., bone and tendon), a strategy with engineering potential. Past attempts involving hard (or soft) phase ratio variation have led to mechanical property inaccuracies because of microscale-material macroscale-property nonlinearity. This study examines 3D-printed voxels from either hard or soft phase to decode this relationship. Combining micro/macroscale experiments and finite element simulations, a power law model emerges, linking voxel arrangement to composite properties. This model guides the creation of voxel-level FG

structures, resulting in two biomimetic constructs mimicking specific bone-soft tissue interfaces with superior mechanical properties. Additionally, the model studies the FG influence on murine preosteoblast and human bone marrow-derived mesenchymal stromal cell (hBMSC) morphology and protein expression, driving rational design of soft-hard interfaces in biomedical applications.

Nanoindentation experiments

We used a TI 950 Triboindenter (Bruker, US) with a diamond conospherical probe with a tip radius of 20 μm to perform the nanoindentation (NI) experiments. We followed a previously described polishing and NI protocol. [19, 20] The NIs were performed in a grid of 33 points along the x direction and 10 points along the y direction, yielding 330 experimental data points per FG. For each FG, the initial position of the nanoindenter was placed at the edge between the regions with only soft and only hard voxels. The distance between successive test points was 500 μm in both directions. Whenever the pull-off forces were >5% of the maximum load, we obtained the reduced elastic modulus (E_r) of each point using the Johnson-Kendall-Roberts (JKR) model. [21] For cases where the pull-off forces were <5% of the maximum load, we used the Oliver-Pharr model.75 Finally, we calculated the associated elastic moduli (i.e., $E_(x)$≈$E_r(1-\nu(x)^2)$) by assuming the Poisson's ratio along the gradient ($\nu(x)$) to be described by the rule of mixtures between the hard and soft phases (i.e., $\nu(x) = \nu_H\rho(x) + (1-\rho(x))\nu_S$, $\nu_H = 0.4$, $\nu_S = 0.495$). For the linear ρ FG results, we compared the resulting elastic modulus functions against predictions made by several existing models for particle-reinforced composites, including those proposed by Nielsen et al. [22] and Counto [23] and both simplified co-continuous models proposed by Davies [24] (i.e., power and logarithmic models). Comparison with these equations allowed us to obtain the most accurate model that fits our data. For obtaining the α value of the modified co-continuous model ($E^{1/\alpha} = E_H^{1/\alpha}\rho + E_S^{1/\alpha}(1-\rho)$), we performed a bi-square nonlinear regression between all available elastic moduli of the linear ρ function and their corresponding values of the hard voxel volume fraction. For the linear, stepwise, and sigmoid $E(x)$ functions, we calculated the coefficients of determination (ordinary R^2 values) between the measured data and the designed functions to validate the accuracy of the selected characterization model.

Material characterization and modeling

Using voxel-based AM technology, we 3D printed two types of prism-shaped specimens with a linear gradient of hard material volume fraction (ρ) projected into their volume (Figs. 7.3A-C). Within these gradients, each respective value of ρ represents the ratio of the number of hard material voxels to the total number of voxels within each corresponding cross-sectional layer of the interface designs. We used VeroCyan (Stratasys, US) UV-curable photopolymer as the hard phase for both specimens. For the soft material, however, we assigned Agilus 30Clear (Stratasys) to the first specimen type and MED625FLX (Stratasys) to the second specimen type. We tested these specimens using a nanoindentation (NI) protocol [19, 20] which allowed us to interrogate multiple locations within the FG transition zones, revealing

the entire elastic behavior achievable by these composites (Figs. 7.3B-E). Furthermore, the mechanical properties of several representative volumetric elements (RVEs) extracted from these specimens were simulated using the finite element method (FEM), which indicated good agreement between the simulations and experimental results (Figs 7.3D and E).

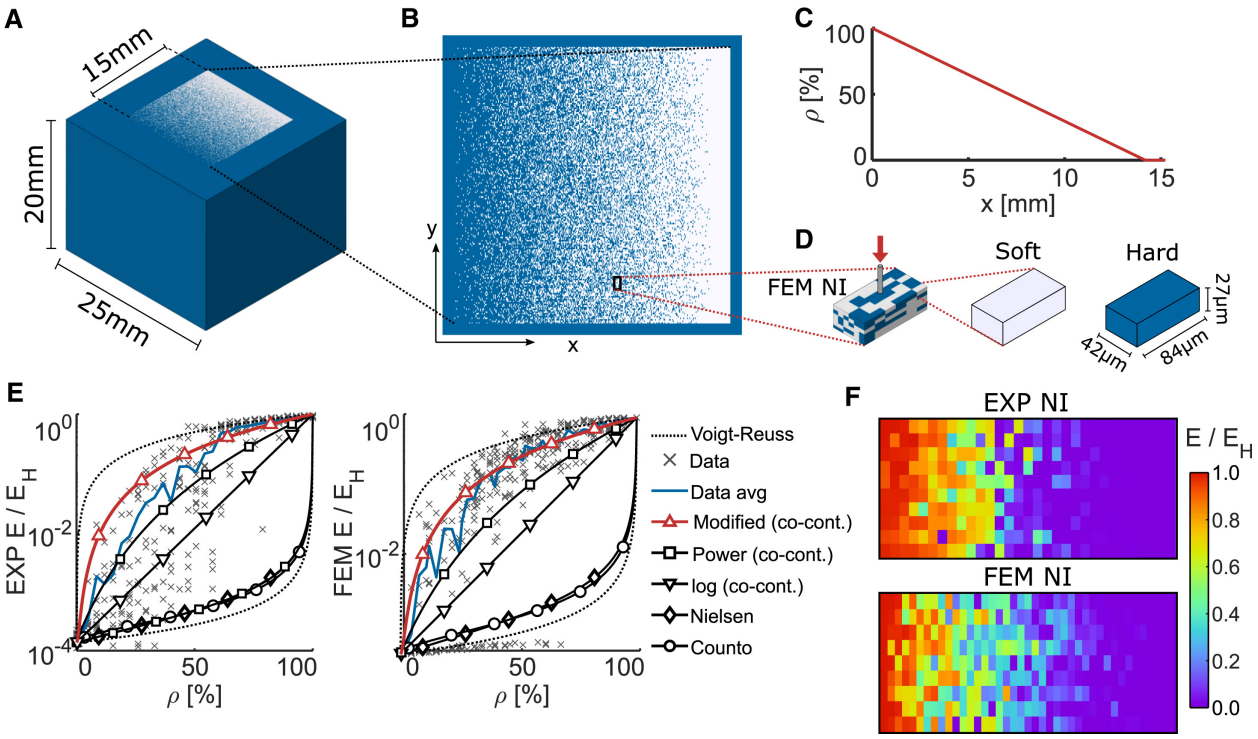


Figure 7.3: The initial characterization results. (A) The design of the 3D-printed specimen used for testing the properties of voxel-based composites via NI. (B) A representative binary image of the NI specimens with a gradient of material properties projected onto their geometry. (C) The function describing the volume fraction of the hard material, ρ, applied to the specimen for measuring the properties of these composites across their entire property space. Each $\rho(x)$ value indicates the ratio of the number of the hard material voxels to the total number of voxels in each crosssectional layer of the interface design. (D) An RVE extracted from a subsection of the NI specimens, used to create the FEM models of NI, accompanied by the dimensions of the voxels. (E) The normalized elastic modulus vs. ρ and the corresponding average response (in blue) measured through NI experiment (EXP) and predicted by computational models (FEM). These values and their associated trend lines are compared with several existing models for these composites. The modified co-continuous model was found to be the most accurate. (F) Heat maps showing the elastic moduli measured through NI as well as the corresponding FE predictions across the FG specimens, demonstrating the linear variation of ρ. These correspond to the plots presented in (E).

7.4 Indentation based stress-strain analysis of fibrolamellar bone

This last work is an ongoing side project that I would like to include in this section as the method presented here has the potential to be applied also to the characterization of the cement line, going beyond stiffness and hardness and unravelling the full inelastic deformation of this interface. The results are preliminary and will be further supported by additional experiments aimed at improving indent placement.

Authors: A Cantamessa[1], S Amini[2], S Blouin[3], G Sandront[1], MA Hartmann[3], D Ruffoni[1].

[1] Mechanics of Biological and Bioinspired Materials Laboratory, Department of Aerospace and Mechanical Engineering, University of Liège, Liège, Belgium;

[2] Department of Biomaterials, Max Planck Institute of Colloids and Interfaces, Potsdam, Germany;

[3] Ludwig Boltzmann Institute of Osteology at Hanusch Hospital of OEGK and AUVA Trauma Centre Meidling, 1st Medical Department Hanusch Hospital, Vienna, Austria.

7.4.1 Introduction

Fibrolamellar bone is a unique tissue found in the long bones of young large, fast-growing mammals such as cows, sheep, and horses. This bone type has evolved to meet two seemingly contradictory requirements: rapid growth during development and the ability to sustain high mechanical loads due to body weight [25, 26]. To achieve this, fibrolamellar bone combines distinct structural elements that together should ensure both high stiffness and sufficient toughness.

A typical fibrolamellar unit (FBU) forms between two large blood vessels and consists of three main components. First, a primary hypercalcified layer (PHL) of disordered bone is rapidly deposited, serving as a scaffold. This layer guides the subsequent formation of parallel-fibered bone (PFB), in which mineralized collagen fibers are well aligned along the longitudinal axis of the bone. As the tissue approaches the blood vessels, PFB is replaced by classical lamellar bone (LB), characterized by well-organized alternating lamellae with differently oriented collagen fibers [25, 26]. Although fibrolamellar bone supports growth and withstands mechanical loading during development, it is a transient structure. As the animal matures, it is gradually replaced through remodeling by secondary Haversian bone, also called secondary osteons [27, 28].

While the microstructure of fibrolamellar bone has been relatively well described [25, 26], its mechanical properties remain poorly understood. In particular, there is a lack of data on the local mechanical behavior of each of its fundamental components. Understanding the mechanical contribution of these basic building blocks is essential, especially given the relevance of fibrolamellar bone as a relevant model for rapid bone formation, such as in fracture callus development [26].

To better understand the structure-function relationship within fibrolamellar bone, we aim to evaluate the specific contribution of each substructure to the overall mechanical behavior of the tissue. For this

purpose, we assess both the local mechanical properties, namely the elastic modulus and the stress–strain response (with standard nanoindentation, nIND), and the mineral content of each component (with quantitative backscattered electron imaging, qBEI). Moreover, focusing on the lamellar region of this tissue, we derive indentation based stress-strain curves [29, 30], which inform on the full inelastic deformation at the nanoscale.

7.4.2 Methods

Sample preparation

A femoral mid-diaphysis segment was harvested from a calf obtained from a local abattoir. A transverse section was cut using a band saw and further subdivided into cubes of approximately 1 cm^3 cube using a water-cooled diamond saw (Buehler Isomet 1000, Switzerland). Sample preparation followed a well-established protocol [31, 32], including dehydration through a graded ethanol series, immersion in ethanol/acetone baths, and embedding in polymethyl methacrylate (PMMA). Transverse surfaces were ground with silicon carbide papers (P1200, P2400), and polished using a 1 μm diamond suspension on a silk cloth under glycol-based lubrication (Logitech PM5, UK) to minimize microcrack formation. A final ion polishing step to remove the damage introduced by mechanical polishing was performed, resulting in a surface roughness of approximately 10 nm.

Quantitative backscattered electron imaging

The local mineral content of fibrolamellar bone was assessed using qBEI, a scanning electron microscopy (SEM) technique that provides two-dimensional spatial maps of calcium content by analyzing the backscattered electron signal intensity [31]. A thin carbon coating was applied to the polished samples by vacuum evaporation (Agar SEM carbon coater, Agar, Stansted, UK) to ensure conductivity. Imaging was performed using a Zeiss SUPRA 40 SEM (Germany), equipped with a zirconium-coated field emission cathode, operated at 20 kV with a 10 mm working distance and a probe current of 280–320 pA. Images of a typical FBU were acquired at 0.57 μm pixel resolution (1024 $\times$ 768 pixels field of view) (Fig. 7.4A, B). Calibration of the grey levels to calcium weight percent (Ca wt %) was performed using carbon and aluminum standards [31, 33]. Additional high-resolution backscattered electron images (HR-BEI) (56 nm pixel size) were acquired for qualitative assessment of microstructure and porosity (Fig. 7.5C).

Quasi-static nanoindentation

The reduced modulus (E_r) was measured via quasi-static nanoindentation using a Triboindenter TI 950 (Bruker, US) equipped with a Berkovich diamond indenter tip (nominal radius: 100 nm tip). A trapezoidal load function was applied: 8 seconds loading, 20 seconds hold at 500 μN, and 8 seconds unloading, resulting in $\simeq$150 nm penetration depth. Indents were spaced 6 μm apart, which is well below the threshold of 7 times the contact depth to avoid overlapping in the inelastic deformation fields [34]. Prior to indentation, each surface was scanned at 2 μN contact force over 50 $\times$ 50 μm areas to assess surface

roughness. As the indentation depth was about ten times the surface roughness, the impact of roughness can be neglected [35, 36]. A total of 147 indents were performed across the different regions of the FBU. Force-depth curves were analyzed with the well-established Oliver-Pharr method [1] to obtain the reduced modulus (E_r).

Intention based stress-strain analysis

To assess local stress-strain behavior, cyclic partial loading-unloading nanoindentation (Fig. 7.7A) was performed using the same equipment, equipped with a conospherical diamond tip (5 μm radius). Tip calibration was based on indentations (n = 132) on fused quartz over a force range of 0 μN-1500 μN (penetration depths: 0-80 nm). The contact radius a was calculated from stiffness S using $a = \frac{S}{2E}$, with E being the known Young's modulus of fused quartz. Contact radii were then fitted to corresponding contact depths h_c using the relation: $a = C_0(1 + h_c)^{C_1}$, $C_0 = 223.3$ and $C_1 = 0.1945$. The tip radius R at each depth was estimated via: $R = \frac{a^2}{2h_c} + \frac{h_c}{2}$. Stress σ and strain ε were finally computed for each cycle (Fig. 7.7B) as: $\varepsilon = \frac{a}{R}$ and $\sigma = \frac{P}{\pi a^2}$, where P is the peak load.

Before measurements, a pre-conditioning phase of five cycles (5-50 μN peak load) was applied to reduce roughness effects. This was followed by 20 partial loading-unloading cycles (5-200 μN) at the same locations. To minimize thermal drift during prolonged testing, the tip was left engaged in imaging mode for at least 30 min before indentation.

Statistical analysis

We compared differences in mechanical properties and mineral properties among the three regions (LB, PFB, and PHL) by performing a Kruskal-Wallis test, selected due to the non-normal distribution of unpaired data. Moreover, differences between thick and thin lamellae were assessed using a Mann–Whitney U test (ranksum), as data were not normally distributed. When significant differences were detected ($p < 0.05$), post-hoc pairwise comparisons were performed using Bonferroni-corrected tests to control for multiple comparisons and reduce the risk of Type I error. All tests were two-sided, and statistical analyses were performed in MATLAB 2022a.

7.4.3 Results and discussion

Mineral content and structure across fibrolamellar substructures

To better understand how fibrolamellar bone combines both rapid growth and mechanical loading, we first examine the microstructural and compositional features of a typical FBU using qBEI and HR-BEI. These analyses reveal a highly organized, layered architecture composed of three distinct substructures: LB, PFB, and a centrally located PHL, consistent with prior descriptions (Fig. 7.4). As can be observed in Figure 7.5A-B, the PHL exhibits the highest average calcium content (28.40 ± 2.58 wt %), followed by the PFB (27.62 ± 1.93 wt %) and the LB (27.37 ± 1.44 wt %) ($p < 0.05$ for all pairwise comparisons). These

differences are relatively modest in magnitude, with percent differences of +3.69% between PHL and LB, +2.78% between PHL and PFB, and +0.91% between PFB and LB.

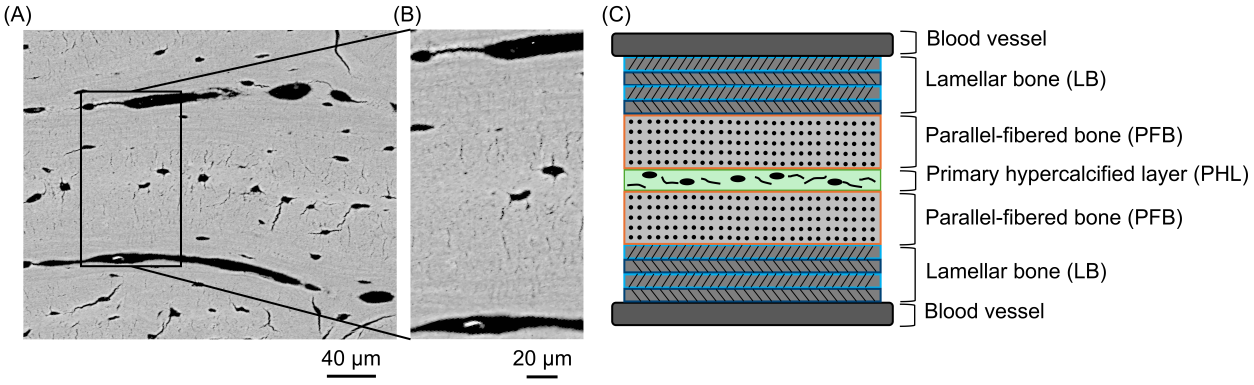


Figure 7.4: Microstructure of fibrolamellar bone. (A) qBEI showing a transverse view of fibrolamellar bone. (B) Magnified image of the fibrolamellar bone unit. (C) Schematic representation of the layered organization: two outer LB regions enclosing bands of PFB, with a central PHL.

High-resolution imaging further highlights structural distinctions among the regions (Fig. 7.5C). The PHL shows increased porosity with a dense alignment of osteocyte lacunae within the layer, suggesting rapid deposition. The PFB displays a pattern of bundled structures, corresponding to collagen fibers oriented longitudinally along the main axis of the bone. LB exhibits a well-defined alternation of thick and thin lamellae, like the architecture seen in secondary osteons.

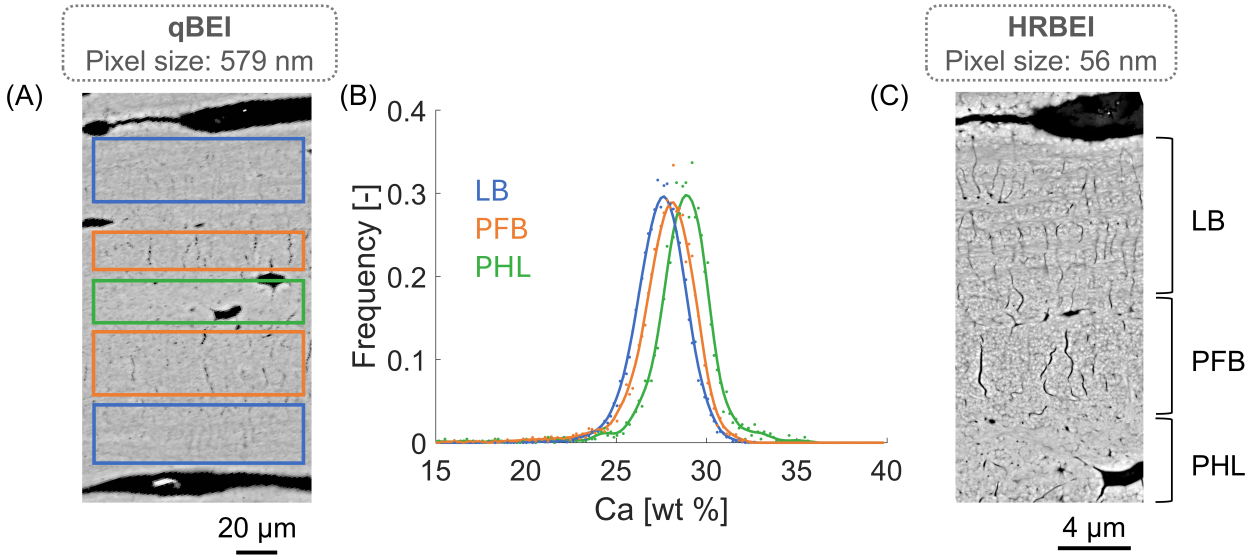


Figure 7.5: Mineral heterogeneity across fibrolamellar structures. (A) qBEI of fibrolamellar showing selected regions of interest corresponding to LB (blue), PFB (orange), and PHL (green). (B) Frequency distribution of calcium content (Ca wt %) for each region. (C) HR-BEI of the same region, revealing fine-scale structural differences between the three regions at high spatial resolution.

Mechanical properties of fibrolamellar substructures

Local stiffness measurements by nanoindentation revealed pronounced differences between substructures (Fig. 7.6A). The PFB exhibited the highest average reduced modulus (30.26 ± 1.73 GPa), significantly higher than both the PHL (24.41 ± 0.77 GPa, +21.4%, $p < 0.05$) and LB (23.88 ± 3.41 GPa, +23.57%, $p < 0.05$). There was no significant difference between PHL and LB when averaged (2.2% difference, $p = 1$).

Notably, within the lamellar bone, stiffness varied systematically between thick and thin lamellae (Fig. 7.6B). Thick lamellae exhibited a significantly higher modulus (26.38 ± 2.44 GPa) than thin lamellae (21.06 ± 1.74 GPa), corresponding to a percent difference of +22.43% ($p < 0.05$). This alternating stiffness pattern mirrors the structural alternation observed in HR-BEI and points to local mechanical heterogeneity within the LB region.

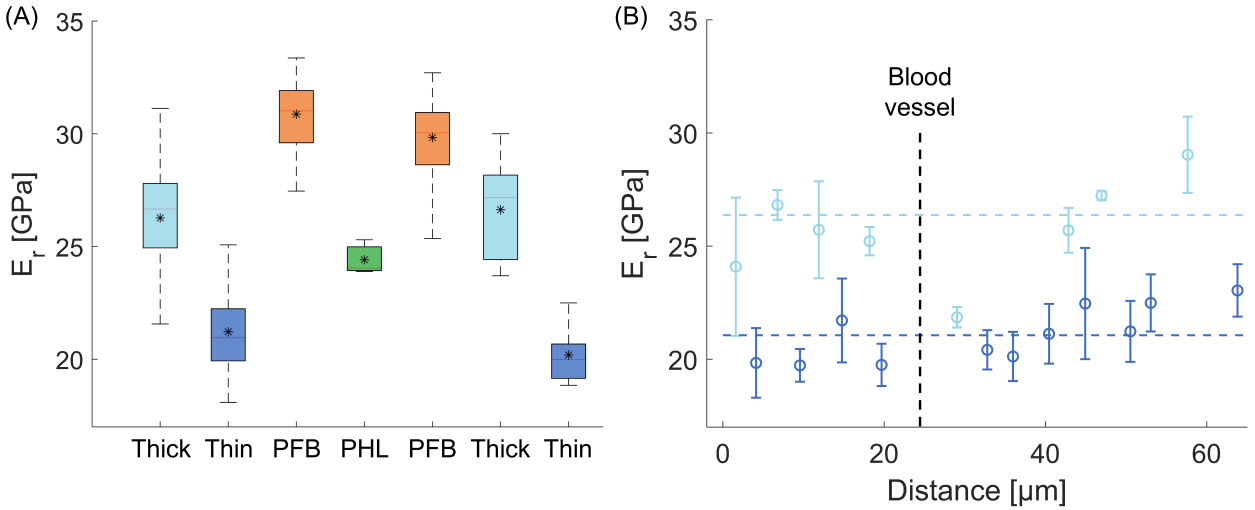


Figure 7.6: Variation of indentation modulus across FBU. (A) Boxplots of reduced modulus E_r measured in each region of the FBU: LB (thick and thin lamellae), PFB, and PHL. (B) Local variation of E_r across the LB surrounding a central blood vessel (indicated by the vertical dashed line). Each point represents the mean ± standard deviation of multiple indents along the same line. Horizontal dashed lines indicate average values in thick (bright blue) and thin (dark blue) lamellae.

Stress-strain behavior

To further characterize the mechanical behavior of the fibrolamellar substructures, additional cyclic nanoindentation tests (Fig. 7.7) were performed, with a particular focus on comparing the stress–strain response of thick and thin lamellae (Fig. 7.8).

In thick lamellae, the stress-strain curves consistently exhibit the same behavior: after the initial liner elastic phase a pronounced strain-hardening is observed, perhaps due to the compaction of the underlying porosities. In contrast, thin lamellae display more variability in their mechanical response. Some curves (e.g., indents 8 and 10) show similar response as the thick lamellae, while others (e.g., indents 7 and 11) reveal a more compliant response, followed by a region of "hyperplastcity". Interestingly, the elastic-inelastic transition in both tissues occurred at very low strains, i.e. about 1-1.5%.

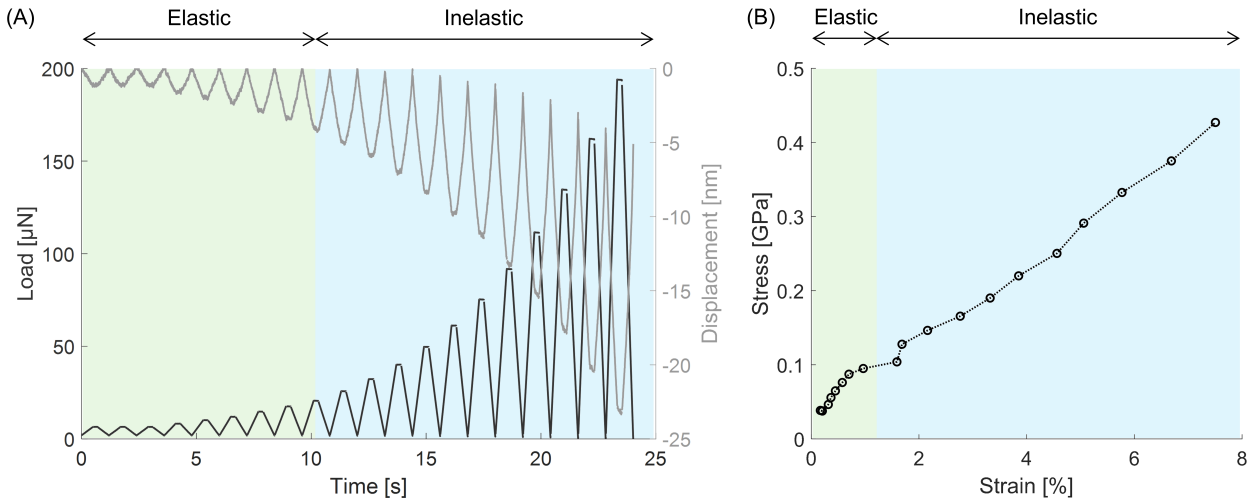


Figure 7.7: Method to extract stress-strain behavior. (A) Cyclic nanoindentation at a single location with progressively increasing loads (indents 4 from Fig. 7.8). (B) Stress-strain curves highlighting the transition from elastic to inelastic.

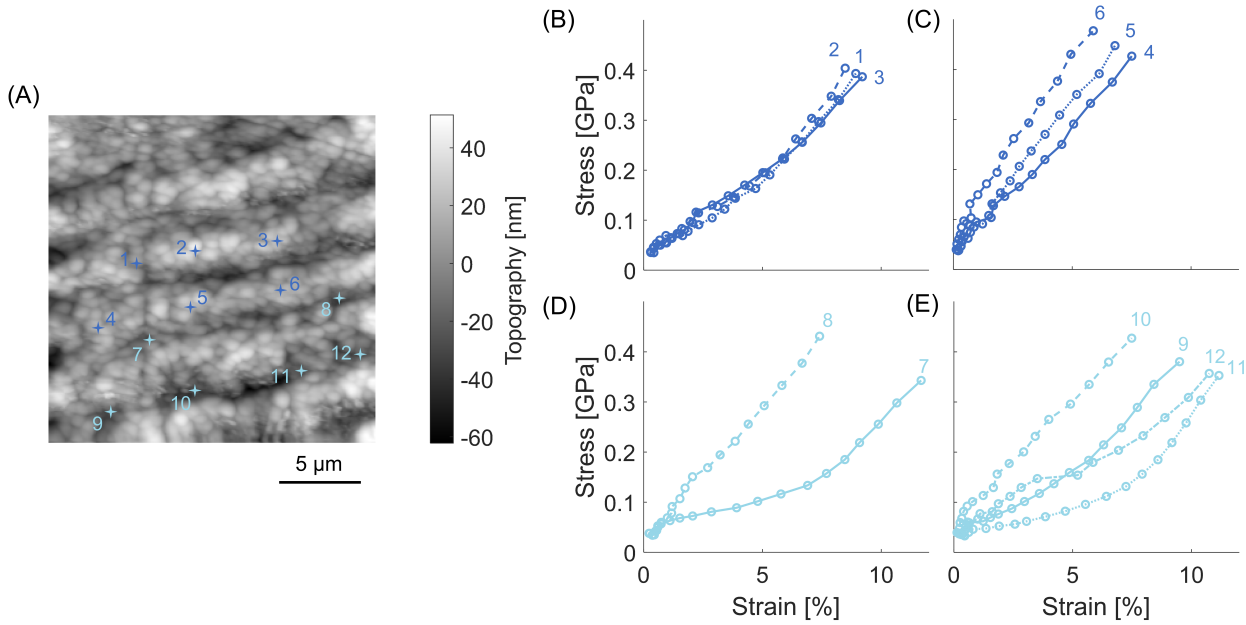


Figure 7.8: Topography and local mechanical behavior of thick and thin lamellae assessed by cyclic nanoindentation. (A) Topography map showing the positions of individual indents. (B-E) Corresponding local stress-strain curves obtained from cyclic nanoindentation at the marked positions in (A). Curves for thick lamellae are shown in darker blue (B, C), whereas those for thin lamellae are shown in lighter blue (D, E).

We assumed part of this variability in the measured response may be due to uncertainty in the indent positions. Indeed it is way more challenging to place indents in the middle of thin lamellae in comparison to thick lamellae. To better resolve this positional uncertainty, future tests will incorporate a final higher residual imprint that can be detected with post-test imaging.

Structure-function implications

Although the PHL is the most mineralized region, it displays the lowest stiffness among the three regions. This apparent mismatch suggests that while the PHL is highly mineralized, its high porosity and disordered microstructure may reduce its effective mechanical stiffness, supporting its role as a rapidly deposited scaffold during early bone formation.

The PFB, with its collagen bundles aligned parallel to the longitudinal axis of the bone, exhibits the highest stiffness, consistent with its structural role in bearing axial load. This alignment likely optimizes load transfer along the growth axis of the bone.

In the lamellar bone, the alternating modulus between thick and thin lamellae—associated with varying collagen orientation—may contribute to crack deflection and energy dissipation, enhancing toughness despite moderate mineralization. Cyclic nanoindentation further revealed that thick lamellae provide a consistent, stiffer response, while thin lamellae exhibit more heterogeneous and, in some cases, hyperplastic behavior.

Together, these results illustrate how the mechanical performance of fibrolamellar bone emerges from a subtle interplay between mineral content, collagen organization, and microstructural design

Bibliography

[1] WC Oliver and GM Pharr. An improved technique for determining hardness and elastic modulus using load and displacement sensing indentation experiments. *Journal of Materials Research*, 7(6):1564–1583, June 1992.

[2] AC Fischer-Cripps. *Introduction to Contact Mechanics*. Springer, Berlin, Germany, vol. 101 edition, 2007.

[3] GR Anstis, Chantikul P, BR Lawn, and DB Marshall. A critical evaluation of indentation techniques for measuring fracture toughness: I, direct crack measurements. *Journal of the American Ceramic Society*, 64(9):533–538, 1981.

[4] Z Huang and X Li. Origin of flaw-tolerance in nacre. *Scientific Reports*, 3(1):1693, April 2013.

[5] S Wang, X Zhu, Q Li, R Wang, and X Wang. Damage-tolerance strategies for nacre tablets. *Journal of Structural Biology*, 194(2):199–204, 2016.

[6] L Pasquini, A Molinari, P Fantazzini, Y Dauphen, JP Cuif, O Levy, Z Dubinsky, E Caroselli, F Prada, S Goffredo, M Di Giosia, M Reggi, and G Falini. Isotropic microscale mechanical properties of coral skeletons. *Journal of The Royal Society Interface*, 12(106):20150168, May 2015.

[7] S Amini and A Miserez. Wear and abrasion resistance selection maps of biological materials. *Acta Biomaterialia*, 9(8):7895–7907, 2013.

[8] C Kearney, Z Zhao, BJF Bruet, R Radovitzky, MC Boyce, and C Ortiz. Nanoscale Anisotropic Plastic Deformation in Single Crystal Aragonite. *Physical Review Letters*, 96(25):255505, June 2006.

[9] CF Böhm, P Feldner, B Merle, and SE Wolf. Conical nanoindentation allows azimuthally independent hardness determination in geological and biogenic minerals. *Materials*, 12(10), 2019.

[10] J Ihli, JN Clark, N Kanwal, YY Kim, MA Holden, RJ Harder, CC Tang, SE Ashbrook, IK Robinson, and Fiona C Meldrum. Visualization of the effect of additives on the nanostructures of individual bio-inspired calcite crystals. *Chemical Science*, 10(4):1176–1185, 2019.

[11] Francois Barthelat, Zhen Yin, and Markus J. Buehler. Structure and mechanics of interfaces in biological materials. *Nature Reviews Materials*, 1(4):16007, March 2016.

[12] JWC Dunlop, R Weinkamer, and P Fratzl. Artful interfaces within biological materials. *Materials Today*, 14(3):70–78, March 2011.

[13] A Miserez, JC Weaver, PJ Thurner, J Aizenberg, Y Dauphin, P Fratzl, DE Morse, and FW Zok. Effects of Laminate Architecture on Fracture Resistance of Sponge Biosilica: Lessons from Nature. *Advanced Functional Materials*, 18(8):1241–1248, April 2008.

[14] Z Deng, HC Loh, Z Jia, CA Stifler, A Masic, PUPA Gilbert, R Shahar, and L Li. Black drum fish teeth: Built for crushing mollusk shells. *Acta Biomaterialia*, 137:147–161, 2022.

[15] E Beniash, CA Stifler, CY Sun, GS Jung, Z Qin, MJ Buehler, and PUPA Gilbert. The hidden structure of human enamel. *Nature Communications*, 10(1):4383, September 2019.

[16] JL Cuy, AB Mann, KJ Livi, MF Teaford, and TP Weihs. Nanoindentation mapping of the mechanical properties of human molar tooth enamel. *Archives of Oral Biology*, 47(4):281–291, 2002.

[17] S Habelitz. Materials engineering by ameloblasts. *Journal of Dental Research*, 94(6):759–767, 2015. PMID: 25800708.

[18] CA Stifler, JE Jakes, JD North, DR Green, JC Weaver, and PUPA Gilbert. Crystal misorientation correlates with hardness in tooth enamels. *Acta Biomaterialia*, 120:124–134, 2021. Biomineralization: From Cells to Biomaterials.

[19] MJ Mirzaali, A Herranz de la Nava, D Gunashekar, M Nouri-Goushki, RPE Veeger, Q Grossman, L Angeloni, MK Ghatkesar, LE Fratila-Apachitei, D Ruffoni, EL Doubrovski, and AA Zadpoor. Mechanics of bioinspired functionally graded soft-hard composites made by multi-material 3d printing. *Composite Structures*, 237:111867, 2020.

[20] L Zorzetto, L Andena, F Briatico-Vangosa, L De Noni, JM Thomassin, C Jérôme, Q Grossman, A Mertens, R Weinkamer, M Rink, and D Ruffoni. Properties and role of interfaces in multimaterial 3D printed composites. *Scientific Reports*, 10(1):22285, December 2020.

[21] JC Kohn and DM Ebenstein. Eliminating adhesion errors in nanoindentation of compliant polymers and hydrogels. *Journal of the Mechanical Behavior of Biomedical Materials*, 20:316–326, 2013.

[22] LE Nielsen. Generalized equation for the elastic moduli of composite materials. *Journal of Applied Physics*, 41(11):4626–4627, 10 1970.

[23] UJ Counto. The effect of the elastic modulus of the aggregate on the elastic modulus, creep and creep recovery of concrete. *Magazine of Concrete Research*, 16(48):129–138, December 1964.

[24] WEA Davies. The theory of elastic composite materials. *Journal of Physics D: Applied Physics*, 4(9):1325–1339, September 1971.

[25] R Almany Magal, N Reznikov, R Shahar, and S Weiner. Three-dimensional structure of minipig fibrolamellar bone: adaptation to axial loading. *Journal of Structural Biology*, 186(2):253–264, May 2014.

[26] M Kerschnitzki, W Wagermaier, Y Liu, P Roschger, GN Duda, and P Fratzl. Poorly ordered bone as an endogenous scaffold for the deposition of highly oriented lamellar tissue in rapidly growing ovine bone. *Cells Tissues Organs*, 194(2-4):119–123, 2011.

[27] JW Barrera, A Le Cabec, and MM Barak. The orthotropic elastic properties of fibrolamellar bone tissue in juvenile white-tailed deer femora. *Journal of Anatomy*, 229(4):568–576, October 2016.

[28] M Kerschnitzki, W Wagermaier, P Roschger, J Seto, R Shahar, GN Duda, S Mundlos, and P Fratzl. The organization of the osteocyte network mirrors the extracellular matrix orientation in bone. *Journal of Structural Biology*, 173(2):303–311, February 2011.

[29] S Amini, M Tadayon, S Idapalapati, and A Miserez. The role of quasi-plasticity in the extreme contact damage tolerance of the stomatopod dactyl club. *Nature Materials*, 14(9):943–950, September 2015.

[30] LH He, N Fujisawa, and MV Swain. Elastic modulus and stress-strain response of human enamel by nano-indentation. *Biomaterials*, 27(24):4388–4398, August 2006.

[31] P Roschger, P Fratzl, J Eschberger, and K Klaushofer. Validation of quantitative backscattered electron imaging for the measurement of mineral density distribution in human bone biopsies. *Bone*, 23(4):319–326, October 1998.

[32] T Tang, W Landis, S Blouin, L Bertinetti, MA Hartmann, A Berzlanovich, R Weinkamer, W Wagermaier, and P Fratzl. Subcanalicular nanochannel volume is inversely correlated with calcium content in human cortical bone. *Journal of Bone and Mineral Research*, 38(2):313–325, December 2022.

[33] MA Hartmann, S Blouin, BM Misof, N Fratzl-Zelman, P Roschger, A Berzlanovich, GM Gruber, PC Brugger, J Zwerina, and P Fratzl. Quantitative backscattered electron imaging of bone using a thermionic or a field emission electron source. *Calcified Tissue International*, 109(2):190–202, August 2021.

[34] SE Campbell, VL Ferguson, and DC Hurley. Nanomechanical mapping of the osteochondral interface with contact resonance force microscopy and nanoindentation. *Acta Biomaterialia*, 8(12):4389–4396, December 2012.

[35] MS Bobji and SK Biswas. Estimation of hardness by nanoindentation of rough surfaces. *Journal of Materials Research*, 13(11):3227–3233, November 1998.

[36] E Donnelly, SP Baker, and AL Boskey. Effects of surface roughness and maximum load on the mechanical properties of cancellous bone measured by nanoindentation. *Journal of Biomedical Materials Research Part A*, 2006.

Curriculum Vitae

Astrid Cantamessa

Born 6 September 1998 in Liège, Belgium
Email address: astrid.cantamessa@outlook.com - astrid.cantamessa@uliege.be
Link to my ORBi profile: https://orbi.uliege.be/profile?uid=p195316

Education

2020 - 2025 **PhD Candidate in Biomedical Engineering**
Mechanics of Biological and Bioinspired Materials Laboratory, University of Liege, Belgium, under the supervision of Prof. D. Ruffoni.

2018 - 2020 **Master in Biomedical Engineering**
University of Liege, Belgium. Graduated with *magna cum laude*. Master Thesis at the Auckland Bioengineering Institute in New Zealand. *Evaluating outcome following knee arthroplasty using inertial measurement units*. Thesis Supervisors: Prof. L. Geris and Prof. T. Besier.

Achievements and grants

2023 **Best Poster Award** (100 Euro) for a poster presentation at the 21st National Day of Biomedical Engineering in Brussels.

2023 **Travel Award** (400 Euro) for an oral presentation at the 28th Congress of the European Society of Biomechanics in Maastricht.

2023 European Synchrotron Radiation Facility, Grenoble, France. **Proposal granted** free beamline access (12 shifts – 4 days) for the project: *High resolution SAXS/WAXS characterization of the cement*.

2020 - 2024 FRIA (Belgian Fund for Scientific Research) PhD **fellowship** for the project: *Biological and biomechanical characterization of the cement lines* (∼160.000 Euro).

2020 Award (750 Euro) for the **best Master Thesis** offered by the AiLg (Association des Ingénieurs de Liège).

Publications

2025 A Cantamessa, S Blouin, M Rummler, A Berzlanovich, R Weinkamer, MA Hartmann, D Ruffoni, *The mineralization of osteonal cement line depends on where the osteon is formed*. JBMR Plus.

2023 MC Saldívar, S Salehi, RPE Veeger, M Fenu, A Cantamessa, M Klimopoulou, G Talò, M Moretti, S Lopa, D Ruffoni, GJVM Van Osch, LE Fratila-Apachitei, EL

Doubrovski, MJ Mirzaali, AA Zadpoor, *Rational positioning of 3D printed microbricks to realize high-fidelity, multi-functional soft-hard interfaces*. Cell Reports Physical Science, 4(9):101552. https://doi.org/10.1016/j.xcrp.2023.101552. IF: 7.83.

2023 T Yeung, A Cantamessa, AW Kempa-Liehr, T Besier, J Choisne, *Personalized machine learning approach to estimating knee kinematics using only shank mounted IMU*. IEEE Sensors Journal, 23(11):12380-12387. https://doi.org/10.1109/JSEN.2023.3267398. IF: 4.33.

2023 AJ Lew, CA Stifler, A Cantamessa, A Tits, D Ruffoni, PUPA Gilbert, MJ Buehler, *Deep Learning Virtual Indenter Maps Nanoscale Hardness Rapidly and Non-destructively, Revealing Mechanism and Enhancing Bioinspired Design*. Matter, 6(6):1975-1991, https://doi.org/10.1016/j.matt.2023.03.031. IF: 19.97.

2023 AJ Lew, CA Stifler, A Tits, CA Schmidt, A Scholl, A Cantamessa, L Müller, Y Delaunois, P Compère, D Ruffoni, MJ Buehler, PUPA Gilbert, *A Molecular Scale Understanding of Misorientation Toughening in Corals and Seashells*. Advanced Materials., 35(28):2300373. https://doi.org/10.1002/adma.202300373. IF: 29.4.

2021 SM Bolam., B Batinica, TC Yeung, S Weaver, A Cantamessa, TC Vanderboor, S Yeung, JT Munro, JW Fernandez, TF Besier, AP Monk, *Remote Patient Monitoring with Wearable Sensors Following Knee Arthroplasty*. Sensors, 21(15):5143. https://doi.org/10.3390/s21155143. IF: 3.85.

Supervision

2023 - 2024 L Pavanetto, *Heavy metal reinforcement in biomaterials: the influence of zinc on the mechanical properties of the mandibles of leafcutter ants Acromyrmex octospinosus workers*. http://hdl.handle.net/2268.2/20910.

2023 - 2024 P Qalaj, *Finite element analysis of nanoindentation across bone interfaces and effects on the measured mechanical properties*. http://hdl.handle.net/2268.2/20434.

2023 - 2024 S Bastin, *Characterization of the osteocyte lacuna-canalicular network and its interplay with the cement line in human osteonal bone*. http://hdl.handle.net/2268.2/20863.

2022 - 2023 G Sandront, *Stress-strain characterization of fibrolamellar bone*. http://hdl.handle.net/2268.2/22264.

2020 - 2021 P Muraro, *Biomechanical characterization of fibrolamellar bone using modulus mapping*. http://hdl.handle.net/2268.2/11555.

Presentation and conference abstracts

Oral presentations

2024 **XXIII Internation Conference on Mechanics in Medicine and Biology**, Brussels, Belgium. A Cantamessa, V Schemenz, S Blouin, S Amini, M Rummler, A Berzlanovich, R Weinkamer, W Wagermaier, MA Hartmann, D Ruffoni, *Exploring material, mechanical and biological features of cement lines in human osteons*.

2024 **European Society of Biomechanics Conference**, Edinburgh, Scotland. A Cantamessa, V Schemenz, S Blouin, S Amini, M Rummler, A Berzlanovich, R Weinkamer, W Wagermaier, MA Hartmann, D Ruffoni, *Cement lines material properties and interplay with the lacuna-canalicular network in human osteonal bone*.

2023 **Annual Benelux meeting of IEEE Engineering in Medicine and Biology Society**, Brussels, Belgium. A Cantamessa, S Blouin, S Amini, M Rummler, A Berzlanovich, R Weinkamer, MA Hartmann, D Ruffoni, *Mineralization and mechanical insights of cement lines in human osteonal bone*.

2023 **European Society of Biomechanics Conference**, Maastricht, The Netherlands. A Cantamessa, S Blouin, S Amini, M Rummler, A Berzlanovich, R Weinkamer, MA Hartmann, D Ruffoni, *Mineral content and mechanical properties of cement lines in human osteonal bone*.

2022 **European Society of Biomechanics Conference**, Porto, Portugal. A Cantamessa, P Muraro, Y Delaunois, P Compère, S Blouin, MA Hartmann, D Ruffoni, *Mineral content and biomechanical properties of fibrolamellar bone*.

Poster presentations

2023 **21st National Day of Biomedical Engineering & Annual Benelux meeting of IEEE Engineering in Medicine and Biology Society**, Brussels, Belgium. A Cantamessa, S Blouin, S Amini, M Rummler, A Berzlanovich, R Weinkamer, MA Hartmann, D Ruffoni, *Mineralization and mechanical insights of cement lines in human osteonal bone*.

2023 **Annual meeting of the American Society of Bone and Mineral Research & Symposium: Osteocytes in Bone Health and Disease and as Therapeutic Target Cells**, Vancouver, Canada. A Cantamessa, S Blouin, S Amini, M Rummler, A Berzlanovich, R Weinkamer, MA Hartmann, D Ruffoni, *A multimodal analysis of cement lines in human osteonal bone*.

2022 **1st National Afterwork of Biomedical Engineering of the National Commit-**

tee of Biomedical Engineering, Brussels, Belgium. A Cantamessa, L Müller, D Ruffoni, *Biological and biomechanical properties of cement lines in human bone*.

Collaborative conference contributions

2023 **International Conference on Mechanics of Biomaterials and Tissues**, Hawaii, USA. A Cantamessa, T Volders, S Blouin, L Zorzetto, S Amini, M Rummler, H Razi, R Weinkamer, MA Hartmann, D Ruffoni, *Properties of cement lines in osteonal bone and damage behavior of osteon-inspired composites*.

2022 **Annual Conference of the European Society for Biomaterials**, Bordeaux, France. MC Saldívar, RPE Veeger, Q Grossman, A Cantamessa, D Ruffoni, EL Doubrovski, MJ Mirzaali, AA Zadpoor, *Characterization and Modeling of Functional Gradients for Enabling Tough Biomimetic Devices*.

Extracurricular experience

2023 - 2025 Member of the Diversity, Inclusion and Membership Committee of the European Society of Biomechanics.

2022 - 2025 Member and vice-president (since Sept. 2024) of the Doctorate Board of ULiège, executive body of the University Council for Doctoral Training and the Doctorate.

2021 - 2023 Communication Manager for the ULiège PhD Community.

